



## City Research Online

### City, University of London Institutional Repository

---

**Citation:** Lockett, John Francis (1987). Heat Transfer from Roughened Surfaces using Laser Interferometry. (Unpublished Doctoral thesis, City, University of London)

This is the submitted version of the paper.

This version of the publication may differ from the final published version.

---

**Permanent repository link:** <https://openaccess.city.ac.uk/id/eprint/20856/>

**Link to published version:**

**Copyright:** City Research Online aims to make research outputs of City, University of London available to a wider audience. Copyright and Moral Rights remain with the author(s) and/or copyright holders. URLs from City Research Online may be freely distributed and linked to.

**Reuse:** Copies of full items can be used for personal research or study, educational, or not-for-profit purposes without prior permission or charge. Provided that the authors, title and full bibliographic details are credited, a hyperlink and/or URL is given for the original metadata page and the content is not changed in any way.

**HEAT TRANSFER FROM ROUGHENED SURFACES  
USING LASER INTERFEROMETRY**

by

**John Francis LOCKETT**

**A dissertation submitted to  
The City University  
in fulfilment of the requirement  
for the degree of  
Doctor of Philosophy**

**APRIL 1987**

**Department of Mechanical Engineering  
The City University,  
LONDON**

## ABSTRACT

Turbulent forced convective heat transfer is often encountered in engineering flows. A method of improving the heat transfer from a smooth surface is to add ribs and generate some turbulence. The precise nature and spacing of these ribs can have a considerable effect on the heat transferred. In this investigation the novel method of holographic interferometry is used to study the thermal fields over numerous two-dimensional ribbed geometries and to ascertain the Nusselt number distribution around them. Full field information is provided as the fringe pattern generated is essentially an isotherm contour map of the flow situation. Hence, this makes it ideally suited to verify the theoretical solutions obtained from Large Eddy Simulations (LES) and Finite Element predictions. This latter predictive technique is used in this investigation and the solutions obtained are compared with the experimental results.

Initially, a smooth surface geometry was investigated to verify the accuracy of the experimental technique. Excellent results were achieved, but a necessity to have momentum field information was identified. Ribbed geometries with a pitch to height ratio of 7.2 : 1 were then studied. Double exposure and real-time techniques enabled both detailed thermal measurements to be made and any time-dependency of the field to be identified. Flow rates up to nuclear reactor conditions ( $e^+ = 600$ ) were studied and typical interferograms are illustrated. A Reynolds number dependency for the heat transfer distribution for a rounded-rib geometry was identified while the square-ribbed geometry distribution was observed to be Reynolds number independent. The addition of an insulating deposit to the surfaces is also studied. It led to smaller peak heat transfer rates and larger surface temperature variations.

For large thermal gradients, usually at high flow rates, a ray crossing regime was identified. This led to a limitation of the technique as no information in this area could be extracted. However, a boundary layer extrapolation from the identifiable regions to the wall eradicates this limitation, but is only possible if momentum field information is available. Hence, this problem did not act as a limit to the smooth surface or square-ribbed geometry but did for all others.

Numerical simulations of the flow were undertaken using the  $k-\epsilon$  and  $q-f$  models employed in the finite element code FEAT. Because a low flow rate was modelled the conventional wall functions were not considered appropriate and hence a low Reynolds number model was used. Incorrect modelling of the length scales in the near wall region using this model led to errors in the thermal field predictions. Hence, only a qualitative comparison with the experimental results is undertaken and a recommendation for improved modelling is proposed based on this comparison.

## LIST OF CONTENTS

	<u>Page</u>
ABSTRACT	1
LIST OF CONTENTS	2
LIST OF FIGURES	4
NOMENCLATURE	7
ACKNOWLEDGEMENTS	11
CHAPTER 1. INTRODUCTION	13
CHAPTER 2. LITERATURE SURVEY	20
2.1. HOLOGRAPHIC INTERFEROMETRY	21
2.1.1. Classical Interferometers	21
2.1.2. Early Holography	25
2.1.3. Laser Development	27
2.1.4. Revival in Holography	30
2.1.5. Early Holographic Interferometry	32
2.1.6. Heat Transfer Applications	34
2.1.7. Variations to the Conventional Holographic Interferometry	36
2.2. TURBULENT CONVECTIVE HEAT TRANSFER	40
2.2.1. Momentum field	41
2.2.2. Heat Transfer Coefficient Distributions around a Ribbed surface	43
2.2.3. Theoretical Predictions of Heat Transfer Coefficients	50
CHAPTER 3. EXPERIMENTAL APPARATUS	53
3.1. DESIGN AND CONSTRUCTION OF THE WIND TUNNEL	53
3.2. HEATING SYSTEM	61
3.3. OPTICAL APPARATUS	63
CHAPTER 4. EXPERIMENTAL PROCEDURE AND DATA ANALYSIS	68
4.1. HYDRODYNAMIC DATA MEASUREMENTS	68
4.1.1. Velocity Profiles	70
4.1.2. Static Pressure	71
4.1.3. Wall Shear Stress	71
4.1.4. Turbulence Intensity	72
4.2. INTERFEROMETRIC DATA MEASUREMENT	74
4.2.1. Holographic Technique	74
4.2.2. Processing Procedure	78
4.2.3. Viewing Procedure	81
4.3. HOLOGRAPHIC ANALYSIS PROCEDURE	85

	<u>Page</u>
CHAPTER 5. TURBULENT MODELLING OF THE FLOW FIELD	88
5.1. BASIC EQUATIONS	88
5.2. TURBULENT MODELS	90
5.3. SOLUTION PROCEDURES	97
5.3.1. Finite difference	97
5.3.2. Finite elements	98
5.4. FEAT ANALYSIS	100
5.5. USING THE FEAT CODE	104
CHAPTER 6. RESULTS AND DISCUSSION	107
6.1. MOMENTUM FIELD EXPERIMENTAL RESULTS	107
6.2. THERMAL FIELD EXPERIMENTAL RESULTS	113
6.2.1. Smooth Surface results	114
6.2.2. Square rib roughened geometry	119
6.2.3. Rounded rib-roughened geometry	124
6.2.4. Deposited surfaces	128
6.3. THEORETICAL PREDICTIONS	131
6.3.1. Ranging conditions	132
6.3.2. Momentum Field Predictions	134
6.3.3. Thermal Field Predictions	135
CHAPTER 7. CONCLUSIONS	140
REFERENCES	144
APPENDIX A. THEORY OF HOLOGRAPHY	152
APPENDIX B ESTIMATION OF EXPERIMENTAL ERRORS	159
APPENDIX C GENERAL THEORY OF FINITE ELEMENT MODELLING	168
APPENDIX D ANALYSIS OF TYPICAL HOLOGRAM	173
APPENDIX E DESCRIPTION OF VIDEO	175
APPENDIX F PUBLISHED PAPERS	178
APPENDIX G FIGURES	179

## LIST OF FIGURES

- FIGURE 1.1. RIBBED PROFILES
- FIGURE.2.1. MICHELSON INTERFEROMETER
- FIGURE.2.2. MACH ZEHNDER INTERFEROMETER
- FIGURE.2.3. PULSED RUBY LASER
- FIGURE.2.4. RUBY LASER ENERGY LEVELS
- FIGURE.2.5. HELIUM-NEON LASER
- FIGURE.2.6. CONVENTIONAL HOLOGRAPHIC INTERFEROMETER
- FIGURE 2.7. GENERAL ILLUMINATION
- FIGURE.2.8. IMAGE PLANE HOLOGRAPHY
- FIGURE.2.9. WOLLASTON PRISM SCHLIEREN INTERFEROMETER
- FIGURE.2.10. SUPERIMPOSING OF TWO HOLOGRAMS
- FIGURE.2.11. USE OF TWO REFERENCE BEAMS
- FIGURE.2.12. COMPARISON OF THE RELATIVE HEAT TRANSFER DISTRIBUTIONS OBTAINED
- FIGURE.3.1. INITIAL INLET GEOMETRY
- FIGURE.3.2. SCHEMATIC ILLUSTRATION OF FAN
- FIGURE.3.3. SCHEMATIC DIAGRAM OF WIND TUNNEL
- FIGURE.3.4. CROSS SECTION THROUGH WORKING SECTION
- FIGURE.3.5. SQUARE RIB GEOMETRY STUDIED
- FIGURE 3.6. ADDITIONAL GEOMETRY PROFILES
- FIGURE.3.7. SCHEMATIC DIAGRAM OF IMAGE-PLANE INTERFEROMETER
- FIGURE 3.8. PHOTOGRAPHIC ILLUSTRATIONS OF TEST RIG
- FIGURE 4.1. COLOUR SENSITIVITY FOR HOLOGRAPHIC PLATES
- FIGURE 4.2. HURTER-DRIFFIELD CURVE
- FIGURE 5.1. MESHES USED TO GENERATE FEAT PREDICTIONS

- FIGURE 6.1. NON-DIMENSIONAL VELOCITY PROFILE
- FIGURE 6.2. ROUGH WALL VELOCITY PROFILE
- FIGURE 6.3. FRICTION FACTOR RESULTS
- FIGURE 6.4. SHEAR STRESS MEASUREMENTS AROUND THE SMOOTH WALLS
- FIGURE 6.5. TURBULENCE LEVELS AT INLET ( $Re = 12,820$ )
- FIGURE 6.6. INTERFEROGRAMS OF SMOOTH WALL
- FIGURE 6.7. NEAR WALL ENLARGEMENT
- FIGURE 6.8. TEMPERATURE PROFILES FOR A SMOOTH DUCT
- FIGURE 6.9. HEAT TRANSFER RESULTS FOR SMOOTH SURFACES
- FIGURE 6.10. REAL-TIME IMAGE OF SMOOTH WALL
- FIGURE 6.11. HIGH SPEED FILM ILLUSTRATING STRUCTURE
- FIGURE 6.12. DEVELOPING FLOW REGION
- FIGURE 6.13. NUSSELT NUMBER DISTRIBUTION FOR DEVELOPING FLOW
- FIGURE 6.14. DOUBLE EXPOSURE IMAGES OF SQUARE RIBBED GEOMETRY
- FIGURE 6.15. ABSOLUTE NUSSELT NUMBERS FOR SQUARE RIBBED GEOMETRY
- FIGURE 6.16. COMPARISON OF ABSOLUTE HEAT TRANSFER DATA WITH OTHER WORKERS
- FIGURE 6.17. NUSSELT NUMBER DISTRIBUTION FOR SQUARE RIB
- FIGURE 6.18. REAL TIME IMAGE OF SQUARE RIB
- FIGURE 6.19. DOUBLE EXPOSURE IMAGES OF ROUNDED RIB SURFACE
- FIGURE 6.20. NUSSELT NUMBER DISTRIBUTION FOR ROUNDED RIB
- FIGURE 6.21. REAL TIME IMAGES OF ROUNDED RIB
- FIGURE 6.22. DOUBLE EXPOSURE IMAGES OF SQUARE RIB DEPOSITED SURFACE
- FIGURE 6.23. DOUBLE EXPOSURE IMAGES OF ROUNDED RIB DEPOSITED SURFACE
- FIGURE 6.24. NUSSELT NUMBER DISTRIBUTION FOR SQUARE RIB DEPOSITED SURFACE
- FIGURE 6.25. NUSSELT NUMBER DISTRIBUTION FOR ROUNDED RIB DEPOSITED SURFACE.

- FIGURE 6.26 REAL TIME IMAGES FOR SQUARE RIB DEPOSITED SURFACE
- FIGURE 6.27 REAL TIME IMAGES OF ROUNDED RIB DEPOSITED SURFACE
- FIGURE 6.28 INITIAL TEST MESH (14 X 10 ELEMENTS)
- FIGURE 6.29 INLET TEST VELOCITIES
- FIGURE 6.30 PREDICTED VELOCITY PROFILES AT WORKING SECTION
- FIGURE 6.31 PREDICTED TURBULENCE LEVELS AT WORKING SECTION
- FIGURE 6.32 ILLUSTRATION OF MESHING PROBLEMS
- FIGURE 6.33 MOMENTUM FIELD PREDICTIONS FOR RIBBED GEOMETRIES
- FIGURE 6.34 ENLARGED MOMENTUM FIELD AROUND RIB
- FIGURE 6.35 THERMAL FIELD PREDICTIONS FOR SMOOTH TUNNEL
- FIGURE 6.36 HEATER PLATE SECTION FOR SMOOTH TUNNEL
- FIGURE 6.37 THERMAL FIELD PREDICTIONS FOR RIBBED GEOMETRIES
- FIGURE 6.38 HEAT FLUX DISTRIBUTION FOR RIBBED GEOMETRIES

#### APPENDIX FIGURES

- FIGURE A.1 LINEARY POLARISED PLANE WAVE
- FIGURE C.1 BOUNDARY CONDITIONS FOR SURFACE  $\Omega$
- FIGURE C.2 STRUCTURE  $\Omega$  DIVIDED INTO ELEMENTS
- FIGURE C.3 CROSS SECTION OF FUNCTION AT NODE  $i$

## NOMENCLATURE

A	area
$A\mu$	modelling coefficient
B	wall constant
$C_{1f}$	modelling coefficient
$C_{2f}$	modelling coefficient
$C_{1\epsilon}$	modelling coefficient
$C_{2\epsilon}$	modelling coefficient
$C\mu$	modelling coefficient
$C_D$	modelling coefficient
$C_f$	friction factor
$C_{Li}$	correction term for refraction
$C_p$	thermal capacity
d	diameter
D	distance around ribbed surface
$D_e$	equivalent diameter
$D_f$	damping function
e	rib height
$e^+$	rib Reynolds number
E	electric field intensity
f	vorticity of large scale eddies
g	gravitational constant
G	Gladstone-Dale constant
h	heat transfer coefficient
H	height of tunnel
I	current
k	turbulent kinetic energy

K	thermal conductivity
$K_1$	displacement constant
$K_2$	displacement constant
$l$	turbulent length scale
n	frequency
N	fringe order
Nu	Nusselt number
p	fluctuating pressure
P	mean pressure
$\tilde{P}$	instantaneous pressure
Pr	Prandtl number
q	turbulence intensity
$q_w$	wall heat flux
Q	heat flux
R	resistance
Ra	Rayleigh number
Re	Reynolds number
Ri	Richardson number
S	rib separation
St	Stanton number
t	time
T	mean temperature
$T^+$	dimensionless temperature $(T_w - T)\rho C_p U^* / q_w$
$\tilde{T}$	instantaneous temperature
u	fluctuating velocity (x direction)
U	mean velocity (x direction)
$\tilde{U}$	instantaneous velocity (x direction)
$U_B$	bulk velocity

$U^*$	friction velocity $(\tau_w/\rho)^{1/2}$
$U^+$	dimensionless velocity $(U/U^*)$
$v$	fluctuating velocity (y direction)
$V$	mean velocity (y direction)
$\tilde{V}$	instantaneous velocity (y direction)
$V_D$	voltage
$w$	fluctuating velocity (z direction)
$W$	mean velocity (z direction)
$\tilde{W}$	instantaneous velocity (z direction)
$W_D$	width of duct
$w^e$	base function
$x$	streamwise direction
$y$	direction normal to upper and lower walls
$y^+$	dimensionless height $(U^*y/\nu)$
$z$	direction normal to side walls

#### Greek symbols

$\alpha$	modelling coefficient
$\alpha_t$	thermal diffusivity
$\gamma$	angle
$\delta$	half channel height
$\Delta$	turbulent energy dissipation
$\epsilon$	dissipation of turbulent kinetic energy
$e$	fluctuating temperature
$\kappa$	wall constant
$\lambda$	wavelength
$\mu$	dynamic viscosity
$\mu_t$	turbulent viscosity

$\nu$	kinematic viscosity
$\rho$	density
$\sigma$	molecular Prandtl number
$\sigma_k$	molecular modelling constant
$\sigma_\epsilon$	molecular modelling constant
$\sigma_q$	molecular modelling constant
$\sigma_f$	molecular modelling constant
$\tau$	shear stress
$\phi$	ray path
$\psi$	phase difference
$\omega$	frequency

### Subscripts

d	referring to hydraulic diameter
i	tensor notation
j	tensor notation
k	tensor notation
l	local position
o	zeroth position
t	turbulence
w	wall position
obj	object wave
rec	reconstruction wave
ref	reference wave
rw	rough wall
sw	smooth wall

## ACKNOWLEDGEMENTS

This study would not have been possible without the sponsorship of the Science and Engineering Research Council and the CEGB Berkeley Nuclear Laboratories under award number EA004.

I would like to express my gratitude to Dr. Michael W. Collins for his considerable help and supervision during my studentship at The City University. Thanks are also expressed to the following members of the Mechanical Engineering Department for their help: Dr. R.S. Neve, Mr. R. Vipond, Dr. R.W.T. Preater and Dr. P. Voke (now at Queen Mary College, London), also, to Mr. R. Croft of the Physics Department.

I should also like to thank Jack Spencer for his help and advice on the construction method of the rig and to Deb for building large parts of it. Additional thanks are expressed to Bob Staines of the Physics Department whose knowledge of laser techniques helped considerably in the early stages of this project. Other members of the technical support staff I would like to thank include: Jim Lee, Joe Heaphy, Ernie Coles, and Len Gonella. Finally special thanks are expressed to Chris Miller whose expert photographic skills aided in the recording techniques used in this thesis.

The advice and comments of Dr. R.T. Szczepura of Berkeley Nuclear Laboratories are also acknowledged. In addition thanks are expressed for the considerable help given by Mr. R.M. Smith and Mr. S. Hickmott during my four month placement at the CEGB.

Finally, I would like to thank the reprobates I have had the pleasure of sharing an office with during the last three years. Their useful discussions and considerable, but not always relevant, advice was most informative.

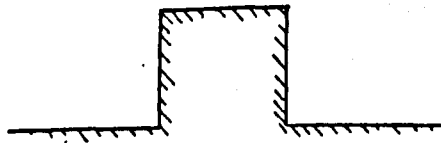
## CHAPTER ONE

### INTRODUCTION

The basic equations for fluid flow, either laminar or turbulent, are three-dimensional and time dependent in character. Solution of these equations may be obtained by time averaging, finite element techniques, or by spacially averaging, Large Eddy Simulations (L.E.S.). Although these flow solution schemes are complex and provide detailed information on the flow situation, it is by no means certain that the data they produce is of a sufficiently accurate nature. Hence experimental verifications for the predictions are required. One technique which has been recently developed that provides detailed information on the thermal fields over complex two-dimensional flow geometries is holographic interferometry. It is this method that has been used throughout this investigation to provide information concerning thermal fields over the flow geometries. Nusselt number distributions around the flow profiles may then be assigned, and the limiting operating conditions for the ribbed geometries decided. In addition, the interferograms produced have been used to verify finite element predictions obtained from the FEAT code at the CEGB Berkeley Nuclear Laboratories.

All the four ribbed geometries selected were chosen so as to represent flow conditions experienced in the centre of an Advanced Gas-Cooled Reactor (A.G.R.). They were assumed to be two-dimensional and range in complexity from a square rib, through a rounded rib, and a square rib with deposit, to a rounded rib with a deposit. These four geometries are illustrated below, in Figure 1.1.

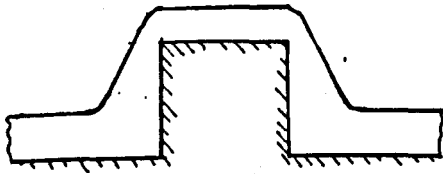
All rib spacing remained fixed for the duration of the study at 7.2 : 1 as this is the one used in the A.G.R. Other variations were not undertaken because of time limitations. The size of the ribs in the reactor are much smaller than those used in this study and are three-dimensional, unlike those used that are two-dimensional. Studies in the past have illustrated that modelling reactors like this gives acceptable results and so justifies this procedure. Comparable turbulent flow rates are studied,  $e^+$   $\approx$  600 for the reactor and the experimental rig but differing thermal gradients. These are typically kept at about  $\Delta T \approx 30^\circ\text{C}$  for the experimental project. This is not considered to be a problem as the holographic technique is being used as a diagnostic tool to ascertain the size and location of the hot spots occurring around the geometries and so enable the operating conditions in the reactor to be established.



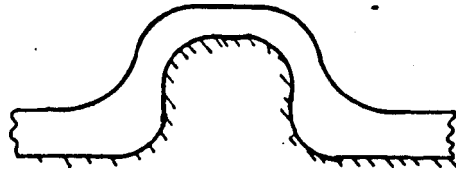
Square



Rounded



Square with Deposition



Rounded with Deposition

FIGURE 1.1. RIBBED PROFILES

An initial investigation using a smooth surface was undertaken to verify the results of the new technique. Some heat transfer information concerning the square-rib is available and this acts as an additional check on the results. But no work has been published on the remaining three surfaces.

Rounded ribs were studied as these are more typical of the type found in the A.G.R. Square ribs have been studied in the past as a theoretical shape for which the governing parameters of the heat transfer were determined. The rounded-rib surface investigation studied conditions more typically encountered in a reactor, while deposited surfaces were studied to determine the effect of a build up of a carbon deposit on the ribs. Its conductivity and flow profile were decided by Mantle (1986) after studying deposits formed on some A.G.R. fuel clusters during experimental trials with coolants. The deposit was cast onto the surface to ensure uniformity of the profile.

The rib spacing throughout the investigation was kept constant at 7.2 : 1, this being the value found in the core of the A.G.R.

Holography was first developed by Gabor (1948). Its introduction enabled the conventional Mach-Zehnder interferometer to be modified by Haines and Hildebrand (1966) to produce a holographic interferometer. This new technique was less experimentally demanding and produced an improved image quality. The basic principle for this method is to pass a coherent beam through an object field on two occasions. Once under ambient conditions and again when the field has been heated. The phase change occurring between the two exposures is then recorded on an interferogram. This is possible because holographic techniques are employed and they are able to record both the amplitude and the phase of coherent light sources. Superimposed on the interferogram is a series of fringes which are directly proportional to the original phase change. In our case, they are isotherms. Hence heat transfer information is readily available.

Two procedures may be followed to record the fringe pattern. The first is a double exposure method that involves recording both images on the plate before photographic processing. A permanent image results that may be viewed at a later date. The second is a real-time technique, whereby only the ambient exposure is recorded before processing. After the plate has dried, it is replaced in its original position and the fringe pattern is viewed in 'real-time'. The power of the technique is that the object field is not disturbed by any invasive probe. Energy absorption from the light beam is negligible when compared to the energy transfer in the observed process.

Initial work undertaken at A.E.R.E. Harwell by Walklate (1983) successfully illustrated the power of the holographic technique. However errors arising in his investigation were corrected in this study. Incorrect modelling of the Biot number relationship between the fuel can and the fluid was identified. Hence, the copper surface was replaced by a stainless steel one, but the exact relationship was not attained because carbon dioxide is the working fluid in A.G.Rs. Walklate (1983) observed negative heat transfer regions at the front of the rib caused by an insulation problem at the base of the rib. Hence, a cement with a similar conductivity to stainless steel is used to attach the square ribs, while the rounded rib surface is machined from one block of steel. Furthermore the addition of the time dimension enables the sequential behaviour of the thermal field to be studied.

A theoretical prediction for the heat transfer distribution around the square and rounded rib profiles is made using the finite element code FEAT (Finite Element Analysis of Turbulent transport). Because of the low Reynolds numbers studied experimentally, a low Reynolds number model was used to predict the flow situation. This investigation was undertaken at Berkeley during a four month placement.

Due to a time limitation only two surfaces were studied. Familiarisation with the FEAT code was obtained by investigating the effect of numerous inlet conditions on the state of development at the working section. Predictions then made for the thermal field over ribs were compared with the experimental results obtained. The discrepancies observed enabled modifications to be proposed in the low Reynolds number model being developed at Berkeley. Hence, only a qualitative comparison was made between the predictions and the experimental results.

The objectives of this project include the following:

1. Prove the viability of the technique using smooth surfaces upon which abundant data is available concerning thermal profiles and heat transfer coefficients.
2. Obtain detailed thermal fields over rib roughened geometries with and without deposition so that Nusselt number distributions may be determined.
3. Verify finite element low Reynolds number predictions made by FEAT, and
4. Provide instantaneous interferograms which may be compared to Large Eddy Simulation predictions.

To observe flow conditions over ribbed geometries a wind tunnel was constructed. The room size acts as a limit for the length of the tunnel and so although the length is sufficient for flow over ribs to develop, it may not be for the smooth surface investigations. Transparent sides to the working section enable the object beam to traverse the measured surface. Problems arising in the construction of the tunnel are discussed along with the measurement techniques employed to document the flow conditions. Validation of the interferometric technique was undertaken by recording numerous interferograms of the flow over a smooth surface. Heat transfer information obtained was compared to universal data to ascertain the accuracy of the technique. An error assessment may then be undertaken so that confidence in the results is achieved.

Results for the thermal fields over the ribbed geometries then forms the main scope of this thesis. The double exposure images permit detailed Nusselt number distributions to be determined that may be compared with other workers' results for the square rib geometry. The three further geometries give insights into the heat transfer processes over ribbed surfaces. A measure of the ability of the FEAT code to predict thermal fields is also obtained. Finally simulated holograms may be produced from Large Eddy Simulations so that a direct comparison with the interferograms is possible.

The layout of this thesis is given as follows:

Chapter Two presents a survey of work related to holographic interferometry and heat transfer from ribbed surfaces.

Chapter Three describes the experimental apparatus constructed to enable interferograms to be taken.

Chapter Four outlines the procedures undertaken to instrument the tunnel and analyse the interferograms.

Chapter Five presents the basic governing equations for turbulent flow and outlines the procedures used to solve them in the FEAT code.

Chapter Six presents the momentum and thermal field experimental results for both the double exposure and real-time interferograms. These are then compared with the theoretical predictions.

Finally, a brief summary of the findings and conclusions is given in Chapter Seven.

## CHAPTER TWO

### LITERATURE SURVEY

Holographic interferometry is a relatively modern and powerful method for investigating convective heat transfer. It enables an entire two-dimensional flow field to be viewed and gives a permanent record of the flow. A fringe pattern is produced over the geometry that is essentially a contour isotherm map. Hence, both qualitative flow visualisation and quantitative results may be obtained. The former produce the real-time eddy behaviour of the coherent structures while the latter give the local surface temperatures and Nusselt numbers.

Forced convection from a smooth surface has been studied in great detail while work on rib-roughened ducts is scarce in comparison. A rib-roughened surface enhances the heat transfer, for a given length, but also increases the drag and hence the pumping power required. A rib spacing of 7.2 : 1, similar to that used for the fuel elements of the Advanced Gas Cooled reactor, is the optimum compromise and that particular geometry is to be studied. This survey concerns the two main fields of interest in this project. Firstly, holographic interferometry is surveyed in some detail with its constituent topics of classical interferometry, holography and coherent light sources. Then a review is made of the specific application of heat transfer with ribbed roughness.

## 2.1. HOLOGRAPHIC INTERFEROMETRY

The discovery of the principles of holographic interferometry followed shortly after the development of the theory of off-axis holography by Leith and Upatnieks (1962). This, combined with the invention of an ideal coherent light source, the laser, produced a surge of activity in this field. The practical limitations of the technique were soon realised but work continued on the qualitative interpretation of the interferograms and to date some sophisticated systems have been developed. A simple explanation of the historical development of the method is illustrated in Chart I. This diagram may act as a guide for the following discussion.

The ability of holography to record both amplitude and phase information makes it ideal for recording the phase changes observed in interferometry. The precision optics necessary for conventional interferometry are not required and the new technique is less experimentally demanding. Numerous variations to the original system have been introduced, some of which are described later. To complete the development of the technique the ideal light source became available. The characteristics of the laser and its principle of operation are described in order to complete the discussion on interferometry.

### 2.1.1 Classical Interferometers

An interferometer is a device capable of measuring the relative movement between two beams to one another to a high degree of accuracy. Usually the two beams which originate at one source to ensure spacial and

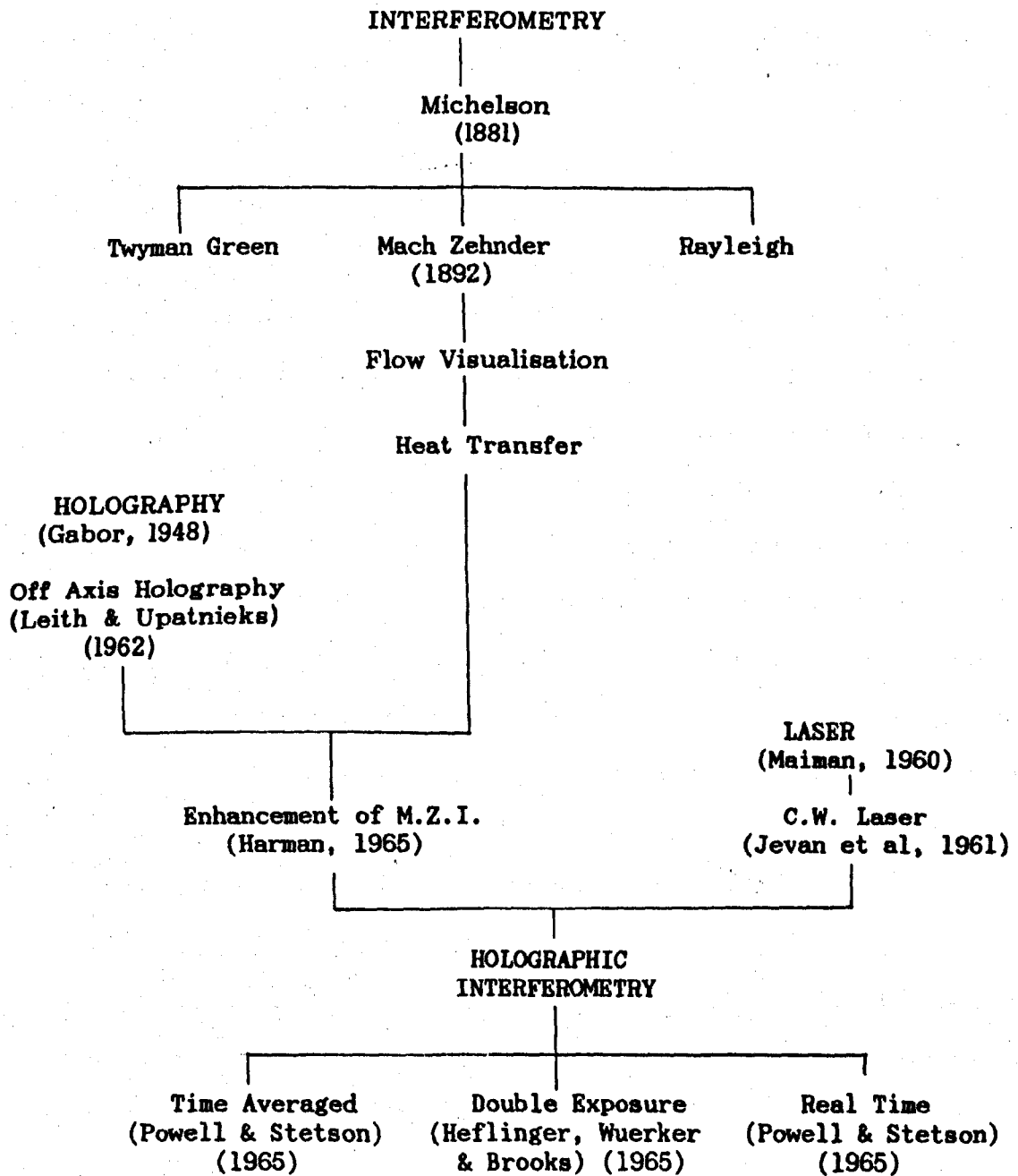


**CHART I. HISTORICAL DEVELOPMENT OF HOLOGRAPHIC INTERFEROMETRY**

temporal coherence, travel different paths. One beam is modified and the other unmodified. Hence upon recombination an interference pattern is observed from which the degree of modification of the beam may be determined.

An early interferometer to achieve this was the Michelson interferometer in 1881. It is still used today to check the stability of optical components. It was originally called the 'interferential refractometer', but renamed on going into commercial production in 1890. For an illustration of its configuration, see Figure 2.1. A light source emits a wave, which is divided into two by a beam splitter. These waves travel to separate plane mirrors to be reflected back to the beam splitter. Parts of the wave then unite and leave the beam splitter in the direction of the screen. They do not recombine exactly and hence interference fringes are observed on the screen. Great care must be taken to ensure both rays undergo the same optical history, hence the compensation plate is inserted. Movement of any mirror then gives distorted fringes that may be analysed and the original movement calculated.

In 1891 Mach and Zehnder developed a modification to the Michelson interferometer. The Mach-Zehnder interferometer (1891-1892) utilises four separate mirrors, two half silvered and two fully silvered, Figure 2.2. The coherent beam is divided into two halves, each travelling two sides of a quadrilateral arrangement. They then recombine and form interference fringes on the screen. Both beams must travel identical paths, hence high quality optics and accurate alignment are necessary. If a refractive index gradient is introduced into the test cell, the beam will be modified and

from the resulting alteration in the fringe pattern, the degree of modification may be determined.

The combining of the beams at the second beam splitter is an important step. If both beams completely coincide then uniform illumination is obtained on the screen. Any modification to the test object, however, gives fringes. This setting is known as the 'infinite fringe' setting because the fringe spacing outside any modification such as a thermal boundary layer, approaches infinity. Hence, the main flow outside the boundary layer appears to have uniform illumination. The thermal boundary layer results in a refractive index gradient. This gives rise to a phase change in the object beam as it traverses through the test section and hence a fringe pattern is produced that maps out isotherms. If the beams do not completely coincide on combining, then the 'finite fringe' setting results. In this case a fringe pattern is observed that completely covers the image. This pattern then distorts when a modification is introduced into the test section.

The Mach-Zehnder interferometer was experimentally demanding and so fell into disuse. However, during the Second World War it was vigorously applied to air flow around model aeroplanes. Since then widespread applications have been found using large apertures and formidably expensive instruments, Gebhart (1966) or Johnstone (1965). Its use has declined since the introduction of holography, but some workers still prefer to use the Mach-Zehnder interferometer, Yih-Jung (1980). He studied natural convection heat transfer in air spaced geometries.

Many other interferometers exist to study a wide range of optical

phenomena. These include the Jamin, Twyman and Green, Rayleigh and Fabry-Perot interferometers. A detailed discussion of the interferometers mentioned may be found in any optics text book, e.g. Hecht and Zajec (1974). However, the Mach-Zehnder interferometer is the most important one for holography, as it is from this interferometer that holographic interferometry developed.

### 2.1.2. Early Holography

To explain holography it is best to compare it with the better known method of photography. A photograph records a two dimensional irradiance distribution, that has been optically formed. A hologram, however, records the object wave itself, together with a reference wave. These two waves form an interference pattern that has to be illuminated later by the reference wave to reconstruct an image of the original object wave. The principles will be explained in greater detail later, but basically photography is a single step process with limited data, while holography requires two steps, but can obtain total reconstruction of the three dimensional object.

Gabor (1948) demonstrated "a new two-step method of optical imagery" that he named holography from the Greek word "holos" meaning whole. Using this technique the amplitude and phase of an object wave could be recorded and subsequently reconstructed to give a three-dimensional image. He formulated the idea after studying Braggs X-ray microscope (1942).

Bragg formed an image of a crystal lattice by diffracting a wave from a photographically recorded diffraction pattern of the crystal lattice. To understand this process, one first must realise that a field diffracted by an object can be represented by a Fourier transform of the light distribution of the object itself. However, all the amplitudes and phases of both transforms have to be recorded. To simplify the technique, Bragg chose objects for which the phase could be predicted, such as crystals with a centre of symmetry, where radiation is "in-phase" or 180° "out-of-phase". Thus a photographic record of this only contains areas of illumination and so no phase information is lost. Diffraction from this photograph yields an image of the original crystal.

Gabor extended Bragg's idea by comparing the diffracted wave (object wave) with a strong reference wave. This means that the phase of the diffracted wave may be modulated by the reference wave provided the two waves are coherent. That is the waves should be capable of displaying interference effects that are stable in time. Provided that the intensity of the reference wave is sufficiently large, it dominates. Hence, the resulting wave has the same phase as the reference but differs in amplitude. A photographic recording of the diffraction pattern is the hologram. On illuminating the pattern with the reference radiation the second diffraction occurs and the image is reconstructed. Unfortunately, the reconstruction gives two waves, the object wave and a complex conjugate "twin wave" that is observed in the foreground when the image is viewed. Other limitations included the low intensity of the illumination and the problems of photographic processing. However, it was the elimination of the twin image that constituted most of the early work in holography.

The aim of Gabor's work was to increase the resolution of an electron microscope from the then theoretical value of 5 Å. He believed that by taking a hologram with electrons and reconstructing with light, the hologram may be scaled up optically in the ratio of the light wavelength to the electron wavelength and so magnified by this same ratio. Although his method was sound, it did not succeed because of the electrical and mechanical instability in his system. The coherent light source, a Mercury arc lamp, acted as an additional restriction due to its poor intensity.

Subsequent workers, Buerger (1950), Haine, et al (1952), Rogers (1950), and Kirkpatrick, & El-Sum (1956), to name but a few, attempted to improve on Gabor's original idea. However, they all failed due to the mechanical stability required for the long exposures, several minutes in some cases. Experimentation in holography became dormant in the middle 1950's due to the lack of a good source of coherent light. Exposure times were long and the resolution of reconstructions never reached theoretical predictions.

### 2.1.3 Laser Development

Further developments in holography required the "discovery of a good source of coherent light". A theoretically ideal light source gives off waves of a single wavelength, (i.e. infinite temporal coherence), and in a constant wave train, (i.e. infinite spacial coherence)\*. The original light

\*Real sources of course emit wave packets at random intervals that have randomly different lengths and contain many wavelength components.

sources for holography were mercury vapour lamps. They had poor temporal coherence and so emitted numerous wavelengths around a mean which resulted in a poor coherence length (the acceptable difference in object and reference beam paths). Its spacial coherence was reasonable, giving a close approximation to a point source and so allowing every object to interfere with every source point. Lasers have both good spacial and temporal coherence and so are ideal for holography. Their development was conceived after the invention of the MASER (Microwave Amplification by the Simulated Emission of Radiation).

In the early 1950's a source of microwave radiation, the MASER, was developed. Immediately afterwards scientists were speculating on expanding the technique into the visible spectrum. The 'break-through' was achieved by Maiman (1960). He developed Light Amplification by Stimulated Emission of Radiation, the LASER. It was a pulsed ruby laser, Figure 2.3, capable of given 0.5 ms of coherent light at a wavelength of 694.3 nm. Its active medium was a cylindrical ruby rod, whose ends were polished flat, parallel and normal to the axis. One end was totally silvered and the other partially, thus forming a resonant cavity. Surrounding the ruby was a flash tube which provided broad band optical pumping. Firing the flash tube generates an intense burst of light which excites chromium ions in the ruby into an absorption state. The ions then relax to a metastable state where they have a relatively long life of  $3 \times 10^{-3}$  s. On dropping to the ground state a photon is emitted. This photon bounces backwards and forwards in the cavity, stimulating other photons to be produced having the same wavelength, 694.3 nm. As one mirror is partially reflective a beam of highly coherent radiation emerges from the mirror. The three energy states of the laser are illustrated in Figure 2.4, hence it is referred to as a three level laser.

The first operation of a continuous wave (C.W.) laser followed shortly in 1961. Jevan, Benett and Herriott (1961) reported the operation of a Helium-Neon C.W. laser that gave an output of a few milliwatts at a wavelength of 632.8 nm, see Figure 2.5. It consisted of a ten centimetre tube, filled with a Helium-Neon mix with flat mirrors at each end, one being partially reflective. Electrodes wrapped around the tube generated radio frequency radiation, that excites the neon to a metastable state. A photon is then emitted as the neon drops to an energy level above the ground state. This photon then stimulates others, and in a similar manner to the ruby laser, a coherent beam leaves through the partially silvered mirror.

Hence a population inversion has occurred, between the two states where stimulated emission occurs, without having to empty the ground state. Therefore the lasing action is able to continue indefinitely, thus giving a continuous wave laser. The process takes only a fraction of a second to give the continuous beam.

Development since these early beginnings has been dramatic. Pulsed ruby lasers are able to give gigawatt pulses. Other solid state lasers have been developed with wavelengths between 500 nm to 2500 nm. These include the trivalent rare earth's Neodymium,  $\text{Nd}^{3+}$ , Holmium,  $\text{Ho}^{3+}$ , Gadolinium,  $\text{Gd}^{3+}$ , etc., which undergo lasing actions in a host of materials that include  $\text{CaWO}_4$ ,  $\text{Y}_2\text{O}_3$  and Yittrium Aluminium Garnet (YAG) to name a few. It should be noted that some Nd:YAG lasers can generate a kilowatt of continuous wave radiation. Gas lasers have been developed to operate from infra-red across the visible spectrum to the ultra-violet. The most important examples of these are the Argon, Krypton and Helium-Neon lasers. Output from the Argon laser is usually several watts, continuous wave.

They are similar in operation to the Helium-Neon but operate at shorter wavelengths, predominantly 514.5 nm and 488 nm.

#### 2.1.4 Revival in holography

Interest in holography was revived by Leith and Upatnieks (1962) when they developed a method of completely eliminating the twin image. An off-axis reference wave was made to interfere with the object wave to form a grating like structure. Reconstruction yields an attenuated reference beam and the two first order waves of the grating: one of these is identical to the original object wave while the second is the conjugate unwanted twin image. [A brief explanation of the theory of holography is given in Appendix A]. Their angle of separation is subject to the inclination of the reference wave. For a more detailed analysis, see Vest (1979). Hence a good clear image of the object is available that may be viewed without looking through the "twin-image". Critical film processing was no longer necessary as any non linearities introduced at this stage give rise to higher diffraction orders at larger angles and hence do not diminish from the clarity of the first order diffraction. The new technique also permitted the use of different objects that did not necessarily have to transmit large portions of the incident wave.

Problems still arose with the new development. Dust and imperfections in the optical components still caused unwanted holograms superimposed on the main hologram. El Sum (1952) attempted to solve this problem by rotating all the optical components in an effort to smear out the holograms

of the noise particles. It worked to a certain extent, but proved highly impracticable.

A major role was then to be played by the laser, which by 1964 had become a widespread source of intense coherent light. It was an ideal solution to the earlier problems encountered with poor light sources. Now, employing the laser as a light source, Leith and Upatnieks (1964) were able to introduce another new concept, that of diffuse illumination.

In this technique an object is illuminated with diffuse light, so that all points on the hologram receive radiation from all points on the object. As the difference in path lengths between the numerous object beams and the reference beam is less than the relatively long coherence length of the laser a hologram is obtained. This meant that holograms of opaque objects could now be taken as they reflect light diffusely. Startling reconstructions could now be achieved as the plate acted as a window through which a perfect three-dimensional image could be viewed.

Additional advantages included the removal of any shadowgram and the fact that there was no longer the necessity of a one to one correspondence between the plate size and object. Any scratches or dirt on the optical components did not detract from the quality of the hologram as they were smeared out. Another advantage was that should the plate be broken it was still possible to form an image, despite a loss of resolution.

The new diffuse illuminated holograms were ideal for the superimposition of images. Rogers (1952), achieved this before diffuse

illumination but now the idea led to the observation of phase changes in an object. By taking two exposures of an object, any phase change between exposures will result in a fringe pattern. Hence the original phase change may be calculated by studying the fringe pattern. This led to a whole branch of holography known as holographic interferometry.

#### 2.1.5. Early Holographic Interferometry

The previous sections describe the separate elements that combined to produce the new subject of holographic interferometry. The method was first demonstrated by Horman (1965), when he employed holography to improve the Mach-Zehnder interferometer. He was able to obtain a multiple fringe interferogram and chose the fringe spacing, including the infinite fringe setting. He also selected the plane of the object field he focussed on and was still able to reconstruct conventional schlieren and shadowgrams from the interferogram. This illustrated the advantages of the new technique and how it could be applied to transient phenomena. Today, the technique has found many applications which include: strain analysis, flow visualisation, vibration analysis and heat transfer. The most commonly employed holographic interferometer for the study of phenomena in transparent media is illustrated in Figure 2.6. The layout is similar to the Mach-Zehnder interferometer, the main difference being in the use of the reference wave. In the Mach-Zehnder interferometer the reference wave is compared directly with the object beam and fringes are formed in real time. In the holographic layout the reference beam forms a hologram on the plate when it interferes with the object beam from the test section. Hence, the fringes are introduced only when a second exposure is taken

of the temperature field. It is important to note that the object beam travels through the test section on two separate occasions and so high quality optics are not necessary as any imperfections will be repeated and so will not form any secondary fringes.

Three approaches may be adopted in recording interference fringes:

- (i) time averaged
- (ii) double exposure
- (iii) real time

(i) The time averaged method involves taking a long exposure of an object vibrating periodically so that upon reconstruction the image, contours of constant amplitude of vibration are mapped out. Powell and Steson (1965) used the technique to study the periodic frequencies of objects.

(ii) With the double exposure technique, two exposures are recorded on the hologram. The first is of the object and the second after a phase change introduced, such as a thermal gradient, to the object. The fringes are then recorded permanently. Heflinger, Wuerher and Brooks (1966) used this technique to study the thermal plume observed in a light bulb. This illustration is important as it demonstrates the above-mentioned fact that optical quality glass is not required. They also investigated shock curves generated by the flight of a bullet.

(iii) The real time technique involves taking one exposure on the plate. It is then processed and replaced in its original position. This positioning is important as the plate has to be replaced to within a wavelength of light ( $10^{-6}\text{m}$ ) and no optical components must move during the photographic processing. The shutter then remains open for the second exposure and the fringes are observed in 'real time'. This technique has the great

advantage that changes with time may be observed. Powell and Stetson (1965a) demonstrated the technique in 1965 by studying vibrating objects.

One application not yet mentioned is that of strain analysis. Haines and Hildebrand (1966) applied interferometric measurements to analyse the minute deformation of arbitrary three-dimensional objects.

#### 2.1.6. Heat transfer applications

Tanner (1966) reviews the classical methods of reconstruction of transparent object fields and also discusses how holography can enhance their results. He illustrated this by choosing a bunsen burner as an object and employed a schlieren finite fringe background with laser illumination. Early applications of the technique were aimed at verifying theoretical predictions of convection. The well known situation of natural convection from a flat vertical plate was investigated by Zinnes (1970) in 1970. He used holographic interferometry to obtain heat transfer coefficients from the surface and then compared them with predictions of the heat transfer coefficients obtained from a finite difference analysis of the heat conduction within the plate. The results showed good agreement. Aung, Sernas and Fletcher (1972) undertook a similar analysis of convection in vertical channels and indicated a relationship between heat transfer coefficient and Rayleigh number. Hot wire anemometry was also used to verify the holographic interferometric results, and theoretical predictions of convection from a vertical plate, Hardwick and Levy (1973). For a good description of the holographic interferometer employed for heat transfer analysis in the early 1970's see Aung and O'Regan (1971).

Using holography as a tool more complex geometries were studied as confidence in the technique grew. Turbulent buoyancy convection in a closed rectangular cavity was investigated experimentally by Steinberner and Reineke (1978). They were limited to two dimensional turbulent structures as was Koster's (1983) investigation of heat transfer in plexiglass boxes. (Although Koster was only interested in the thermal influence of the walls on the flow pattern). He chose plexiglass as it has a 'high temperature-dependent refractive index' and so enabled the determination of the wall effect. Cesini et al (1982) investigated convection in rectangular enclosures with two isothermal walls at different temperatures. They varied Grashof numbers and aspect ratios and compared their results with other authors. Again holographic interferometry yielded good results as it did for Faw and Dullforce (1981) when they studied convection from an inverted square plate for various Rayleigh numbers. Hatfield and Edwards (1981) studied the effect of wall radiation and conduction on the stability of a fluid in a finite slot heated from below. Their theoretical determination of critical Rayleigh numbers using the Galerkin technique were confirmed experimentally with a real time holographic interferometer. As a final illustration of its application, and of significance for the current work, Walklate (1981) used a holographic interferometer to obtain heat transfer coefficients in a turbulent two-dimensional thermal boundary layer. Qualitative measurements were taken as opposed to quantitative, and specific values for the heat transfer coefficients and Nusselt numbers determined in the near wall region.

Interferograms are also ideal images for comparison with numerical predictions. Grötzbach (1985) applied the TURBIT-3 subgrid scale model to

determine heat flux coefficients for turbulent natural convection. When compared to results of experimental interferograms a close agreement was attained which led to a better understanding of low Prandtl number flow.

A detailed survey of all optical methods in heat transfer was published by Hauf and Grigull (1970). They presented a detailed analysis of the changes in refractive index that enable a temperature field to be calculated. That is, they explained how to interpret the fringe patterns. For two-dimensional fields Goldstein, (1976) gives a less stringent analysis. He discusses the end effects and errors due to refraction in the working section, when a thermal gradient is present. This analysis is particularly relevant to the work in this investigation.

#### 2.1.7. Variations to the conventional holographic interferometer

Numerous modifications to the conventional system have been employed, one of the more important being that of diffuse illumination. The methods of achieving this are illustrated in Figure 2.7. The advantage of diffuse illumination is that large objects may be viewed to give an overall picture of the heat transfer. However, fringes next to the surface are blurred and analysis is difficult as the light enters the working section from all directions and angles. But diffuse illumination enables three dimensional fields to be analysed to a certain extent, (Sweeney and Vest (1974)).

The advantages of parallel illumination of the test section and diffuse illumination of the hologram may be achieved using the layouts illustrated in Figure 2.7(b) and Figure 2.7(c). Jahn and Reineke (1974) employed

these techniques to study natural convection of a fluid with internal heat sources. Method 2.7(b) may only be used with low fringe densities while method 2.7(c) enables high fringe densities to be recorded that give high quality interferograms. For a more detailed analysis see Mayinger and Panknin (1974).

Another variation that enables three dimensional fields to be studied is that of phase grating illumination. The diffuser in Figure 2.7(a) is replaced with a sinusoidal phase grating, Vest and Sweeney (1970). With the grating numerous beams pass through the test section, but their paths are known. Hence, if a separate hologram of each beam is recorded, the three dimensional field may be determined. A scatter plate may also be employed to redistribute the illumination, Tanner (1967), but the object size will be limited.

Additional optical components between the test section and the hologram, see Figure 2.8, enable image plane holograms to be taken, Brandt (1969). The advantage with this technique is that the hologram may be reconstructed with white light, the complex conjugate being viewed. The image suffers from a loss in the depth of field, but the speckle inherent light reconstruction has been eliminated. The technique has been mainly applied to flow visualisation where the refractive index changes have been due to shock waves, but it may easily be applied to heat transfer when double exposures are employed. Brandt, Rozelle and Patel (1975) used this technique to visualise shock waves on a turbine blade and Bryanston-Cross (1981) studied turbine cascades at varying Mach flows.

By replacing the knife edge in a conventional schlieren system with a Wollaston prism and two polarisers, a Wollaston prism schlieren

interferometer results, see Figure 2.9. Since its inception in 1965 by Merzkirch (1965) it has been used extensively to study heat transfer. When a temperature gradient is present the fringes are displaced an amount proportional to the temperature gradient and not the local temperature as in the Mach-Zehnder interferometer or holographic interferometer. Hence, heat flux may be calculated from a single fringe reading, Sernas (1983). The position of the prism enables either a finite background, Sernas and Fletcher (1970) or an infinite background, Oertel and Buhler (1978), to be chosen.

There are some experimental variations to the techniques discussed that enable both exposures to be viewed separately, and so add a degree of flexibility to the reconstructed image. An obvious technique is to record each exposure on separate plates, Mayinger and Panknin (1974). They were able to vary the reconstructed image to give an 'infinite' or 'finite' background. The reconstruction was undertaken using a high quality optical semi-transparent mirror, see Figure 2.10. However this process requires accurate alignment of all the optical components and so it is experimentally demanding. But by varying the angle of one of the plates, the object field may be viewed with an 'infinite' or 'finite' background. Employing two plates also enables large temperature gradients to be studied. This is achieved by taking an exposure of the small temperature gradient and then employing one of the exposures as a reference for the next exposure. Hence, using a stepping technique, one is able to determine large temperature gradients.

A less experimentally demanding technique that enables two views to be reconstructed separately, utilises two reference beams, Ballard (1968). This

method allows each object exposure to have a separate reference beam, see Figure 2.11, and therefore each image may be viewed separately or together to form an interferogram. A 'finite' or 'infinite' background may be chosen by varying the angle of one of the reference beams, Trolinger (1979). It is also possible to record the initial exposure using both reference beams and then take the two subsequent exposures with only one reference beam for each. The two resulting interferograms may be reconstructed separately or superimposed to form a Moire pattern, Trolinger (1977) that enables comparison between two states of the object.

An interesting technique recently applied to transparent media is that of heterodyne holographic interferometry. This method involves taking two or more exposures of a stationary image, and introducing a phase change into the reference beam between exposures. In this way numerous sets of fringes are introduced onto the image and so allows a more accurate analysis. Farrell, Springer and Vest (1982) used the technique to measure specie concentration in dilute binary gas mixtures and obtained close agreement with analytical solutions.

The techniques discussed earlier have now been employed for several years. In recent years systems have become more sophisticated with the refinement of optical components, improvement in photographic processing and with the inception of higher power lasers. Examples of the application of holographic interferometry are numerous and diverse, and a few will be described here to illustrate the diversity. Craig, Lee and Bachelo (1982) used a Nd:YAG laser capable to delivering 150 ms pulses to investigate flow around aerofoils in a large tunnel, the object field was two metres square. Witte (1972) developed a 180' holocamera, capable of

recording 3-D flows, and studied turbulent wake phenomena. Seftor (1974) used a two wavelength holographic interferometer to study electron density variations in exploding wires. Finally, Eisfeld (1983) investigated the propagation and the structure of low luminous turbulent flames by high-speed real time holographic interferometry, using a high speed camera (4000 ff/s) to record the images.

## 2.2. TURBULENT CONVECTIVE HEAT TRANSFER

Heat transfer from any surface is governed by the thickness of the boundary layer, and high values are given by thinner layers. Therefore, to improve the heat transfer from a smooth surface artificial roughness elements may be added to promote turbulence and so break down the boundary layer near the surface. Commercial Advanced Gas Cooled reactors (A.G.R's) contain transverse ribs, spaced at regular intervals, to improve the heat transfer. Hence, this particular surface has been studied in depth to improve the performance of reactors and so reduce power generation costs. A brief discussion of previous investigations on the thermal situation around ribs now follows, with particular emphasis being given to the determination of the Nusselt number distribution around the rib. However, to aid in the understanding of the thermal field a summary of the results of momentum field investigations is presented.

### 2.2.1. Momentum field

The characteristics of the momentum field govern the thermal field present for any flow situation. Hence, early work was directed at determining the momentum field around ribbed surfaces. Usually square ribs were investigated as their shape was easily defined and roughness parameters associated with them enabled all studies to be universally compared. However, no investigation was undertaken on typically rounded rib surfaces that are normally found in the core of an A.G.R. reactor.

An early important investigation on sand roughened surfaces was undertaken by Nikuradse (1950). He added sand grains to smooth surfaces to create surfaces with a known relative roughness. From his results he proposed the universal law of the wall from which heat transfer rates may be successfully predicted. His roughness was geometrically defined by the height of the sand grains, but all other types, such as rib-roughened surfaces, require more than one parameter to define them. Patel and Head (1969) studied skin friction and velocity profiles in fully developed pipes and channels. They identified different criteria for the specification of fully developed turbulent flow, such as the fact that pipe and channel flows become turbulent at different Reynolds numbers. Also, at high Reynolds numbers the law of the wall successfully predicts the velocity profile for channels and not pipes. Hence, additional information will be required for the hydrodynamic results in this investigation as a channel and not a pipe is used.

Studies of the flow structure around square ribs are numerous. Hanjalic and Launder (1972) studied the central region of a channel where the two dissimilar flows (generated by a smooth and a rough surface) interact. Strong diffusional transport of turbulent shear stress and kinetic energy from the rough towards the smooth wall region result in a separation of the zero shear stress plane from the maximum mean velocity. The near rough wall velocity profiles were independent of Reynolds number and a more co-ordinated eddy structure was suggested for this region. A further isothermal investigation by Meyer (1980) confirmed these results and presented a transformation method that enables all data on rectangular and annular channels to be compared. A detailed study of the velocity and static pressure distribution for flow around a rib-roughened surface was carried out by Lawn (1976). He hoped to optimise the heat transfer after gaining information on the several complex flow regions present. The presence of high turbulent intensities close to the inter-rib surfaces give rise to high heat transfer rates in this region. They also indicate the necessity of including a diffusivity model in any future theoretical calculations for heat transfer to allow for the effect of convected turbulent energy. Aytakin and Berger (1979) present similar results for rectangular ducts of low aspect ratios under isothermal conditions.

Investigations became more sophisticated with the introduction of laser doppler anemometry. This technique permitted velocities, turbulence levels and Reynolds stresses to be determined anywhere in the flow field. Martin and Drain (1986) investigated flow over a rib-roughened surface and gained detailed knowledge of the turbulent flow that may be compared to theoretical investigations.

Early heat transfer investigations determined a thermal performance for a surface. Warburton (1972) surveyed numerous surfaces and concluded that a typical Advanced Gas Cooled reactor surface gives a 48% improvement in thermal performance over a smooth surface. However, a wedged shaped surface gave a massive 111% improvement. This surface is not used in A.G.Rs because stainless steel has a high neutron absorption and hence the material volume has to be kept to a minimum. Wedges have the greatest potential for neutron absorption and hence the resultant shape employed is a design compromise between the several conflicting requirements. Dalle Done and Meyer (1977) give a comprehensive survey of ribbed surface heat transfer comparing not only rib spacing geometries but also rib clusters. They illustrate a transformation method that enables data extracted from annulus and duct experiments to be applied to reactor fuel elements. Detailed information concerning the heat transfer from the surface is therefore available. However, relatively little is known on the distribution of local heat transfer coefficients around these surfaces. Work that has been undertaken on this problem will now be discussed in detail.

### 2.2.2. Heat Transfer Coefficient Distribution around a Ribbed Surface

Knowledge of the heat transfer distribution around a ribbed surface is useful as it enables a limit to the heat rating of the surface to be determined. This is calculated from the temperatures of the element cladding. Also, a better understanding may be gained into the manner in which ribs influence the heat transfer. An example of this is an estimation of the heat flow along or just below the surface to areas of high heat transfer.

Methods of determining the heat transfer distribution include:-

- (i) Thin film naphthalene
- (ii) Evaporation of water from absorbent paper
- (iii) Electro-chemical technique
- (iv) Copper foil
- (v) Holographic interferometry

The first three techniques predict the distribution from mass transfer data while the later two measure the heat transfer coefficients directly.

(i) Naphthalene Technique

Utilising the heat transfer - mass transfer analogy, the heat transfer from a surface may be determined by measuring the mass transfer from it of a relatively volatile solid. An ideal substance is naphthalene. Early workers, Kattchee and Mackewicz (1963) coated a metal surface with naphthalene and measured the amount removed after a predetermined period of flow exposure. Then, using the analogy, the heat transfer distribution around the four ribs investigated was determined, and is illustrated in Figure 2.12. The local coefficients were larger than those for a smooth surface, except at the base of the rear facing rib and the area immediately surrounding it. Peak values were observed at the leading edge of the upper face of the rib. From their results they postulated that high heat transfer coefficients were present at the point of boundary layer separation and broad peaks at boundary layer reattachment. Recirculation regions at the rear of the flow produced thicker boundary layers and so low heat transfer coefficients are observed. Their results were only able

to predict the distribution, they were not able to determine the absolute values of heat transfer.

An alternative naphthalene procedure is to coat the surface to be investigated with a very thin layer and then observe the time taken for the localised surface to become completely clear. Wilkie and White (1966) adopted this technique and published a similar distribution to Kattchee and Mackewicz. Again absolute values were not determined. Young (1972) used the method to investigate the heat transfer from a multistart fuel pin with a pitch to height ratio of 12 : 1. Again, similar distributions were observed, but problems with coating the surface with a uniform layer of naphthalene were highlighted. However, they developed a natural convective test that enabled the uneven distribution on the surface to be corrected for and so minimised this error.

Neal, Northover and Hitchcock (1970) developed a spraying tube facility that was able to produce a uniform layer of naphthalene on a surface. By photographing the evaporation at numerous time intervals they were able to determine absolute values for the heat transfer. For their early studies the forced convective heat transfer rate from a tube was determined as this is a simple surface on which to test the technique. Conical, flat or any other surfaces may be sprayed but the comparative coating thickness must be calculated for all points on the geometry. Further developments of the technique are reported by Neal (1973) who illustrated its ability to predict forced convective heat transfer coefficients accurately and economically in a wide variety of situations.

The two major disadvantages of the technique are the changing characteristics of the surface as evaporation proceeds and the accurate determination of the thickness of the naphthalene upon application and during testing. Problems of coating the surface with a consistent thickness are also encountered. Direct measurement of coating thickness is not possible and hence photographic enlargements are employed which are subject to a random error. All of these errors combine to make this technique an experimentally demanding one if a reasonable degree of accuracy is to be obtained.

#### (ii) Evaporation of water from absorbent paper

Another mass transfer analogy technique, developed by Watts and Williams (1970), measures the evaporation rate of water from cobaltous chloride impregnated paper. The surface to be investigated, in this case a rib-roughened one, is covered with a layer of absorbent paper which has previously been soaked in a cobalt chloride solution. At the start of the test the surface is sprayed with water, care being taken to obtain an even distribution, and then placed in a wind tunnel. The flow is then started and the time taken for the chloride to change colour from pink to blue at each location determined. The heat transfer coefficient may then be estimated as the heat transfer rate is directly proportional to the time taken for the chloride to change colour. Their results are illustrated in Figure 2.12 and are observed to agree with the naphthalene results. The rib runs noticeably cooler and Williams and Watt (1970) estimate that it contributes 46% of the total heat flux through only 34% of the total surface area.

The drawbacks with the technique are the difficulty in achieving an even distribution of water and the capillary effects observed in the paper that reduce the evaporation rates. Again, it is an experimentally demanding technique and hence few studies have been undertaken with it.

### (iii) Electro-chemical Technique

This technique models mass transfer between a liquid and solid surface by measuring the transfer rate of certain ions in aqueous solutions to an electrode. Analogies between the transport phenomena may then be applied to determine the convective heat transfer. Mizushima (1971) discusses the theory of the method in detail.

An investigation into the local heat transfer distribution on surfaces roughened with square ribs has been carried out by Berger and Hau (1979) using the electro-chemical technique. They employed an aqueous solution of potassium ferri- and ferro-cyanide with sodium hydroxide as the inert electrolyte to act as the fluid. Nickel electrodes were used, the ribbed surface being the cathode and a simple strip is made the anode. The potential across the electrodes is increased until a stable value is attained. Under these conditions the ion transfer rate is determined by molecular and turbulent diffusion through the boundary layer. So when flow is introduced it is a simple matter of measuring the electric current present at the local stations to obtain the heat transfer rate as these are directly proportional to the current. Hence, the heat transfer distribution may be determined and is illustrated in Figure 2.12. Unfortunately Berger and Hau's results are for a rib spacing of 7 : 1 and not 7.2 : 1 and so the distribution is not exactly correct. The same trends are still observed and a reasonable agreement is observed.

The advantage of this technique over the mass transfer methods discussed earlier is that it avoids the surface characteristics changing as the experiment proceeds. This method also enables high Prandtl number flows to be simulated. Again, it is an experimentally demanding technique and great care must be exercised in the prediction of mass/heat transfer rates in moderate Schmidt/Prandtl number situations as direct extrapolation is not viable. Errors of over 50% occur and hence correction factors are available to allow for the error. Hence, data for low Prandtl number flow are only qualitative. For more reliable answers using this method, an accompanying theoretical prediction is necessary or other confirmatory experiments.

#### (iv) Copper foil analysis

An alternative to the mass transfer analogies, is the use of a secondary surface for direct measurement of heat transfer. Harris and Wilson (1960) describe how nickel foil strips attached to a surface provide a method of controlling local heat fluxes and in conjunction with thermocouples embedded in the surface allow the local heat transfer coefficients to be determined. Problems of coating the surface with a uniform layer of nickel and of positioning the thermocouples correctly make it a complex and demanding technique to use correctly and efficiently. Hence, Watts and Williams (1981) developed an alternative foil technique that was simple and easy to use, and did not require the thermocouples to measure temperature.

Watts and Williams (1981) used copper foil mounted on a stiff laminate base as the film. This is then attached to a rib-roughened surface made

from a blockboard base and wooden ribs, having a pitch to height ratio of 7 : 1. Voltage tappings and power connections are attached to the edges of the strips and led away through the wooden base so as not to disturb the flow field. A known current  $I$  is passed through the copper strip and the power dissipated calculated once the voltage drop is recorded. Using the same information the resistance of the strip may be calculated [ $R = V_{\rho}/I$ ] and the temperature of the strip determined as the resistance is directly proportional to it. The average heat transfer coefficient for the strip may then be found using the relationship:

$$h = \frac{Q}{A\Delta T} = \frac{V_{\rho}I}{A(T_s - T_r)}$$

The bulk temperature  $T_r$  is estimated using a bank of thermocouples mounted in the tunnel. To improve the resolution of the technique transverse cuts in the foil may be undertaken to form more individual strips. More circuits are generated and hence an improved accuracy may be attained around complex geometries. However, more unheated gaps are present and these given rise to exaggerated heat transfer coefficients and prevent heat flow between the strips. The results for the square rib investigation are illustrated in Figure 2.12 and a good agreement with previous results is observed.

Watts and Williams estimate their error to be in the order of 16%, most of which is attributed to incorrect determination of the voltages. As in all techniques discussed it is an experimentally demanding one, but this one enables direct measurement of the heat transfer coefficients and is able to yield absolute values. The major disadvantage of the technique is that it is very time consuming to set up as special surfaces have to be made, one cannot simply coat a previously manufactured surface.

#### (v) Holographic Interferometry

Heat transfer from the surface is measured directly without the need for special preparation of surfaces. The technique has already been discussed and will be discussed in greater detail and so no explanation of this technique is given here. Workers using the method have been able to obtain accurate measurements of heat transfer coefficients from numerous geometries.

Walklate's (1983) study of the heat transfer from a rib-roughened surface is illustrated in Figure 2.12 and agrees well with the other workers. In particular the resolution is excellent and absolute values are determined. He illustrated the capability of the technique for the determination of the heat transfer distribution. Copper was used as the metal surface and hence incorrect Biot number flows were investigated if A.G.R. surfaces are to be simulated. Heat flow along the surface would be high because of the good conductivity of the copper and hence local hot spots would fail to develop to their correct value.

Errors and the advantages of the technique will be discussed later in Appendix B.

#### 2.2.3. Theoretical Predictions of Heat Transfer Coefficients

After the introduction of the large powerful modern computers, the development of Computational Fluid Mechanics (CFM) has been dramatic.

Facilities are now available to model two- and three-dimensional geometries. One such model, FEAT, will be discussed in Chapter 5. Early predictions of the heat transfer distribution are presented and their reliability is discussed.

The effect of heat flowing axially for a given heat transfer coefficient distribution was investigated theoretically by Mantle, Freeman and Watts (1971) using a finite difference computer code. A constant temperature inner wall boundary condition was assigned to the model and only one rib pitch was meshed, periodic end boundary conditions being employed. They illustrated that the Biot number governs the temperature distribution on a ribbed heat transfer surface for a given geometry and heat transfer coefficient distribution, obtained by Williams and Watts (1970). By varying certain physical parameters such as wall thickness they were able to predict the corrections necessary for any particular ribbed surface to be investigated. However, in this study no attempt was made to model the flow conditions. More detailed information on different physical geometries is given by Watts (1971). He illustrates the effect of changes in rib profile on the overall heat transfer performance of the surface, and how refining the mesh can result in more accurate estimates of the heat transfer.

An attempt to model the flow over transverse ribs and so predict the heat transfer was carried out by Wilkes (1981). He used a  $k-\epsilon$  model of turbulence to obtain predictions for the flow and undertook experimentation on a water rig to validate them. The temperature is then solved as a passive scalar, with heat flux boundary conditions on the wall. Comparing the predictions with empirical results led them to conclude the correlation

to be qualitatively quite good but quantitatively the prediction for the overall Stanton number was about 40% too low. Their error was thought to be in the treatment of the wall condition. The same problem with the wall condition arose in the present study and so is discussed in greater detail in Chapter 5.

A study of rib-roughened geometries using Laser Doppler Anemometry (L.D.A.), Cocking and Dalzell (1984), enabled detailed information of the flow field to be obtained. Water was used as the working fluid as it is easier to use L.D.A. in a liquid than a gas. Two component velocity measurements enabled the kinetic energies and Reynolds stresses to be determined, and compared with  $k-\epsilon$  theoretical predictions. This initial investigation was improved upon by Martin and Drain (1986). They enhanced the optical and signal processing systems and increased the measuring volume to enable more than one rib to be studied. Thus, the experimental results are detailed and provide an excellent reference for any theoretical investigation of fluid flow over a rib-roughened geometry. Hence, these momentum field results will be compared with the theoretical predictions reported later in this project.

## CHAPTER THREE

### EXPERIMENTAL APPARATUS

The experimental apparatus was designed, constructed and tested during the course of the present research. It enabled surface temperatures and heat transfer coefficients to be determined for numerous surface geometries. This chapter outlines the design criteria for the apparatus, gives a description of its construction and discusses the modifications undertaken as work progressed. The apparatus consists of a wind tunnel with a heated working section and numerous optical components set out to form a holographic interferometer.

#### 3.1. DESIGN AND CONSTRUCTION OF THE WIND TUNNEL

To investigate forced convective heat transfer from roughened surfaces a tunnel has to be constructed. It should provide fully developed thermal and momentum fields (or a good approximation to them) at the working section. Interferometry adds further constraints in that the flow must be as close to two dimensional as possible. Numerous, easily selected, turbulent flow rates have to be available, up to a limit of  $Re_D = 60,000$ . Finally, optical access is required to permit the laser beam to traverse the test section. Due to its availability and known refractive index properties air is obviously chosen as the working fluid and hence a wind tunnel is constructed.

In an earlier investigation by Walklate (1981) at AERE Harwell, a tunnel was constructed to observe similar phenomena using the same experimental technique. Using data about this tunnel Voke (1984) had a design constructed that could be used to study turbulent flow. A schematic illustration of this tunnel is given in Figure 3.1., the size of the laboratory limiting its length. The centrifugal fan, Fischbach type DF770, made available to the project was mounted at the inlet and blows down the tunnel via a simple contraction section made of rubber. This was thought to damp out any high frequency vibration of the tunnel introduced by the fan. Also no attempt was made to mix the flow and so remove any flow asymmetry introduced by the fan.

Early tests indicated that this tunnel was unsuitable for the study of developed flows. The major problem was the asymmetry introduced by the fan. It consists of a drum of blades that rotates around a central drive shaft. An electric motor mounted on the shaft drives it, but also acts as a baffle to the inlet flow on one side of the drum. A central support ring for the blades is present and this gives a central portion where no flow is generated. Hence, in the horizontal plane two jets are produced from the fan one stronger than the other. Also in the vertical plane the centrifugal fan produces faster moving flow on the outside than on the inside, and so a further asymmetry is introduced. This is illustrated in Figure 3.2.

Early attempts to remove this problem consisted of placing obstructions in the flow to generate turbulence. Gauzes, honeycombs and numerous aerofoils in many combinations were placed around the contraction at the inlet. All failed to remove the dominant cross stream asymmetries and

hence a redesign of the inlet condition was carried out. The eventual solution of a settling plenum and shaped inlet contraction is illustrated in Figure 3.3. The method of arriving at this condition is described in detail by Lockett (1985) in his report. The relevant sections are reprinted in Appendix F.

An aspect ratio of 4 : 1 was chosen for the tunnel as previous studies, (e.g. Beavers, Sparrow and Lloyd (1971)), indicated that this was close to the limit that enabled a two dimensional flow to be assumed. The interferometric technique placed a limit on the width of the tunnel beyond which refraction effects would become significant and produce errors. Walklate's (1981) results were obtained on a tunnel with a width of 304.8 mm and he was able to attain sufficient resolution for comparable flows without significant refraction effects. A width of 300 mm was therefore decided upon as the best compromise between resolution and end effect errors. This gives a tunnel height of 75 mm and a hydraulic diameter of 120 mm.

The size of the laboratory acts as a limit to the development length of the tunnel once its cross sectional size has been decided. Ultimately a rib-roughened flow is to be investigated thoroughly and the smooth surface tests are to act as an introduction to the technique. Hence, a development of 20 hydraulic diameters ( $D_e$ ) was decided upon as this is sufficient to achieve fully developed flow conditions for rib-roughened surfaces. The smooth surface investigations, therefore, may not have fully developed conditions but the additional length required is impracticable for the given laboratory size. This development section leads into a heated working section of 4  $D_e$ . All the working section has transparent sides and so enables the development of the thermal boundary layer to be

investigated along with its developed condition. Hence, the degree to which the thermal layer has developed may be assessed easily. An exit section completes the tunnel that discharges into atmosphere. It is present to aid continuity of the flow in the working section.

In the new design, the fan no longer blows straight down the tunnel but is turned around and blows into the base of a large settling plenum. A box placed next to the inlet has numerous small holes in it and acts as a diffuser. In this manner the flow entering the plenum comes in the form of numerous small jets and not one large jet. The plenum is sufficiently large 1.7 m x 1 m x 0.9 m to ensure complete mixing of the many jets and so ensures a uniform velocity at its exit. A bell shaped contraction is present to take the flow smoothly from the plenum to the tunnel and so produce a uniform flow at the tunnel. A 6 mm honeycomb is then present to remove the swirl generated in the plenum. This completes a description of the design of the tunnel; its construction will now be discussed.

Running down the entire length of the tunnel is a wooden frame resting on three metal supports. The aluminium tunnel rests on this frame. However, at the working section the wood forms a vital part of the tunnel as this part is constructed in a different manner. The frame is constructed from softwood (30 x 80 mm) that is joined together in 'H' sections to give a rigid structure. It was painted in an attempt to prevent warping from moisture variations of the wood, but this had only partial success. This frame rests on three metal supports made from 25 x 50 mm channel iron that holds the wooden frame 1400 mm above floor, 200 mm above the optical tables. At the base of the iron frames threaded bolts are attached that enable the height of the frames to be varied and

so ensure that the tunnel is horizontal. Having constructed a support frame the tunnel may now be assembled.

The side walls and upper surface of the working section are constructed from 6 mm thick float glass sheets whose edges are ground flat. This ensures a perpendicular face when they are joined together [Schlieren quality glass was not necessary as schlieren conditions are not required for holographic interferometry. A cyanoacrylate adhesive is applied to the joining surfaces which are then clamped together. A machined square is used to ensure a right-angle is achieved during the clamping. The resultant 'U' shaped section then rests on a grooved slot in the wooden former. It is clamped down using steel bars, one each end, and two threaded bolts for each bar. A rubber mask between the two ensures that the glass does not fracture when the bolts are secured. The lower wall of the test section is a stainless steel plate. Later in the project this smooth base plate is replaced with a rounded rib-roughened plate having the same base dimensions. The plate sits on thin strip p.t.f.e. insulation that is fastened to the wooden former. A schematic cross section through the working section is illustrated in Figure 3.4.

Aluminium plate (6 mm) is used for the flow entry and flow exit sections. Two identical box sections are made for the development length which are joined together to produce the  $20 D_0$  length. The ends and side faces of the plate were machined square, and all inside surfaces were rubbed down with fine grade emery paper to ensure a smooth surface is achieved. Holes were drilled and tapped through the lower surface into the side walls to form the rectangular 'U' sections. Care was taken to ensure they were perpendicular so that the tunnel width did not vary by

more than 1 mm around the 300 mm distance. The lower surface is 362 mm wide, thus giving a 25 mm flange either side of the duct that enables it to be attached to the wooden former. Resting on this channel is the upper surface that is clamped down using similar clamps to those used for the working section. To ensure no step occurred at the interface between the two sections, the adjoining faces were cut to have a 45° angle. Hence, when the two were joined together a small channel is formed, which is subsequently filled with an isopon filler. After rubbing down with a fine grade emery paper no variation of surface roughness was detectable at the joint. This procedure was repeated with the upper surface after it was fixed together. It was then placed into position as one long section. Using this technique for the glass-aluminium joint at the interface between the entry section and the working section is impracticable. Hence, care was taken to ensure that any small step that occurred at these locations was rear facing for all three sides, and not forward facing. A seal was achieved at these locations by surrounding the joint with plastic tape. All exterior aluminium surfaces were then painted matt black to comply with the safety regulations for the laboratory, Collins (1987). The flow exit section is constructed in an identical manner to the flow entry section.

The shaped inlet contraction joining the plenum to the tunnel was built to give a contraction ratio of 8 : 1. It is constructed from a corrugated composite material which gives it flexibility and rigidity. This permits it to be formed into the correct shape and allows it to hold that shape. It is then strengthened further by laminating the exterior surface. Although the structure is relatively weak it has survived the project intact.

Chipboard is used in the construction of the settling plenum because exact dimensional stability is not required. Also, it is cheap, and may be cut and shaped easily. Lengths of softwood, 50 x 25 mm, are attached around the edge of the six chipboard sides using wood screws and glue. When assembling the plenum rubber linings are placed along adjoining faces to act as seals. Forty 150 mm bolts are then used to join the sides together. The plenum sits on the floor of the laboratory and the fan discharges into its base via a diffuser. Made from similar corrugated composite material as the inlet contraction the diffuser was strengthened further using polystyrene sheets 25 mm thick. Exits from this are 8 mm in diameter and break up the asymmetry introduced by the fan.

Finally the flow rates available are produced by the fan that is capable of discharging  $5000 \text{ m}^3\text{hr}^{-1}$  of air against pressure differentials of 600 Pa.

After completing the smooth surface investigation, 7.95 mm square ribs were attached along the entire length of the tunnel, at a pitch to height ratio of 7.2 : 1. Key mild steel ribs were used for the development and exit sections while key stainless steel ribs were employed through the working section. Key steels were employed as they are available in the correct sizes and so no time consuming and difficult machining steps were necessary. They were supplied by CJA Stainless Steel Ltd., of Surrey. A cyanoacrylate adhesive was used to attach the mild steel ribs while a cement, Quarini (1986), was employed for the stainless steel ribs. This was undertaken to ensure a good thermal contact between the ribs and the base plate in the heated working section. To ensure the ribs were flat and parallel, each one was attached individually, beginning at the inlet. A machined parallel spacer ensuring that the correct separation is observed.

Glue is applied to each rib and it is then securely clamped and allowed to dry before the next rib is inserted. The procedure is repeated until all the ribs are in position. To study rounded ribs the working section is removed, and a new plate inserted. Although this only gives eight rounded ribs for the flow to develop, it is sufficient because of the number of square ribs preceding it.

A casting rubber compound is used to simulate a deposition on the ribbed surfaces. Mantle (1986) provided data concerning the deposit found on some A.G.R. fuel pins and using this information typical profiles were decided upon for the square and the rounded rib. These are illustrated in Figures 3.5 and 3.6. Information concerning the conductivities of the materials in the reactor and the experiment are given in the table below.

Material	K in Reactor W/mK	K in Experiment W/mK
Stainless steel	24	19
Deposition	0.6	0.54
Gas	0.058	0.024

As may be observed the ratio of the deposit to the steel is not the same. However, they have the same order of magnitude and so qualitative information will be available. The rubber deposit was applied by technicians at the CEGB Berkeley Nuclear Laboratories. An edging strip surrounding the plate enables the correct thickness of deposit to be achieved in the inter-rib region when the rubber is poured onto the flat plate. After this has set, a machined mould of the deposit around the rib is clamped around a rib. The plate is then inclined and the rubber poured down the gap. Repeating the procedure for each rib enables the correct deposited surface to be achieved. Ribs in the development section were not deposited because of the time involved to achieve this. However, sufficient ribs are available with the deposition to give a developed profile at the rear of the plate.

### 3.2. HEATING SYSTEM

Early investigations used a smooth stainless steel base plate, 500 x 300 x 20 mm, to act as the heating surface to the gas. Attached to the underside of the plate using silicon rubber adhesive are 8 electrical pad resistance heater (supplied by W.J. Furse & Co.Ltd, of Nottingham) that are able to supply 3.5. kW of heat. The whole assembly is then surrounded by insulating material in the form of p.t.f.e. strips and glass fibre wool. This reduces heat loss and enables working conditions to be achieved quickly.

A second stainless steel base plate was introduced into the project

when rounded ribs were studied. Unfortunately, it was a different steel. The original stainless steel was an expensive magnetic one, B.S. 970/430, that was purchased with the intention of using magnetism to secure the ribs. This method was later to be abandoned when problems in machining ribs 7.95 mm square and 300 mm long were encountered. [Residual stresses in the metal caused it to bow in different directions each time a layer of material was removed]. The second plate, 500 x 300 x 30 mm, was the more readily available and cheaper 18/8 stainless steel, ATSI 301. The ribs were machined into this thicker block at CEGB Berkeley to ensure a good thermal contact is attained for the more complex rib geometry.

Power to the pad heaters was taken directly from the 240 Volt mains supply and controlled using a panel of dimmer switches. In this manner the heat flux to any part of the plate may be controlled as the pads are distributed so as to completely cover the underside of the plate. Hence, should any heater appear more efficient than the others its power supply can be reduced and so a constant heat flux over the plate is ensured. A small 3 mm gap is present between the heaters that enables thermocouple probes to be inserted into the plate. The power supplied, 3.5. kW, is able to bring the plate to a working temperature, around 30°C above ambient, relatively quickly and so reduce time wastage in the laboratory. Once the working temperature is achieved, the power is switched off or in some cases, reduced. Then, on attaining a steady temperature the hologram is exposed.

No monitoring of the power levels supplied was undertaken. The only instrumentation of the heated section is the insertion of Chrome/Aluminium

thermocouples, through holes in the base, to within 0.5 mm of the surface. They are secured using a water soluble thermocouple cement, supplied by Quarini (1986), that has a similar conductivity to stainless steel. To ensure a good electrical contact is achieved the tips are welded together before insertion using an argon flame welder. The temperatures were recorded using an Analog Devices digital thermometer AD2036 that was first calibrated for the thermocouples.

Surrounding the edges of the plate are 2 mm thick strips of p.t.f.e. insulation. These reduce the heat loss and prevent the wooden former from getting too hot. In doing this it prevents drying out of the wood and so stops it warping. Under the heaters is a thick layer, 40 mm, of glass fibre wool insulation. This is present to stop the heat loss through the base of the working section. This is important as any stray thermal currents entering the laser beams would result in additional phase changes and so lead to incorrect analysis of the hologram.

### 3.3. OPTICAL APPARATUS

During a holographic exposure no optical component after the beam has been split must move any distance greater than a quarter of a wavelength of light ( $0.12 \mu\text{m}$ ) for the exposure to be successful. Hence, the optical components have to be mounted on an optical table that damps out any vibration that may be introduced from the floor. Therefore, this introduces a major design constraint on the layout for the interferometer.

Two optical tables were loaned to the project from the Physics Department. They were constructed in house, and hence were not ideally suited for the work, but this was only to become apparent later in the project. Each table consisted of a large concrete block, 1.5 x 1 x 0.4 m, that was cast in the laboratory. A sheet of boiler plate, 12 mm thick, is secured to the top of the block and this acts as the table surface. Three millimeter diameter holes were drilled and tapped in one table to form a matrix of 100 mm squares and so enable optical components to be clamped down. This structure rests on rubber tyre inner tubes that are inflated to a pressure of 5 lb/f. A working height of 1.2 m is achieved by supporting the tyres on a frame made from 50 mm angle iron. The large mass [concrete] resting on springs and dash-pots [inner tube] effectively damps out oscillations emanating from the floor and so results in a stable base for holography. Stability checks on the tables indicated that although each was interferometrically stable, relative movement between the two necessitates clamping them together. A 'T' shaped working area is produced by clamping the end of one table to the middle of the other using four thick metal bars and four long threaded bolts.

Constraints imposed upon the layout of the interferometer included the relatively long focal length, 2 m, of a schlieren mirror. Also, the fact that the beam splitter gives only a 10° beam separation and a parallel beam has to traverse the 300 mm wide test section. Finally, all optical components have to be arranged on the optical tables.

Before assembling the interferometric layout all optical components were thoroughly cleaned to remove any dirt and grease that could introduce

secondary wavefronts onto the beam. A schematic layout of the final optical arrangement is illustrated in Figure 3.7. An image-plane interferometer was set out on the recommendation of Walklate (1984). To help explain this layout a brief description of each component now follows.

**Laser:** - a 3 watt spectra physics 2020 argon-ion type giving radiation with a wavelength of 514.5 nm. An air speed etalon, model no.589, is fitted to give single frequency radiation and so increase the coherence length to in excess of 20 m. However, by so doing, the power output is reduced to 1 watt. The laser is water cooled and mounted on a separate bench to reduce the likelihood of vibration being introduced onto the optical tables. Being a class 4 laser the beam has to be piped to the table until expansion occurs to comply with safety regulations. Earlier proving tests used a small 5 mW spectra physics helium-neon type laser, that produced radiation having a wavelength of 632.8 nm and a coherence length of 0.2 m.

**Shutter:-** a manual one capable of giving exposure times down to a millisecond was adequate for this investigation.

**Beam steering mirrors:-** these are front surfaced to reduce the possibility of introducing additional diffraction patterns onto the wavefront. Where possible, screw threads are included in the mounting, thus enabling the mirror to be rotated through two co-ordinate directions, and so aid beam alignment. This is particularly important for the mirrors that throw the beam onto the optical tables as any movement here is magnified at the plane of the hologram. A screw thread of 80 teeth per inch is present on one of these mirrors.

**Half wave plates:-** inserted to enable the plane of polarisation of the beam to be varied. Hence, planes may be matched exactly at the hologram.

**Beam splitter:-** a calcite crystal wollaston prism beam splitter, 8 mm square gives a 10' beam separation at exit. If the input polarisation is changed the ratio of the two exit beam intensities also alters. Hence the beam splitter used in conjunction with a half wave plate enables an exact object to reference beam intensity ratio to be selected, without the wasteful insertion of neutral density filters.

**Spacial filters:-** act as beam expanders and consist of a microscope objective and a pin hole that is positioned at the focal point of the lens. A 2.5X objective is used for the object beam and a 10x objective for the reference beam. [The higher the value the sooner the beam expands]. Ten micron pin holes are used for both beams and are present to remove undesirable diffraction rings caused by dust and imperfect mirrors in the system prior to expansion.

**Mirrors:-** all are front surfaced. The schlieren mirror produces a parallel beam that traverses the test section. A mirror is employed here as this introduces fewer aberrations onto the beam front than a lens.

**Plateholder:-** a kinematic plate holder, Ennos (1985), is used for both the double exposure and real-time investigations. Of the two sizes made the larger of them was not used for real-time work as it proved too difficult to replace the plate accurately.

**Holographic plates:-** high resolution Agfa-Gevaert 10E56 H.D. holographic plates are used for the argon-ion laser while 10E75 plates were used for the early investigations with the helium-neon laser. One side of the plates has an emulsion on it and this side faces the wind tunnel.

**Bi-convex lens (not shown):-** at a later stage a 0.15 m diameter lens was introduced to focus the object beam onto the hologram. This was necessary because of reduced space arising from the use of larger size holographic plates.

All components discussed after the half wave plate rest on the optical tables. The mounting of mirrors off these tables failed to produce a hologram. The beam travels over 4 m from the laser head to the hologram and hence any slight movement of these mirrors would result in large variations at the hologram. Precision mirrors were therefore purchased, especially as one of them was to be mounted on a wall, and no problems arose.

Other features that are relevant to the optical layout include the laboratory. It is in the basement of the University and so floor vibration is minimised. There are no windows to the room and so sources of natural light are absent. Hence, when the lights are switched off a good darkroom quality is attained. Finally, all walls and equipment have a matt finish to help prevent any reflections.

Two photographs illustrating the wind tunnel and optical apparatus are illustrated in Figure 3.8a and Figure 3.8b. The former image is taken under normal lighting conditions while the latter has reduced lighting and so illustrates the beam path.

## CHAPTER FOUR

### EXPERIMENTAL PROCEDURE AND DATA ANALYSIS

This chapter presents the experimental procedure undertaken to record both the hydrodynamic and interferometric results. The instrumentation employed and the techniques used to measure fluid flow rates, velocities, turbulence levels and temperature fields are outlined. Analysis procedures for the results are also presented with particular emphasis being placed on the novel holographic procedures.

#### 4.1. HYDRODYNAMIC DATA MEASUREMENTS

Ideally, flow conditions through the test section should be fully developed, or as near to this condition as possible so that a similar situation to that in an A.G.R. may be studied. Hence, the hydrodynamic measurements taken should enable the degree of development to be determined in this tunnel as it is far shorter than the  $60 D_0$  presently recommended to attain fully developed flow conditions. For turbulence levels to develop the length has to be even greater. Good documentation of the flow is essential for any comparison with other work to be undertaken.

To establish the flow conditions in the rig, an experimental programme was organised to record hydrodynamic information for the complete range of volume flow rates available in the tunnel. This procedure was used for both the smooth and rib-roughened surfaces with only minor changes occurring. The data recorded includes:-

I. Both cross stream velocity profiles along the centre lines at a station  $19 D_e$  after the inlet using a pitot static tube.

II. Static pressure drop down the entire length of the tunnel using tappings on the upper wall.

III. Shear stress distribution around the smooth walls at a station  $19 D_e$  downstream of the inlet using a Preston tube. When ribs are present results for only the three smooth walls are recorded.

IV. Turbulence levels along the vertical centre line  $1 D_e$  after the inlet using hot wire anemometry at a single Reynolds number of 12600 (taken at this value because of the theoretical investigation, see Chapter 5).

Using the above information the friction factors and flow rates in the tunnel may also be determined. Hence, a complete description of the flow conditions may be achieved. The instrumentation necessary to record the information and the experimental procedure for each measurement technique now follow.

#### 4.1.1. Velocity Profiles

Mean fluid flow velocities were measured using pitot static tubes inserted through the side walls 19  $D_0$  after the inlet. Both horizontal and vertical traverses were taken at the centre of the side and upper walls. Small diameter plastic tubing (diameter of 2 mm) is used to connect the probe to a Furness digital micromanometer type FC002. This reduces the rapid turbulent fluctuations and so results in a more stable reading. Unfortunately, two separate probes had to be used for the two co-ordinate directions traversed. The probe used for the vertical traverse had a screw thread adjustment ranging from 0 to 50 mm and hence two separate traverses from each wall were required to obtain the flow profile. A larger probe was used for the horizontal traverse which was able to cross from one wall to the opposite one. However, no accurate traversing mechanism was available and hence spot measurements were taken. No readings could be taken in the near wall region, (less than 2 mm from the walls), as the bulky probe could not enter these regions.

The mean velocity is determined using the following relationship:

$$\frac{\Delta P}{\rho g} = \frac{U^2}{2g} \quad (4.1)$$

The density of air was extracted from tables for room temperature conditions. Each traverse was repeated to ensure the experimental accuracy of the probe.

Volume flow rates are estimated from the velocity profiles by superimposing the vertical profile along the horizontal traverse.

Simpson's rule is used to estimate the area under the curves.

#### 4.1.2. Static Pressure

Tappings flush mounted in the upper wall at 0.11 m intervals enable the pressure drop down the tunnel to be recorded. Lengths of plastic tubing lead from the tappings to a manifold and selector switches. These enable each point to be measured quickly and accurately. Each pressure is recorded relative to atmospheric conditions using a Furness digital micromanometer. The pressure drop is indicative of the degree of flow development. A constant drop indicates that the flow is fully developed. Combining the flow velocity information with the pressure drop measurements enables the friction factor ( $C_f$ ) for the tunnel to be determined using the following relationship:

$$\frac{\Delta P}{\rho g} = 4 \frac{C_f l}{D_e} \frac{U_B^2}{2g} \quad (4.2)$$

Repeating the procedure for numerous flow rates enables a check on the friction factor to be undertaken. The estimated error is  $\pm 0.9\%$  and this is explained in Appendix B.

#### 4.1.3. Wall Shear Stress

A thin pitot tube (3.96 mm diameter) inserted through the exit of the tunnel enables the static pressure at the wall to be recorded at a position

19  $D_o$  after the inlet. Provided the tube does not protrude outside the log law region of the boundary layer, it may be assumed to be a Preston tube. This enables the wall shear stress to be determined using Preston's (1954) relationship:

$$\log_{10} \left\{ \frac{\tau_w d^2}{4\rho V^2} \right\} = -1.396 + 0.875 \log_{10} \left\{ \frac{(P_o - P) d^2}{4\rho V^2} \right\} \quad (4.3)$$

The probe is placed next to the wall at numerous locations around the tunnel so that a distribution may be achieved. The addition of ribs allows only the three smooth walls to be studied. However, as the pressure drop down the tunnel is known conditions on the fourth wall can be determined, and so the rough wall friction factor found. Again, numerous flow rates were investigated to obtain a more detailed analysis.

Accuracy for these measurements was poor. An error of  $\pm 4.6\%$  is given in Appendix B. The main reason for this is the poor location of the tube on the wall.

The friction factor may also be determined from the value of wall shear stress using the following equation:-

$$\tau_w = C_f \frac{\rho U_B^2}{2} \quad (4.4)$$

This acts as a further check on the static pressure tapping results.

#### 4.1.4. Turbulence Intensity

At a later stage in the project it was decided to record the turbulence intensity at the inlet of the tunnel for a single flow rate of  $Re = 12800$ .

This was undertaken to obtain the turbulence level at inlet and so verify estimated inlet conditions for the theoretical modelling in Chapter 5.

A single hot wire probe, type 55P01, mounted in a probe support is inserted through the roof of the tunnel  $1.0 D_0$  after the inlet and is connected to a Disa type 55M10 standard bridge. Because only turbulent intensities are required a calibration of the wire is not necessary, a Disa type 55010 lineariser is simply used to compare the mean flow and r.m.s. voltages/velocities. An r.m.s. voltmeter records the voltages. The ratio of mean to r.m.s. velocities is independent of absolute values and so turbulence intensity, being expressed as:-

$$q = \frac{u}{U} \times 100\% = \frac{[(u)^2]^{1/2}}{U} \quad (4.5)$$

requires no calibration procedure. A crude clamping arrangement enabled particular stations along the vertical traverse to be selected. Conditions were allowed to stabilise before mean and r.m.s. voltages were recorded. Again, wall conditions were not recorded because the bulky probe could not enter these regions.

No turbulence intensity measurements were taken for the rib-roughened tunnel as similar inlet turbulent conditions would exist.

Again, the errors are discussed in Appendix B and were estimated to be  $\pm 1.4\%$ .

## 4.2. INTERFEROMETRIC DATA MEASUREMENT

The interferometric procedure is divided into three sections: the first discusses the experimental procedure undertaken to expose the hologram while the second discusses the processing procedure for the plates, and the third outlines the viewing techniques.

### 4.2.1. Holographic Technique

Before assembling any optical configurations all of the components were thoroughly cleaned using acetone and lens tissues to remove any dirt and grease present. The procedure is repeated periodically to ensure good quality holograms are recorded. When not in use the components are covered with protective plastic covers to prevent fouling of the clean surfaces by the pollution present in the air. To help reduce the pollution an air purifier, supplied by Air Improvement Products, type EF10X, is left running and this removes any dust particles larger than 0.1  $\mu\text{m}$ .

Stability checks were performed on the optical components and table by setting up a Michelson interferometer, Michelson (1881), on the tables.

Initially the stability of the tables were tested by observing the movement, if any, of the fringe pattern. A low frequency oscillation of 0.5 Hz was observed. This illustrates the poorer quality of 'home-made' optical tables. However, the exposure times used, less than 0.1 seconds for all cases, means that the oscillation may be effectively ignored for all the double exposure holograms. It will affect the real time work when high

framing rates are used and this affect will be discussed in Chapter 6. Another problem that became apparent was the relative movement between the tables. Clamping the tables effectively solved this one. All optical components proved to be stable if mounted less than 200 mm above the table. Finally, mounting the shutter on the table provided a severe source of vibration when opening and closing. Hence, this had to be mounted externally.

The optical configuration illustrated in Figure 3.7 was then set-up on the tables. Each mount was of sufficient mass to ensure that a slight knock would not move it. Mounts in critical positions, such as those near the edge of the table and those near the hologram, were clamped to the table using the tapped holes. Mirrors on the final approach to the hologram had threaded adjustment to facilitate fine tuning of the angle of the beams. This was especially necessary on the beam traversing the test section as this has to be exactly parallel to the working surface. Whilst arranging the layout a low laser light intensity, less than 20 mW, is used and relatively high background light levels are observed. When operating the laser the procedure recommended by Collins (1987) for safety requirements was followed.

Before interferograms of the flow conditions were taken, a series of proving tests were carried out to determine the optimum procedure to produce holograms. This consisted of taking holograms of three chessmen and by varying exposure times, beam ratios and angles, processing chemicals and processing times, a procedure may thus be found that results in the brightest reconstructed image. This is a time-consuming

procedure and so to decrease the time taken in processing, small plates, 25 mm square, were used. Hence, a series of six plates could be processed at any one time, and so the variable set relatively quickly after studying the resultant image clarity.

These early tests were undertaken using a small 5 mW Helium-Neon laser because the larger Argon-ion one was not available. However, the results would not differ drastically, the only major alteration being a reduction in exposure time when the more powerful laser is introduced.

The tests illustrated that the best images are achieved when the plate is developed to give a neutral density of 0.7 for the He-Ne laser and 2 for the Argon-ion laser. Ferric nitrate bleach proved to be the most suitable as this resulted in the highest diffraction efficiencies of all the bleaches tested. Relatively long exposure times are required to produce the necessary neutral density. Shortening them, however, is possible, but a poorer image results. Because the turbulent structures move quickly and a quicker exposure gives less blur, image quality was sacrificed in an attempt to reduce exposure times. Real time work requires the brightest image possible and hence the optimum values were chosen. The 'stopping' of the turbulent structures occurs in the viewing device (camera, video, etc.) and not the hologram.

The reference to object beam intensity proved insensitive to image clarity above the ratio of 4 : 1. Light intensities are measured using a lightmeter supplied by Evans Electroselenium Ltd. This gives a reading in foot-candles. Adjusting the intensities is simply achieved by rotating the

half-wave plate preceding the beam splitter. Unfortunately, the beams do not remain on one horizontal plane above the table, and so a second half-wave plate is required in the reference beam to match the planes of polarisation at the hologram. To detect the orientation of the planes a screen is substituted for the hologram and the light falling on this is viewed through a polarised sheet of plastic. On rotating the sheet the intensities of the two laser beams varies and one merely adjusts the half-wave plate to ensure that the intensities vary in sequence. The final check of matching path lengths is not necessary for the Argon-ion laser as the air spaced etalon ensures a coherence length in excess of 20 m.

Exposing the hologram is a simple matter of opening the shutter for a set duration. Exposure times vary depending on the size of the hologram and the type required, double exposure or real time. For double exposure holograms the shutter speed was  $1/100$ th of a second for flow rates less than a Reynolds number of 15000. This was reduced to  $1/250$ th of a second for faster flow rates to prevent significant movement in the fringes. Although these latter holograms only developed to give a neutral density of 0.2, they still resulted in an image that could be analysed. The real time reference exposures were  $1/10$ th of a second and this gave a developed neutral density of 2 which was found to be ideal to obtain a bright reconstruction. Once replaced in the kinematic plate holder the two object beam intensities, reconstructed and actual, were matched by rotating the first half-wave plate. In this fashion the best contrast between the fringes may be achieved.

#### 4.2.2. Processing Procedure

Processing of the holographic plates is carried out in the laboratory immediately after exposure. This entails developing, fixing and then bleaching the plates in a dark room, with a washing stage between each step to prevent chemicals mixing. A description of the plates and the chemical action they undergo to form the hologram is given next to aid in the understanding of holography.

Silver halide photographic emulsion plates are used as they have a relatively high sensitivity and are easily purchased. The emulsions are sensitised for laser light emissions and a sample of emulsions suitable for holography include Agfa-Gevaert 10E56, 8E56, and 10E75 plates. Figure 4.1 illustrates the approximate sensitivity curves for the emulsions described. From the diagram it may be observed that Agfa-Gevaert 8E56 plates would be suitable for radiation having a wavelength of 514.5 nm, that from an Argon-ion laser, and hence these plates are used. The emulsion must be capable of resolving fringes at the frequency of the interference pattern formed at the hologram. This frequency is dependent upon the offset angle of the reference beam  $\gamma$  and is determined by:-

$$n = \frac{\sin\gamma}{\lambda} = \frac{\sin 60^\circ}{514.5 \times 10^{-9}} = 1,680 \text{ lines/mm}$$

Agfa 8E56 plates have a resolution in excess of 5000 lines/mm and hence easily meet this condition.

Exposure and development requirements must be decided upon to ensure the assumed linear relationship between irradiance and amplitude transmittance is satisfied. That is, exposure must occur on the linear portion of the Hunter-Driffield curve, illustrated in Figure 4.2, to prevent distortion of the reconstructed image. This linearity condition governs two important experimental parameters, the exposure time and the beam ratios. Failure to fulfil this condition results in additional diffraction components and hence a noisy image. The proving tests discussed earlier in fact are a method for determining the linear response condition experimentally.

High resolution photographic emulsions basically consist of minute ( $\sim 0.4 \mu\text{m}$ ) crystals of silver halide suspended in a gelatin. Also present are sensitising agents that will not be discussed as they take no part in the reconstruction process. When the resulting  $7 \mu\text{m}$  layer is exposed to light, the halide absorbs photons and forms tiny regions of metallic silver called development centres. The higher the light intensity the greater the number of development centres. On placing the plate in a solution of developer, a complex reaction occurs that converts the silver to a metallic form in crystals with a development centre. For crystals without a development centre no reaction occurs. This remaining unexposed silver halide is then removed using a fixing solution. This results in regions that are opaque where grains of metallic silver are present while areas that were exposed to low light levels are transparent. We have a negative image. The diffraction efficiency of this absorption hologram is poor as large areas are opaque. However, it may be converted to a phase hologram with a higher diffraction efficiency by bleaching. A bleach

bath converts the opaque silver to a transparent silver salt, usually a halide. After numerous bleaches were tested during the proving exercise the one chosen and used for the rest of the work consists of a ferric nitrate and potassium bromide mix. The multiple valency iron is reduced to a lower valency while the silver is oxidised to form silver bromide (AgBr).



This procedure increases the diffraction efficiency from below 15% to 60-80% and hence is a worthwhile step.

The processing procedure is summarised below, along with the relevant times for each step. Exposure of the plate occurs initially and then the following:-

I. Develop for 4 minutes in Ilford autophen developer whilst continually agitating the dish. Originally neophin blue (tetenal) was used but this was expensive and hence abandoned when supplies diminished.

II. Wash in a bath of flowing water at room temperature, 17°C, for a period of 5 minutes.

III. Fix for 3 minutes in a bath of Agfa-Gevaert G334 fixer and hardener.

IV. Wash in a bath of flowing water at room temperature, 17°C, for a period of 15 minutes.

V. Bleach in a ferric nitrate and potassium bromide solution for a period of  $1\frac{1}{2}$  times the clearing time (the time taken for the plate to become transparent).

VI. Wash in a bath of flowing water at room temperature, 17°C, for 3 minutes. Add photo-flo 600 to the final rinse, then remove the plate and allow it to dry.

The above routine was employed throughout the project for both the double exposure and real time holograms. Safety lighting is used when developing and fixing the plates. The standard red darkroom light is used for Argon-ion plates, but a dark green must be used for Helium-Neon plates. As the project progressed the quality of the holograms improved as techniques and procedures were refined. The most notable improvement being the reduction of straining and dust deposit on the final holograms. However, all holograms produced were able to be viewed, if not necessarily analysed.

#### 4.2.3. Viewing Procedure

To view the interferograms the plate has to be illuminated by a reconstruction beam which is identical to the reference beam. However, a

white light source hitting the plate from the same angle is sufficient for double exposure focussed interferograms. Two solutions may therefore be employed. The first is to replace the interferogram back in the plateholder, block off the object beam and use the reference beam as the reconstruction beam. Photographing the interferogram then gives a permanent image that may be photographically enlarged. This enables analysis of the interferogram to proceed, but a loss of resolution occurs because of the granularity of photographic emulsion.

A second and more efficient process is to use a Vickers projection microscope to enlarge the boundary layers directly. A white light source is used to illuminate the interferogram, which was placed in the focal plane of the microscope. Numerous magnifications may then be selected, up to a maximum of 36X, and the interferogram viewed. Because the resolution of the hologram is better than 1000 lines/min (see Section 4.2.2.) no granular effects are observed. The fringe spacing may then be determined directly off the screen of the microscope or it may be photographed and analysed later. Hence, a more accurate solution is obtained. And so for all double exposure interferograms this second technique is used.

For real-time investigations the viewing has to occur on the optical tables. Hence photographic recording is the only method available to give permanent images of the flow that enables analysis to proceed. The best method found for achieving this was to remove the imaging lens of the 35 mm camera and record the fringes directly on the film. This, however, is only possible with 35 mm cameras with exposure memories, such as the one used in this study, an Olympus OM4. Unfortunately, the resolution is

reduced using real-time recording, but there is sufficient information present for an automated analysis. Hand analysis was estimated to give a minimum error of  $\pm 10\%$  and so was not used on these images. However, resolution is sufficient for the visualisation of structures in the outer wall and main flow regions, when using 35 mm stills, video or high speed film recording techniques. Hence the real-time images were used generally for this purpose rather than for detailed analysis.

#### 4.3. HOLOGRAPHIC ANALYSIS PROCEDURE

An interferogram is a record of the phase change between two object waves, usually referred to as the reference and test object waves. The reference object exposure records a uniform object field as the speed of the wavefront through it remains constant. However, the test object exposure records a non-uniform field as the speed of light varies through the medium. This variation is caused by thermal gradients generating small refractive index gradients, hence different light speeds through the medium, and ultimately a different phase to the light emerging. Each fringe formed on the interferogram represents a phase change of  $2\pi$  and is a line of constant temperature, an isotherm.

To determine the temperature field described by the interferogram the equation of interferometry given by Hauf and Grigull (1970) for an incompressible two-dimensional boundary layer is used. This states:-

$$T_{(z,y)} = T_r \left[ 1 - \frac{N \Delta C \rho_i}{G \rho_r W} \right] \quad (4.6)$$

where  $C\theta_i$  is a correction factor that allows for the deviation of the measured ray path from the ideal one parallel to the heated surface. That is, it corrects refraction errors. Hence, the temperature at any point in the field may be determined by counting fringes, or parts of fringes, away from the reference ambient condition. Wall temperatures may then be estimated by fitting a curve to the flow field temperature. It is not measured directly as a fringe does not occur on the wall, only very close to it. Heat flux in the near wall is then determined by assuming that in the laminar sub-layer heat transfer takes place by conduction only. Heat transfer coefficients and local Nusselt numbers may then be determined using the standard relationship:-

$$Nu = \frac{h D_e}{k} = \frac{q_w D_e}{(T_w - T_r)k} \quad (4.7)$$

Numerous stations on the surface may be studied and a mean value of the heat transfer coefficient evaluated. This procedure is relatively straight-forward for the smooth surface investigation, but the rib-roughened surface has added complications in that the heat transfer varies significantly around the surface. Hence, the heat transfer coefficient around the entire rib is plotted and the maximum and minimum values determined. Hot spots may therefore be located, and their size estimated.

The correction term introduced in equation (4.6) allows refraction effects to be determined up to certain limits after which ray crossing occurs. It is determined using an iterative ray-tracing technique as outlined by Walklate (1981). The correction factor is given by the expression:-

$$C\phi_i = W \left[ T(x,y)_{z=0} \int_{\phi} \frac{\delta\phi}{T(x,y)} \right]^{-1} \Big|_{i-1} \quad (4.8)$$

where the actual ray path  $\phi_{z,y}$  is traced using refraction theory which gives the change in gradient as:-

$$\frac{d^2y}{dz^2} \Big|_{z,y} = \frac{1}{n} \frac{dn}{dy} \Big|_{z,y} = \left[ \frac{G\rho_r}{(T/T_r + G\rho_r)T} \right] \frac{dT}{dy} \Big|_{z,y} \quad (4.9)$$

To perform the integration the following Taylor series expansions are necessary. Assuming that  $\Delta z$ , the step distance, is small when compared to the plate width  $W$ :-

$$\frac{dy}{dz} \Big|_{z + \Delta z} = \frac{dy}{dz} \Big|_z + \Delta z \frac{d^2y}{dz^2} \Big|_z$$

and

(4.10)

$$Y \Big|_{z + \Delta z} = Y \Big|_z + \Delta z \frac{dy}{dz} \Big|_z + \frac{\Delta z^2}{2} \frac{d^2y}{dz^2} \Big|_z$$

A first estimate for the temperature field is made with  $C\phi_i$  set to unity and then the ray path is traced through the test section assuming two boundary conditions:-

(I)  $\frac{dy}{dz} \Big|_{z=0} = 0$  (ray enters parallel to wall)

(II)  $y \Big|_{z=0}$  (measured displacement from wall)

Having determined the ray path a new estimate for  $C\theta_i$  is made and hence a new temperature field. The process is then repeated until the value for  $C\theta_i$  converges and the correct temperature field is determined. A practical limit to the technique is imposed when high heat transfer coefficients are studied. Large thermal gradients are present and so a large amount of refraction occurs. A stage is therefore reached when ray crossing occurs and once this happens the analysis procedure breaks down. To increase the range of study a thinner test section could be constructed which would reduce the amount of refraction. However, a thinner field would also lead to a loss of two-dimensionality of the flow conditions and so introduce an end-effect error. These are the effects introduced from the side walls and estimating them is a complicated procedure. Hence, a compromise between the two effects is necessary to decide the tunnel width. And as refraction effects are easier to deal with the tunnel size is chosen so as to minimise the end effects.

Spanwise averaging of the field results in problems when analysing the interferogram. The interference fringes in the flow become coarser as the field is not exactly two-dimensional. This problem is negligible in the near wall region, but is exacerbated in the middle and outer flow regions by the spanwise averaging contributions from the spanwise structures in the flow. Thus the outer wall fringes are often broad and diffuse and so make quantitative determinations of the temperature field substantially more difficult.

Holographic interferometry also suffers, as do all interferometric techniques, from diffraction effects, which limit its ability to make accurate

measurements very close to solid boundaries. Hence, resolution is often lost in the region near to the wall as two sets of fringes are present, those due to the thermal gradient and those arising from diffraction. The exact location of the wall is therefore difficult to determine and so a spline fitting routine is employed to determine the plate position and the corresponding wall temperature and temperature gradient.

The fluid temperature fields are estimated to have an experimental tolerance of 5.22%, at low Reynolds numbers which rises to 6.73% at higher flow rates. These errors may be reduced by the introduction of heterodyne techniques or by automatic fringe analysis. Details of these error estimations are discussed in Appendix B.

## CHAPTER FIVE

### TURBULENT MODELLING OF THE FLOW FIELD

The equations and turbulent models used to describe Newtonian flows are described in this Chapter. A Reynolds averaging of these governing equations results in a set of Reynolds stresses that are modelled by transport equations. This averaging is an important procedure because no unsteadiness in the turbulent structures should be introduced. Hence, there may be an unsteadiness after the averaging but it is ignored. The predictions employed to solve these additional stresses are outlined, with particular reference to the finite element code FEAT (Finite Element Analysis of Turbulent transport).

#### 5.1. BASIC EQUATIONS

The governing equations for the flow of a Newtonian fluid are the continuity equation, the Navier-Stokes equations and the energy equation. It is assumed that the fluid properties of density, molecular viscosity and thermal conductivity are constant within the volume considered. Under these conditions, the governing equations can be written for the instantaneous dependent variables in Cartesian tensor form as follows:-

Continuity:

$$\frac{\partial \tilde{u}_j}{\partial x_j} = 0 \quad (5.1)$$

Navier-Stokes:

$$\begin{aligned} \frac{\partial \tilde{u}_i}{\partial t} + \tilde{u}_j \frac{\partial \tilde{u}_i}{\partial x_j} &= \frac{1}{\rho} - \frac{\partial \tilde{p}}{\partial x_i} \\ &+ \frac{\partial}{\partial x_j} \left[ \nu \left( \frac{\partial \tilde{u}_i}{\partial x_j} + \frac{\partial \tilde{u}_j}{\partial x_i} \right) \right] \end{aligned} \quad (5.2)$$

Energy:

$$\frac{\partial \tilde{T}}{\partial t} + \tilde{u}_j \frac{\partial \tilde{T}}{\partial x_j} = \frac{\partial}{\partial x_j} \left( \frac{\nu}{\sigma} \frac{\partial \tilde{T}}{\partial x_j} \right) \quad (5.3)$$

where  $\sigma$  is the molecular Prandtl number.

These equations are difficult to solve for turbulent phenomena and so Reynolds (1895) decomposed them into a mean and fluctuating component so that:

$$\left. \begin{aligned} \tilde{u}_j &= U_j + u_j \\ \tilde{p} &= P + p \\ \tilde{T} &= T + \theta \end{aligned} \right\} \quad (5.4)$$

These may be substituted into the original governing equations and then Reynolds averaged. This is possible even for unsteady flows and the following equations result:

Continuity:

$$\frac{\partial U_j}{\partial x_j} = 0 \quad (5.5)$$

Navier-Stokes:

$$U_j \frac{\partial U_i}{\partial x_j} = -\frac{1}{\rho} \frac{\partial p}{\partial x_i} + \nu \frac{\partial^2 U_i}{\partial x_j^2} - \frac{\partial}{\partial x_j} (\overline{u_i u_j}) \quad (5.6)$$

Energy:

$$U_j \frac{\partial T}{\partial x_j} = \frac{\partial}{\partial x_j} \left[ \frac{\nu}{\sigma} \frac{\partial T}{\partial x_j} - \overline{u_j \theta} \right] \quad (5.7)$$

In the above equations the time averaged products of the fluctuating velocity components ( $\overline{U_i U_j}$ ) represent the Reynolds stresses and may be expressed in matrix notation as:-

$$\overline{u_i u_j} = \begin{vmatrix} \overline{u^2} & \overline{uv} & \overline{uw} \\ \overline{uv} & \overline{v^2} & \overline{vw} \\ \overline{uw} & \overline{vw} & \overline{w^2} \end{vmatrix} \quad (5.8)$$

The exact nature of these Reynolds stresses is not known, but transport equations can be derived that describe their behaviour. These are discussed in the following section.

## 5.2. TURBULENT MODELS

The introduction of the Reynolds stresses implies that the flow may be regarded as a combination of a steady laminar-like motion upon which a turbulent fluctuation field acts. A proposal attributed to Boussinesq (1877)

was that the turbulent fluctuations had the effect of an additional viscosity on the mean flow, a quantity he termed the 'turbulent viscosity'. The total shear stress would then be:-

$$\tau_{12} = \mu \frac{du_1}{dx_2} + \mu_t \frac{\partial u_1}{\partial x_2} = \left\{ \mu + \mu_t \right\} \frac{du_1}{dx_2} \quad (5.9)$$

Unlike the laminar viscosity  $\mu$  the turbulent viscosity  $\mu_t$  is not a property of the fluid, but is largely dependent on the structure of the turbulence. The problem still arises of how to estimate  $\mu_t$ . By assuming the fluctuations in the lateral velocity are proportional to the longitudinal ones and these are proportional to the mean velocity gradients and distance to the wall, Prandtl (1926) developed an expression for the turbulent viscosity -

$$\mu_t = \rho \left[ \frac{\tau}{\rho} \right]^{1/2} \ell \quad (5.10)$$

The only unknown is an estimate of the length scale,  $\ell$ , and numerous proposals were made for how it should be determined. Prandtl proposed it was proportional to the distances from the nearest wall. However, no one method is correct for a universal situation and hence numerous variations have been proposed to date.

All of the proposals had similar shortcomings. The major one being that zero turbulence is predicted at reattachment points because the velocity gradients fall to zero. This is obviously incorrect as maximum turbulence and heat transfer occur at these locations. A more universal model can therefore be proposed that relates the turbulence intensity to a turbulent property. A scalar quantity chosen in the one equation model is the turbulent kinetic energy  $k$ , defined as (Prandtl (1945)):-

$$k = \frac{1}{2}(\overline{u^2} + \overline{v^2} + \overline{w^2}) \quad (5.11)$$

The bar refers to time averaged phenomena. It is based on the fluctuations of velocity from a mean value.

For plane two dimensional boundary layer flows at high Reynolds numbers the turbulent transport equation may be derived from the Navier-Stokes equations and has the form:-

$$\rho \frac{Dk}{Dt} = - \frac{\partial}{\partial x_2} (\overline{\rho v k} + \overline{v p}) - \overline{\rho u v} \frac{\partial u}{\partial x_2} - \mu \Sigma \left[ \frac{\partial u_i}{\partial x_2} \right]^2 \quad (5.12)$$

Convective = Diffusion + Production - Dissipation  
 flux term term term

The first term represents the diffusion of the turbulence and so has the effect of redistributing the energy in space. It is analogous, for example, to conduction in convective heat transfer. The second term is the generation of the turbulence from the mean flow gradients. Moving with the flow, variations in velocity across the profile give rise to a rotary motion or a 'large eddy'. These large structures then generate smaller ones and the process is then repeated down a cascade of eddies until viscous effects dominate and dissipation to thermal energy occurs. The third term is the above-mentioned dissipation. The transport equation may then be modelled (i.e. approximated) using certain simplifying assumptions and by determining the proportionality constants from experiments. The eddy viscosity is then determined using:-

$$\mu_t = C_\mu \rho k^{1/2} l_\mu \quad (5.13)$$

In addition to the flow equations (5.5 to 5.7), only one extra partial differential equation has to be solved and this is for  $k$ . Hence, the model is termed a 'one equation model'.

However, from (5.13) it is still necessary to prescribe the length scale, algebraically. In a one-equation model this is achieved using Van Driest's (1957) proposal. Wolfshtein (1969) recommended a length scale specified as follows:-

$$l_{\mu} = C_1 l \left[ 1 - \exp \left\{ -A_{\mu} \frac{k^{1/2} l}{\nu} \right\} \right] \quad (5.14)$$

where  $l$  is the perpendicular distance to the wall. Far from the wall  $l$  is large and as the wall is approached it is damped by a factor  $A_{\mu} k^{1/2} l / \nu$ . This behaviour is typical for experimentally observed flows next to walls.

This one-equation model is therefore able to predict turbulence at reattachment and hence is a major advance from the mixing length hypothesis. However, the transport of the turbulence length scale is not accounted for and so an improved model is necessary that gives more universality.

Another parameter is therefore required that is able to model the transport of the turbulent length scale. This yields two additional equations to be solved and is termed a 'two-equation model'. The most popular additional parameter is  $\epsilon$  as it is easily derived from the  $k$  equation and models the length scale. Hence, a two-equation model that specifies a partial difference equation for the length scale is the  $k$ - $\epsilon$  model. Here the transport properties are  $k$ , the turbulence energy and  $\epsilon$  the

turbulence energy dissipation rate, Rodi (1980).  $k$  is easily defined, but the length scale is estimated from the dissipation in the laminar sub-region. High turbulence is found in the low frequency large eddies of the main flow but a length scale cannot be assigned that successfully locates all the energy present. By assuming the inertia sub-region is merely a region of energy transfer where no energy is dissipated or generated, an estimate for  $\epsilon$  may be obtained by dimensional analysis. A length scale would be:-

$$l \approx k^{3/2} / \epsilon$$

Hence, an expression for a suitable length scale is:-

$$l = C_\mu \frac{k^{3/2}}{\epsilon} \quad (5.15)$$

where  $\epsilon$  is the dissipation rate of the energy by the generation of heat in the very small eddies and  $C_\mu$  is a turbulent model constant.

For two dimensional incompressible turbulent flow the  $k$ - $\epsilon$  transport equations are:-

$$U_j \frac{\partial k}{\partial x_j} = \nu_t \left[ \frac{\partial U_i}{\partial x_j} + \frac{\partial U_j}{\partial x_i} \right] \frac{\partial U_i}{\partial x_j} + \frac{\partial}{\partial x_j} \left[ \left( \frac{\nu + \nu_t}{\sigma_K} \right) \frac{\partial k}{\partial x_j} \right] - \epsilon \quad (5.16)$$

where:

$$\epsilon = \overline{\frac{\partial u_i}{\partial x_j} \left( \frac{\partial u_i}{\partial x_j} \right)} \quad (5.17)$$

and

$$\begin{aligned} U_j \frac{\partial \epsilon}{\partial x_j} = & C_{1\epsilon} \nu_t \frac{\partial U_i}{\partial x_j} \left( \frac{\partial U_i}{\partial x_j} + \frac{\partial U_j}{\partial x_i} \right) \frac{\epsilon}{k} \\ & - C_{2\epsilon} \frac{\epsilon^2}{k} + \frac{\partial}{\partial x_j} \left[ \left( \frac{\nu + \nu_t}{\sigma_\epsilon} \right) \frac{\partial \epsilon}{\partial x_j} \right] \end{aligned} \quad (5.18)$$

where  $C_{1\epsilon}$ ,  $C_{2\epsilon}$ ,  $C_\mu$ ,  $\sigma_K$  and  $\sigma_\epsilon$  are empirical constants.

Numerous values for the modelling constants have been proposed by Launder et al (1973) for free shear flows or for boundary layer and recirculating flows, Rodi (1980).

The  $k-\epsilon$  model is able to predict high Reynolds number flow, but is not suitable close to a solid boundary. Hence empirical wall functions are usually introduced to describe flow conditions close to boundaries. [These obey the log law of the wall]. However, for low Reynolds number flow the law of the wall extends a considerable distance into the flow and so an alternative method of modelling these conditions is required.

Jones and Launder (1972) presented a model of turbulence in which the local turbulent viscosity is determined from the turbulent kinetic energy and the energy dissipation rate and so included a viscous diffusion term for  $k$  and  $\epsilon$ . Also the constants become Reynolds number dependent and further terms must be added as the dissipation process is non-isentropic. Their proposed turbulent energy dissipation is:-

$$\Delta = \frac{C_D \rho k^{3/2}}{\rho} + \frac{2\nu k}{\rho^2} \quad (5.19)$$

where  $\rho$  is the perpendicular distance away from the wall. Hassid and Poreh (1975) extended their concept and introduced a two-part dissipation term, one corresponding to the Reynolds stresses and a second modelling to velocity gradient fluctuations near a wall. This gives a total expression for the dissipation of:-

$$\Delta = \frac{2\nu k}{\rho^2} + \frac{C_D \rho k^{3/2}}{\rho} \left[ 1 - \exp \left[ -A\mu \frac{k^{1/2} \rho}{\nu} \right] \right] \quad (5.20)$$

This form satisfies the requirements that the dissipation near a wall is balanced by the viscous diffusion and so describes several features of the flow quite satisfactorily.

Wolfshtein (1975) proposed a further simplification of this model that eliminates one empirical constant. It also gives a simpler and physically clearer form to the dissipation which becomes:-

$$\Delta = \frac{2(\nu + \epsilon)k}{\rho^2} \quad (5.21)$$

where  $\epsilon = C_\mu k^{1/2} \rho$ .

After correcting the values for the constants this new simpler wall model produced negligible variations to the turbulent quantities.

### 5.3. SOLUTION PROCEDURE

Solution of the transport equations described in the previous section may be undertaken using finite differences, or finite elements. Each scheme will be outlined by discussing the solution procedure of a particular code. TEACH, Gosman et al (1977), uses finite differences to solve the transport equations while FEAT, Smith (1985), used finite elements. For further information on the schemes the references given should be consulted.

Both schemes divide the flow field into smaller parts, and apply the differential equations over the grid cells or elements, discretise these equations into algebraic equations and so reduce the number of degrees of freedom of the system, and then solve to obtain the flow field. The methods of discretisation and solution differ but each uses a cyclic process to achieve the final result. Each solution procedure is now outlined.

#### 5.3.1. Finite difference.

A scheme using this method of solution is the TEACH program, Gosman et al (1977). It uses the concept of universality for the transport equations for convection, diffusion and source terms. All these are solved using the single algorithm used for TEACH, which is outlined below.

The flow field is divided into smaller cells by overlaying it with a rectangular grid whose intersection points, or nodes, denote the location at which all the variables, except velocity, are calculated. The governing equations are then integrated over each small volume to produce incremental versions of them. Each node therefore has a set of non-linear equations describing the flow.

These equations are then solved using inner and outer iteration techniques. The outer sequence begins by obtaining a velocity field by solving the momentum equations. Continuity is enforced by solving the discretised equations for pressure (actually an adapted one for pressure correction) and this determines the adjustments to the velocities and pressures. The remaining variables are solved for in turn and the whole process then repeated until a satisfactory solution is obtained. Hence, the equations are solved algebraically using direct methods. Numerous sweeps are required to obtain the solution.

The inner iteration sequence is used to solve the equation sets for the individual variables. A form of block iteration is used to solve the variables along each grid line. Complete convergence is not required as this sequence is usually weighted to give only small changes and so prevent overshooting of the variables.

### 5.3.2. Finite elements

Again the flow field is divided into smaller cells but this time by a mesh that need not be rectangular. The intersection points or nodes

again denote the location at which the variables are defined, but this time they are joined by a 'finite element'. The method of discretisation is different. Instead of applying the governing equations to produce incremental versions of them, an approximate solution is initially guessed by fitting a polynomial in space. Each point and its surrounding elements are then studied and a value for a solution obtained everywhere. The difference between the polynomial and the correct solution is then minimised by integrating the equations over the polynomial and weighting each solution with its surrounding polynomials. Hence, a set of non-linear algebraic equations is obtained that have to be solved.

For a direct method of solution the non-linear equations are linearised using Newton-Raphson iterations and so a new set of equations is obtained.

Initial guesses for the velocity field, the effective viscosity, and the length scale are made. The latter two turbulent parameters are chosen as these are easily estimated. Values for  $k$  and  $\epsilon$  may then be determined by assigning boundary conditions. The new  $\epsilon$  gives a new length scale which then enables the procedure to be repeated until a converged turbulent field arises. A new turbulent viscosity  $\mu_t$  is then predicted and this enables a new velocity field to be determined: hence a new turbulent field and so on, until a converged solution is obtained. Because the non-linear terms for each parameter are assigned to an individual group parameter the solution converges after 10-20 cycles, far fewer than that for finite differences.

To help explain the finite element technique the method of solution for a one dimensional heat transfer problem is illustrated in Appendix C.

#### 5.4. FEAT ANALYSIS

The results presented in this project were obtained using the finite element code FEAT at CEGB Berkeley Nuclear Laboratories. Smith (1982) illustrated that  $k-\epsilon$  solutions are not suitable for direction solution by finite element schemes without employing numerical damping. Hence the solution scheme incorporated into FEAT is based on the  $q-f$  turbulence model, where  $q$  is the positive square root of the turbulence energy and  $f$  is a frequency which is interpreted as the vorticity of the large scale eddies. These quantities are chosen in an attempt to decouple the transport equations and so reduce the number of non-linear terms. No  $f$  terms are found in the  $q$  equation, only the length scale  $\rho$ . Also only velocities and  $q$  at the wall are found in the  $f$  equation and so  $f$  is independent of  $q$ . This enables the two to be solved independently and so give a solution in a shorter period of time. It also reduces the possibility of the Newton-Raphson iterations overshooting.

The table below summarises the terms solved for both the FEAT code and the TEACH one.

Code	One-equation (term)	two-equation	
		(term)	(symbol)
TEACH	$k$	$k^{3/2}/\rho$	$\epsilon$
FEAT	$k^{1/2} = q$	$k^{1/2}/\rho$	$f$

The turbulent viscosity for this model is:-

$$\mu_t = \frac{\rho}{Re} C_\mu q^2 / f \quad (5.22)$$

The transport equations for q and f are:-

$$2U_j \frac{\partial q}{\partial x_j} = \ell \left[ \frac{\partial U_i}{\partial x_j} \left( \frac{\partial U_i}{\partial x_j} + \frac{\partial U_j}{\partial x_i} \right) \right] + \frac{\partial}{\partial x_j} \left[ \frac{\ell}{\sigma_q} \frac{\partial q^2}{\partial x_j} \right] + \frac{2\ell}{q} \left[ \frac{\partial q}{\partial x_j} \right]^2 - \frac{C_\mu q^2}{\ell} \quad (5.23)$$

$$U_j \frac{\partial f}{\partial x_j} = C_{1f} C_\mu \frac{\partial U_i}{\partial x_j} \left( \frac{\partial U_i}{\partial x_j} + \frac{\partial U_j}{\partial x_i} \right) - C_{2f} + \frac{\partial}{\partial x_j} \left[ \frac{C_\mu g^2}{2\sigma_f f^2} \frac{\partial (f)^2}{\partial x_j} \right] \quad (5.24)$$

where  $C_{1f}$ ,  $C_{2f}$ ,  $C_\mu$ ,  $\sigma_q$  and  $\sigma_f$  are empirical constants. Unlike those for the  $k-\epsilon$  model, the above constants have not been fitted to a wide range of data, and hence some source terms are included in the  $f$  transport equation to make the two models identical.

This model, like the  $k-\epsilon$  one, breaks down in the near wall regions and so the standard wall functions are also used in FEAT. However, a low Reynolds number model is available that is a combination of the one equation  $q-\ell$  and two equation  $q-f$  models. The  $q$  equation is identical to the high Reynolds number version except for the inclusion of a damping function  $D_f$ . [This is similar to the Hassid and Poreh (1975) model]. The  $q$  equation is:-

$$2U_j \frac{\partial q}{\partial x_j} = D_f \ell \left[ \frac{\partial U_j}{\partial x_j} \left( \frac{\partial U_i}{\partial x_j} + \frac{\partial U_j}{\partial x_i} \right) \right] + \frac{2\ell}{q} \left[ \frac{\partial q}{\partial x_j} \right]^2 + \frac{\partial}{\partial x_j} \left[ \frac{\ell}{\sigma_q} \frac{\partial q^2}{\partial x_j} \right] - \frac{C_\mu D_f q^2}{\ell} \quad (5.25)$$

where

$$D_f = 1 - \exp\left\{-A_\mu \frac{q\ell}{\nu}\right\} \quad (5.26)$$

$$A_\mu = 0.0285$$

The damping function  $D_f$  is a measure of the amount of turbulent viscosity. The  $f$  equation used ensures that at high Reynolds numbers the standard  $q$ - $f$  model is calculated. No attempt to model  $f$  in the low Reynolds number region is made, as here the length scale is calculated from  $C_\mu^{1/4}\kappa y$ . The damping factor  $D_f$  has been applied to the turbulent diffusivity of  $f$  to limit the effect of the  $f$  calculated in the near wall region. So the length scale is determined from:-

$$\ell = C_\mu^{1/4} \kappa y (1 - B) + C_\mu \frac{q}{f} B \quad (5.27)$$

where

$$B = \frac{1}{2}(1 - \tanh[\alpha\kappa(y^+ - y_0^+)]) \quad (5.28)$$

and

$$y^+ = \frac{\rho U g}{\mu} \quad y_0^+ = 30 \quad \alpha = 0.2387$$

The boundary conditions at solid walls for turbulence variables are:-

$$q = 0 \quad \text{and} \quad \frac{\partial f}{\partial y} = 0 \quad (\text{natural condition}) \quad (5.29)$$

An investigation by Smith (1986a) details the characteristics of this model when the constants are varied, and gives the following advantages for using a one-equation model near the wall.

1.  $\epsilon$  is a difficult concept to model near a wall and often predicts unrealistic length scales
2. a linear function of wall distance for the length scale is supported by experimentation
3. it is numerically more stable
4. as complicated geometries are usually studied this concept is a sensible first approximation.

The major drawback for the model is that relaminarisation is not predicted, and so the model is limited in its physical generality.

To summarise the discussions on the one-equation wall models the prescriptions for the turbulent viscosity and the dissipation are given in the table below.

Proposer	$\mu_t$	$\Delta$
Wolfshtein	$C_\mu \rho k^{1/2} y (1 - \exp(-A_\mu Re_T))$	$C_D \rho k^{3/2} / [y (1 - \exp(-A_D Re_T))]$
Hassid & Poreh	"	$(C_D \rho k^{3/2} / y) (1 - \exp(-A_\mu Re_T)) + 2\nu k / y^2$
Hassid & Poreh + Wolfshtein	"	$2(\nu + \epsilon) k / y^2$
Jones & Launder	$(C_\mu f \mu) \rho k^{1/2}$	$C_D \rho k^{3/2} / l + 2\nu k / \rho^2$
Smith (FEAT)	$\rho q l (1 - \exp(-A_\mu \frac{q l}{\nu}))$	$C_\mu (1 - \exp(-A_\mu \frac{q l}{\nu})) k^{3/2} / \rho + \frac{2\nu}{\rho} (\frac{dk^{1/2}}{dy})$

The manner in which the turbulent Reynolds number  $Re_T$  is defined is important in the above table. Two effects dominate close to the wall and a compromise between the two has to be made when deciding on the damping function. These two effects are the wall and the turbulence at low flow rates. That is, should the length scale be based on wall distance, or the scale of the eddies in the wall region. Hence, numerous parameters have been chosen by the separate workers and this explains the numerous different constants specified for low Reynolds number models.

### 5.5. USING THE FEAT CODE

All theoretical predictions presented in this work were made using the fluid flow code FEAT at CEGB Berkeley Nuclear Laboratories during a four

month placement. The code runs on the CMS computing system at Berkeley, with the finite element analysis batched to the main computer facilities in London.

The code has been written in a modular form so that the nature and form of the governing equations can be easily changed. To control the finite element procedure the user provides the code with several different types of information. These are listed by Hickmott (1986) and are summarised here:

- I. the type of equations to be solved and parameters to describe them
- II. parameters that control informational messages produced by the code
- III. initial guesses to start the Newton-Raphson iterations
- IV. parameters to define the result files to be used.

This information is supplied to the FEAT package using fortran routines and so makes the system flexible, e.g. previously defined data may be used to make data initialisation easier.

The information specified by the routines is:

- A. Parameter definitions in routine UPARAMS
- B. Equation types and boundary conditions in BOUNDS
- C. Initial values for the variable in YSET.

Detailed information on how to run the code is given by Smith (1986b) and on the adaptability of the code by Hickmott (1986).

The meshes used to generate the fields for the predictions are illustrated in Figure 5.1. They are refined in the near wall regions to enable the strong flow gradients to be modelled without the use of wall functions. Both the heater plate and the tunnel conditions are meshed and the energy equation is solved for both the fluid and the solid. To reduce the modelling required, the ribbed geometries have a cyclic repeat plane, illustrated in Figure 5.1. The flow leaving this plane is used as an entry condition for the inlet plane. In this manner the flow can be cycled until a developed state occurs. The second rib is merely present to ensure that the flow gradients cycled are correct. There is no need to mesh it accurately as 'wiggles' were not important on this rib. When the thermal field is generated a limit of seven cycles is imposed so that the eighth rib is studied. This is comparable to the experiment as interferograms are taken of the seventh and eighth rib.

## CHAPTER SIX

### RESULTS AND DISCUSSION

Chapter Six presents the experimental results and later compares them with the theoretical predictions obtained using FEAT. The momentum field investigations are verified against universal profiles to ascertain the amount of flow development. Detailed turbulence recordings were not made and hence the results of Martin and Drain (1986) are used to verify the more detailed momentum field predictions. Both double exposure and real-time images of the thermal fields are presented for numerous flow rates. Plots of the heat transfer coefficient for the smooth and rough surfaces are compared to other workers' results and with the FEAT predictions. However, no work is available to verify the deposited surface results.

#### 6.1. MOMENTUM FIELD EXPERIMENTAL RESULTS

Both rough and smooth hydrodynamic data recordings were undertaken using the probes described in Chapter Four. However, information concerning flow conditions in the inter-rib regions could not be obtained as the bulky probes were not able to enter these areas.

The initial tests using a yaw probe indicated that the flow direction was parallel to the side walls at a distance  $19 D_e$  after the inlet. When placed at the inlet a similar result occurred.

Velocity profiles across the centre of the smooth tunnel,  $19 D_e$  after the inlet, were measured and compared with the universal velocity distribution given by Nikuradse (1950) as:

$$U^+ = 5.75 \log_{10} Y^+ + 5.5 \quad (6.1)$$

The overall agreement illustrated in Figure 6.1 is good, but the results deviate from the log-law sooner than might be expected. This is due to the geometry interacting with the turbulence to produce secondary mean flows in the corners of the duct, Ahmed and Brundett (1971). The pattern of these secondary motions is such that they convect higher longitudinal momentum towards the corners and along the boundaries. Hence the log-law is satisfied by a smaller wall shear, and so gives rise to a larger central velocity.

The addition of the ribs to the lower wall of the tunnel drastically changes the velocity profile. It is no longer symmetrical; the peak velocity is now typically 17 mm away from the smooth wall. The roughness geometry profile is illustrated in Figure 6.2, and is compared to that recommended by Lawn (1976) for a similar geometry as:

$$U^+ = 5.5 \log_{10} (Y/e + 1) + 2.1 \quad (6.2)$$

A good agreement between the two is observed. The coefficient 2.1 is recommended by Lawn for ribs with sharp corners. For more rounded corners the value would increase to nearer 3. This explains Walklate's (1983) results differing from those reported here.

Mass flow rates and Reynolds numbers may then be determined once the velocity profiles are known. This is achieved by assuming the vertical profile shape is constant and superimposing it along the horizontal traverse, matching peak velocities. In this manner an estimate for the bulk velocity is made. A correlation between peak velocities and the Reynolds number it produces is undertaken so that to determine flow rates one only has to record the maximum velocity. Peak flow rates for the tunnel were found to be  $Re \approx 72000$  for a smooth tunnel and  $Re \approx 55000$  ( $e^+ \approx 610$ ) when ribs are added to one surface.

An indication of the amount to which the flow has developed was obtained when the pressure drop down the tunnel was measured. At the beginning of the inlet section the drop was relatively large. This decreased until a near steady fall was observed in the tappings prior to the working section. The larger drop at inlet is caused by the higher wall shear (velocity gradients). When the flow develops, the profile becomes more parabolic in shape and the wall velocity gradients decrease, and so does the pressure drop. For the smooth surface a near constant fall is observed in the last three tappings. The change is typically 5-10% over the range of Reynolds number investigated. The flow has therefore not reached a developed state, but is a reasonable approximation to one.

When ribs are attached the pressure drop rises for a given mass flow rate, and develops earlier. Over the same three tappings prior to the working section a near constant drop, to within 1-3%, was observed. Flow over ribs is known to develop sooner and these results concur with that. One can conclude that a developed state has occurred.

Assuming that the pressure drop is constant a friction factor for the smooth tunnel may be determined using Darcy's formula, equation 4.2. The results are illustrated in Figure 6.3 and are compared to the relationship proposed by Beaver and Sparrow (1971) for a duct given below:

$$C_f = 0.127 Re^{-0.3} \quad (6.3)$$

The secondary flow in the corners yield higher velocity gradients. These then give increased wall shear stresses and so larger friction factors. A good agreement between the results is obtained and one can therefore conclude that the flow is close to fully developed after  $20 D_e$ .

All friction factors determined above assumed the tunnel wall was smooth. To verify this a portable Talysurf was taken to the tunnel and values for the average asperitif height were measured. An average value of  $0.72 \mu\text{m}$  was recorded, which may be corrected to give a relative roughness value of 0.000024. This is a very smooth surface and hence all approximations assuming this are believed to be correct.

To complete the analysis, a Preston tube was traversed around the four smooth walls and an average value for the wall shear stress determined.

These agree well with those calculated from the pressure drop readings. This also acts as a validation for the use of the Preston tube to determine the friction factors when ribs are added to the tunnel. This is necessary because the shear stresses are no longer identical for each wall. So they have to be determined from a force balance in the following manner.

The overall shear stress for the duct has three contributing constituents, the rough wall, the top smooth wall and two side wall shear stresses. This may be written:

$$\frac{\Delta P}{\Delta x} WL = w\tau_{wr} + \int_0^W \tau_{ws} dz + 2 \int_0^H \tau_{ws} dy \quad (6.4)$$

where  $\Delta P/\Delta x$  is the static pressure drop recorded by the tappings in the upper surface. Rearranging this expression and carrying out the integration yields an expression for the rib-roughened wall friction factor of:

$$C_{f_{rw}} = \frac{2}{\rho U_B^2} \frac{\Delta P}{\Delta x} L - f_s \left[ A + \frac{2BL}{W} \right] \quad (6.5)$$

where A and B are constants of integration, found to have average values of 0.896 and 0.463 respectively. These values were determined from Preston tube measurements of the shear stress on the smooth walls. A typical profile at a Reynolds number of 31670 ( $e^+ = 300$ ) is illustrated in Figure 6.4 beside the results of Thomas (1964) for a geometrically similar duct.

A similar profile is observed but Thomas' results are larger. A possible explanation for this is that Thomas employed a device to artificially thicken the boundary layer of the rib-roughened side in order to aid the development of the flow. Hence, the side wall boundary layers might be thinner and so have larger shear stresses.

Using the shear stress measurements, the rough wall friction factor may be determined for numerous flow rates. It was observed to be independent of Reynolds number having a constant value of 0.0575, see Figure 6.3. It agrees with the value for rib-roughened walls given by Baumann and Rehme (1975). This indicates that the flow is developed and so justifies using this value for the normalisation of the flow rates to yield rib-roughness Reynolds numbers. Also plotted in Figure 6.3 is the smooth wall centreline and the roughened duct friction factor to complete the description of the rib-roughened tunnel.

At a later stage 'U' component turbulence levels at the inlet to the tunnel were recorded for a single Reynolds number flow of 12820 ( $e^+ = 122$ ). A profile taken  $1 D_e$  after the inlet contraction is illustrated in Figure 6.5. It enables a comparison to be made with the inlet conditions that are used in the FEAT prediction. At the centre of the duct the level is in the region of 3-5% while nearer the walls it rises to 25-30%. The absolute values are distinctive for the tunnel and depend upon the geometry prior to the measuring station. Hence these values are not compared to other solutions. The results however appear reasonable as larger levels are generated by the wall, while the smaller levels at the centre are generated

by the honeycomb gauze. Bradshaw (1970) quotes levels below 10% to be acceptable for experimental investigations and this will be easily satisfied at the test section because the honeycomb turbulence will be dissipated.

## 6.2. THERMAL FIELD EXPERIMENTAL RESULTS

All double exposure interferograms taken were viewed and analysed using a Vickers projection microscope, type MO 51560. It enlarges the image by a factor of up to 36X and so enables the near wall fringes to be viewed easily. A permanent record may then be obtained by photographing the enlarged image with a standard 35 mm camera. Because the real-time images are recorded photographically, straightforward photographic enlarging enables the analysis to proceed. This latter method suffers from a loss of resolution at high Reynolds numbers in the near-wall boundary layer.

The analysis of the interferograms was performed by eye using an optical comparitor. This is subject to operator error, estimated in Appendix B to be  $\pm 4.7\%$ . Hence an automatic image analysis investigation was undertaken by Hunter (1987) to reduce this error and provide detailed information on the entire field. Fringe displacement due to refraction was minimised by ensuring the virtual image was focussed onto the centre of the test section. This is easily achieved for the smooth surface, as the entire near wall field is uniform, but not for the rib-roughened surface as the temperature gradient varies around the geometry. In the latter case, the rear of rib top is focussed correctly as this gives the best

compromise for the surface. However this proved unsatisfactory for high flow rates,  $Re > 45000$ , and hence numerous images for various focus planes were recorded. The correction for the light rays further away from the wall are less well optimised, but the corresponding displacement effects are also smaller and so not as significant.

The exposure times used throughout the investigation were sufficient to 'freeze' the motion of the turbulent structures in the main flow. Some fringe movement is apparent at high Reynolds numbers but the spanwise averaging is believed to contribute to this. Sufficient light levels are available to prevent this when the images are recorded on high speed 16 mm film. Exposure times down to 0.5 ms were used, but the near wall region could not be resolved on the small image size.

### 6.2.1. Smooth surface results

Typical double exposure interferograms taken when the thermal field is fully developed are illustrated in Figure 6.6(a) and Figure 6.6(b) at Reynolds numbers of 9800 and 22000 respectively. Images of the enlarged near wall regions are illustrated in Figure 6.7(a) and Figure 6.7(b). From these the temperature fields and profiles are determined that enable the Nusselt number for each flow condition to be calculated.

The dimensionless temperature profiles for numerous Reynolds numbers are illustrated in Figure 6.8. They are compared to the temperature profile for a rectangular duct given by Eckert and Drake (1959). A good

agreement is observed in the near wall flow region,  $Y^+ < 15$ , and so justifies the extrapolation procedure undertaken to determine the Nusselt numbers. Above  $Y^+ = 15$  the profiles diverge and a Reynolds number dependency is observed. This is due to the two-dimensional assumption breaking down in the outer wall regions and so introduces a time dependency into the results. A broadening of the fringes confirms this. In the main flow, where only one fringe is observed, the two-dimensional assumption fails. No analysis is possible here, except for an estimate of the temperature increase from ambient conditions that is based on the number of broad fringes present.

The Nusselt numbers determined are illustrated in Figure 6.9 next to Walklate's (1981) results and the empirical relationship for heat transfer in a tube is given by:

$$Nu = 0.023 Re^{0.8} Pr^{0.4} \quad (6.6)$$

An excellent agreement between the results is observed at Reynolds numbers below 15000 but the Nusselt number is underestimated for higher flow rates. This may be attributed to the refraction and end effect errors. The former gives an uncertainty in the wall position and hence a boundary layer convection term is determined that enables the wall position to be exactly located. Then the refraction correction term  $C2_1$  (equation 4.2) is determined using the aforementioned technique described in Section 4.3. All results presented have undergone this procedure. The latter end effect error arises because of the non two-dimensionality of the tunnel and is estimated to given an error of 1.9% (Appendix B). At low

transition flow rates  $Re < 5000$  buoyancy effects were found to be negligible. The Richardson number, Bradshaw (1969), has a value of 0.01 which is equivalent to a mild curvature on the flow geometry. At  $Re = 3500$  it was estimated to give a +0.3% change (Appendix B) and so is negligible.

Introduction of the real time technique enables time dependent effects to be studied. Figure 6.10 illustrates six typical images recorded over a duration of two seconds for a flow having a Reynolds number of 10200. No continuity of flow structures in the main flow region is observed. Each illustrates a condition after several structures have passed. Hence one could imagine a continuous structure in a few of the images but this is not the case. The real-time images, however, reveal three distinct regions of interest. These are:-

1. The Near Wall: a sub-layer where uniform fringes are present.
2. The Outer Wall: a region where two or three broad fringes oscillate in a transition state.
3. The Main Flow: the bulk of the flow where very broad and sometimes circular fringes are observed.

The width of the fringe, therefore, gives a measure of the two-dimensionality present in the flow. In the near wall the fringes are uniform and observed to be time independent. This is indicative of a two-dimensional flow. The main flow region has very broad fringes that

are randomly located in space and time. Here, the flow is three-dimensional and so little information is available from a spanwise average. The outer wall transition region has relatively narrow fringes, compared to the main flow, but broader ones than the near wall area. Hence, in this region some turbulent activity may be resolved. The two-dimensional assumption is beginning to break down, but information may be extracted from an average taken from numerous images. Higher framing rates would enable continuous structures to be observed in this region and so provide additional information on the flow.

Images taken from a high speed film 600 ff/s at a Reynolds number of 3750 are illustrated in Figure 6.11. A structure is clearly evident in the outer wall region. Extracting information directly from the film enables the size and velocity of the structure to be determined. These were found to be  $0.96\delta \times 0.58\delta$  and  $0.91 U_B$  respectively, where  $\delta$  is the half channel height. Cantwell (1981) when reviewing boundary layer flows suggests that the size of the typical outer large eddy is between  $\delta \rightarrow 2\delta \times 0.5\delta \rightarrow \delta$ . Its width is  $0.5\delta \rightarrow \delta$  and the eddy centres are spaced  $2\delta \rightarrow 3\delta$  apart in the spanwise direction. The width of the test section  $8.6\delta$  will permit more than one structure to be formed in the cross stream direction at any one streamwise location. Hence, the image illustrated is an average through more than one structure because if it were only a single eddy a spanwise average would not reveal it.

Prior to the structure appearing the fringes converge which is indicative of an area of cooler fluid moving towards the wall. As the structure passes the fringes diverge and also appear to broaden. The

\* Eddy width refers to the spanwise scale of the structures.

passing of the structure is believed to coincide with a bursting phenomena, Kim (1983), where hot fluid is ejected from the near wall regions. These occur periodically in the spanwise direction and so the broad fringed structure is thought to be an average of more than one bursting phenomena.

After the structure has passed a second appears 0.5 s later. This is preceded by a narrowing of the fringe spacing as in the previous case. However, this structure is not as pronounced as the earlier one, but it has similar characteristics. A third structure may be viewed 0.48 s later, just prior to the end of the film. These repetitions of the structure support the argument that bursting is occurring as it should occur periodically. For higher flow rates, similar repetitious structures are observed in the near wall regions. However, they are small and the information available is restricted by the loss of resolution.

To help visualise the time-dependent effects, a video, Lockett (1987), was recorded of the flow. A complete description of its contents are given in Appendix E. Using the low framing rates of conventional video cameras, 25 ff/s, continuity of structures is observed at low flow rates, but above a Reynolds number of 10000 little continuity of the turbulent structures is observed. Also, the resolution is poor and hence the video is useful for a qualitative illustration of the flow, but not for quantitative analysis.

To conclude the smooth surface investigation, the beginning of the test section was studied. A typical interferogram, at a Reynolds number of 9800, is illustrated in Figure 6.12. The determination of the leading edge

position is not possible as it progresses up the tunnel beyond the transparent test section windows. Hence, the detailed analysis began at the start of the heater plate. Heat transfer is observed to be high initially, and then falls asymptotically to the developed state values, but did not reach them at the trailing edge of the interferogram, see Figure 6.13. One can conclude that the maximum heat transfer occurs when the boundary layer thickness is at a minimum.

### 6.2.2. Square rib-roughend geometry

Typical double exposure interferograms taken of the thermal field over square ribs are illustrated in Figure 6.14 for Reynolds numbers ranging from 10000 to 30000 ( $95 < e^+ < 285$ ). The improved heat transfer rates of this geometry produce larger refraction errors and so limit the analysis. At low flow rates,  $e^+ < 60$ , the boundary layer extrapolation is not necessary. For higher flows, momentum field information for flow over a similar ribbed geometry, Martin (1987), was used to enable the boundary layer extrapolation to proceed. Because no focussing was undertaken for this geometry an upper limit for Reynolds number of 30000 ( $e^+ = 285$ ) was imposed. Beyond this, it was not possible to image the fringes.

Analysis of the interferograms yields the absolute heat transfer coefficients illustrated in Figure 6.15. An average heat transfer coefficient may then be assigned for each Reynolds number. A comparison with the smooth surface results may be undertaken and the table below summarises this.

Reynolds Number	Nusselt number		Gain
	(Smooth)	(Square rib-roughened)	
7400	25	56	2.24
13100	39.4	79.5	2.01
29870	76.1	128	1.68

The gain is observed to decrease with increasing Reynolds number. Although one would expect this, the extent to which it occurs is too great. Resolution errors are larger for higher flow rates and so make the determination of the wall position particularly difficult. Any error here is magnified in the Nusselt number determination and so confidence is lost in the results. The Stanton number for each flow rate may then be determined and is compared to other workers' results in Figure 6.16. This is only an 'order of magnitude' comparison as previous workers used numerous definitions for the Reynolds number. There is some agreement observed even though the results of this present study are at lower flow rates. Also, the extrapolation estimated by Watts and Williams (1981) may not necessarily be the correct one.

To facilitate comparison of each Reynolds number plot, all are normalised by dividing each absolute value by the average for the surface. The resulting plot is illustrated in Figure 6.17. To within experimental error, it can be seen that the distributions are independent of Reynolds number. Peak values occur at the leading edge of the rib top, whilst the base of the rear facing rib wall has the lowest value. In the inter-rib region a gradual climb is observed before sharp fluctuations arise prior to the forward facing rib. Finally a dramatic climb is then apparent as the

leading rib face is traversed. The four regions mentioned above are now discussed separately so that the salient features of each region may be examined individually.

i) Forward Facing rib wall (0 to 1)

An increasing heat transfer coefficient is apparent as the rib is traversed from its base to the tip. Refraction effects are severe in this region, especially as the tip is approached and hence the boundary layer extrapolation is necessary. The recirculation region is relatively small as the boundary layer is thin. No problems were observed in imaging this face and so the problem of negative heat transfer encountered by Walklate (1983) is assumed to be caused by the adhesive he used to attach the ribs. The insulation layer formed in his work prevents the rib being representative of working conditions in a reactor.

ii) Rib top (1 to 2)

The maximum heat transfer for the entire geometry occurs at the leading edge of the rib tip. It then decreases and increases again which is indicative of a recirculation region just after the tip. It becomes more pronounced at a flow rate of  $Re \approx 30000$  ( $e^+ = 285$ ) which is due to the forward facing recirculation growing in size until it reaches the same height as the rib at this velocity. These conditions would then be favourable for a recirculation region to form on the top of the rib, immediately proceeding the sharp leading corner. No other documentation could be found to confirm the existence of a recirculation region here.

The probes used by Lawn (1976) would cause the flow to reattach locally and Martin and Drain (1986) admit difficulty in recording data next to a wall.

Of the other heat transfer studies over ribs only the blotting paper technique of Williams and Watts (1970) detected twin peaks, but they were very close together. Finally, the ribs are particularly sharp in this investigation which increases the tendency for a separation region to form.

### iii) Rear facing rib wall (2 - 3)

A dramatic decrease in heat transfer occurs in this region because the trailing edge recirculation is entered. Broad and widely spread fringes are apparent and hence ray tracing is particularly difficult. A spline fitting routine is essential for an accurate determination of the heat transfer. However, this region does not suffer from refraction effects and so the wall position is easily located, which aids in assessing the wall location in the other regions. The introduction of a finite fringe background would increase the resolution here and make an accurate determination of the heat transfer far easier.

### iv) Inter-rib region (3 - 9.2)

By far the largest region for heat transfer and yet it does not yield a proportionate amount. (The rib, for its size, is the better region). A peak in heat transfer occurs at  $0.35e$  in front of the rib, which agrees well with Walklate's (1983) value of  $0.4e$ , for the entire Reynolds number range. A similar peak is given by the copper foil technique of Watts and Williams

(1981), but the naphthalene results give a peak of  $0.7e$  in front of the rib while the other methods failed to identify it. The error for the naphthalene result could be explained by the change in the surface geometry as the test progressed. The turbulence intensities and shear stress measurements of Lawn (1976) observe a similar peak. An explanation for this phenomena is that the flow around the forward facing rib face, is convected to the inter-rib region by the primary recirculation. A secondary recirculation in the corner then causes this flow to reattach at  $0.35e$  in front of the rib. Hence at the point of reattachment a high heat transfer rate is observed. No experimental evidence for the secondary recirculation was found but it is commonly believed to exist.

Another peak in heat transfer, lower than the first one, is observed in the inter-rib region. It is not, as one would expect, at the reattachment point of the trailing recirculation region, but is displaced towards the trailing rib. Two effects are combining here. The boundary layer is growing after reattachment and so one would expect the heat transfer rate to fall. However, this effect is opposed by faster moving fluid approaching the wall after it has passed over the rib top. Hence the heat transfer continues to increase until the second peak occurs nearer to the trailing rib. Its exact location is Reynolds number dependent and so cannot be identified precisely.

In the trailing edge recirculation the heat transfer rate is poor, and so refraction effects are small. This enables the wall position to be located easily and so aids locating the wall when refraction becomes a problem in the higher heat transfer regions further along the rib cavity.

Time dependent effects are observed in the trailing edge recirculation when real time interferograms are taken. These are illustrated on a video taken of the flow field, see Appendix E. Three dimensional effects are more pronounced in the near wall location for this region, and so causes the time dependency. In the other near wall regions no time dependency was observed. Real time stills taken with a 35 mm camera illustrate the Reynolds number independency of the flow, see Figure 6.18. Because the thermal conditions are similar for each case the effect of Reynolds number is observed. Reattachment is seen to occur at a similar position for each flow rate and peak heat transfer is observed over the front and rib top regions. For the higher flow rates,  $R < 29000$ , the thickening and thinning of the thermal boundary layer over the rib top is easily observed. High speed film further emphasises the time dependent effects, but no images are illustrated because of the poor resolution obtained on a 16 mm frame.

The heat transfer distribution for the square ribs agrees well with the other workers' results illustrated in Figure 2.12. Correct modelling of the Biot number relationship in this investigation have removed the errors in Walklate's (1983) study.

### 6.2.3. Rounded rib-roughened geometry

Typical double exposure interferograms taken of the thermal field over rounded ribs are illustrated in Figure 6.19 for Reynolds numbers ranging from 7330 to 53900 ( $70 < e^+ < 602$ ). The addition of the focussing lens has enabled reactor rib Reynolds numbers to be modelled. Unfortunately, no

data is available concerning the momentum field over this geometry and so the boundary layer extrapolation was not able to be made. Hence, absolute values for the heat transfer could not be determined.

To obtain a normalised distribution for the geometry the fringe spacing was determined up to the ray crossing regime. The temperature gradient at this location was then used to assess the local Nusselt number by assuming that the ray crossing error is consistent around the geometry. This is a reasonable assumption given that there are no sharp corners for the flow to navigate. However, this technique will enhance the heat transfer in the recirculation region relative to the rest of the geometry. But, as the heat transfer rate is poor in this area, the relative increase will have a minor effect on the distribution. Analysis of the square ribbed geometry using this assumption gave a maximum variation of  $\pm 5\%$  to any one local value, and so the assumption was believed to be a reasonable one.

The normalised Nusselt number distribution obtained for the rounded rib geometry is illustrated in Figure 6.20. Immediately apparent is a Reynolds number dependency at the rear of the rib. This arises because the rounded geometry is more 'streamline' and so enables the reattachment condition to vary with numerous flow rates. There are no sharp corners to dictate where flow separation occurs and hence it is flow rate dependent. Peak heat transfer still occurs at the leading edge of the rib top and the distribution in the inter-rib region is similar to that of the square rib geometry. For this geometry, therefore, the rib is discussed as one entity followed by a description of the inter-rib region heat transfer.

i) Rounded rib (0 to 3.43)

The sharp peak heat transfer at the leading edge of the square rib has disappeared for a more gradual variation in heat transfer. This is particularly apparent for the low Reynolds number flows. The sharp decrease in heat transfer at the rear of the rib top has also disappeared to be replaced by a more gradual change. This is not so obvious for low flow rates but for higher flows there is no distinguishable position where a fall in heat transfer occurs. Trailing edge recirculation regions are driven relatively faster by the main flow so that an appreciable amount of heat is transferred down the rear facing wall. Also, the bottom of the rib is now a curved surface and this prevents a region of flow moving fluid forming. An increased heat transfer down this face is therefore observed.

No recirculation regions were apparent over the rib top, even at flow rates of  $Re \approx 30000$  where they are most likely to occur. Hence, if a separation region does occur it is a very small one.

ii) Inter-rib region (3.43 to 8.55)

For this geometry no peak in heat transfer was detected just prior to the forward facing rib wall. At low flow rates a fall and rise was observed but no peak. Reattachment of the trailing edge recirculation varies depending upon the Reynolds number. The higher the flow rate the closer the reattachment is to the trailing rib face. Also, a more uniform heat transfer region is observed after reattachment. The flow approaching the wall after passing over the rib is not as strong for this geometry because

the rib is more streamline. As a result the peak in heat transfer for the region occurs further from the rib. For example, at a Reynolds number of 53800 ( $e^+ = 602$ ) a relatively constant heat transfer region is observed from  $3.5e$  to  $0.5e$  prior to the rib face, with a peak occurring at  $1.25e$  before the rib. This illustrates the reduced effect of the flow approaching the wall.

Flow over this surface was observed to be time dependent, but not to the same extent as the square ribbed geometry. Hence, this flow is assumed to be more two-dimensional in the near wall regions, especially in the trailing edge recirculation region. Part of the video, Appendix E, illustrates flow over the rounded rib geometry and an oscillation of the fringes in trailing edge recirculation may be observed.

Real time images taken with a 35 mm camera are illustrated in Figure 6.21. The Reynolds number dependency is easily observed if the trailing face of the rib is studied for each flow rate. At the low flow rates,  $Re = 4130$ , the fringes here are coarse and widely spread. But as the speed increases they become narrower and more easy to analyse. Eventually, at  $Re = 41250$  refraction errors appear down the rear side of the rib which is indicative of a region where an appreciable amount of heat is transferred. [If the real-time images of the square rib are studied again, Figure 6.18, the fringes at the rear of the rib remain coarse, even at a Reynolds number of 40000]. The length of the uniform section in the latter half of the inter-rib region is observed to grow as the flow rate increases. This further verifies the Reynolds number dependency for this geometry.

Again, no images of the high speed film are illustrated because of the loss of resolution when recording on a 16 mm frame.

#### 6.2.4. Deposited surfaces

Typical double exposure interferograms for the square and rounded rib deposited surfaces are illustrated in Figure 6.22 and Figure 6.23 respectively. Problems in imaging the rough rubber surface resulted in the failure of the analysis technique at high flow rates. A 'best' image position was unable to be attained. Hence, multiple images were taken and a heat transfer distribution estimated from numerous images. This appeared to have solved the problem. Again, no absolute values for the heat transfer coefficient could be determined because of the lack of detailed momentum field measurements for the surface geometries. A normalised distribution was obtained for both surfaces by making the same assumption as that illustrated for the rounded rib geometry, see section 6.2.3. These distributions are illustrated in Figure 6.24 and Figure 6.25 for the square and rounded rib deposited geometries respectively.

A Reynolds number dependency is observed for the rounded rib deposited geometry and not for the square rib deposited geometry. Hence, even though the profiles are more streamline than the rounded rib undeposited, the underlying metal geometry appears to have a dominant effect. The thickness of the deposit is insufficient to mask this. Variations between the deposited and undeposited surfaces are apparent, particularly when the surface temperature is studied. The top of the deposited rib is 6° to 8°C cooler than the inter-rib region, whereas the undeposited ribs are only 2° to 3°C cooler. This is an effect arising from the Biot number change. The rubber insulation is not able to conduct the heat in sufficient quantities to the favourable areas of heat transfer at the top of the rib.

Peak heat transfer values occur at the leading edge of the rib top but are not as high, relatively, to the remainder of the surface. A change has occurred in the inter-rib region. The normalised Nusselt plots are more uniform, containing fewer peaks. Especially noticeable in the rounded rib deposited surface is the decline in heat transfer that begins  $2e$  before the forward facing rib wall, and continues to the rib. The boundary layer growth has become the dominant effect in the heat transfer rate in this region.

i) Rib region (0 to 3.49 for square rib)

(0 to 3.55 for rounded rib)

The point of maximum heat transfer at the leading edge of the rib top is observed to be Reynolds number dependent, for both deposited surfaces. Also, the profile is more rounded at the tip for both surfaces. The more streamline surfaces have yielded lower normalised peaks and so reduced the variation in heat transfer around the surface. No evidence of a separation point on the rib top occurs for any flow rate. The deposited square rib has a definite region where the Nusselt number falls dramatically but no such region is observed down the rear side of the deposited rounded rib surface. Finally, the refraction error around the rib is reduced because of the lower heat transfer rates. But image quality is retracted by the rough surface that fails to give a knife edge for the focussing procedure. This latter effect is observed to dominate for higher flows and so limit the Reynolds number range.

ii) Inter-rib regions (3.49 to 7.845 for square rib)

(3.55 to 7.93 for rounded rib)

No sharp peak in heat transfer is observed just prior to the forward facing rib wall for either geometry. Hence there is no indication of a secondary recirculation region at the base of the rib. The peaks that occur are at 1.0e and 2.1e before the rib for the square and rounded rib respectively. It is then interesting to observe that the heat transfer decreases for the rounded rib deposited surface as the rib is approached. Flow no longer moves towards the surface at speed as the rib profile is now more streamline. So the boundary layer growth produced a decline in the heat transfer. For the square rib deposited surface steady increase in heat transfer occurs from the rear of the rib to 1.0e in front of the next rib for high flow rates. At low flow rates, the heat transfer peaks at 2.2e in front of the rib and then a uniform level is observed. Hence, the boundary layer growth becomes less dominant for the higher flow rates over this geometry. This effect is also apparent over the rounded rib deposited surface although not to the same extent.

The length of the recirculation region has diminished for both geometries. For high flow rates reattachment occurs at a point less than one rib height away from the rib. This arises because of the more streamline geometry of the deposited surfaces.

Time dependent effects over these surfaces were again observed but of a reduced nature. The trailing edge recirculations do not oscillate as strongly as for the previous cases, this may be observed on the video, Appendix E. Real-time images taken of the flows are illustrated in Figure

6.26 and Figure 6.27 for square and rounded rib deposited surfaces respectively. The Reynolds number dependency of the trailing edge for the latter geometry may be observed by the contraction of the fringes around the rib. Although this effect is apparent for the former geometry it is not as significant. Refraction errors are also seen to be smaller in these images. This arises because of the poorer heat transfer capabilities of the surfaces. Biot number effects prevent heat flow in the solid surface to areas conducive to heat transfer and a boundary layer does not vary along the length because of the more streamline profile.

No high speed film images are illustrated because of the loss of resolution on a 16 mm frame. The film does however illustrate the time dependent effect in the outer wall and main flow regions.

### 6.3. THEORETICAL PREDICTIONS

Finite element predictions for the flow may be verified against the results obtained using holographic interferometry. Once one correct prediction is made, by varying the modelling parameters, additional predictions for moderate changes in the geometry or flow rate are justified. Hence, the time consuming experimental investigations to obtain the information would not be necessary because the computer program can give predictions quickly and more efficiently. However care must be taken to assume the modelling parameters are correct, and so experimental investigations will always be required.

Inlet conditions for the tunnel were not known when the predictions were made. Hence, a selection of entry conditions was used to determine the variations occurring at the working section. The q-f model, with source terms which make it formally identical to k- $\epsilon$ , was used throughout these ranging tests. While flow over the rib roughened geometries was investigated using the genuine q-f models. Reynolds numbers were based on the hydraulic diameter even though it is an artificial concept for the parallel plate 2-D prediction because it conforms with the experimental results presented. To determine the thermal field, the energy equation is solved after the momentum field has been predicted. Martin and Drains (1986) results are used to verify the momentum predictions. Ranging calculations were not necessary for the ribbed geometries, because the flow develops faster and so it is assumed to be fully developed.

### 6.3.1. Ranging conditions

A simple rectangular mesh 14 x 10 elements, illustrated in Figure 6.28, was generated as a test mesh for the inlet conditions. A constant mass flow rate of 0.022 kg/s ( $Re = 12660$ ) was imposed for all entry variations. Two velocity profiles illustrated in Figure 6.29 were chosen to be extremes that would produce a significant variation at the test section if one exists. Turbulence intensity levels of 2.5%, 10% and 40% of the main stream velocity were assigned for each profile to determine its effect. Inlet length scales were fixed for all the tests at a value of 0.002 m, this being dependent upon the diameter of the honeycomb at inlet.

Comparison of the flow conditions at a point  $20 D_0$  after the inlet indicated that the variations had little effect on the flow. The two inlet

velocity profiles produced a similar velocity profile, to within 2%, at the entry to the working section. The different inlet turbulence levels produced a smaller discrepancy. Identical velocity profiles were produced for the 2.5% and 10% inlet conditions but a smaller maximum velocity was observed for the 40% level. The variations were again less than 2% for the velocity profiles and this fact is illustrated in Figure 6.30.

Turbulence levels are not so well developed. Figure 6.31 illustrates the turbulence intensities at the inlet to the test section for the various entry conditions. The overall change is not dramatic and so a typical average value of 10% is chosen for all further tests. This confirms that turbulence levels develop slower than the mean velocities.

Mesh refinement problems were highlighted during the proving tests. When the variables in the near wall region are plotted as a traverse 1 mm above the surface, several changes in gradient are observed, see Figure 6.32(a). These are termed 'wiggles' and are characteristic of a coarse finite element mesh, if no upwinding has been used. A new mesh was therefore generated to eliminate the wiggles. Because the tunnel is symmetrical only half of it has to be modelled. The new mesh is 32 x 10 elements and so increases the resolution by a factor of more than four. The new wall plot, Figure 6.32(b), displays no 'wiggles' and so indicates that the problem has been solved. The momentum field may then be generated on this new mesh and subsequently interpolated onto a full size mesh of the tunnel. A thermal field may then be predicted.

### 6.3.2. Momentum Field Predictions

Predictions for the smooth wind tunnel momentum field have been discussed earlier and were shown to have a good agreement with the experimental results. The streamwise peak velocity was predicted to be  $1.85 \text{ m s}^{-1}$  which compares favourably with the experimentally measured value of  $1.9 \text{ m s}^{-1}$ . This discrepancy is due to the secondary flows in the corners of the ducts producing faster mean flows in the centre.

Velocity field predictions for the square and rounded ribs are illustrated in Figure 6.33. They were obtained using the low Reynolds number model and indicate the recirculation regions around the ribs. Strong velocity gradients are observed along the top of the ribs where large turbulent intensities are predicted.

Comparing the results, for a set mass flow rate, illustrates the differences between the two surfaces. The peak streamwise velocity for the square ribs is slightly larger,  $2.41 \text{ m s}^{-1}$  as opposed to  $2.27 \text{ m s}^{-1}$ , than the rounded rib. The experimentally recorded peak velocity is  $2.17 \text{ m s}^{-1}$ . This is lower because of the effects of the side walls which are not modelled in the 2-D predictions.

Higher peak turbulence levels are also predicted for the square rib, 69% of the mean stream velocity, compared to 63%. The length of the recirculation regions differs for the two surfaces. Predictions for the square rib give a trailing edge reattachment point 3.6 rib heights after the rib. Martin and Drain (1986) determined that the reattachment occurs at

just over 3.8 rib heights. Further confidence in the low Reynolds number model is therefore gained. A secondary recirculation at the base of the rear face is highlighted by the prediction, see Figure 6.34. But experimental verification of this is not possible because of the difficulty of performing measurements close to a solid surface. It is, however, believed to be a real effect. The rounded rib predictions give a reattachment 2.8 rib heights after the rib. No experimental results are available to verify this, but it appears reasonable as the rounded surface geometry presents a more streamwise geometry to the flow. No evidence of a secondary recirculation was observed for this surface. Leading edge recirculation regions are observed to be smaller than the trailing ones. The square rib prediction gives a length 1.4 rib heights while the rounded rib gives it a value of 1.2 rib heights. No experimental results were found to confirm these values.

Momentum field predictions therefore illustrate the differences between the two surfaces. When comparing the results to experimental values, the three dimensional aspect of a real flow is not modelled and so exact agreement is not possible. However, the predictions give a good estimate that may be used as an initial starting point for the behaviour of the flow. Improving the grid refinement would also give a better estimate for the predictions.

### 6.3.3. Thermal Field Predictions

A plot of the temperature field generated using the low Reynolds number two-equation model for the smooth surface is illustrated in Figure 6.35. It is enlarged by a factor of 10 in the y-direction to enable the

contours to be observed. The thermal boundary layer leading edge has crept along the bottom of the tunnel to  $3 D_e$  upstream of the heater plate. This increases the development length of the temperature field and so gives a more developed field at the latter stage of the test section. A heat flow is also observed to the leading edge of the plate where the heat transfer is larger because of the smaller thermal boundary layer. An enlargement over the heater plate is illustrated in Figure 6.36 to enable the contours to be viewed.

The wall temperature predicted for a uniform heat flux of  $1330 \text{ W/m}^2$ , applied at the base of the heater plate, peaks at  $144^\circ\text{C}$  at the end of the plate. The near wall temperature gradient here produces a Nusselt number of 37.7, which compares favourably with the experimental results of 38.1. Hence, the low Reynolds number model is able to predict the heat transfer coefficients for flow over a smooth surface. A linear region in the near wall vicinity is predicted and so further justifies determining Nusselt numbers from near wall temperature gradients.

A contour plot of the ribbed temperature fields produced by the low Reynolds number model are illustrated in Figure 6.37. Both fields are still developing as indicated by the diverging contours in the main flow. This is as expected as there is only a relatively small development length. Heat input for these predictions was fixed at  $800 \text{ W/m}^2$  and applied along the base of the heater plate. This value was chosen as it would yield a thermal field similar to that of the interferograms ( $\Delta T \approx 30^\circ\text{C}$ ). Cyclic boundary conditions were enforced so that flow leaving the repeat plane entered at the inlet. In this manner the contour plots produced may be

directly compared with the interferograms recorded for similar Reynolds number flows illustrated in Figures 6.14 and 6.19 for the square and rounded rib geometries respectively.

Upon examining the predictions, the most striking discrepancy with the experimental interferograms is in the small recirculation region at the leading edge of the rib. The experimental results illustrate that the thermal field does not diverge from the wall until 0.3 rib heights before the leading face of the rib, indicating there is only a small recirculation region.

Theoretical predictions using FEAT, however, give a diverging field 2 rib heights prior to the rib. It is almost symmetrical about the centre of the inter-rib region. This incorrect prediction arises because of fixing the length scale in the near wall. The flow impingement on the wall is not modelled and so incorrect length scales arise. The final result is that the wall has too dominant an effect on the boundary layer and does not permit convection. A possible solution for this is to separate the eddy length scale into a vertical and horizontal component and model each separately. This is because the former component is restricted by the size of the boundary layer while the latter is not.

Comparing the predicted absolute temperature values shows that the rounded rib geometry is a better surface for heat transfer. With a given heat input the maximum temperature attained for the rounded rib is 45.1°C while it is 50.4°C for the square rib. Hence, smaller temperature gradients are required to drive the same heat flow. However, this prediction is incorrect and disagrees with the experimental results.

Sharper corners result in thinner boundary layers, especially at the leading edge of the rib top, and so the better heat transfer occurs with the square rib geometry. The error is again due to the set length scale in the near wall region. It prevents the impingement of flow in the potentially high heat transfer region in the latter half of the inter-rib region. Rib top temperatures are predicted to be 2°C lower than those of the inter-rib region. Also no variation of surface temperature was predicted in the rib cavity regions, and this agrees with the results taken from the interferograms.

Incorrect modelling of the length scale made predictions for the absolute heat transfer coefficients redundant. However, the variation of these values around the surface is studied and compared with the experimentally determined Nusselt number distribution. The perpendicular wall heat fluxes in the boundary layer were determined and are illustrated in Figure 6.38. Because of the different surface areas for the two geometries, the x-axis is not consistent between the two plots.

General trends for the heat flux distributions agree well with the experimental results. Peak heat transfer is predicted over the rib top, while the rear of the rib produces the lowest values. However, an incorrect inter-rib region is predicted. Maximum values occur close to the rear rib, see Figure 6.17, while the FEAT code gives peak values in the centre of this region. Hence, the incorrect modelling of the length scale is again emphasised. Also the sharp changes in the heat flux values may not be genuine effects. An improved mesh in these near wall regions would be required to determine if they are genuine effects or merely 'wiggles'.

No conclusions may therefore be drawn on these sharp peaks and valleys as they are mesh dependent. Additional work is required with finer meshes to determine if the effects are genuine.

## CHAPTER SEVEN

### CONCLUSIONS AND RECOMMENDATIONS

Flow conditions down the tunnel have been shown to be well developed for the ribbed geometries, but not for smooth surfaces. However, the near well developed state that occurs over the latter surface was found to be sufficient in this investigation. The secondary recirculation regions formed in the corners of the duct lead to slight irregularities in the velocity profiles, but a two-dimensional flow profile was justified. Friction factors and shear stress measurements were shown to agree favourably with other workers. Hence the momentum field was assumed to be adequate for the interferometric investigation of fully developed turbulent forced convection.

Detailed information concerning the thermal field over the smooth surface was obtained. Nusselt numbers for each flow rate were then plotted and observed to agree well with universal theory. Hence, it can be concluded that the holographic technique, coupled with knowledge of the momentum field, enables a good estimate for the heat transfer coefficient over smooth surfaces to be obtained. A further advantage is that a permanent record of the thermal situation is obtained and so there is no need to repeat the experiment if additional information is required. Photographic records of the interferograms then enable the images to be viewed without the need for holographic reconstruction.

Holographic interferometry has been shown to be a useful diagnostic tool for the engineer to investigate thermal fields. It has been used in this study to determine the heat transfer distribution and so locate the hot spots, around ribbed geometries, three of which have not been studied previously. Hence, new information is available to enable the operating limits of flow over rounded-ribs, and in particular deposited ribs, to be established. The heat transfer distribution was found to be Reynolds number dependent for the rounded rib geometry and independent for the square-ribbed ones. This fact is easily observed by viewing the fringes at the rear of the rib. This illustrates a further advantage of the technique in that both qualitative and quantitative information is readily available from the single image.

Development of a real time system has enabled full field time-dependent information to be obtained, for the first time, of flow over ribbed geometries. Rapid thermal field fluctuations in the trailing edge recirculation provide interesting information concerning the oscillation of the boundary layer reattachment location. As yet, this information has not been analysed as image processing procedures are required to obtain all the information in a relatively short time period.

The excellent resolution time-dependent information and quantitative results that are easily available make this technique an excellent diagnostic tool. Any two-dimensional, and possibly three-dimensional surfaces in the future, may be investigated and analysed quickly and easily with hot spots being identifiable immediately.

Real-time recording techniques introduced the problem of emulsion shrinkage. Bowing of the plate caused by the shrinkage produces a set of circular fringes that are superimposed on the image. The problem was observed to be plate dependent, some plates produced only 1-2 fringes whilst the worst ones gave 6-8 fringes. The latter plates were discarded.

Time-dependent effects over the smooth surface were observed in the outer wall regions. Repetitious structures travelling at  $0.9 U_B$  indicated that some information is available on the flow structure even though a spanwise average is taken. The speckle, inherent with coherent light illumination, produces large errors when a hand analyse is undertaken. This is mainly due to the difficulty in determining fringe position. Hence, an automated fringe analysis procedure is recommended to obtain detailed information of real-time images.

Nusselt number distributions have been plotted for the thermal fields around the ribbed geometries. The point of maximum heat transfer always occurred at the leading edge of the rib top. And the minimum value at the base of the rear facing rib wall. A Reynolds number dependency was identified for the rounded rib geometry, but not for the square rib. The best heat transfer surface was the square ribbed one. Deposits on the surface lead to a reduction in the overall heat transfer because the relative roughness is reduced and heat flow is prevented to favourable areas for heat transfer. A consequence of this is that a larger surface temperature variation is observed around the deposited geometries.

Absolute values for the heat transfer coefficient cannot be obtained for three of the four roughened geometries because of the lack of

information on the momentum field. The technique under-estimates the heat transfer coefficients because the conduction assumption is not valid outside the boundary layer. The absolute readings for the square ribbed geometry were observed to be more reliable at lower flow rates.

Resolution effects on the real-time images over ribs meant that no detailed analysis was undertaken. They were, however, useful for flow visualisation purposes, but it must be remembered that the Prandtl number is 0.7 and so the two fields, momentum and thermal, are not exactly related.

The low Reynolds number model used in the FEAT code to predict the heat transfer distribution requires further refinement. Analysis of the predictions demonstrated that only a qualitative comparison, that illustrates the salient features, may be undertaken. Mesh refinement would reduce the error but not eliminate it. Hence, a new model was proposed based on the experience gained on this work. It involved separating the length scale into horizontal and vertical components and then modelling each separately.

#### RECOMMENDATIONS FOR FURTHER WORK

Detailed momentum field information is essential for any further investigations on ribbed geometries if absolute values for heat transfer are required. Techniques such as Laser Doppler Anemometry (L.D.A.) could be used in conjunction with holographic interferometry to provide detailed information over any two-dimensional surface.

Such investigations should concentrate on the secondary flows generated in the corners of the duct as these give rise to relatively large variations of velocity in the spanwise direction.

The addition of an automated fringe analysis procedure would enhance the information available from the interferograms. At present only the thermal wall boundary layers have been studied, but the full field could be analysed quickly and easily with this addition. Resolution errors would be reduced because the location of the fringes would be assigned to a higher degree of accuracy. Furthermore, the addition of heterodyne techniques would reduce the resolution error to negligible proportions. Early work by Hunter (1987) has illustrated the viability of this procedure.

An extension to three-dimensional field analysis by using diffuse illumination, Sweeney and Vest (1974), would enhance the applicability of the technique. Hence, upon combination with an automated analysis procedure, the technique would provide a useful tool for the engineer to analyse numerous different heat transfer situations.

The two-dimensional spanwise interferograms act as a perfect data base for comparison with theoretical predictions. It is recommended that fluid flow modellers take advantage of these images to validate their predictions. Work at Berkeley Nuclear Laboratories has already led to a new low Reynolds number model being developed.

## REFERENCES

- AHMED, S. and BURNETT, E. (1971) Characteristic length for non circular ducts. *Int. J. Heat and Mass Trans.*, 14, p.157.
- AUNG, W., FLETCHER, L.S., and SERNAS, V. (1972) Developing laminar free convection between vertical flat plates with assymetric heating. *Int. J. Heat and Mass Trans.*, 15, p.2293
- AUNG W. and O'REGAN, R. (1971) Precise measurement of heat transfer using holographic interferometry. *Rev. Sci. Instrum.*, 42, p.1755-1759.
- AYTEKIN, A. and BERGER, F.P. (1979) Turbulent flow in rectangular ducts with low aspect ratios having one rough wall. *Nuclear Energy*, Vol.18, pp.55-63.
- BALLARD, G.S. (1968) Double exposure holographic interferometry with separate reference beams. *J. Appl. Phys*, 39, p.4846.
- BAUMANN, W. and REHME, K. (1975) Friction correlations for rectangular roughnesses. *Int. J. Heat and Mass Trans.*, 18, p.1189.
- BEACH, K.W., MULLER, R.H. and TOBIAS, C.W. (1973) Light deflection effects in the interferometry of one dimensional refractive index gradients. *J. Opt. Soc. Am.*, 63, p.559.
- BEAVERS, G.S., SPARROW, E.M. and LLOYD, J.R. (1971) Low Reynolds number flow in large aspect ratio ducts. *Trans. A.S.M.E. J. Basic Eng.*, 38, p.181.
- BERGER, F.P. and HAU, K.F. (1979) Local mass/heat transfer distribution on surface roughened with small square ribs. *Int. J. Heat and Mass Trans.* Vol.22, p.1645.
- BOUSSINEZQ, J.S. (1877) Essay on the theory of flowing water. French Academy of Sciences.
- BRADSHAW, P. (1969) The analogy between streamline curvature and buoyancy in turbulent shear flow. *J. Fluid Mech.*, Vol.36, p.177.
- BRADSHAW, P. (1970) *Experimental Fluid Mechanics* (2nd Ed.), Pergamon Press.
- BRAGG, W. (1942) The X-ray microscope. *Nature*, Vol.149, p.470.
- BRANDT, G.B. (1969) Image Plane Holography. *Applied Optics*, 8, pp.1421-1429.
- BUERGER, M.J. (1950) Generalised microscopy and the two wavelength microscope. *J. App. Phy.* Vol.21, p.909.
- BRYANSTON-CROSS, P., LANG, T., OLDFIELD, M. and NORTON, R. (1981) Interferometric measurements in a turbine cascade using image-plane holography. *Trans. A.S.M.E. J. Engineering for Power*, Vol.103, p.124.

- CANTWELL, B.J. (1981) Organised motion in turbulent flow. *Ann Review, Fluid Mech.*, pp.457-515.
- CESINI, G., FILIPPO, P., LUCARANI, G., PARONCINI, M. and PIERPAOLI, P. (1982) Investigation of natural convection in rectangular enclosures using holographic interferometry. *Proc.U.S.-Italy Joint workshop on heat transfer and combustion. Purdue Univ. U.S.A, Univ. Pisa, Italy, Vol.II, pp.1-16.*
- COCKING, S.J. and DALZELL, W. (1984) Two component velocity measurements on turbulent flow. *UKAEA Report No.AERE-R-11231.*
- COLLINS, M.W. (1987) Operating procedures for Argon-ion laser use. *Internal communication.*
- CRAIG, J., LEE, G. and BACHELO, W. (1982) Nd:YAG holographic interferometry for aerodynamic research. *S.P.I.E. Proc. Conf. on industrial applications of holography, San Diego.*
- DALLE DONNE, M.D. and MEYER, L. (1977) Turbulent convective heat transfer from rough surfaces with two dimensional rectangular ribs. *Int. J. Heat and Mass Transfer, 20, pp.582-620.*
- ECKERT, E.R.G. and DRAKE, R.M. (1959) *Heat and Mass Transfer, McGraw-Hill, New York.*
- EISFELD, F. (1983) The investigation of fast changing flows using the high-speed interferometer. *3rd Int. Symp. on Flow, Vol.5., Ann Arbor.*
- EL-SUM, H.M.A. (1952) Reconstructed wavefront microscopy. *Ph.D. Thesis, Stanford Univ.*
- ENNOS, A. (1985) *Private communication.*
- FARRELL, P.V., SPRINGER, G.S. and VEST, C.M. (1982) Heterodyne holographic interferometry: concentration and temperature measurements in gas mixtures. *Applied Optics, 21, pp.1624-1627.*
- FAW, R.E. and DULLFORCE, T.A. (1982) Holographic interferometric measurement of convective heat transport beneath a heated horizontal plate in air. *Int. J. Heat and Mass Trans., 25, p.1157.*
- GABOR, D. (1948) Microscopy by reconstructed wavefronts. *Proc. Roy. Soc. A197, pp.454-487.*
- GEBHART, B. and KNOWLES, C.P. (1966) Design and adjustment of a 20 cm M.Z.I. *Rev. Sci. Instrum. 37, p.12.*
- GOLDSTEIN, R.J. (1976) Optical techniques for temperature measurement. *Measurements in Heat Transfer. Publ. Hemisphere McGraw-Hill (2nd Ed).*

GOSMAN, A.D., KHALIL, E.E., and WHITELAW, J.H. (1977) The calculation of two dimensional turbulent recirculating flows. Procs. Symp. on Turbulent Shear Flows. Pennsylvania State Univ.

GROTZBACH, G. (1986). Application of TURBIT-3 subgrid scale model to scales between large eddy and direct simulation. Procs.of Euromech Colloquium No.199, Munich, p.43.

HAINES, M.E. and MULVEY, T. (1952) The formation of the diffraction image with electrons in the Gabor diffraction microscope. J. Opt. Soc. Am., 42., p.763.

HAINES, K.A. and HILDEBRAND, B.P. (1966) Interferometric measurement using the wavefront reconstruction technique. Applied Optics 5, p.172.

HANJALK, K. and LAUNDER, B.E. (1972) Fully developed asymmetric flow in a plane channel. J. Fluid Mechs. Vol.51, pp.301-335.

HARDWICK, N.E. and LEVY, E.K.(1973). Study of laminar free convection wake above an isothermal vertical plate. Am. J. Heat Transfer., 95, p.289.

HARRIS, M.J. and WILSON, J.T. (1960). The use of secondary surface for heat transfer with clean gases. Proc. Symp. I. Mech. E. Paper 7, pp.115-122.

HASSID, S. and POREH, M. (1975). A turbulent energy model for flows with drag reduction. Trans. A.S.M.E. J. Fluid Eng., p.234.

HATFIELD, D.W. and EDWARDS, D.K. (1981) Edge and aspect ratio effects on natural convection from a horizontal heated plate facing downwards. Int. J. Heat and Mass Trans., 24, p.1019.

HAUF, W. and GRIGULL, W.(1970) Optical methods in heat transfer. Adv. in Heat Transfer, 6, pp.133-365.

HECHT, E. and ZAJAC, A.(1974) Optics. Addison-Wesley, Publ. London.

HEFLINGER, L.O., WUERKER, R.F. and BROOKS, R.E. (1966). Holographic interferometry, J. Appl. Phys., 37, pp.642-644.

HICKMOTT, S. (1986) Private Communication

HORMAN, M.H. (1965) An application of wavefront reconstruction to interferometry. Applied Optics, 4, pp.333-336.

HOWES, W.L. and BUCHELE, D.R. (1966) Optical interferometry of inhomogeneous gases. J. Opt. Soc. Am., Vol.56, p.1517.

HUNTER, J.C. (1987) Image analysis of holographic fringes. Ph.D. Thesis, The City University. To be Submitted.

- JAHN, M.J. and REINEKE, H.(1974). Free convection heat transfer with internal heat sources. *Procs. 5th Int. Heat Trans. Conf. Tokyo, Japan.*
- JEVAN, A., BENNETT, W.R. and HERRIOTT, D.R. (1961) Population inversion and continuous optical maser oscillation in a gas discharge containing He-Ne mixture. *Phys. Rev. letters*, 6, p.106.
- JOHNSTONE, R.K.M. and SMITH, W. (1965) A design for a 6" field M.Z.I. *J. Sci. Inst.*, 42, p.231.
- JONES, W.P. and LAUNDER, B.E. (1972) The prediction of laminarisation with a 2-equation model of turbulence. *Int. J. Heat and Mass Trans.* Vol.15, p.301.
- KATTCHIEE, N. and MACKEWICZ, W.V. (1963) Effects of boundary layer turbulent promoters on the local film coefficient of ML.1 Fuel elements. *Nuclear Sci. and Eng.*, 16, pp.31-38.
- KIM, J. (1983) On the structure of wall bounded turbulent flows. *Phys. Fluids*. Vol.26, p.2088.
- KIRKPATRICK, P. and EL-SUM, H.M.A. (1956) Image formation by reconstructed wavefronts. 1. Physics principles and methods of refinement. *J. Opt. Soc. Am.*, 46, p.825.
- KOSTER, J.N. (1983) Interferometric investigation of convection in plexiglass boxes. *W. Ger. Exp. Fluids.*, Vol.1, p.3.
- LAUNDER, B.E. and YING, W.M. (1973) Production of flow and heat transfer in ducts of square cross-section. *Proc. I. Mech. E.*, Vol.187, p.455.
- LAWN, C.J. (1976) Flow measurements for establishing heat transfer. *C.E.G.B. Report RD/B/N3514.*
- LEITH, E.N. and UPATNIEKS, J. (1962) Reconstructed wavefronts and communication theory. *J. Opt. Soc. Am.*, Vol.52, pp.1123-1130.
- LEITH, E.N. and UPATNIEKS, J. (1964) Wavefront reconstruction with diffuse illumination and three dimensional objects. *J. Opt. Soc. Am.*, 54, p.1294.
- LOCKETT, J.F. (1985) Investigation of heat transfer from smooth and rib-roughened ducts. *T.C.U. Res. Memo. ML 153.*
- MACH, L. (1892) Uber einen interferenzrefraktor. *Z Instrumentenk* 12, p.89.
- ZEHNDER, L. (1891) Ein neuer interferenzrefraktor. *Z Instrumentenk* 11, p.275.
- McLARNON, F.R., MULLER, R.H. and TOBIAS, C.W. (1975) Reflection effects in interferometry. *Applied Optics*, Vol.14, p.2468.

- MAIMAN, T.H., HOSKINS, R.H., D'HAENENS, I.J., ASAWA, C.K. and EUTUHOV, V. (1961). Stimulated optical emissions in fluorescent solids. *Phys. Rev.* Vol.123, No.4, p.1145.
- MANTLE, P. (1986). Private communication.
- MANTLE, P., FREEMAN, A.R. and WATTS, J. (1971) Conductivity effects of ribbed surface heat transfer. *Int. J. Heat and Mass Trans.* 14, p.1825.
- MARTIN, S. and DRAIN, L.E. (1986) Investigation of turbulent flow in a ribbed wall flow channel using two component L.D.A. UKAEA Harwell Report. AERE-R-12080.
- MAYINGER, F. and PANKNIN, W. (1974) Holography in heat and mass transfer. *Proc. 5th Int. Heat Trans. Conf., Tokyo, Vol.6, paper IL3, pp.28-43.*
- MERZKIRCH, W.F. (1965) A simple schlieren method for heat transfer studies. *A.I.A.A. Journal*, 3, p.1974.
- MEYER, L. (1980) Turbulent flow in rough channels. *Int. J. Heat and Mass Trans.* Vol.23, pp.591-606.
- MICHELSON, A.A. (1881) The relative motion of the earth and the luminiferous ether. *Am. J. Sci.* 3d. Ser.22:120.
- MIZUSHINA, T. (1971). The electro-chemical method in transport phenomena. *Adv. in Heat Trans.*, 7, pp.87-161. Academic Press, London.
- NEAL, S.B.H.C. (1973) The development of the thin film naphthalene mass transfer analogue technique for the direct measurement of heat transfer coefficients. C.E.G.B./C.E.R.L. RD/L/N132/73.
- NEAL, S.B.H.C., NORTHOVER, E.W. and HITCHCOCK, J.A. (1970) The development of a technique for applying naphthalene to surfaces for mass transfer analogue investigations. *J. Phys. E.*, Vol.3, p.636.
- NIKURADSE, J. (1950) Stromungsgesetze in rahren rohren. *Forshtlft Ver.Dt. Ing* 361, NACA TM 1292.
- OERTEL, Jr. H. and BUHLER, K. (1978) A special differential interferometer used for heat convection investigations. *Int. J. Heat and Mass Trans.*, Vol.21, p.1111-1125.
- PATEL, V.C. (1965) Calibration and Limitations of the Preston Tube. *J. Fluid Mech.*, Vol.23, p.185.
- PATEL, V.C. and HEAD, M.R. (1969) Some observations on skin friction and velocity profiles in fully developed pipe and channel flows. *J. Fluid Mechs.* Vol.38, Part I, pp.181-201.
- POWELL, R.L. and STETSON, K.A. (1965) Interferometric vibration analysis by wavefront reconstruction. *Applied Optics Am.*, 55, p.1593.

- POWELL, R.L. and STETSON, K.A. (1965a) Interferometric hologram evaluation and real time vibration Analysis of diffuse object. Applied Optics Am., pp.1694-1695.
- PRANDTL, L. (1925) Uber die ausgebildete turbulenz. ZAMM, Vol.5, p.136.
- PRANDTL, L. (1945) Uber ein neues formelsystem fur die ausgebildete turbulenz. Nachr. Akad Wiss Gottingen, Math-Phys. Klasse, p.6.
- PRESTON, J.H. (1954) The determination of turbulent skin friction by means of pitot tubes. J. R. Ae. S., Vol.58, p.109.
- QUARINI, J. (1986) Private communication.
- REYNOLDS, O. (1895) On the dynamical theory of incompressible fluids and the determination of the criterion. Phil. Trans. Roy. Soc. A1, Vol.186, p.123.
- RODI, W. (1980) Turbulence models and their application in hydraulics. IAHR State of the art paper, Delft, Netherlands.
- ROGERS, G.L. (1950) Gabor diffraction microscopy: the hologram as a generalised zone plate. Nature, 166, p.237.
- ROGERS, G.L. (1952) Experiments in diffraction microscopy. Proc. Roy. Soc. Edinburgh, A63, p.193-221.
- SCHMIDT, F.W. and NEWELL, M.E. (1968) Evaluation of refraction errors in interferometric heat transfer studies. Rev. Sci. Instru. Vol.39, p.592.
- SEFTOR, J.L. (1974) Two wavelength holographic interferometry of exploding wires. J. Appl. Phys., 45, p.2903.
- SERNAS, V. and FLETCHER, L.S. (1970) A schlieren interferometer method for heat transfer studies. A.S.M.E. J. Heat Trans., Vol.92, p.202-204.
- SERNAS, V. (1983) Interferometric methods in heat transfer. Proc. 3rd Int. Symp Flow Visualisation, Ann Arbor.
- SMITH R.M. (1982) On the finite element calculation of turbulent flow using the  $k-\epsilon$  model. Int. J. Num. Mech. Fluids. Vol.4., p.303.
- SMITH, R.M. (1985) The current status of turbulence modelling in the fluid flow code FEAT. C.E.G.B. Report No.TPRD/B/0591 N85
- SMITH, R.M. (1986) Private communication.
- SMITH, R.M. (1986a) Private Communication
- STEINBERNER, U. and REINEKE, H. (1978) Turbulent buoyancy convection heat transfer with internal heat sources. Proc. 6th Int. Heat Transf. Conf., Toronto,

SWEENEY, D.W. and VEST, C.M. (1974) Measurement of 3-D temperature fields above heated surfaces by holographic interferometry. Int. J. Heat and Mass Trans., 17, p.1443.

TANNER, L.H. (1966) Some applications of holography in fluid mechanics. J. Sci Instrum., 43, p.81-83

TANNER, L.H. (1967) The scope and limitations of 3-D holography of phase objects. J. Sci. Instrum., 44, p.1011.

THOMAS, P.L. (1974) The B.N.L. wind tunnel C.E.G.B. Report. RD/B/N2989.

TROLINGER, J.D. (1979) Application of generalised phase control during reconstruction to flow visualisation holography. Applied Optics, 18, pp.766-774.

VAN DRIEST, E.R. (1956) On turbulent flow near a wall. J. Aero Sci. Vol.23, p.1007.

VEST, C.M. (1979) Holographic interferometry. John Wiley & Sons.

VEST, C.M. and SWEENEY, D.W. (1970) Holographic interferometry of transparent objects with illumination derived from phase gratings. Applied Optics, 9, pp.2321-2325.

VOKE, P.R. (1984) Private communication.

WALKLATE, P.J. (1981) A two wavelength holographic technique for the study of two dimensional thermal boundary layers. Int. J. Heat and Mass Trans., 24, p.1051.

WALKLATE, P.J. (1983) A holographic technique for the study of heat transfer from a rib-roughened surface. Proc. 3rd Int. Symp. on Flow visualisation, p.763, Ann Arbor.

WALKLATE, P.J. (1984) Private communication.

WARBURTON, C. (1972) The results of heat transfer and pressure drop tests in the B.N.C. air rigs on surface roughened by transverse ribs. C.E.G.B. Internal Report RD/B/M1956.

WATTS, J. (1971) Effects of rib shape and spacing on conductivity corrections to ribbed surface heat transfer data. C.E.B.G. Internal Report RD/B/N2106.

WATTS, J. and WILLIAMS, F. (1981) A technique for the measurement of local heat transfer coefficients using copper foil. C.E.G.B. Report Rd/B/5023/N81.

WILKES, N.S. (1981) The prediction of heat transfer from surfaces roughened by transverse ribs. UKAEA Harwell Report AERE-R-10293.

WILKIE, D. and WHITE, L. (1966) Calculation of flow resistance of passages bounded by a combination of rough and smooth surfaces. Nuclear Eng., Vol.11, pp.596-599.

WILLIAMS, F and WATTS, J. (1970) The development of rough surfaces with improved heat transfer performance and a study of the mechanisms involved. 4th Int. Heat Trans. Conf. Versailles.

WITTE, A.B. (1972) Flow visualisation and data reduction Symp. on Engineering applications of holography (S.P.I.E.) pp.219-235.

WOLFSHTEIN, M. (1969) The velocity and temperature distribution in one dimensional flow with turbulence augmentation and pressure gradients. Int. J. Heat and Mass Trans., Vol.12, p.301.

YEH-YIH-JUNG, Y. (1980) Interferometric studies of natural convective heat transfer in various air spaced geometries. Ph.D. Thesis, New York Univ.

YOUNG, C.N. (1972) The variation of heat transfer coefficients over a rib pitch of two twelve start helically ribbed surfaces. UKAEA Report. RPC/HT/P(72)2.

ZINNES, A.E. (1970) The coupling of conduction with laminar natural convection from a vertical flat plate with arbitrary surface heating. Am. J. Heat Trans. 92, p.528.

WOLFSHTEIN, M. (1975). Foot note addition to Hassid & Poreh (1975)

APPENDIX A  
THEORY OF HOLOGRAPHY

Holography is a two stage imaging process that enables both the amplitude and phase information of an electromagnetic wave to be recorded. To explain how a hologram is able to achieve this, some basic concepts concerning interference and coherence need to be understood. These are outlined initially before the theory and practice of holography is developed.

If a linearly polarised plane wave (in the y direction) is travelling in the z direction through a homogeneous media its electric field intensity will be given by the expression:-

$$E(y) = E_0(y) \cos(2\pi nt - K_{12}z) \quad (A.1)$$

where  $E_0$  is the amplitude of the wave,  $n$  is the temporal frequency and  $K_{12}$  is the wave number. Figure A.1. below illustrates the wave.

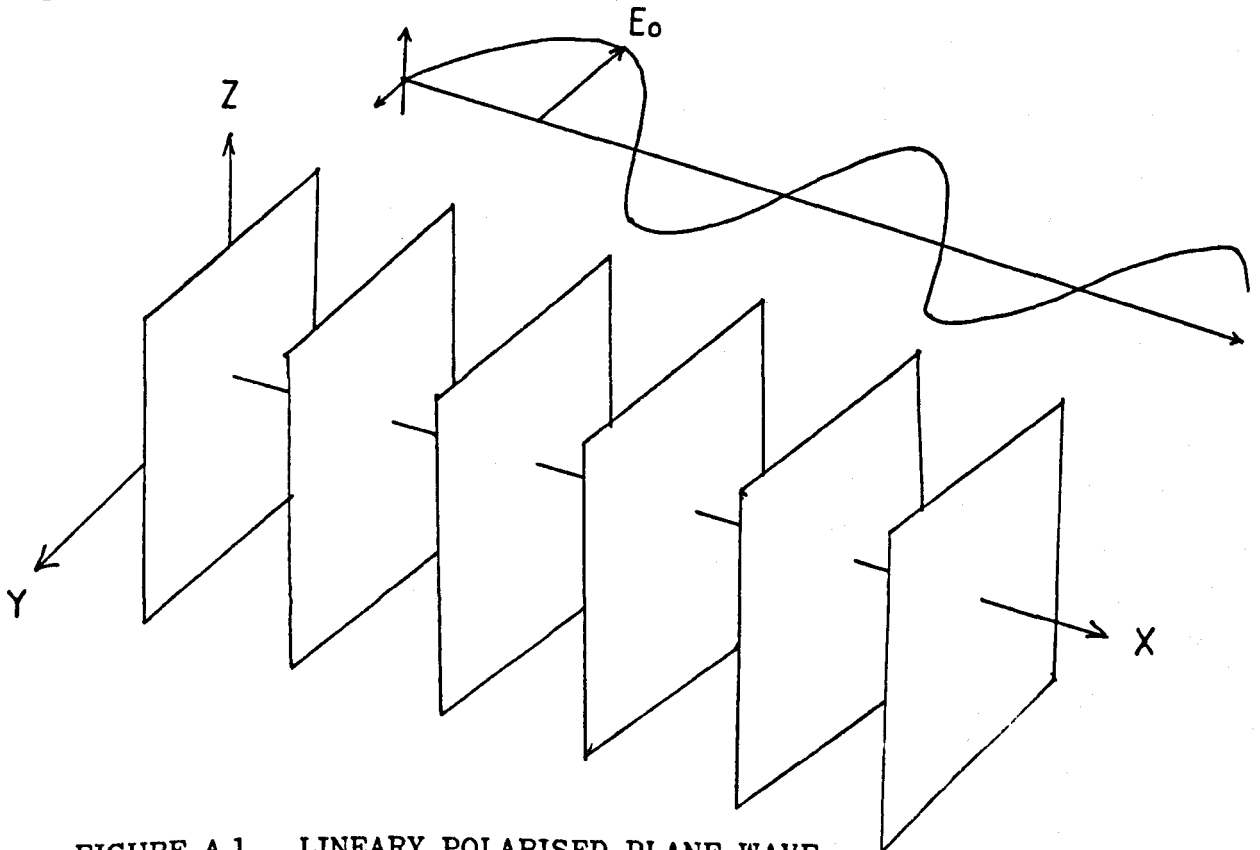


FIGURE A.1 LINEARLY POLARISED PLANE WAVE

This is the type of radiation produced by a laser for short durations, see section 2.1.3. Its frequency would be in the order of  $10^{15}$  Hz, and the wavelengths for visible light in the range  $0.38 < \lambda < 0.75 \mu\text{m}$ . The eye is unable to detect these high frequencies. It only observes irradiance levels, i.e. the time average of the electric field intensity squared denoted by  $I$  and defined as:-

$$I = e v \langle E^2 \rangle$$

where  $e$  is the electrical permittivity of the medium the light travels through and  $v$  is the speed of that propagation. Because only relative irradiances are important, the constants may be neglected:

$$I = \langle E^2 \rangle \quad (\text{A.2})$$

If this first light wave,  $E_1$ , interferes with a second linearly polarised light wave  $E_2$  which has the same frequency, the resultant irradiance is:-

$$\begin{aligned} I = \langle E^2 \rangle &= \langle E_1 + E_2 \rangle^2 \\ &= \langle E_1 \rangle^2 + \langle E_2 \rangle^2 + 2\langle E_1 E_2 \rangle \end{aligned} \quad (\text{A.3})$$

If both waves are polarised in the same direction, they are described by:-

$$E_1 = E_{0(1)} \cos (2\pi n t - K_1 z) \quad (\text{A.4})$$

$$E_2 = E_{0(2)} \cos (2\pi n t - K_2 z + \psi) \quad (\text{A.5})$$

where  $\psi$  is the phase difference between the two waves.

Considering the last term in the expression only at the moment, this interference term becomes:-

$$\begin{aligned}
 E_1 E_2 &= E_{O(1)} E_{O(2)} \cos(2\pi mt - K_1 z) \cos(2\pi mt - K_2 z + \psi) \\
 &= E_{O(1)} E_{O(2)} [\cos(K_1 z) \cos(2\pi mt) + \sin(K_1 z) \sin(2\pi mt)] \\
 &\quad \times [\cos(K_2 z + \psi) \cos(2\pi mt) + \sin(K_2 z + \psi) \sin(2\pi mt)] \\
 &= E_{O(1)} E_{O(2)} [\cos^2(2\pi mt) \cos(K_1 z) \cos(K_2 z + \psi) \\
 &\quad + \cos(2\pi mt) \sin(2\pi mt) \cos(K_1 z) \sin(K_2 z + \psi) \\
 &\quad + \sin^2(2\pi mt) \sin(K_1 z) \sin(K_2 z + \psi) \\
 &\quad + \cos(2\pi mt) \sin(2\pi mt) \sin(K_1 z) \cos(K_2 z + \psi)]
 \end{aligned}$$

Using the following equalities:

$$\cos(2\pi mt) \sin(2\pi mt) = 0$$

and

$$\cos^2(2\pi mt) = \sin^2(2\pi mt) = \frac{1}{2}$$

(A.6)

$$\begin{aligned}
E_1 E_2 &= E_{O(1)} E_{O(2)} [\frac{1}{2}(\cos(K_1 z) \cos(K_2 z + \psi)) \\
&\quad + \sin(K_1 z) \sin(K_2 z + \psi)] \\
&= \frac{1}{2} E_{O(1)} E_{O(2)} [\cos(K_1 z - (K_2 z + \psi))] \quad (A.7)
\end{aligned}$$

Substituting equation A.7 back into equation A.3 remembering equality equation A.6:

$$\begin{aligned}
I &= E_{O(1)}^2 \cos^2(2\pi n t - K_1 z) + E_{O(2)}^2 \cos^2(2\pi n t - K_2 z + \psi) \\
&\quad + 2 \times \frac{1}{2} E_{O(1)} E_{O(2)} [\cos(K_1 z - (K_2 z + \psi))] \\
&= \frac{1}{2} E_{O(1)}^2 + \frac{1}{2} E_{O(2)}^2 + E_{O(1)} E_{O(2)} \cos(K_1 z - K_2 z + \psi) \\
&\hspace{15em} (A.8)
\end{aligned}$$

The last term represents the phase difference between the two waves at any location.

The irradiance pattern will consist of alternate light and dark fringes from which the original phase shift  $\psi$  may be determined. It may be recorded using photography or viewed on a diffusing screen. Interference information may therefore be used to convert a phase distribution into an irradiance pattern. It is this concept that is the key to holography.

Gabor (1948) developed holography by forming an interference pattern from object and reference waves and recording it on photographic film. A replica of the reference wave then illuminates the developed film and is diffracted in such a manner so as to reproduce the original object wave. This process is now explained.

Assuming the x-y directions are the plane of the hologram, the reference wave may be described by:-

$$E_{\text{ref}} = E_{0\text{ref}} \cos(2\pi nt - \Psi_{\text{ref}}(x,y)) \quad (\text{A.9})$$

where the phase  $\Psi(x,y)$  is a known function. That is to say, if the wave were simply rotated through an angle  $\gamma$  about the y axis, the phase at any point would only depend on x, so that:

$$\Psi_{\text{ref}} = \frac{2\pi}{\lambda} x \sin\gamma = Kx \sin\gamma$$

The wave scattered by the object may be expressed as:-

$$E_{\text{obj}} = E_{0\text{obj}} \cos(2\pi nt + \Psi_{\text{obj}}(x,y)) \quad (\text{A.10})$$

However, in this case the amplitude and phase may not be described easily, they are complicated functions of position corresponding to an irregular wavelength. An object acts as a series of point sources for regular waves and so generates a complicated irregular wavefront. When the two waves superimpose and interfere at the hologram the resulting irradiance pattern is given by:-

$$I(x,y) = \frac{E_{obj}^2}{2} + \frac{E_{ref}^2}{2} - E_{obj} E_{ref} \cos(\psi_{ref} - \psi_{obj}) \quad (A.11)$$

A correctly exposed and processed hologram has an amplitude transmittance proportional to the intensity of the illuminating wave. If this hologram is illuminated with a reconstruction wave,  $E_{rec}$ , where:

$$E_{rec} = E_{0rec} \cos(2\pi nt + \psi_{rec}(x,y)) \quad (A.12)$$

travelling in the same direction as the original reference beam, then the final wave,  $E_{fn}$ , would be proportional to  $E_{rec} I$ . Thus:

$$\begin{aligned} E_{fn} &= E_{rec} I \\ &= \left[ \frac{E_{obj}^2}{2} + \frac{E_{ref}^2}{2} + E_{obj} E_{ref} \cos(\psi_{ref} - \psi_{obj}) \right] E_{0rec} \cos(2\pi nt + \psi_{rec}) \\ &= \frac{1}{2} \left\{ (E_{obj}^2 + E_{ref}^2) E_{0rec} \cos(2\pi nt + \psi_{rec}) \right\} \\ &\quad + E_{obj} E_{ref} E_{0rec} (\cos(\psi_{ref} - \psi_{obj}) \cos(2\pi nt - \psi_{rec})) \\ &= \frac{1}{2} E_{0rec} (E_{obj}^2 - E_{ref}^2) \cos(2\pi nt + \psi_{rec}) \\ &\quad + \frac{1}{2} E_{obj} E_{ref} E_{0rec} [\cos(2\pi nt + \psi_{rec} - \psi_{ref} + \psi_{obj}) \\ &\quad + \cos(2\pi nt + \psi_{rec} + \psi_{ref} - \psi_{obj})] \quad (A.13) \end{aligned}$$

Because

$$\psi_{\text{ref}} = \psi_{\text{rec}} \quad (\text{A.14})$$

$$\begin{aligned} E_{\text{fn}} = & \frac{1}{2} E_{\text{orec}} (E_{\text{obj}}^2 + E_{\text{ref}}^2) \cos(2\pi mt + \psi_{\text{ref}}) \\ & + \frac{1}{2} E_{\text{orec}} E_{\text{obj}} E_{\text{ref}} \cos(2\pi mt + 2\psi_{\text{ref}} - \psi_{\text{obj}}) \\ & + \frac{1}{2} E_{\text{orec}} E_{\text{obj}} E_{\text{ref}} \cos(2\pi mt + \psi_{\text{obj}}) \end{aligned} \quad (\text{A.15})$$

These three terms describe the light issuing from the hologram. The first is simply an attenuated reconstruction beam, the zeroth-order undeflected reference beam. It contains no information about the phase of the object beam and is of little concern. The remaining two beams are first-order waves. The former of these has the same amplitude as the object wave,  $E_{\text{obj}}$ , except for a multiplicative constant and contains a  $2\psi_{\text{ref}}$  phase contribution that arises from moving the reference beam off axis. It also contains the negative of the object wave. This term therefore produces a pseudoscopic image of the object. The remaining term, except for a multiplicative constant, has precisely the same form as the object wave. Hence the object beam has been recorded and reconstructed exactly using interference theory.

## APPENDIX B

### ESTIMATION OF EXPERIMENTAL ERRORS

#### PITOT STATIC TUBE

Bradshaw (1970) discusses errors of pitot probes and indicates that their accuracy is of the order of 0.25% provided the tube is aligned correctly, is not close to a wall, that the turbulence intensity is less than 5% and the total pressure does not change by more than 1 to 2 percent across the diameter. The first two points are satisfied while the latter two are not. However, turbulence levels are not significantly higher than 5% in the core region and so would not lead to large errors. Because the probe does not enter the near wall locations the total pressure failed to change by more than 4% and so an error of 0.5% is estimated based on this knowledge.

An additional error in positioning the probe to within  $\pm 0.25$  mm gives an error of 0.7%. The combined error is then determined by taking the square root of the sum of the squares of the contributions. This results in an estimated error of  $\pm 0.9\%$  for the pitot probe measurements.

## STATIC PRESSURE

Pressure measurement in the wall of a tunnel avoids many of the errors associated with probes in the stream. Turbulent fluctuations fall to zero at the surface and so the only error introduced is the fluctuation of flows into and out of the tapping. This falls to zero for a first order approximation, Bradshaw (1970). The only remaining error source is the difference between the pressure on a solid surface and the pressure in the hollow tapping. This has been assumed negligible for half a century for low speed flows where the tapping diameter is between 0.5 - 1.0 mm. Hence, this error is assumed negligible. Finally an error in the position of the tapping of  $\pm 1$  mm, leads to an error of  $\pm 0.9\%$ . This is assumed to be the only error present in the static pressure measurements.

## PRESTON TUBE

Repeatability of the shear stress readings was poor, an error of  $\pm 3.5\%$  was observed in the results taken. This arose because of the difficulty in flush mounting the probe with the wall. It has to be inserted through the exit and test sections which have to be disassembled to mount the probe and then reassembled for the measurement to be taken. During this procedure the probe may move slightly and so cause the discrepancy. Intrinsic errors were estimated by Patel (1965) to have a maximum of 3% at a similar Reynolds number to the present study,  $Re_D = 13000$ . These arise because of calibration curve errors and turbulent fluctuations causing the velocity profile to depart from the log law of the wall. The total error may therefore be estimated to be  $\pm 4.6\%$  for the Preston tube measurements.

### HOT WIRE PROBE

Errors are reduced when using this probe as only relative values are required, not absolute ones, to determine the turbulence intensity. Errors in the voltage measurement are considered negligible, but the fluctuations in signal lead to an observed error of  $\pm 0.5\%$ . The probe was positioned crudely, to within 1 mm, and this gives an error of  $\pm 1.3\%$ . The total error was therefore estimated to be  $\pm 1.4\%$ .

### HEAT TRANSFER DATA

Error sources in the determination of the temperature fields may be separated into the intrinsic ones and the experimentally observed ones. Contributions to the former include:

- (a) Refraction effects
- (b) Diffraction effects
- (c) End effects
- (d) Buoyancy

and to the latter include:

- (e) Resolution of the fringes
- (f) Stray thermal currents
- (g) Shrinkage of holographic emulsion
- (h) Misalignment of the optics.

Using equation 4.8 to determine the ray path through the test section a correction for refraction may be estimated. However, in the near wall region, at heat transfer rates, ray crossing occurs, Schmidt and

Newall (1968). So no estimate of the error may be undertaken because no fringes exist. Correct focussing helps minimise this effect, Howes and Buchele (1966), but fails to eliminate it. In the outer wall regions the correct focus position was chosen to eliminate refraction errors. The ray tracing technique indicated that they were negligible, which confirms the work of Beach, Muller and Tobias (1973). They illustrated that the correct focus position reduces the phase to the same magnitude as that expected without light deflection.

To determine absolute values of heat transfer at the high flow rates and large temperature gradients, an extrapolation from the buffer layer (where fringes exist) to the boundary layer (where conduction only may be assumed) has to be made. The effect is minimised by smaller overall temperature differences but is still apparent. Using the experience gained analysing low flow rates the wall position is determined, usually observed to be at the jet black interface with the flow. The thickness of the grey area (ray crossing regime) is then determined. Converting this measured distance to a non-dimensional one enables its size to be determined in  $Y^+$  units. Universality of the temperature profile is then assumed, a reasonable estimation given, Figure 6.8. which enables the wall distance to the nearest fringes to be determined. If they are in the laminar sub-layer no extrapolation is required, but if they are located in the turbulent buffer region the temperature gradient is extrapolated into the conduction sub-layer and the Nusselt number determined. The error introduced by the measurement is connected to the fringe resolution and so is discussed later.

The extrapolation procedure is easily undertaken for the smooth wall investigation where wall shear velocities,  $U^*$ , are readily available. For the square rib investigation the wall shear stress distribution given by Martin (1987) was used. However, no momentum field data is available for the other surfaces and so only the Nusselt number distribution is determined.

Diffraction errors are again minimised by focussing correctly. Sharp edges to the test section also reduce this error, McLarnon et al (1975). Fringes formed by diffraction effects were observed to be uniform, parallel to the surface, and much finer than those resulting from thermal gradients. At low Reynolds number there were typically 4-6 fringes superimposed on the near wall fringe. This gives a banding of intensity to the fringe and an estimated error of  $\pm 1\%$  results from this. At high Reynolds numbers the diffraction is negligible because it is only dominant in the ray crossing regime where no fringes are present.

End effects are estimated to be at a maximum for low Reynolds numbers because this is when the side wall boundary layers will be thicker with respect to the tunnel width. A thermal boundary layer extending a typical distance of 10 mm gives an error in fringe shift of:

$$\frac{\Delta S}{S} \approx \frac{2}{3} \frac{\delta}{W_0} \approx 0.02$$

This results in an error of  $\pm 1.9\%$  for low flow rates. At high Reynolds numbers, the boundary layer is thinner, and the error becomes negligible.

Buoyancy effects may be estimated by evaluation of the Richardson number given by:

$$Ri = \frac{Ra}{Re^2 Pr} \quad (B.1)$$

where Ra is the Rayleigh number. For Richardson values below  $10^{-3}$  buoyancy is negligible, Bradshaw (1969). At the lowest flow rate of  $Re = 3600$  and a temperature difference of  $30^\circ\text{C}$ , the Richardson number has a value of  $1.5 \times 10^{-2}$ . This has the effect of adding a mild convex curvature to the surface and so has a small effect on boundary layer growth. It is estimated to be no greater than  $\pm 0.3\%$ .

The accuracy of the fringe order when assigned by visual observation is estimated by Vest (1979) to be between 0.25, when assigned by crude interpretation, and 0.02 when a micro-densometer is used. By fitting a cubic spline to measurements taken from one interferogram at various times, the fringe position was estimated to be within 0.05. [This good value was able to be achieved because the interferogram was enlarged directly on the projection microscope]. This results in an error for the temperature gradient of  $\pm 4.7\%$ . Automatic fringe analysis or heterodyne techniques would reduce this error significantly.

Errors from stray thermal currents are assessed by assuming the largest eddy structure, 75 mm across, raised by  $0.37^\circ\text{C}$ , the rise at the highest flow rate enters the laser beam when the hologram is exposed. An extra  $1/20$ th of a fringe would result. This gives an error of  $\pm 0.4\%$ . Because of the heavy insulation around the heater plate no stray thermal

currents are assumed. If any did exist the tunnel's wooden support would channel it away to the exit of the flow.

Shrinkage of the emulsion is negligible when double exposure holograms are taken. No fringes are formed by processing and so an excessive shrinkage of, say, 10 fringes ( $5 \mu\text{m}$ ) is well below the resolution possible when determining the fringe separation. However, for real-time work the shrinkage of the emulsion becomes important because fringes are now formed when the plate is replaced in its original position. Careful processing reduces the emulsion shrinkage but on a 4" x 2½" plate some fringes were always present. They are spherical, centred on the middle of the plate, and produced by a slight bowing of the plate. Two solutions to minimise their effect were undertaken. One, was to move the plate and so form a set of 'finite fringes', Section 2.1.1., perpendicular to the isotherms. A finite fringe analysis then makes the reference fringes negligible. This procedure may be used when an accurate result is required. The second solution was to accept the few fringes present, centre them on the wall interface, and use the images formed for flow visualisation purposes. Effectively, the only fringes generated were in the isothermal main flow regions and so aided in the viewing of the field. The effect of shrinkage is therefore negligible for both double exposure and real-time interferograms.

Misalignment of the object beam as it enters the test section would cause a severe error. Beach, Muller and Tobias (1973) show how a misalignment of  $+2.3^\circ$  gives an error of  $+0.3\%$  to the wall position in a cathodic boundary layer. To ensure the beam is correctly aligned a flat polished mirror was placed on the test section surface. The object beam

orientation was then varied until no interference fringes were formed on a screen placed at the plane of the hologram. It was then assumed that the beam entered in the correct plane and so made alignment errors negligible.

To ensure the correct focus position is obtained interferograms were taken at numerous focal planes until the correct one is achieved. To aid in this process a real-time system was established whereby the focussing lens and a screen were moved until refraction effects appeared negligible. Hauf and Grigull (1970) estimated the error to be 1% of the thermal field gradient once the focus position is attained.

A summary of the experimental errors discussed above is given in the following table for the high and low Reynolds number cases:

Source	Tolerance Low Re	Tolerance High Re	Comment
(a) Refraction effects	-	4.7%	Providing wall shear velocities are available
(b) Diffraction effects	0.6%	-	
(c) End effects	1.9%	0.4%	Important for narrow tunnels
(d) Buoyancy	0.3%	-	
(e) Resolution	4.7%	4.7%	Improved by automatic fringe analysis
(f) Stray thermal currents	0.3%	0.4%	
(g) Emulsion shrinkage	-	-	Important for some real-time work
(h) Optics Misalignment	1.0%	1.0%	Incorrect focus position
Combined error margin	5.22%	6.73%	

This demonstrates that the only significant error is the resolution of the fringes. The end effects make a minor contribution at low flow rates, but it is negligible for higher flows. Hence, if an automated fringe analysis system is introduced the resolution error is removed and the combined error would be of the order of 1% due mainly to the position of the focus plane. At reactor flow rates therefore detailed absolute values of Nusselt numbers would be available provided that momentum field investigations are undertaken along side the thermal field investigation.

Optimisation of the refraction error by focussing leads to smaller errors in the near wall region but larger errors in the outer wall region. Hence, the estimated error may be optimistic because of the error arising in the fringe location when a curve is fitted. The field would not have a linear error. It will peak somewhere in the outer wall layers and decline in the main flow and near wall regions. The location of the peak error varies with Reynolds number but is calculated to give an error of no greater than 2% in the fringe location. This figure should be added to the list of tables given on the previous page.

## APPENDIX C

### GENERAL THEORY OF FINITE ELEMENT MODELLING

To explain the Galerkin finite element method used in the FEAT code a steady state heat conduction problem is chosen and the method of solution, using finite elements, is presented. The steady state heat conduction equation in one dimension may be written:-

$$\frac{1}{\rho C_p} \frac{\partial}{\partial x} \left( K_x \frac{\partial T}{\partial x} \right) = \frac{\partial T}{\partial t}$$

Substituting  $\alpha_t = -\frac{1}{\rho C_p}$  gives:-

$$\frac{\partial}{\partial x} \left( K_x \frac{\partial T}{\partial x} \right) = -\frac{1}{\alpha_t} \frac{\partial T}{\partial t} \quad (C.1)$$

To proceed the boundary conditions need to be specified and these are illustrated below in Figure C.1.

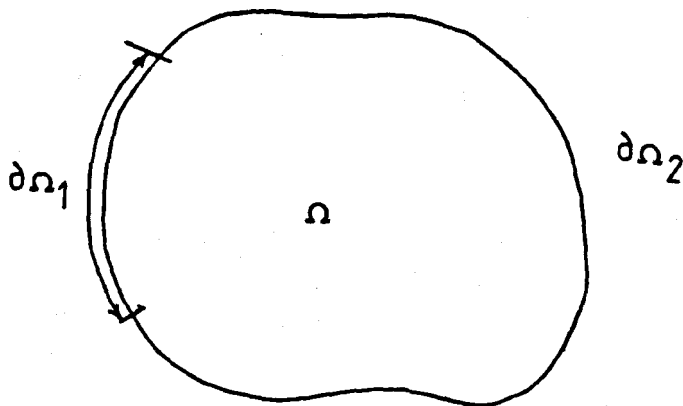


FIGURE C.1 BOUNDARY CONDITIONS FOR SURFACE  $\Omega$

The surface  $\Omega$  has a temperature specified on the  $\partial\Omega_1$  boundary and a heat flux on the  $\partial\Omega_2$  boundary. Let the inlet temperature  $t$  be  $\hat{t}_0$  and the heat flux on the remaining boundary be  $\hat{q}_0$ . Therefore:-

$$t = \hat{t}_0$$

$$K \frac{\partial T}{\partial x} - \hat{q}_0 = 0 \quad (C.2)$$

The Galerkin finite element method then proceeds as follows.

An integral formation is required that satisfies the boundary conditions and differential equations. Each side of equation C.1 is multiplied by an arbitrary test function  $V = 0$  on  $\partial\Omega$ :-

$$\int_{\Omega} \left[ \frac{\partial}{\partial x} \left( K \frac{\partial T}{\partial x} \right) + Q \right] V \, dx = 0 \quad (C.3)$$

and equation C.2 by the same function:-

$$\int_{\partial\Omega_2} \left( K \frac{\partial T}{\partial x} - \hat{q}_0 \right) V \, dx = 0 \quad (C.4)$$

Combining the two equations and integrating by parts yields the following expression:-

$$\int_{\Omega} K \frac{\partial T}{\partial x} \frac{\partial V}{\partial x} \, dx - \int_{\Omega} QV \, dx = \int_{\partial\Omega_2} \hat{q}_0 \, dx \quad (C.5)$$

This is known as the method of weighted residuals as the solution of equation C.5 for arbitrary functions  $V$  is equivalent to the original differential equation and boundary conditions.

To discretise the integral formation into matrix form the region is divided into numerous smaller parts, each one referred to as a finite element. The division of the region is illustrated in Figure C.2, where each element of size  $\Omega_e$  has  $n$  nodes  $x_i$ .

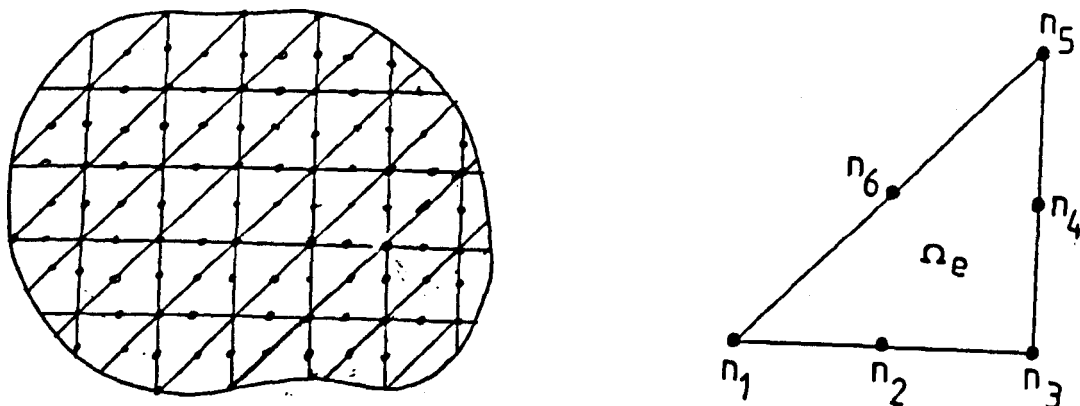


FIGURE C.2    STRUCTURE  $\Omega$  DIVIDED INTO ELEMENTS

For each triangular element there are 6 nodes and so six functions,  $W_i^e(x)$ , referred to as basis functions, are defined. They are made quadratic and have the property that at the node under investigation the function has a value of 1, and zero at all the other nodes.

$$W_i^e(x_i) = 1$$

$$W_i^e(x_j)_{j \neq i} = 0$$

The global function  $W_i(x) = \sum_e W_i^e(x)$  is a piece-wise quadratic localised at node  $i$ . To explain this a cross-section is taken through the grid at node  $i$  and is illustrated in Figure C.3.

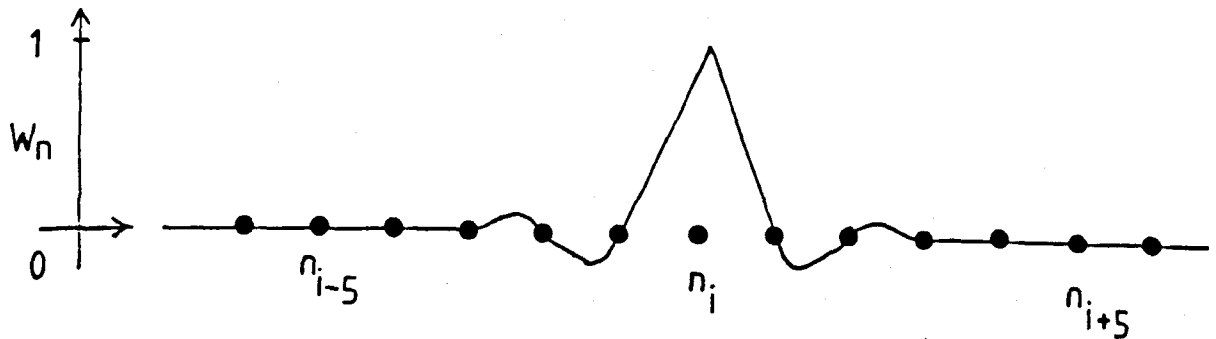


FIGURE C.3 CROSS SECTION OF FUNCTION AT NODE i

The temperature of the region may now be determined in discretised form using the basis functions  $W_i$ :-

$$T = \sum T_i W_i(x) \quad (C.6)$$

Substituting those values into C.5 gives:-

$$\int_{\Omega} K \frac{\partial(\sum T_i W_i(x))}{\partial x} \frac{\partial v}{\partial x} dx - \int_{\Omega} Q v dx = \int_{\Omega} \hat{q}_0 v dx \quad (C.7)$$

(any v)

In the Galerkin method, the arbitrary weighting function  $V$  is discretised like  $T$ , in terms of  $W_j$ , which gives:-

$$\int_{\Omega} K \frac{\partial(\sum T_i W_i(x))}{\partial x} \frac{\partial W_j}{\partial x} dx = \int_{\Omega} Q W_j dx = \int_{\Omega} \hat{q}_0 W_j dx \quad (\text{any } j) \quad (C.8)$$

$T_i$  may now be taken outside the integral as they are just coefficients.

Hence:-

$$\begin{aligned} & \sum_i T_i \int_{\Omega} K \frac{\partial W_i}{\partial x} \frac{\partial W_j}{\partial x} dx - \int_{\Omega} Q W_j dx \\ &= \int_{\partial \Omega_2} \hat{q}_0 W_j dx \end{aligned} \quad (C.9)$$

Because the integral over the whole body is equal to the sum of the integrals for each element and the integral around the boundary is equal to the sum of the integral for each boundary element, equation C.9 may be re-written as:-

$$\begin{aligned} & \sum_e \left\{ \sum_i T_i \int_{\Omega_e} K \frac{\partial W_{ie}}{\partial x} \frac{\partial W_{je}}{\partial x} dx - \int_{\Omega_e} Q W_{je} dx \right\} \\ &= \sum_e \int_{\partial \Omega_e} \hat{q}_0 W_{je} dx \end{aligned}$$

This equation may now be expressed as a set of algebraic equations suitable for solution on a computer. In the FEAT code the matrix is solved using the Newton-Raphson iterative technique. The iterations are terminated when the error reaches some predetermined value.

## APPENDIX D

### ANALYSIS OF TYPICAL HOLOGRAM

The smooth surface interferogram illustrated in Figure 6.6(a) is analysed below.

Full field magnification: 1 : 1.15  
Boundary layer magnification: 1 : 9.8  
Reference temperature,  $T_r$  291 K

Fringe Order	Displacement $y$ (mm)	Temperature (K)	$T^+$	$y^+$
5	7.5	300.64	10.41	38.87
6	5.306	302.64	9.62	27.5
7	3.597	304.67	8.83	18.64
8	2.806	306.73	9.01	14.54
9	2.296	308.82	7.19	11.90
10	1.952	310.94	6.35	10.12
11	1.645	313.08	5.51	8.53
12	1.352	315.26	4.65	7.01
13	1.097	317.46	3.78	5.69
14	0.842	319.70	2.90	4.36
15	0.561	321.97	2.03	2.91
16	0.306	324.27	1.09	1.59
17	0.102	326.41	0.12	0.53

$$q_w = K \frac{dT}{dy} = 2.624 \times 10^{-2} \times \frac{(326.41 - 324.27)}{(0.306 - 0.102) \times 10^{-3}} = 275$$

$$Nu = \frac{q_w D}{K \Delta T} = \frac{275 \times 0.12}{2.624 \times 10^{-2} \times (326.41 - 291)} = 35.5$$

TEST

$$Nu = 0.023 Re^{-0.8} Pr^{0.4} = 31.4$$

## APPENDIX E

### DESCRIPTION OF VIDEO

A ten minute video in the University Library is available that illustrates the time dependent effects for the flow over numerous geometries. A description of its contents follows, besides the counter position at which the event occurs.

Counter Position	Description
------------------	-------------

#### Smooth Surface

000	Re $\approx$ 8000, then flow rate increase to in excess of 25000
010	Re $\leq$ 25000 High speed flow
020	Flow slows down to give natural convection
025	Natural convection [Large boundary layer]
035	Flow reintroduced and a laminar flow is observed
040	Turbulent flow Re $\approx$ 12000 Turbulent structures in the outer wall region are observed
055	Flow slows to Re = 6000
070	Re $\approx$ 4000 Transition flow where it jumps from turbulent to laminar flow in outer wall regions
085	Laminar flow Re $\approx$ 3500
092	Flow stops. Natural convection
100	High speed film at Re = 5000 [1 min is equivalent to 2½ seconds]
120	High speed film at Re = 30000

### Rounded Rib Surface

- 145 Turbulent flow at  $Re \approx 4500$
- 155 Flow slows to give natural convection
- 160 Flow introduced to give turbulent conditions
- 163  $Re \approx 8000$ . Oscillation of fringes is easily observed in the recirculating region at the rear of the rib
- 170  $Re \approx 30000$
- 180  $Re \approx 50000$ . A small amount of oscillation in the fringes in the recirculating region is observed
- 195 Flow slows down steadily
- 200 Natural convection
- 215 Flow reintroduced giving laminar and turbulent conditions in quick succession

### Square Rib Deposited Surface

- 219 Natural convection
- 226 Flow introduced
- 230 Turbulent conditions  $Re \approx 8000$
- 235  $Re \approx 15000$  Recirculation region contracts as
- 240  $Re \approx 50000$  speed increases

### Rounded Rib Deposited Surface

- 245 Natural convection
- 248 Flow introduced
- 250 Turbulent conditions  $Re \approx 8000$
- 260  $Re \approx 40000$ . Flow was increased steadily to this value and the recirculation region decreased in size
- 265 Fan is stopped and flow slows to give natural convection
- 270 Natural convection
- 275 Video finishes

Comments:

- i) No images of the square rib geometry are illustrated as they were erased by mistake.
- ii) Image quality is poor for the square rib deposited surface and the high speed film of flow over the smooth surface.
- iii) Framing rate of the video is 25 ff/s.

## APPENDIX F

### PUBLISHED PAPERS

Investigation of heat transfer from smooth and rib-roughened channels using holographic interferometry, Part 1. Double exposure results for a smooth channel. The City University, Internal Report, No.ML 153, (June 1985).

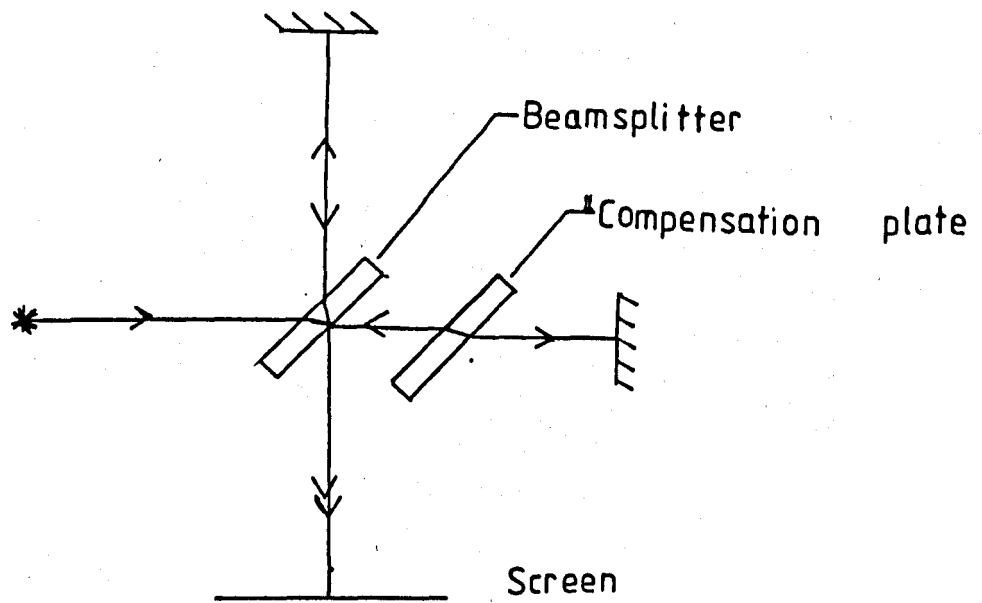
Investigation of convective heat transfer enhancement using real time holographic interferometry. Optical Methods in Fluid Mechanics, Inst.of Physics Conference, Series 77, (Vith Int. Conf. Photon Correlation and other Optical Techniques in Fluid Mechanics). Bristol, p.129. (July 1985)

Holographic interferometry and its applications to turbulent convective heat transfer. Int. J. Optical Sensors, Vol.1., p.191. (May 1986)

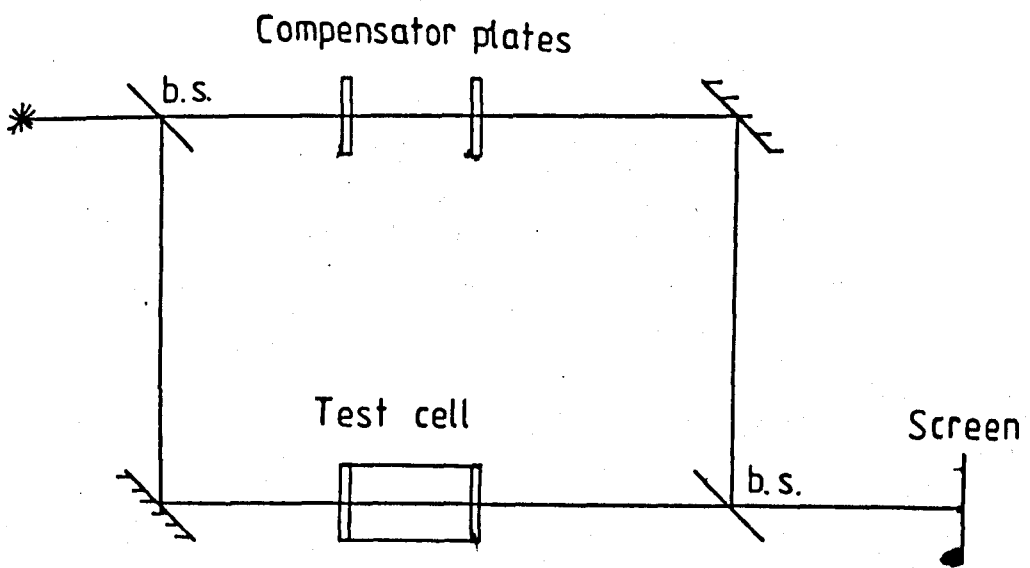
Problems using holographic interferometry to resolve the four dimensional character of turbulent, Part 1: Theory and experiment. Int. J. Optical Sensors, Vol.1., p.211. (May 1986)

**APPENDIX G**

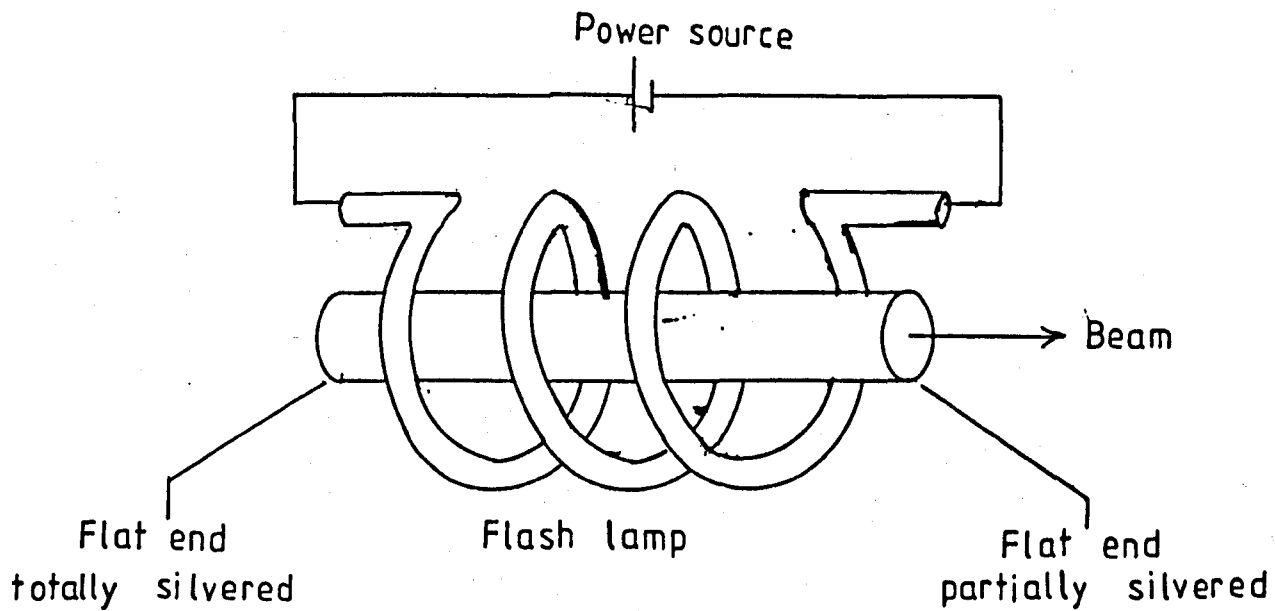
**FIGURES**



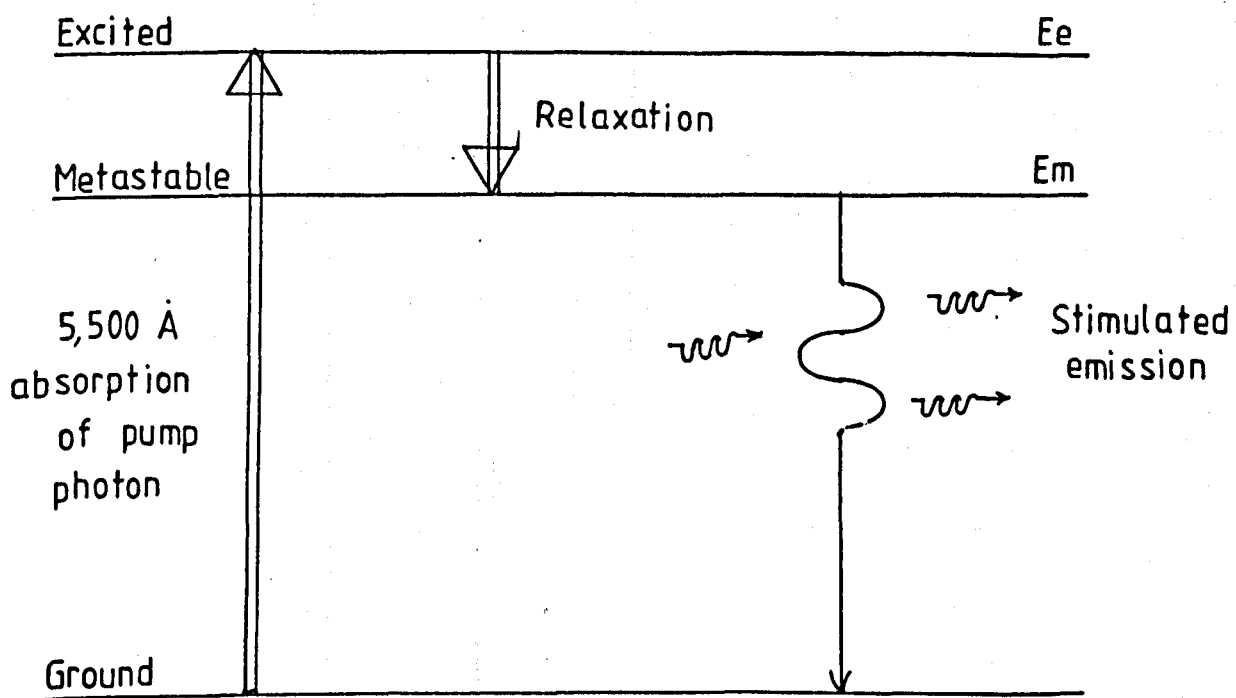
**FIG.2.1. MICHELSON INTERFEROMETER**



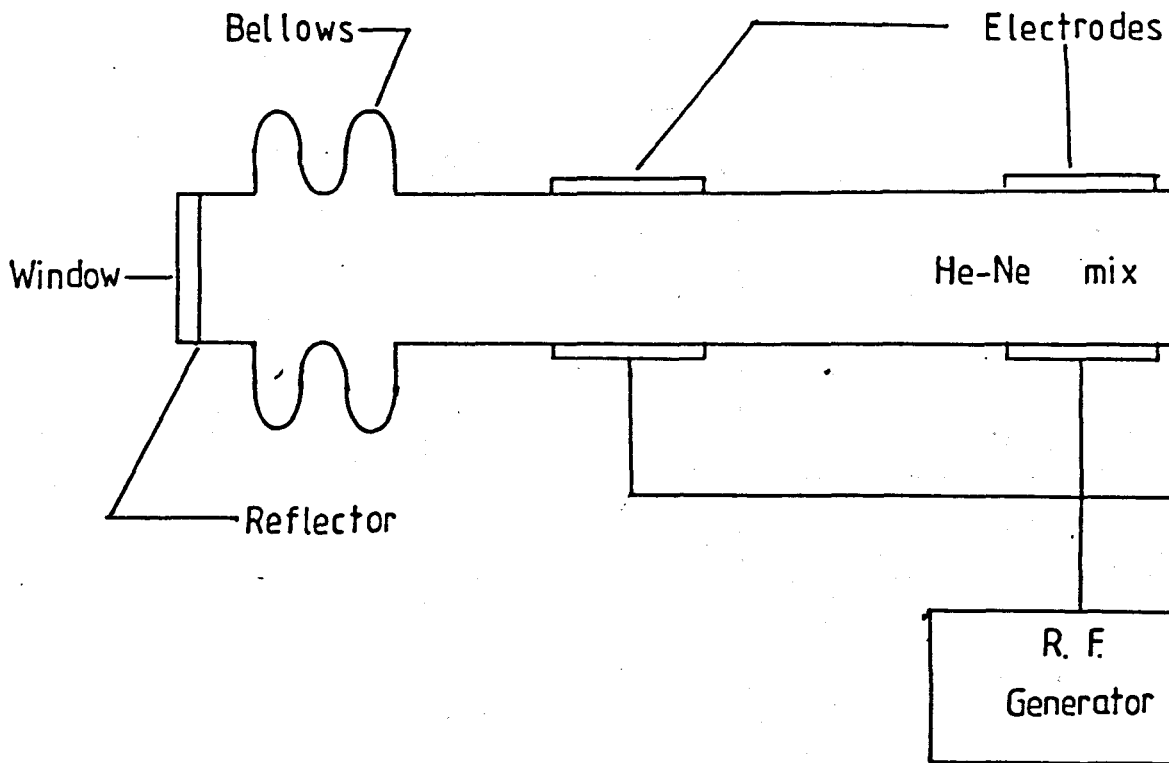
**FIG.2.2. MACH ZEHNDER INTERFEROMETER**



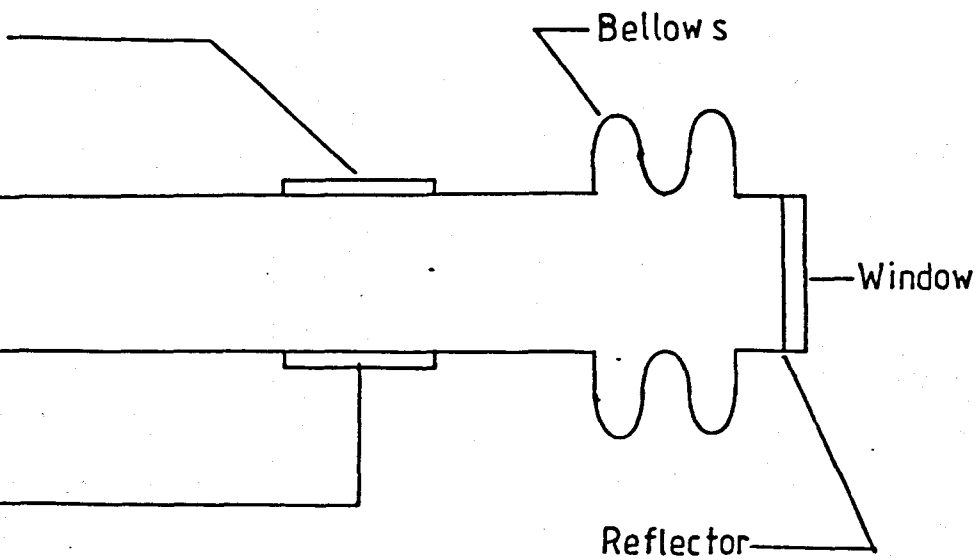
**FIG.2.3. PULSED RUBY LASER**



**FIG.2.4. RUBY LASER ENERGY LEVELS**



**FIG.2.5. HELIUM-NEON LASER**



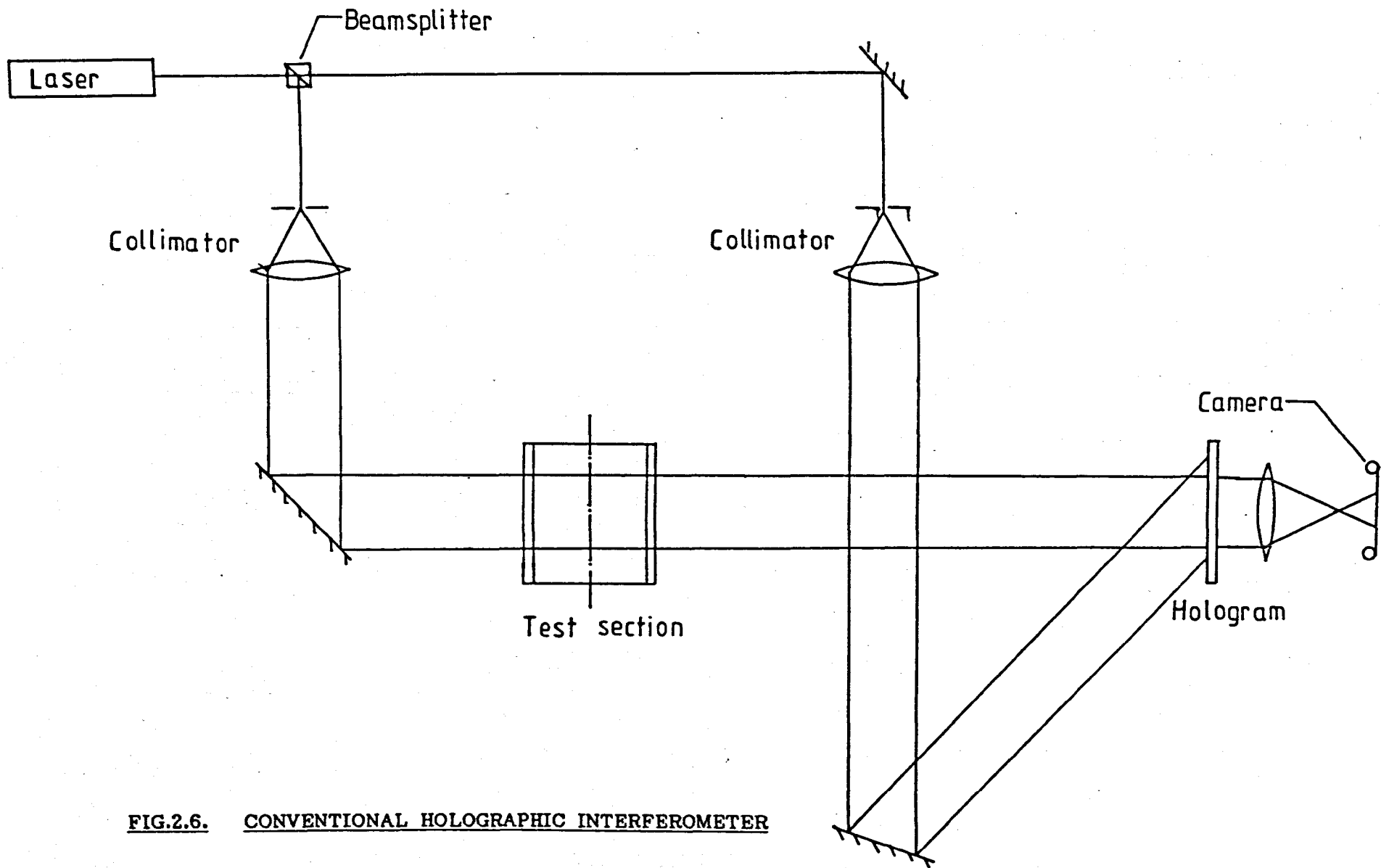


**FIG.2.6. CONVENTIONAL HOLOGRAPHIC INTERFEROMETER**

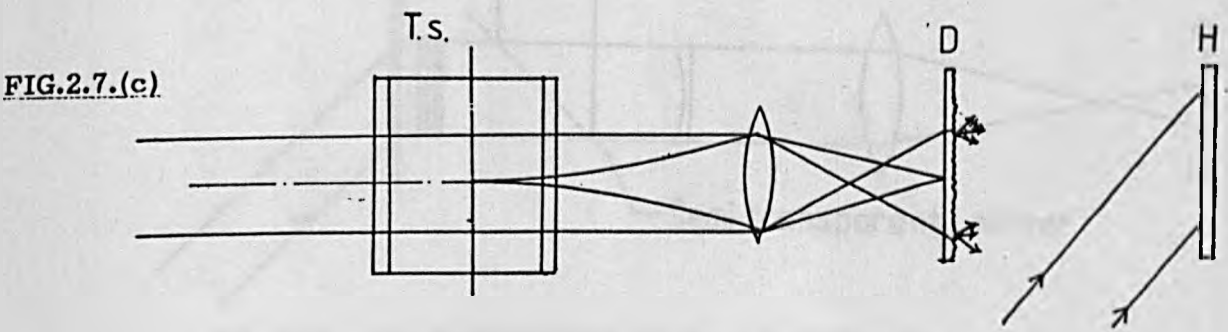
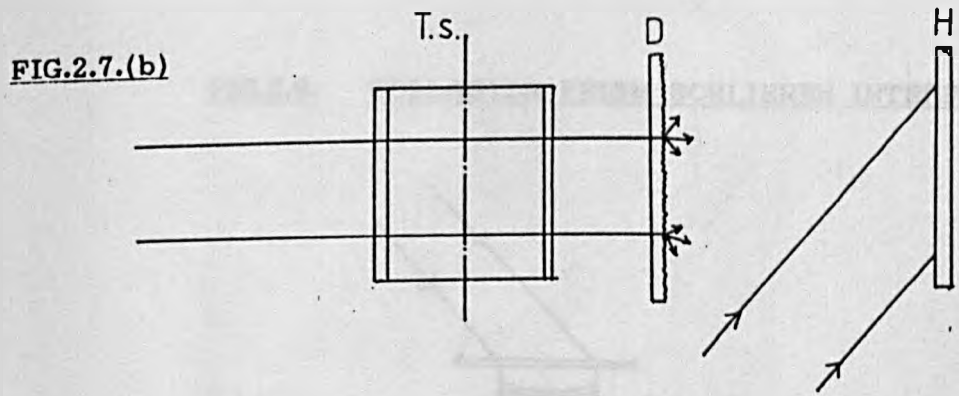
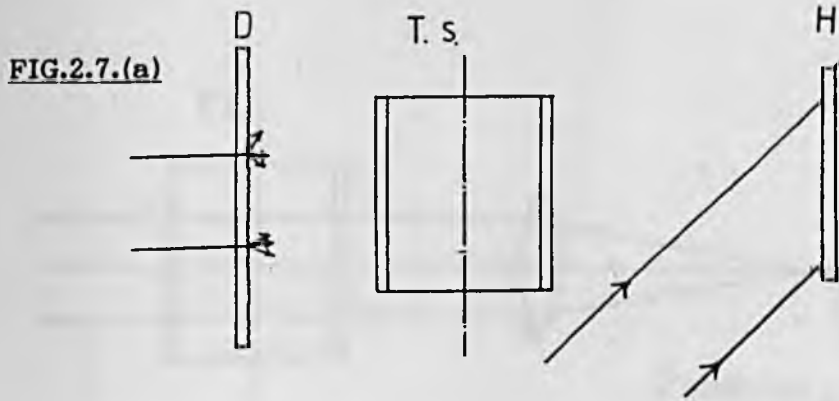


**FIG.2.7. GENERAL ILLUMINATION**

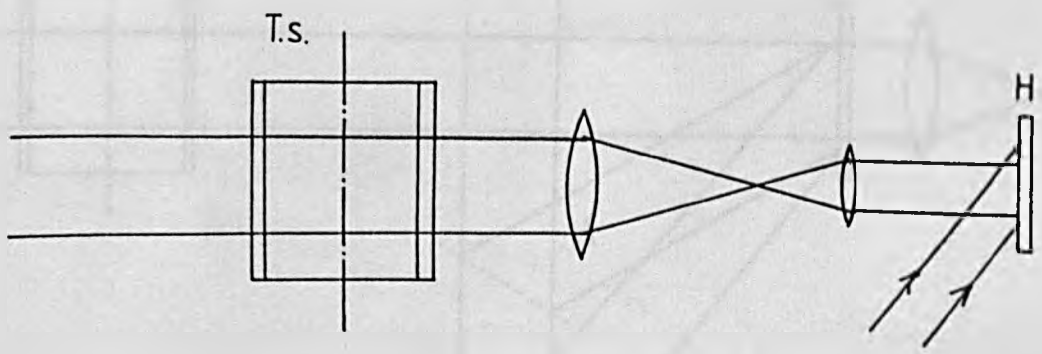


**FIG.2.8. IMAGE PLANE HOLOGRAPHY**

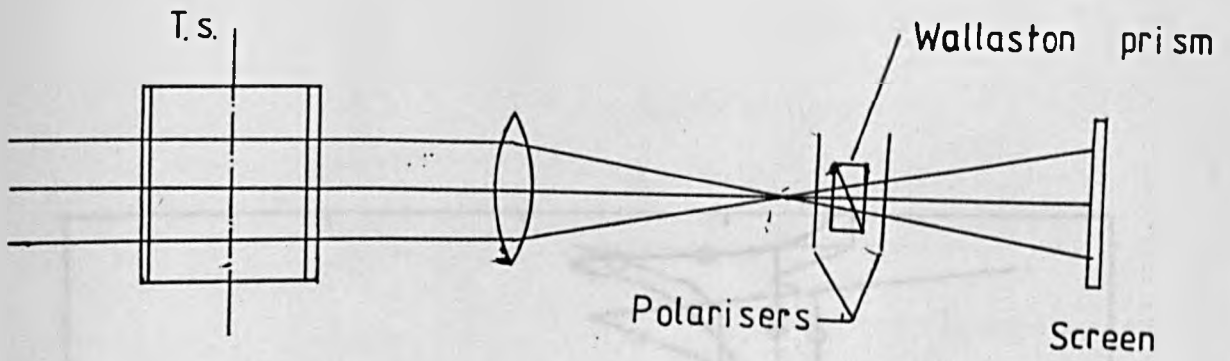


**FIG.2.9. WOLLASTON PRISM SCHLIEREN INTERFEROMETER**

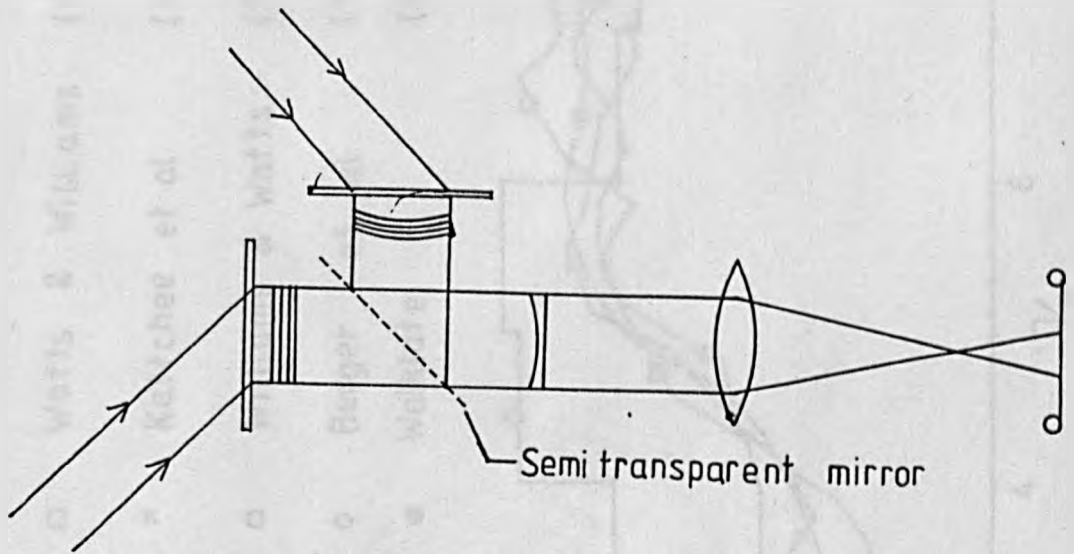


**FIG.2.10. SUPERIMPOSING OF TWO HOLOGRAMS**

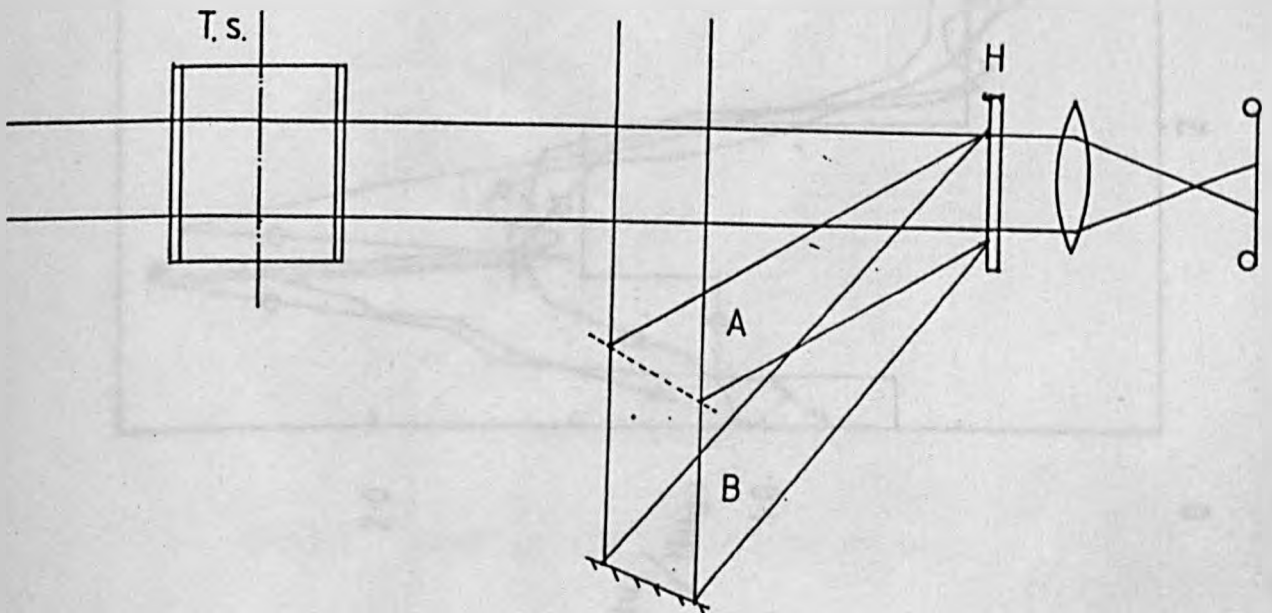


**FIG.2.11. USE OF TWO REFERENCE BEAMS**

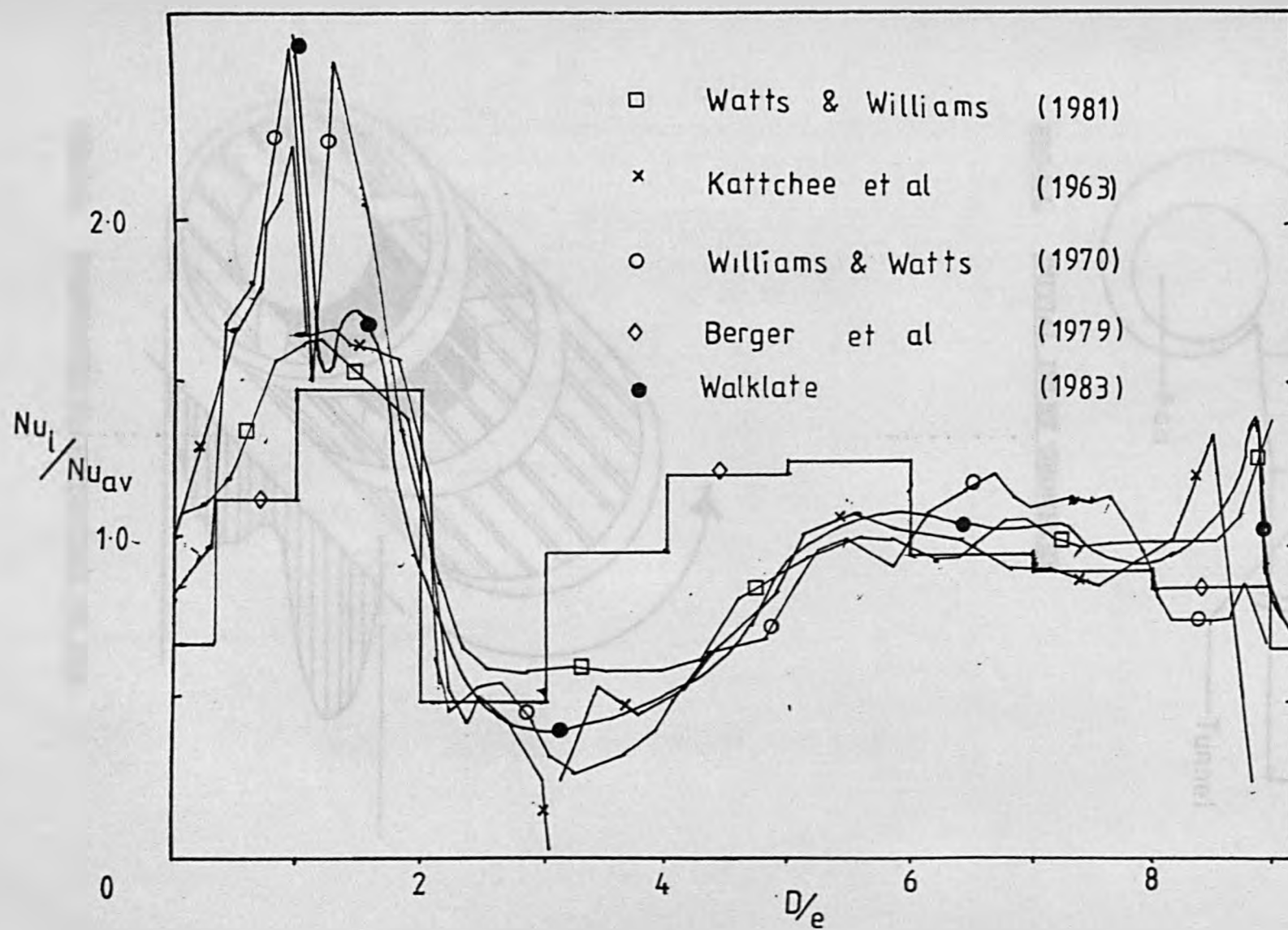


**FIG.2.12. COMPARISON OF THE RELATIVE HEAT TRANSFER DISTRIBUTIONS OBTAINED**

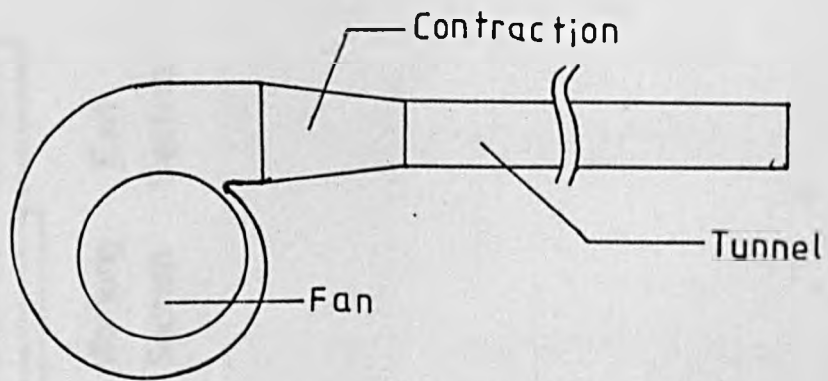


**FIG.3.1.** INITIAL INLET GEOMETRY

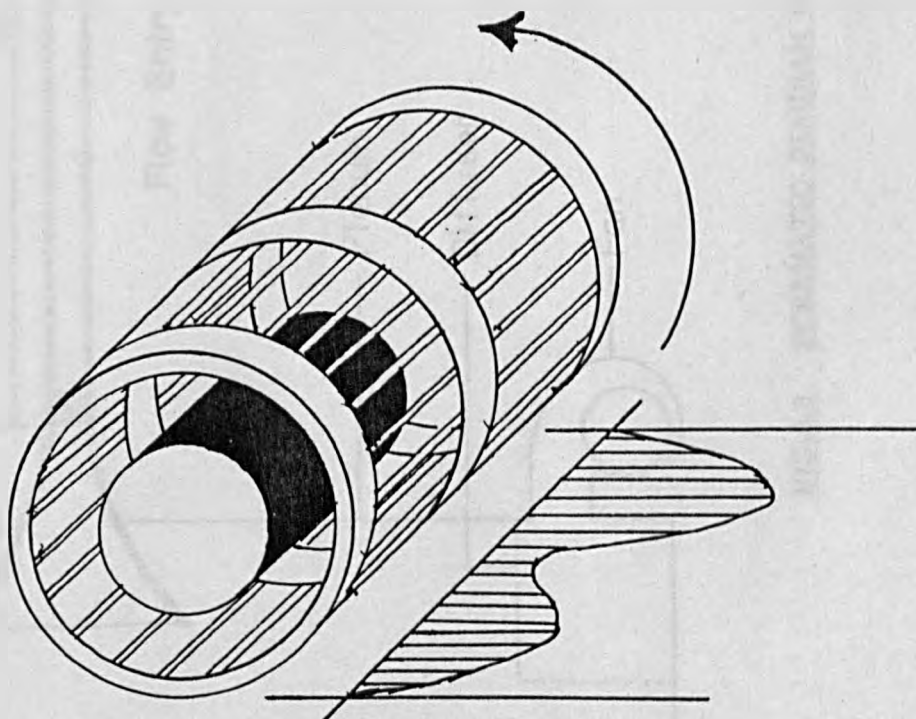


**FIG.3.2.** SCHEMATIC ILLUSTRATION OF FAN

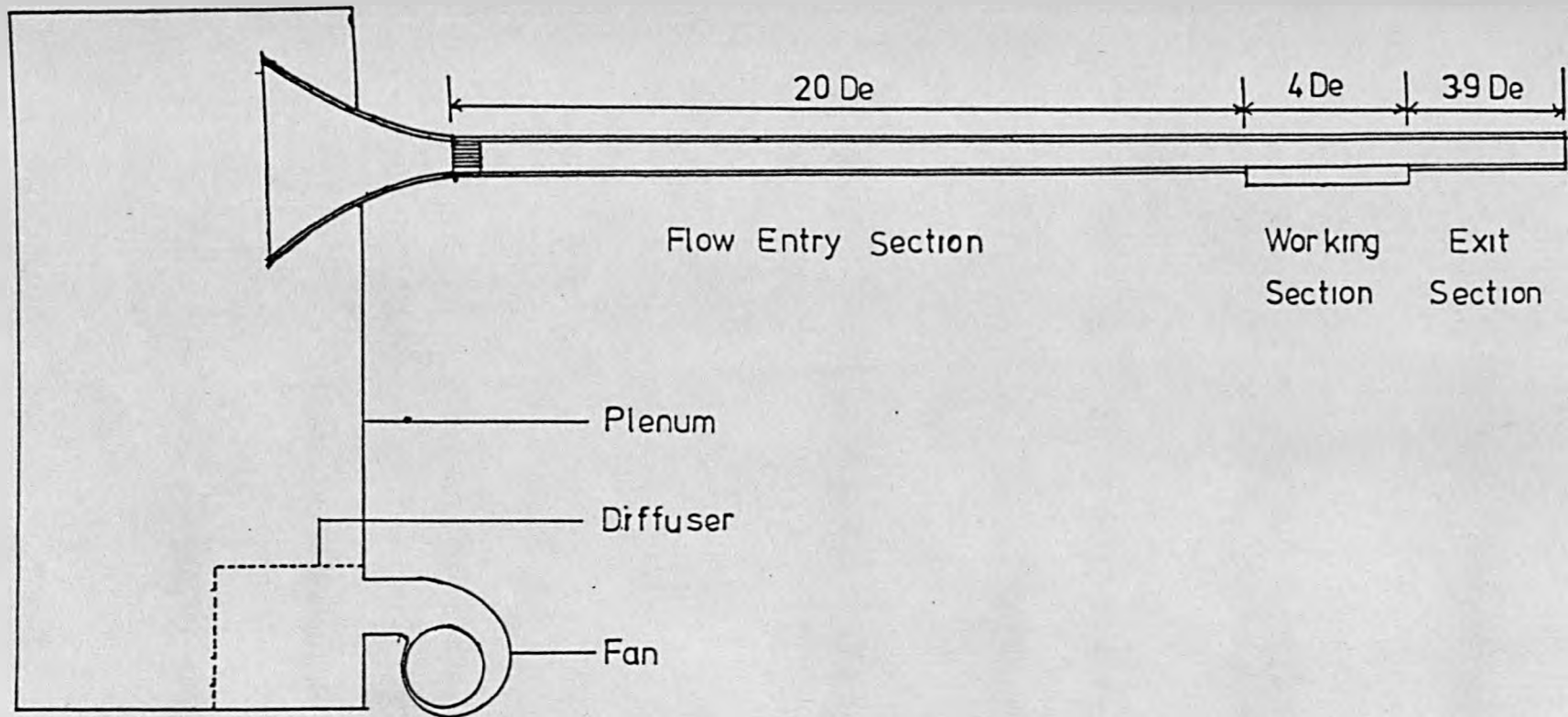


**FIG.3.3. SCHEMATIC DIAGRAM OF WIND TUNNEL**

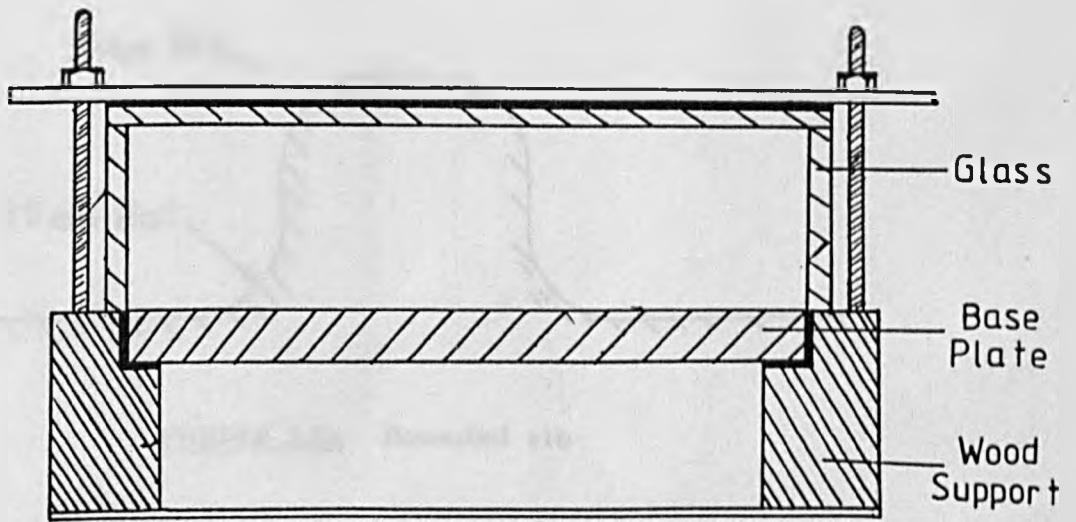


**FIG.3.4. CROSS SECTION THROUGH WORKING SECTION**

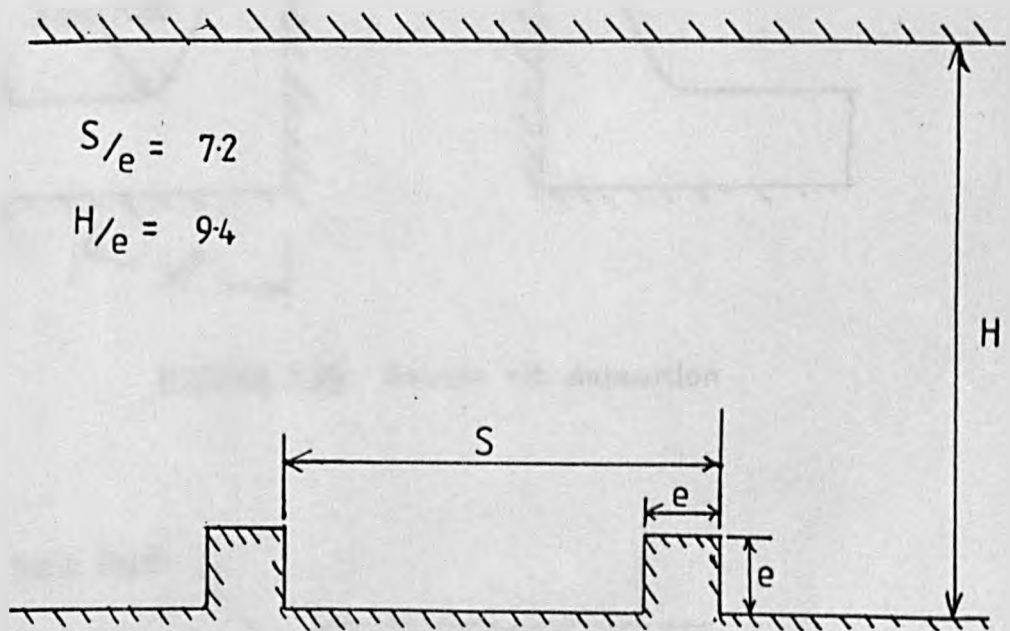


**FIG.3.5. SQUARE RIB GEOMETRY STUDIED**

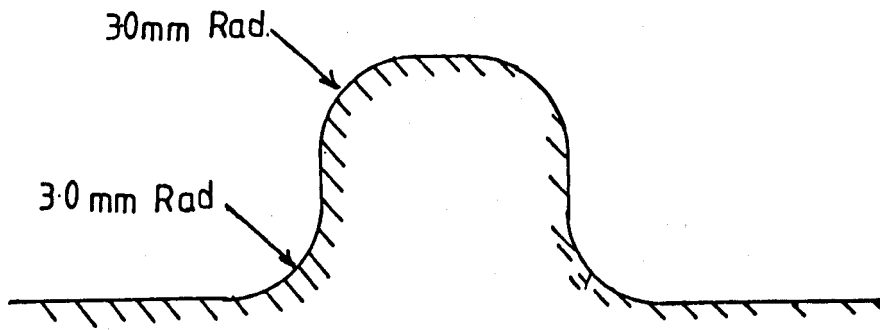


**FIGURE 3.6a** Rounded rib

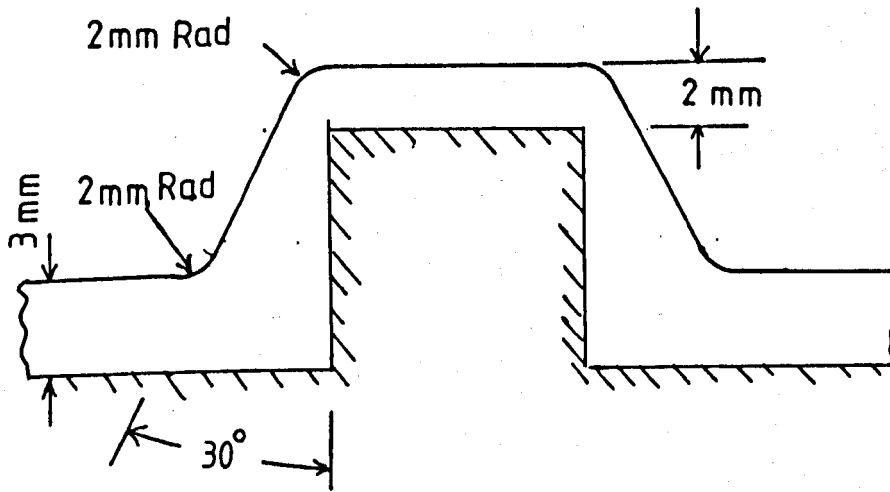


**FIGURE 3.6b** Square rib deposition

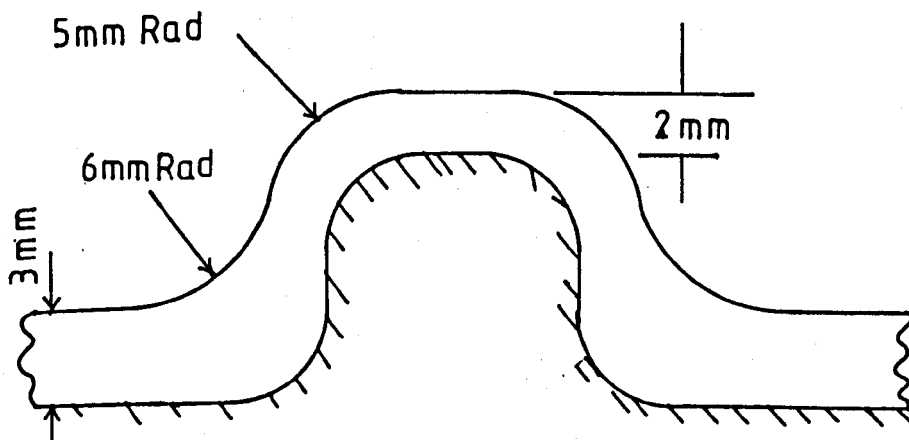


**FIGURE 3.6c** Rounded rib deposition

**FIGURE 3.6. ADDITIONAL GEOMETRY PROFILES**

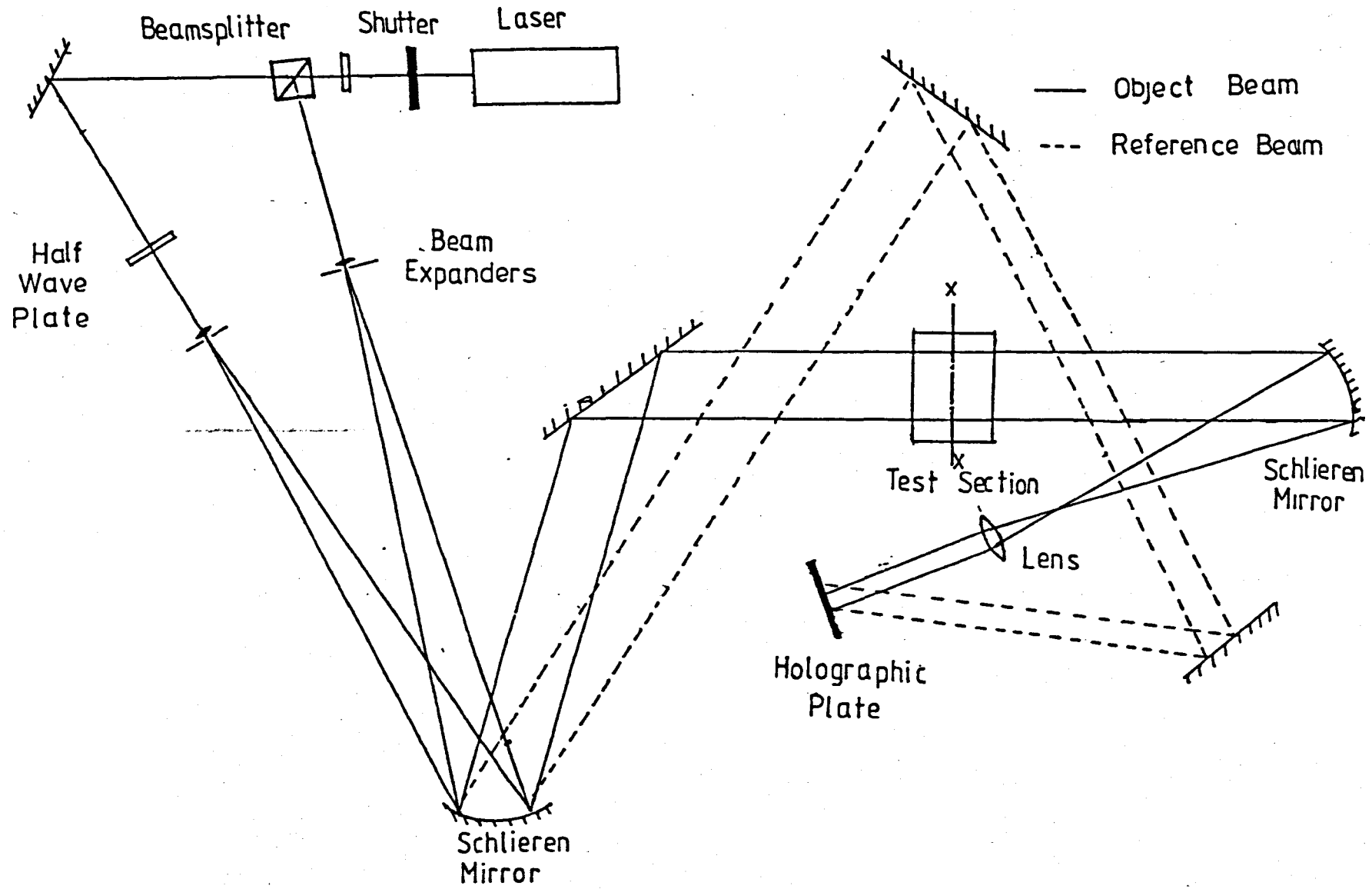


**FIG.3.7. SCHEMATIC DIAGRAM OF IMAGE-PLANE INTERFEROMETER**

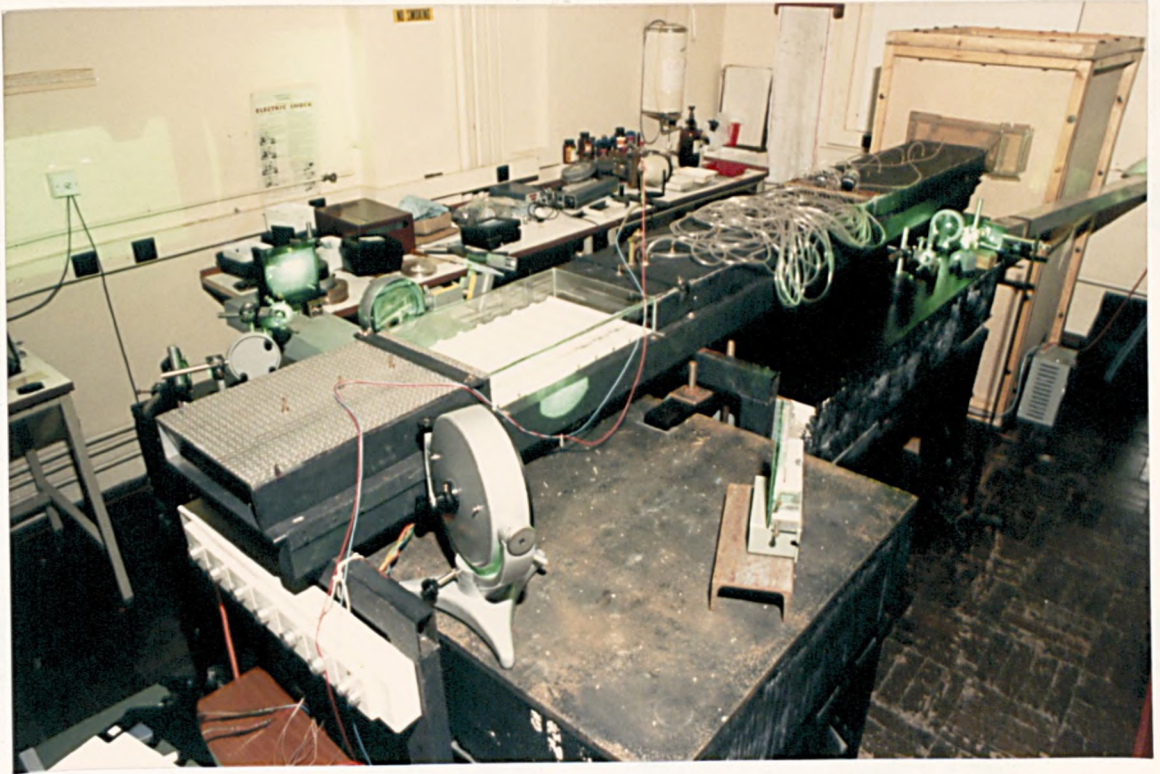


FIGURE 3.3(a)      NORMAL LIGHTING CONDITIONS

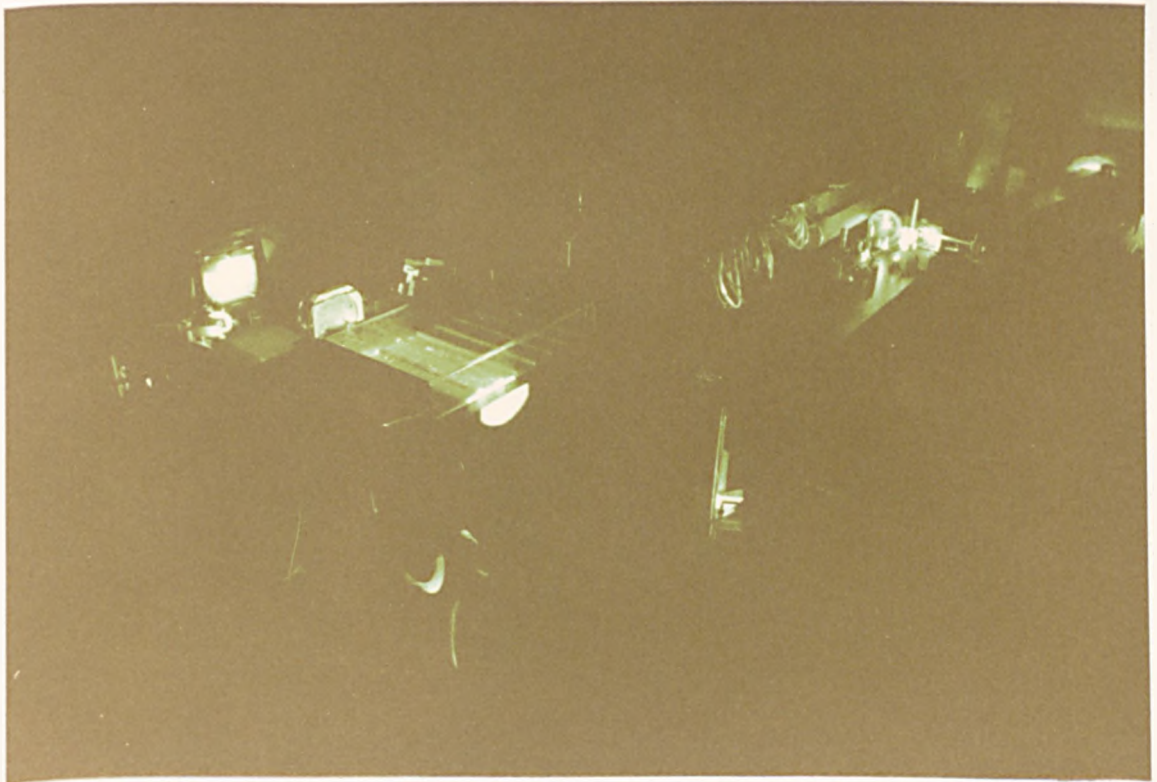


FIGURE 3.3(b)      DARKROOM CONDITIONS

FIGURE 3.3.      PHOTOGRAPHIC ILLUSTRATIONS OF TEST RIG

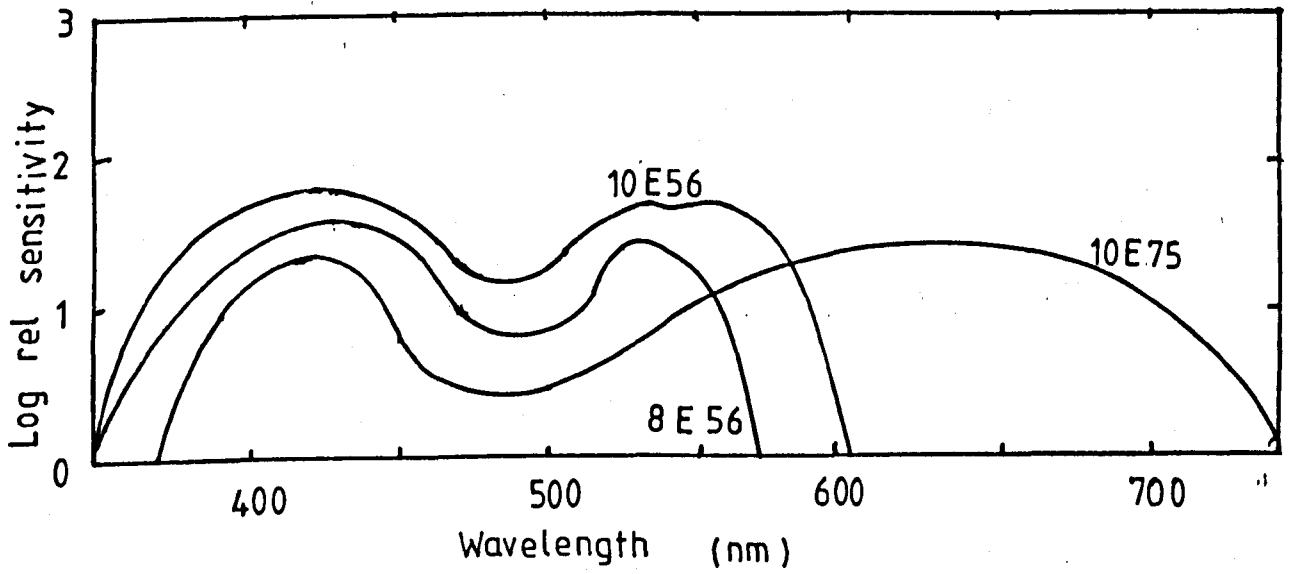


FIGURE 4.1. COLOUR SENSITIVITY FOR HOLOGRAPHIC PLATES

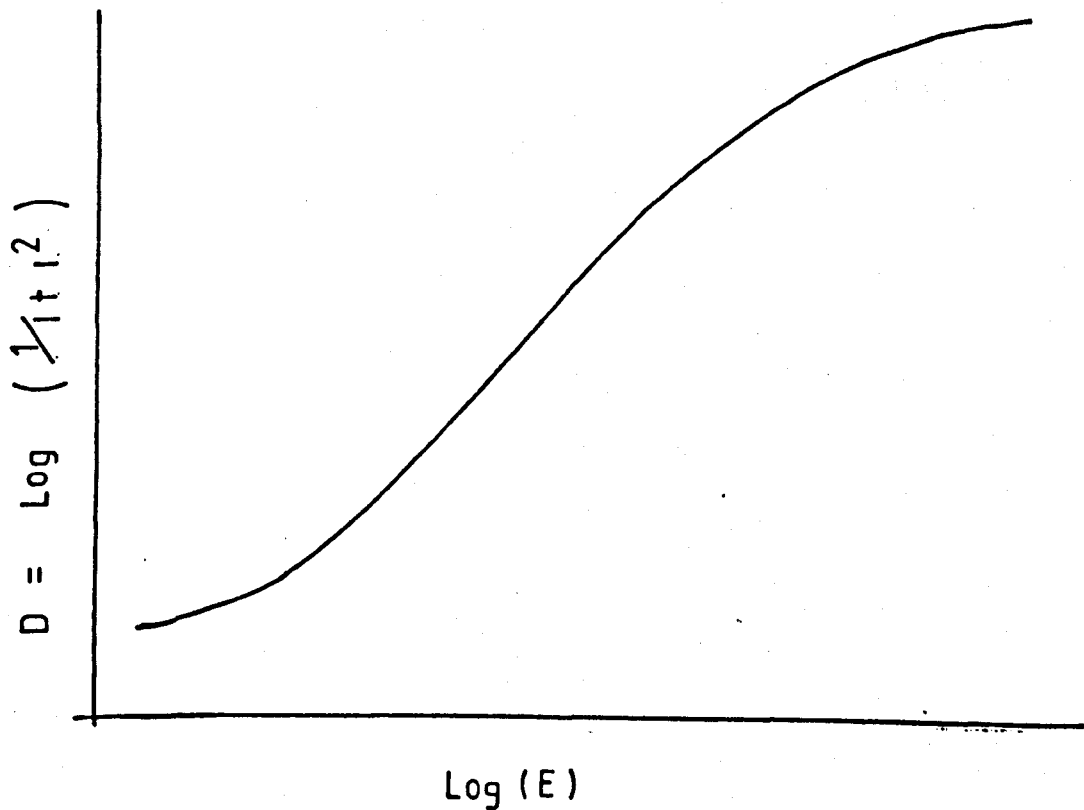
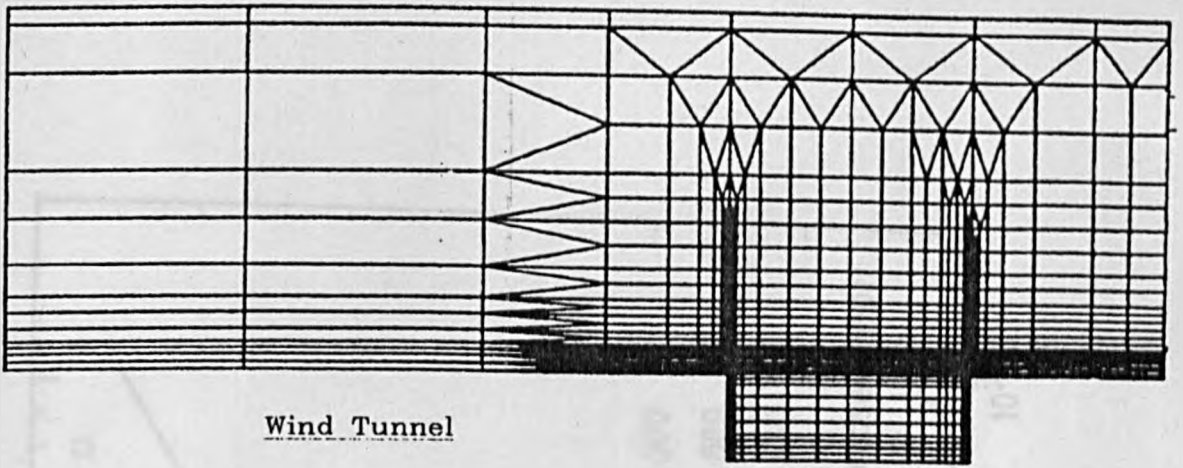
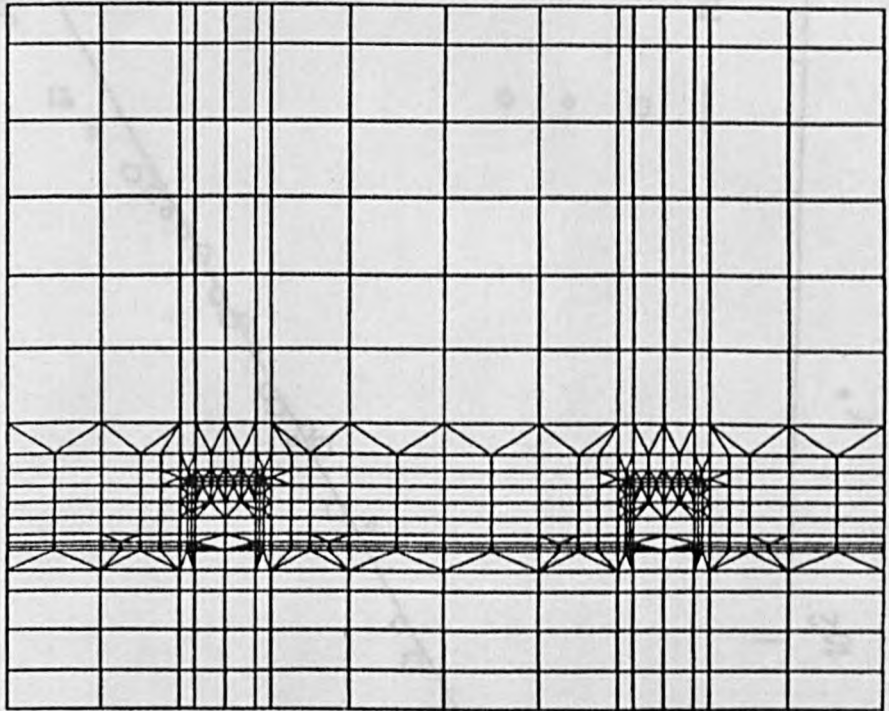


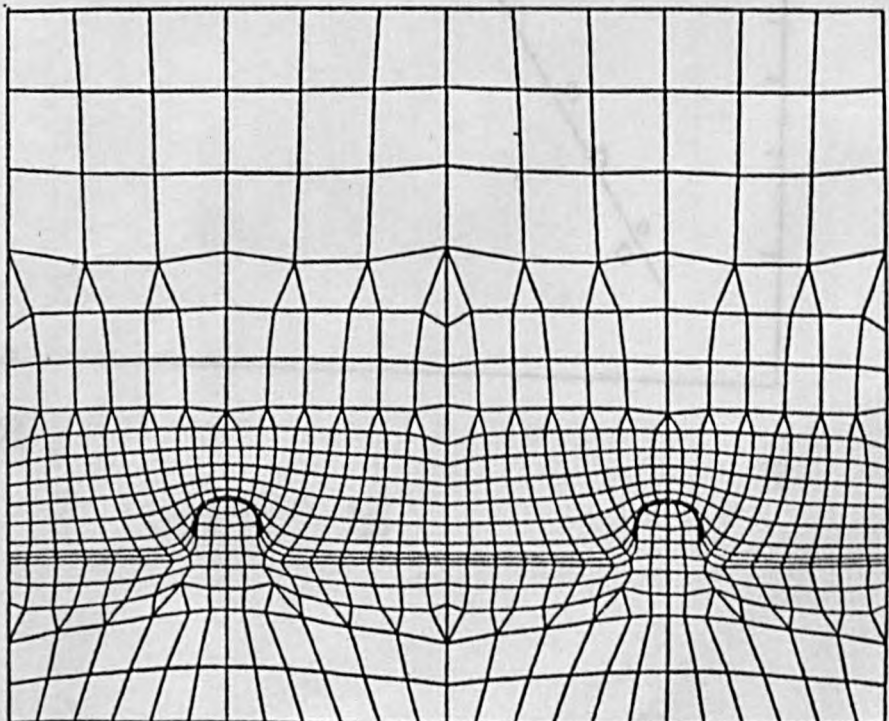
FIGURE 4.2. HURTER-DRIFFIELD CURVE



Wind Tunnel



Square rib



Rounded rib

**FIGURE 5.1. MESHES USED TO GENERATE FEAT PREDICTIONS**

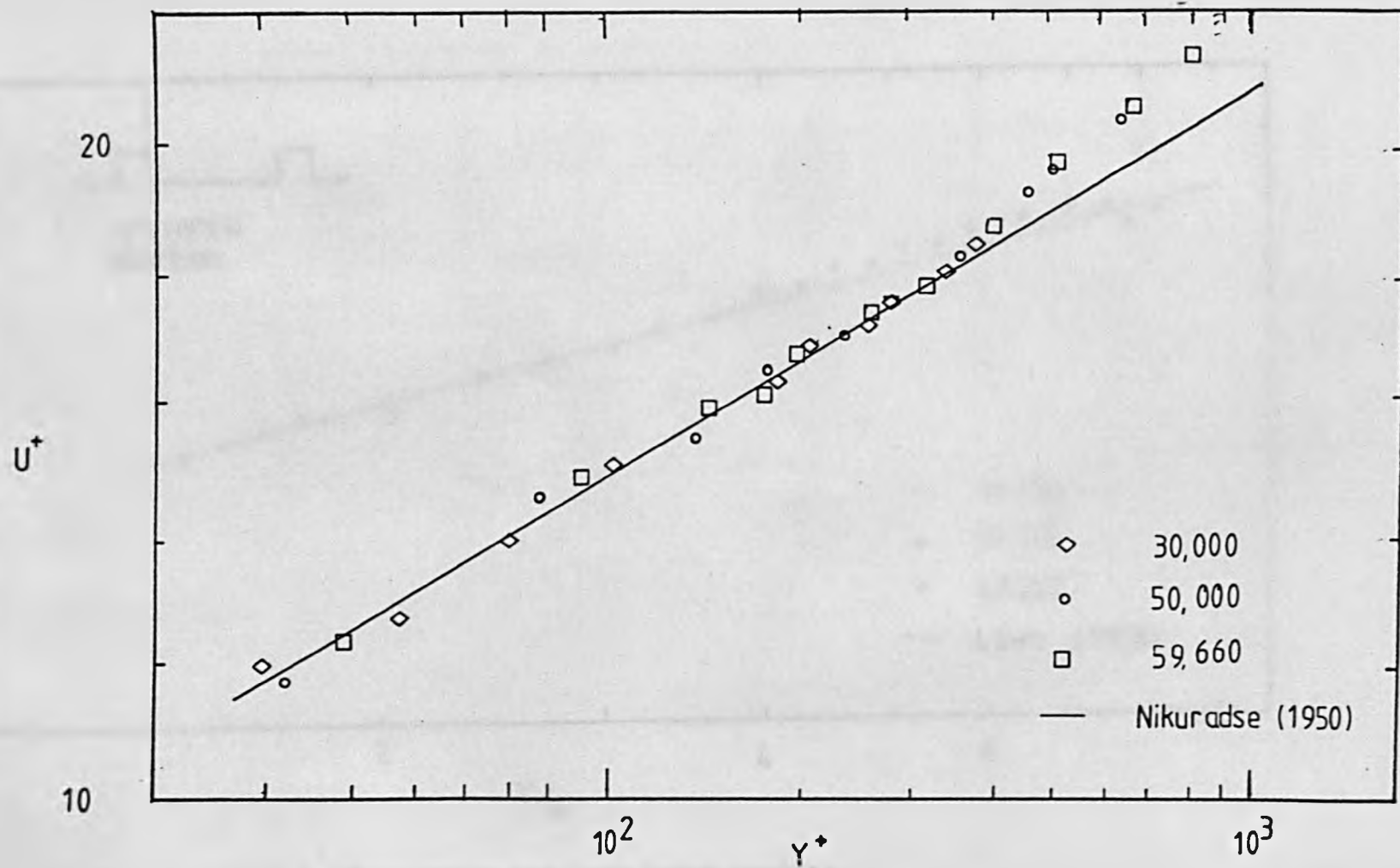


**FIGURE 6.1. NON-DIMENSIONAL VELOCITY PROFILE**

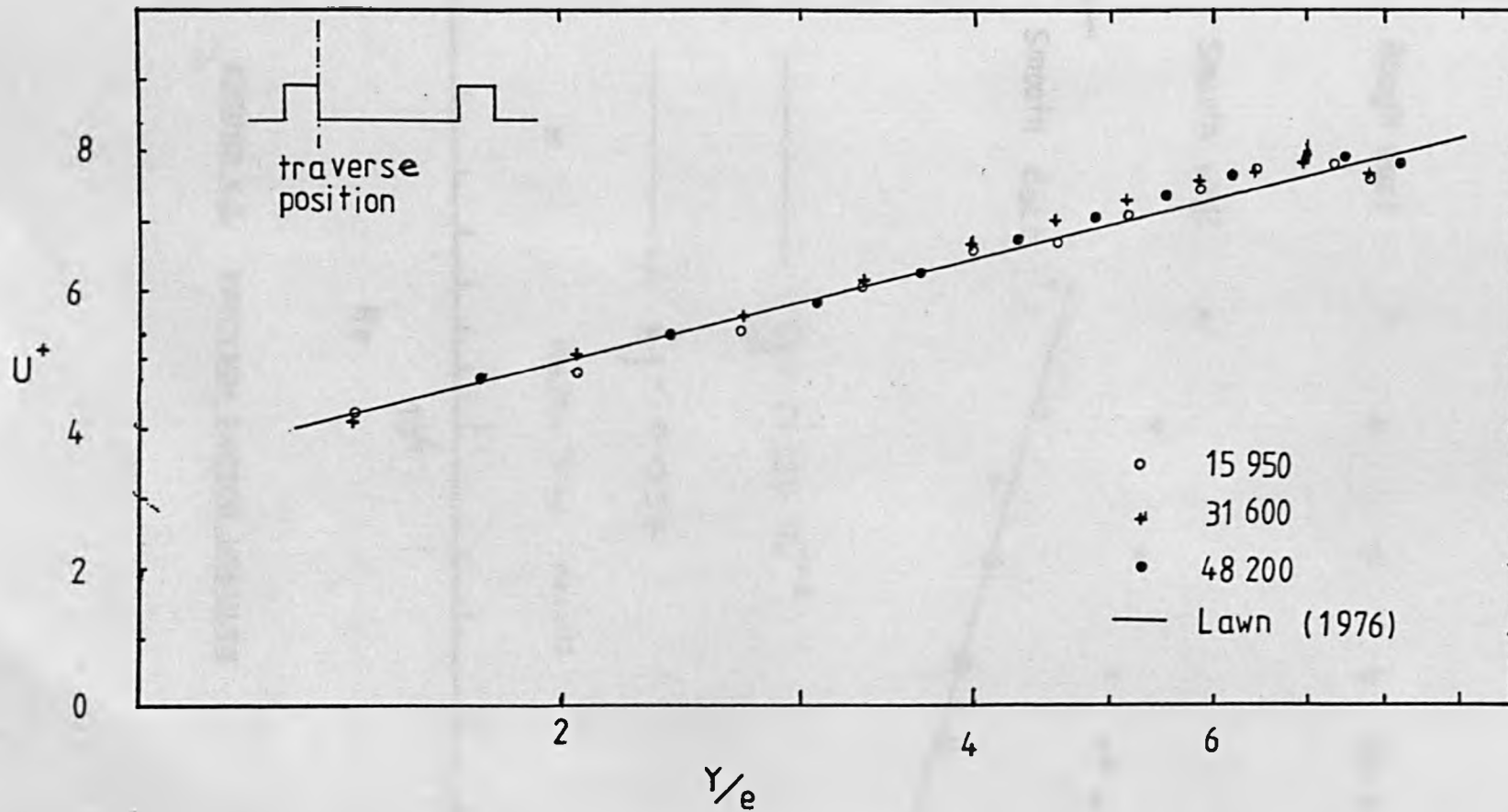


**FIGURE 6.2. ROUGH WALL VELOCITY PROFILE**

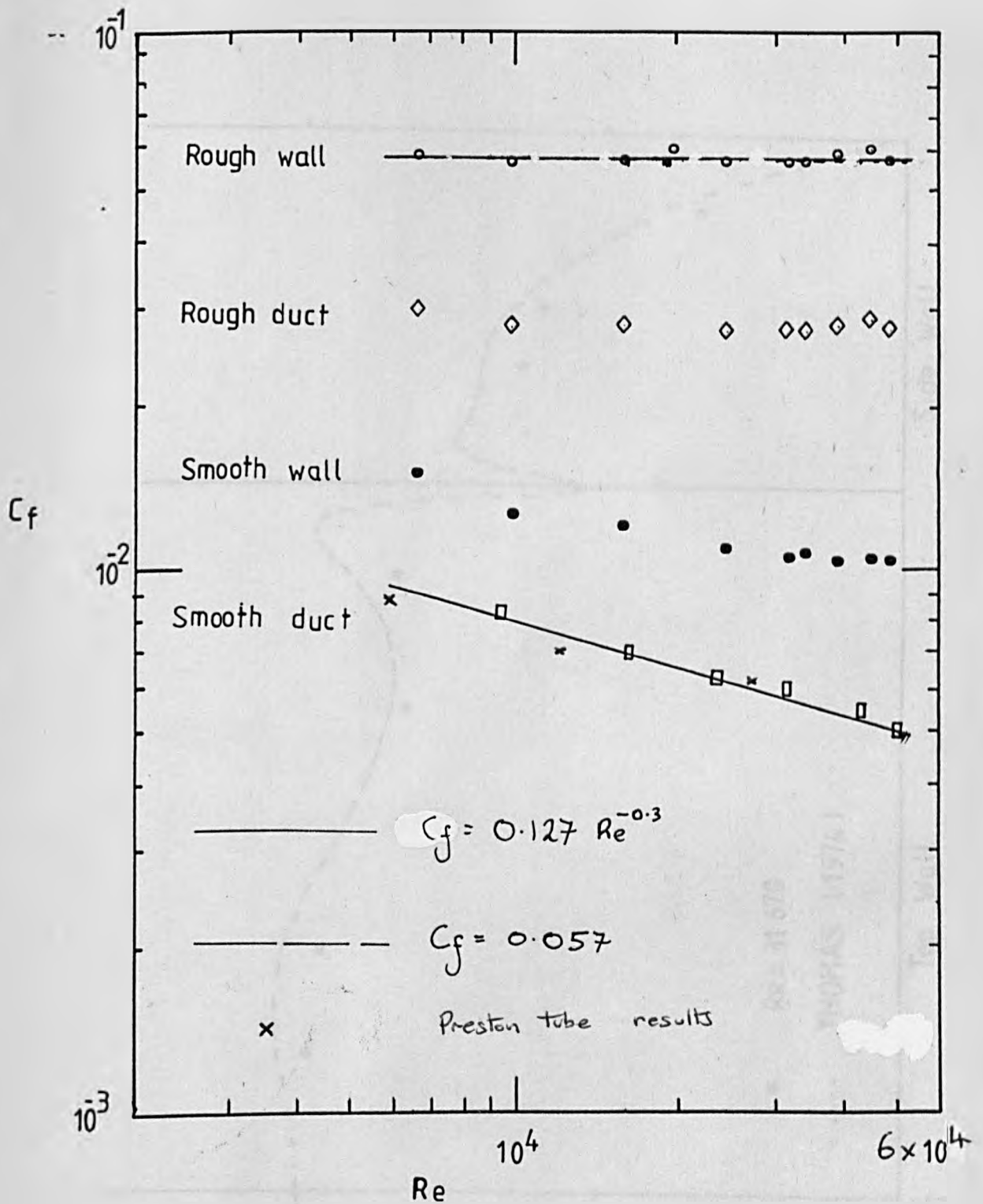


**FIGURE 6.3. FRICTION FACTOR RESULTS**

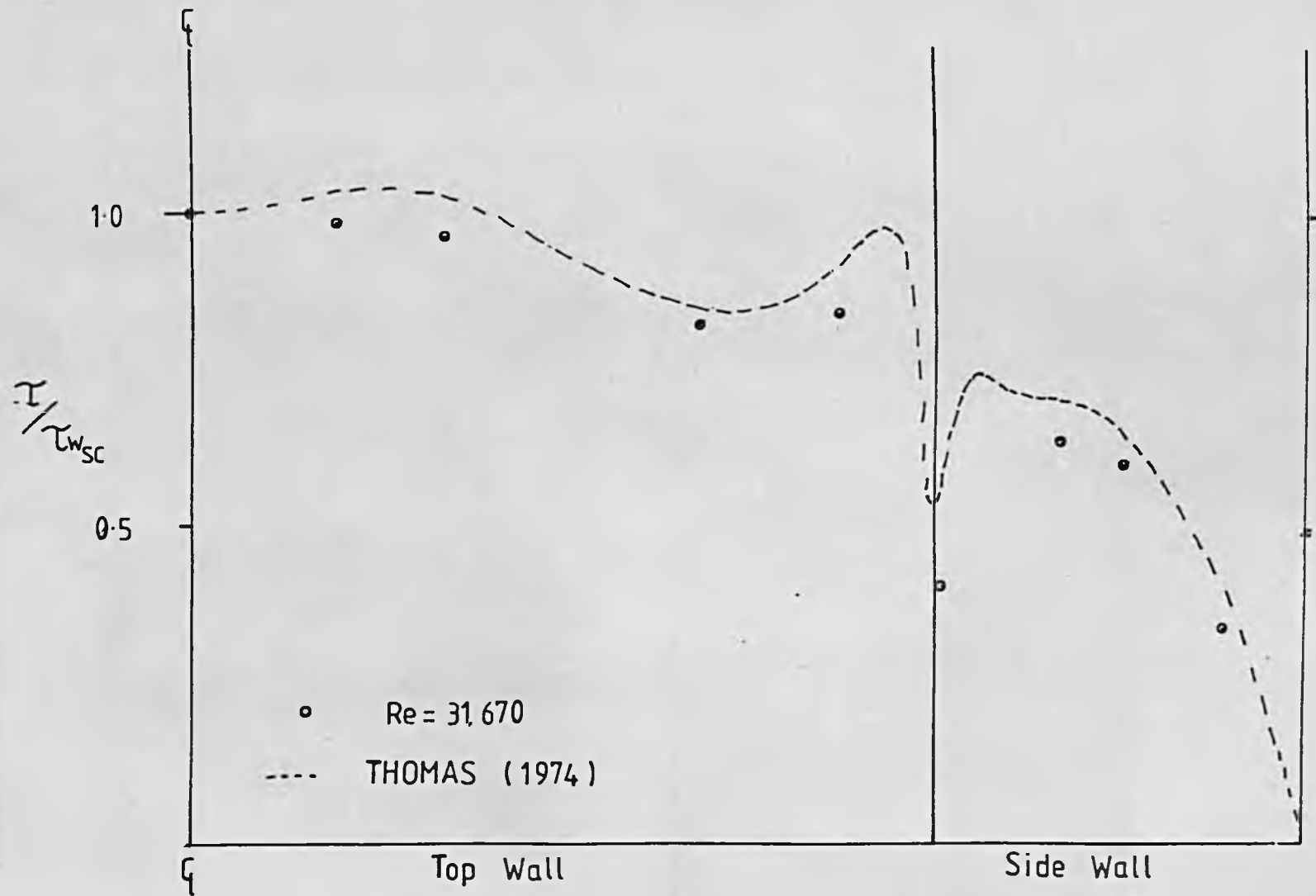


**FIGURE 6.4. SHEAR STRESS MEASUREMENTS AROUND THE SMOOTH WALLS**

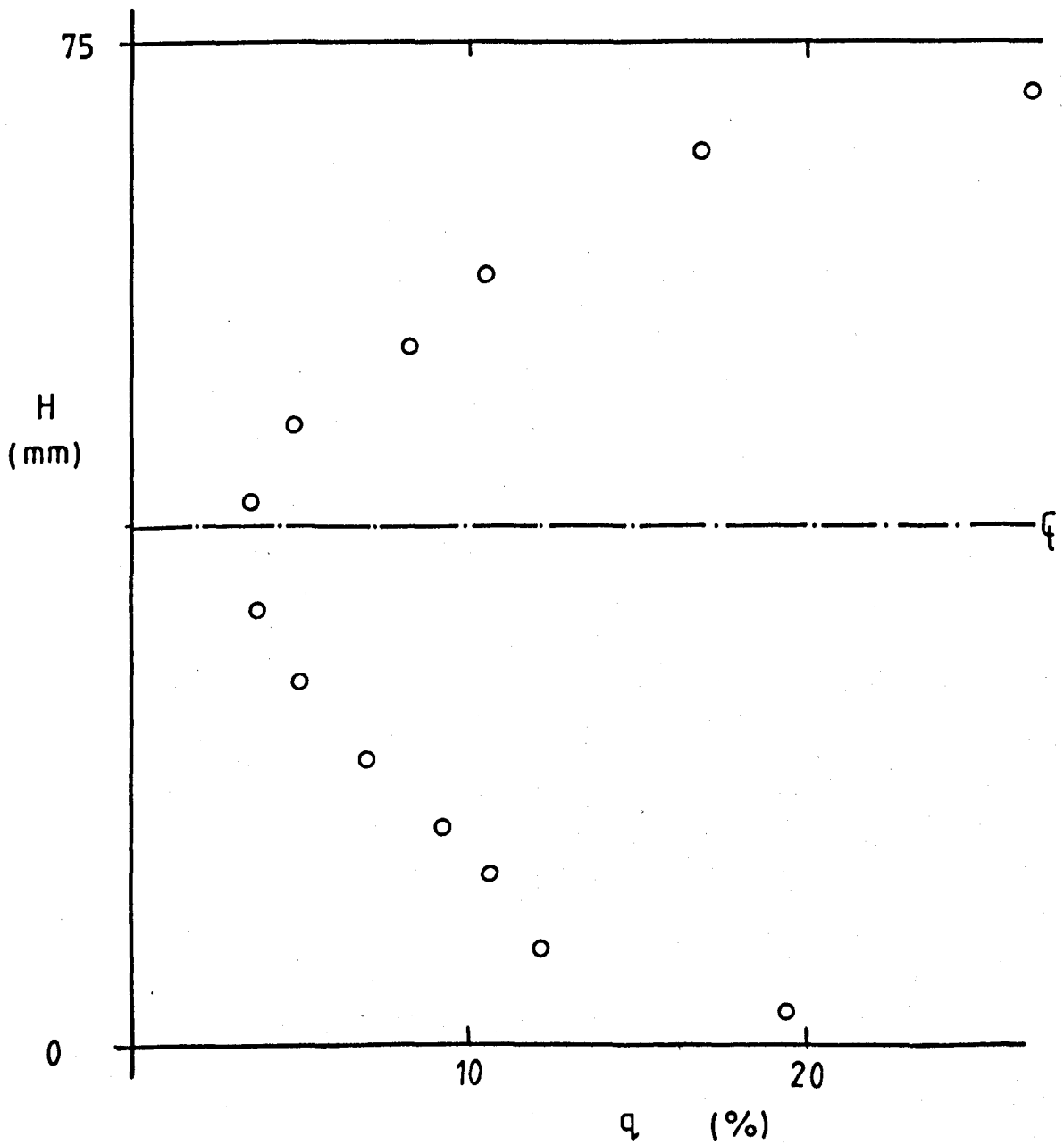


**FIGURE 6.5. TURBULENCE LEVELS AT INLET ( $Re = 12,820$ )**

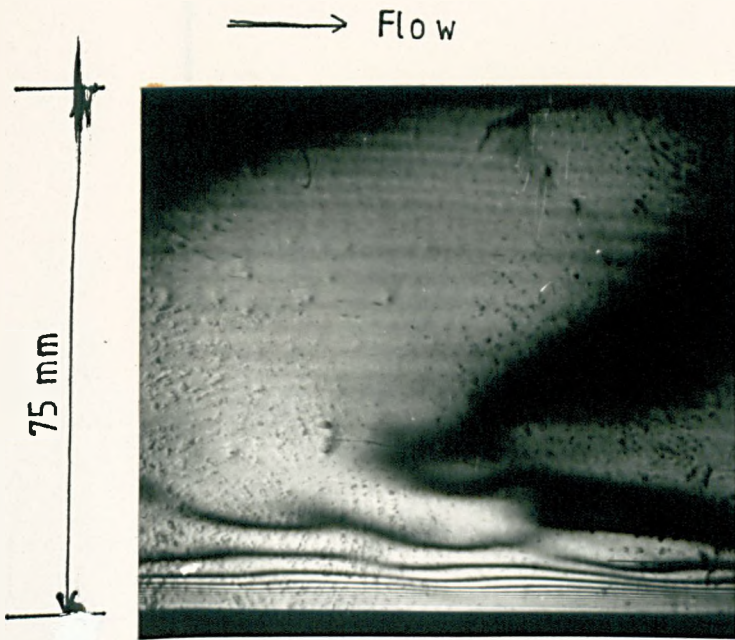


FIG.6.6(a) Re = 9800

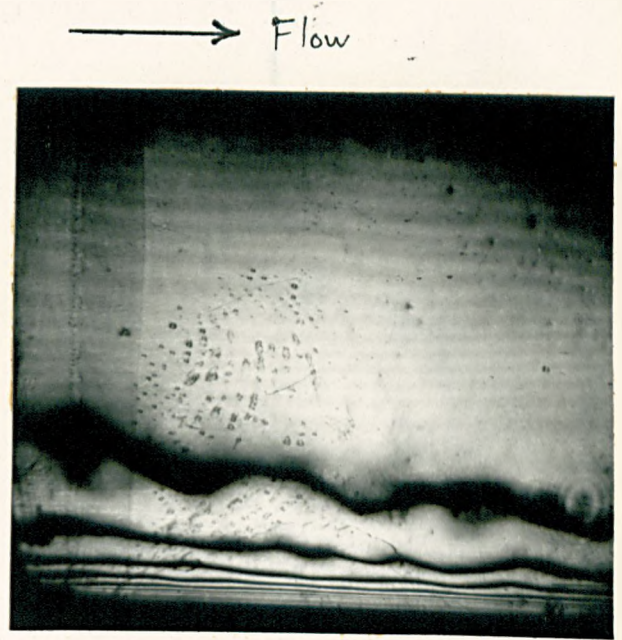


FIG.6.6(b) Re = 22000

FIG.6.6. INTERFEROGRAMS OF SMOOTH WALL

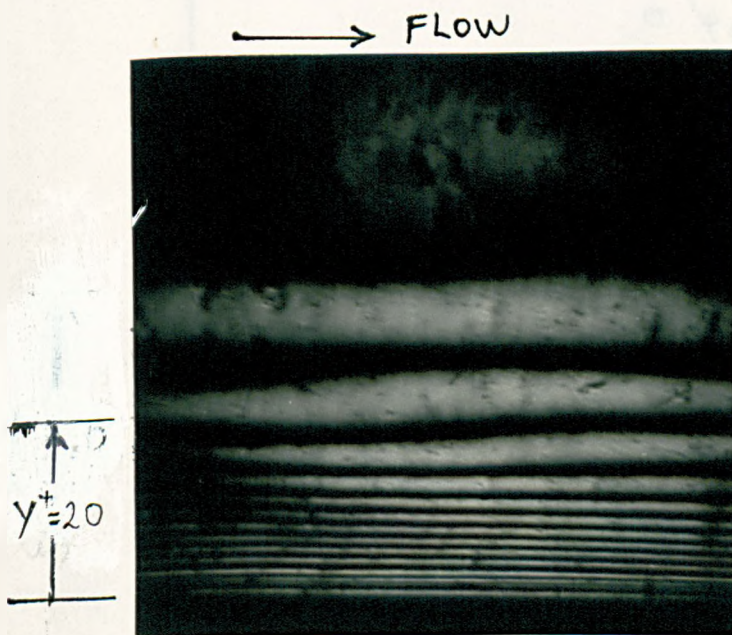


FIG.6.7(a) Re = 9800

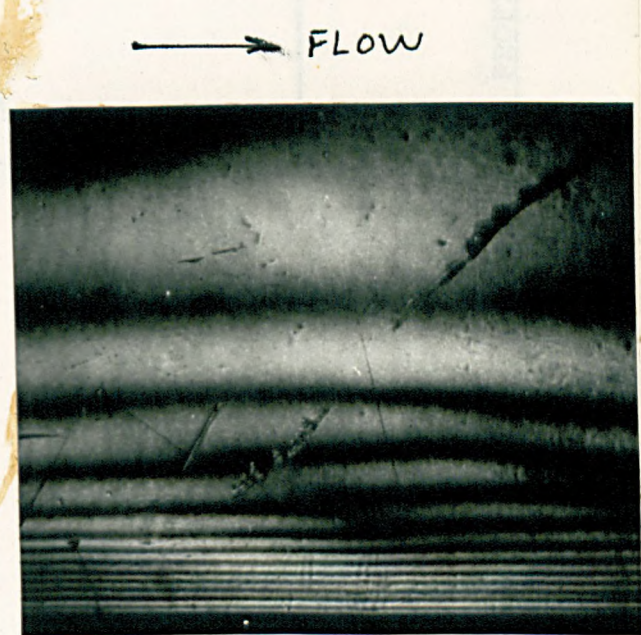


FIG.6.7(b) Re = 22,000

FIG.6.7. NEAR WALL ENLARGEMENT

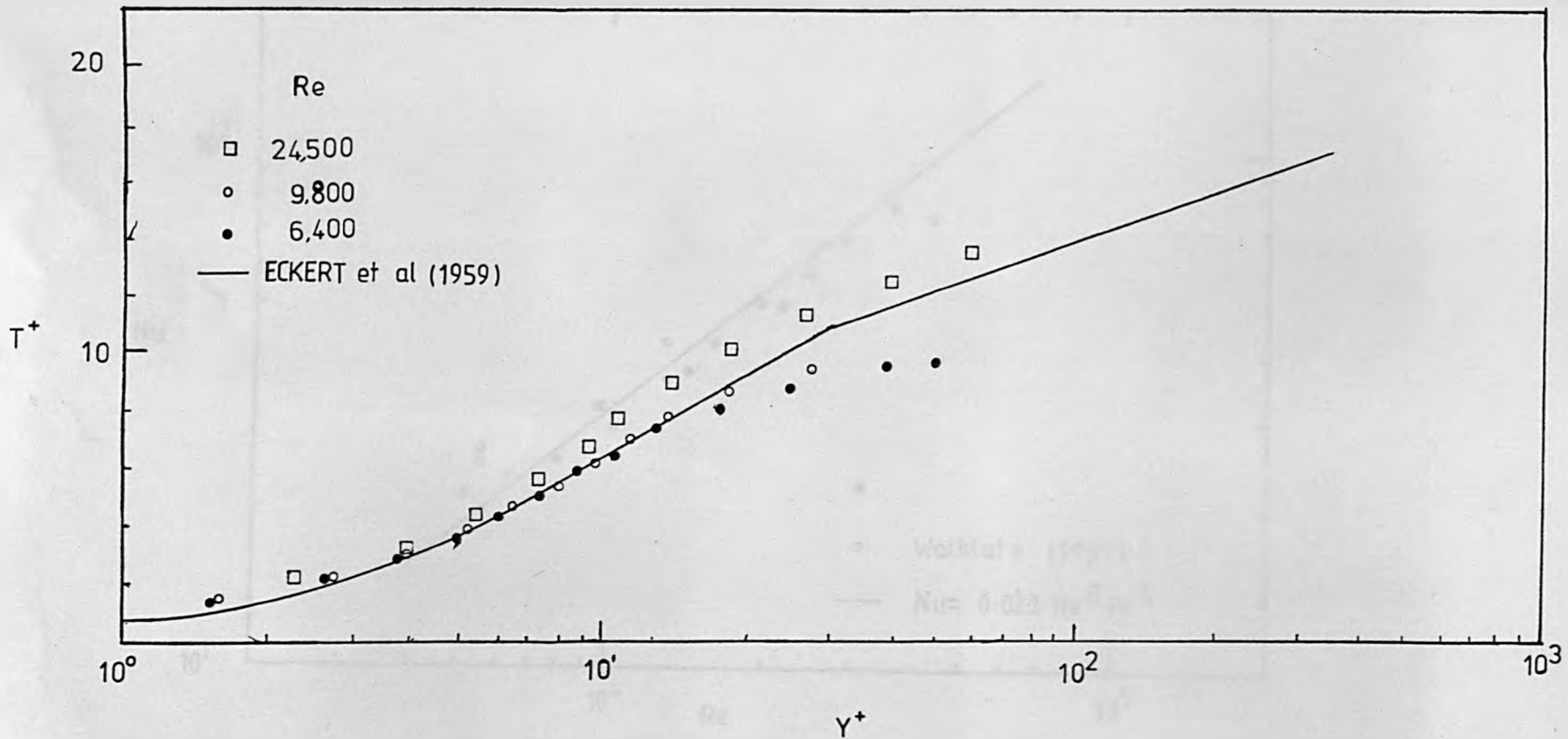
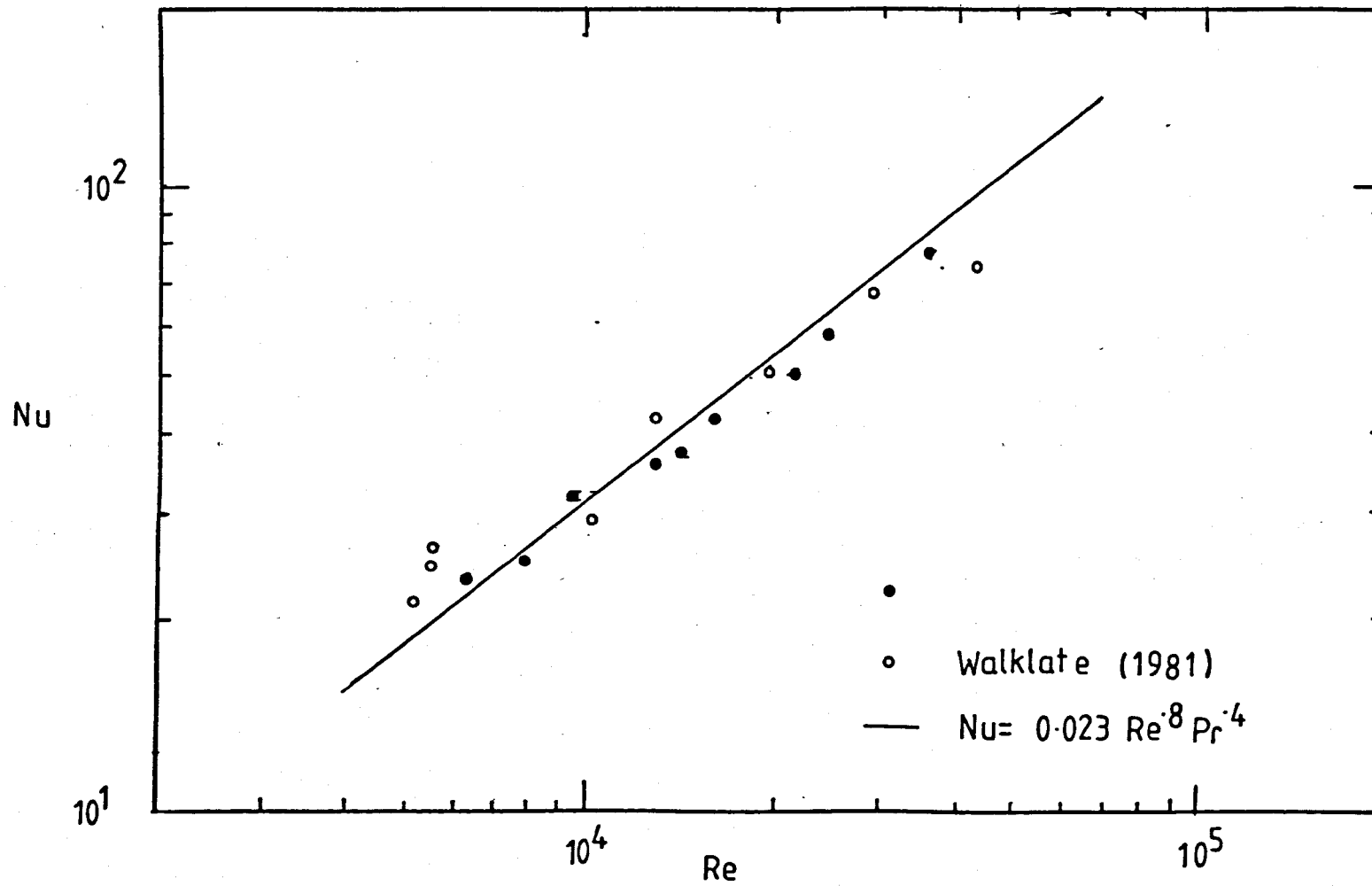
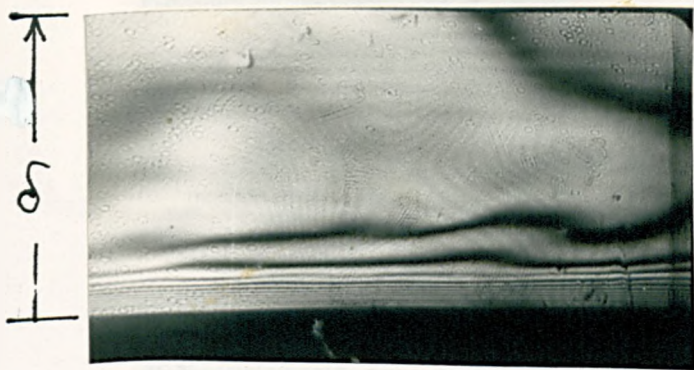


FIGURE 6.8. TEMPERATURE PROFILES FOR A SMOOTH DUCT



**FIGURE 6.9. HEAT TRANSFER RESULTS FOR SMOOTH SURFACES**

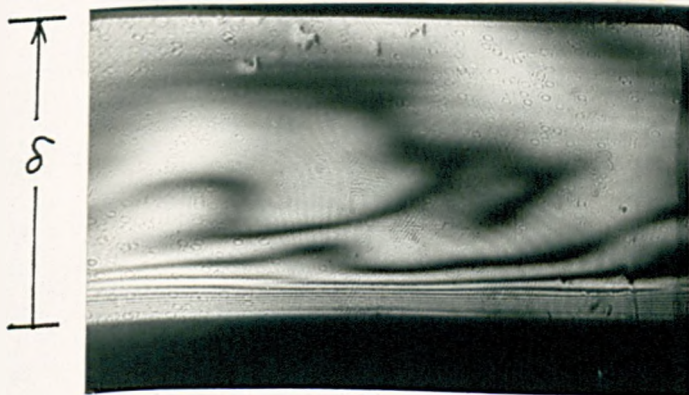
→ Flow



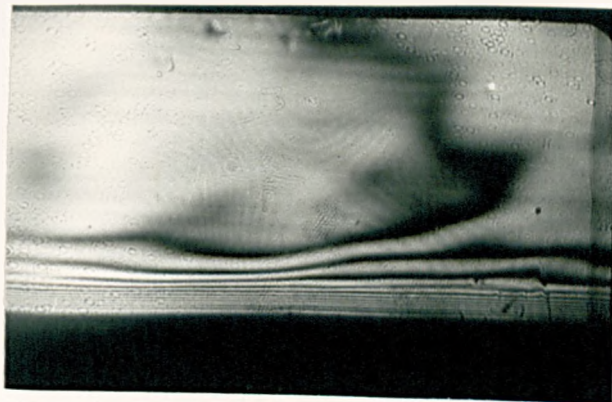
(0 s)



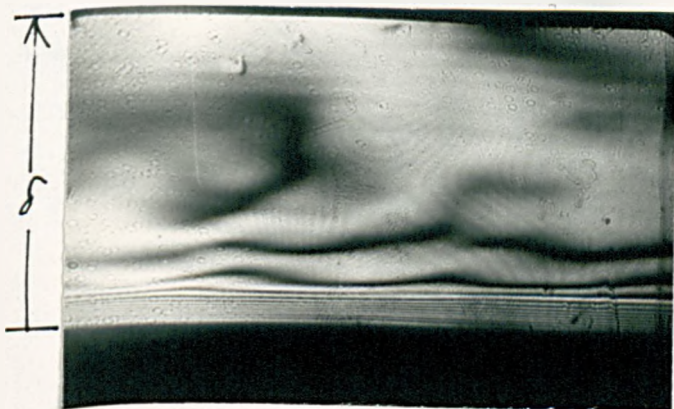
(0.4 s)



(0.8 s)



(1.2 s)



(1.6 s)



(2.0 s)

FIG.6.10. REAL-TIME IMAGE OF SMOOTH WALL

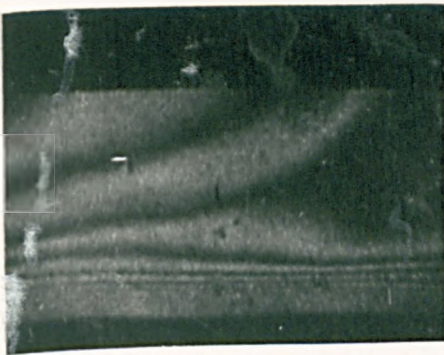


Beginning

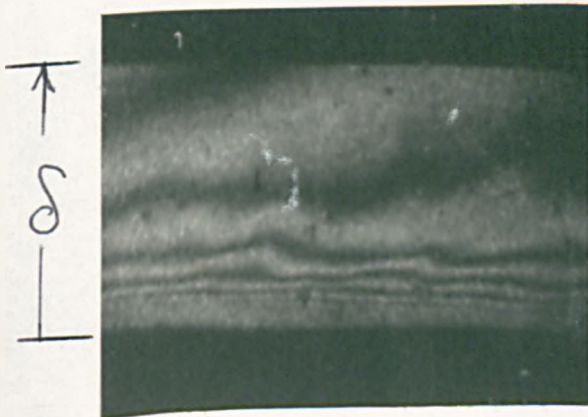


Middle

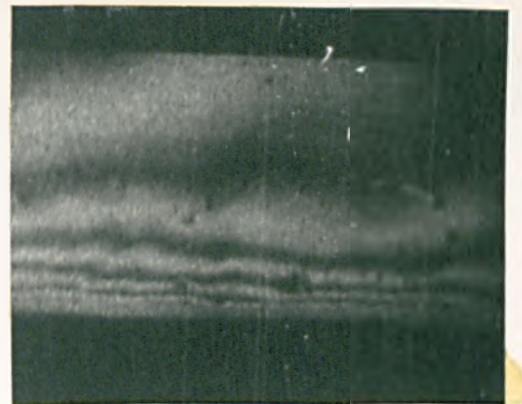
Re = 3755



End



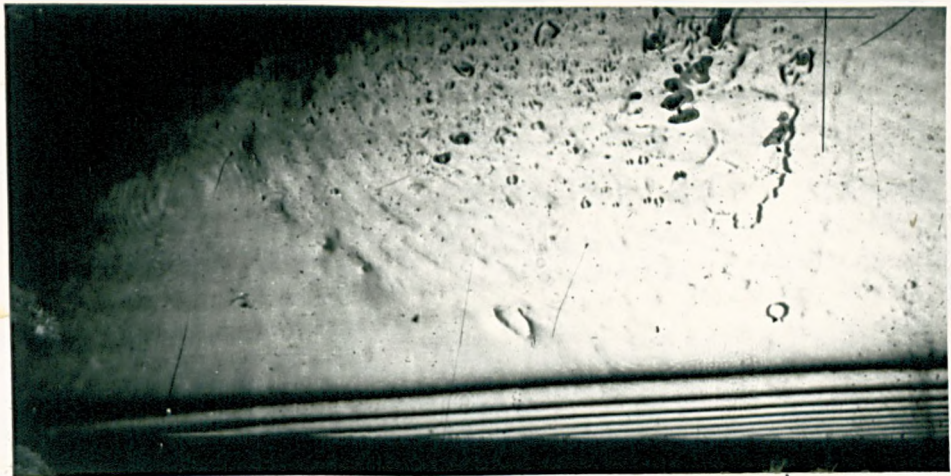
Re = 11990



Re 30400

FIG.6.II. HIGH SPEED FILM ILLUSTRATING STRUCTURE

→ Flow



0 100mm  
FIG.6.12. DEVELOPING FLOW REGION (Re = 9800)

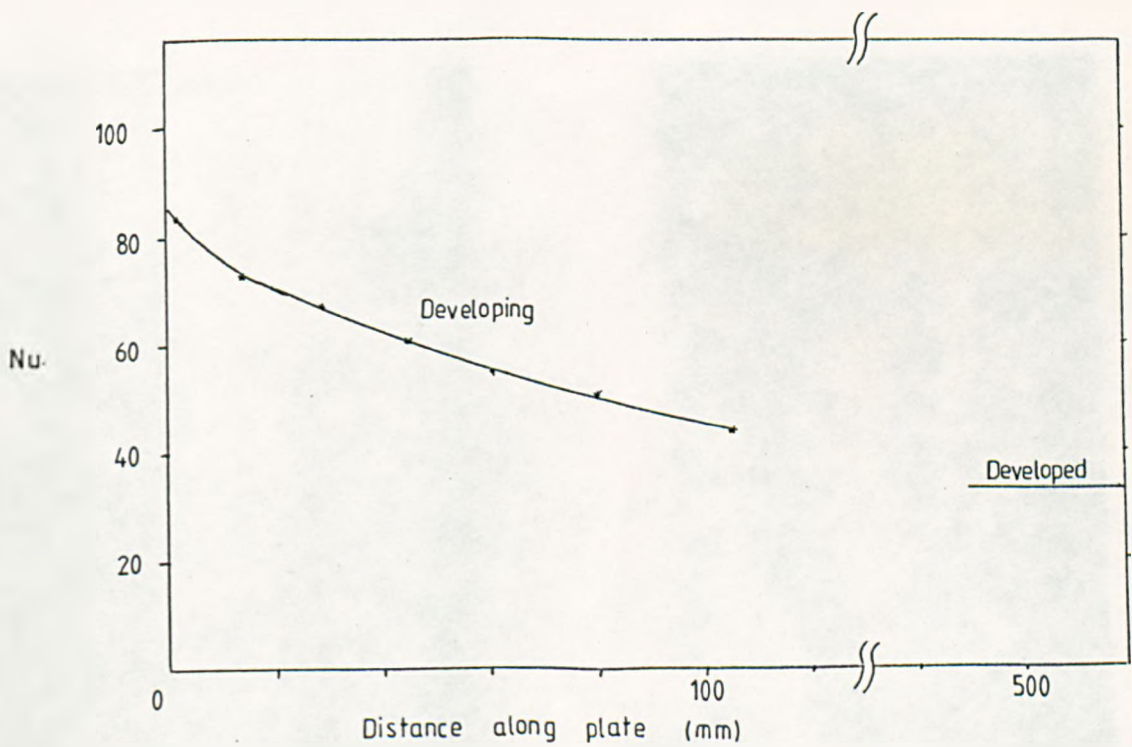
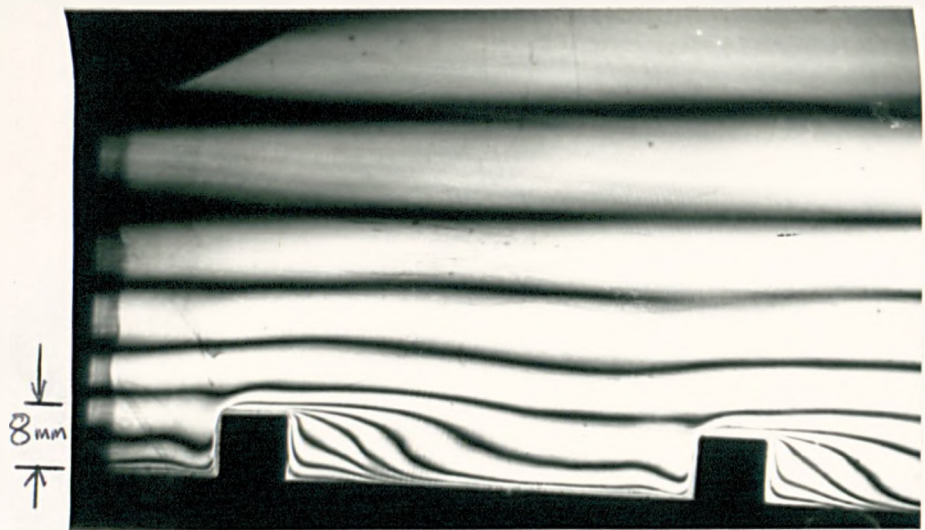


FIGURE 6.13. NUSSELT NUMBER DISTRIBUTION FOR DEVELOPING FLOW

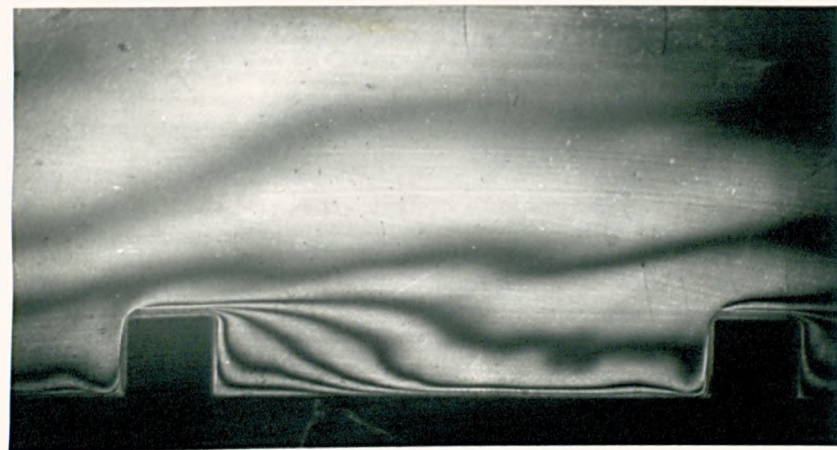
Flow →



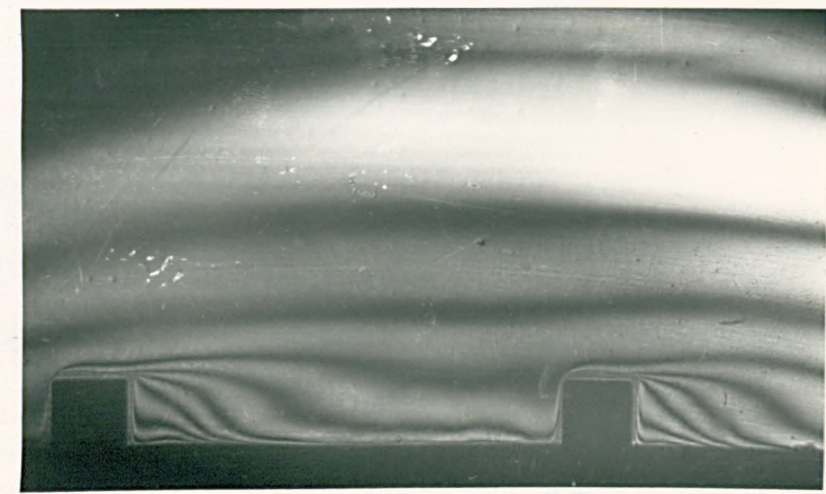
Re = 10800



Re = 15500



Re = 20900



Re = 29870

FIGURE 6.14. DOUBLE EXPOSURE IMAGES OF SQUARE RIBBED GEOMETRY

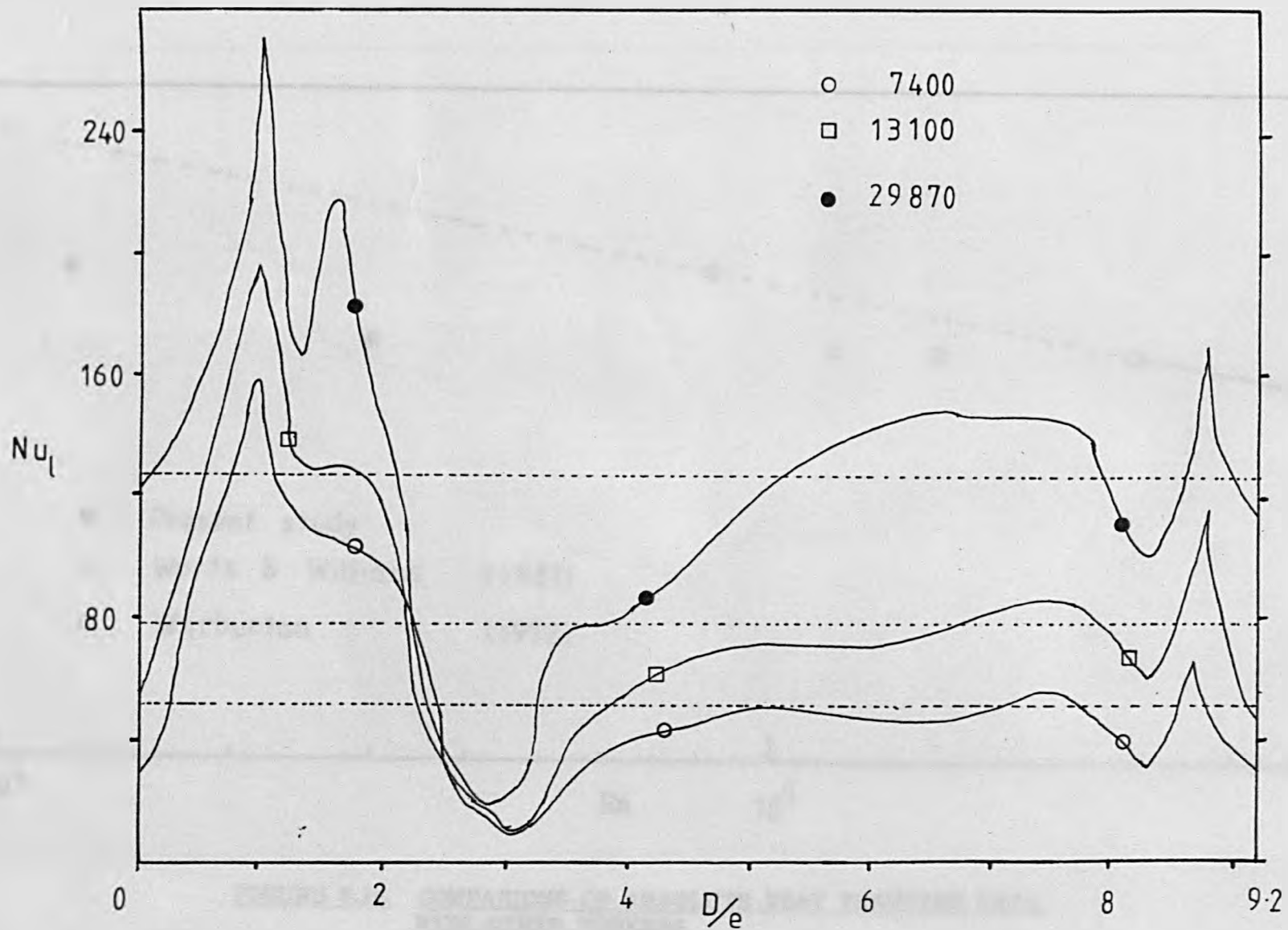


FIGURE 6.15. ABSOLUTE NUSSELT NUMBERS FOR SQUARE RIBBED GEOMETRY

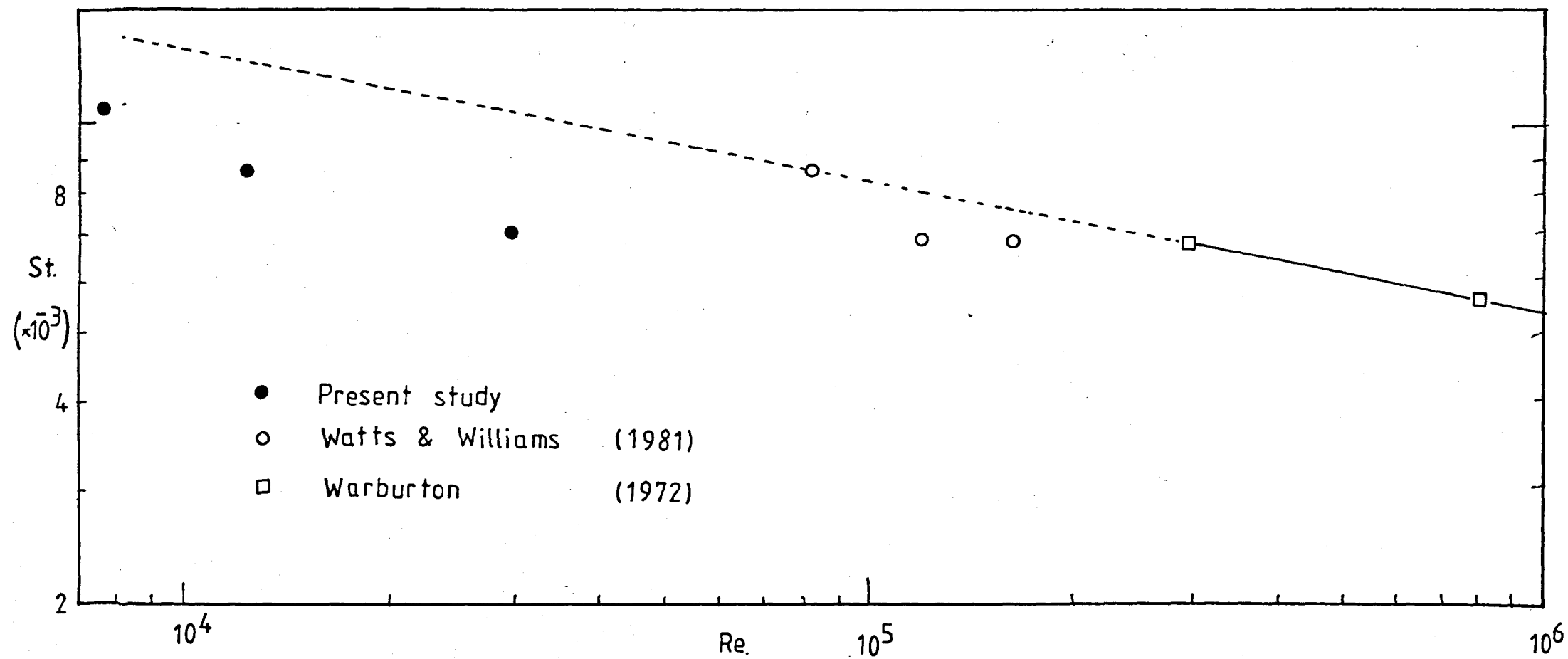


FIGURE 6.16. COMPARISONS OF ABSOLUTE HEAT TRANSFER DATA WITH OTHER WORKERS

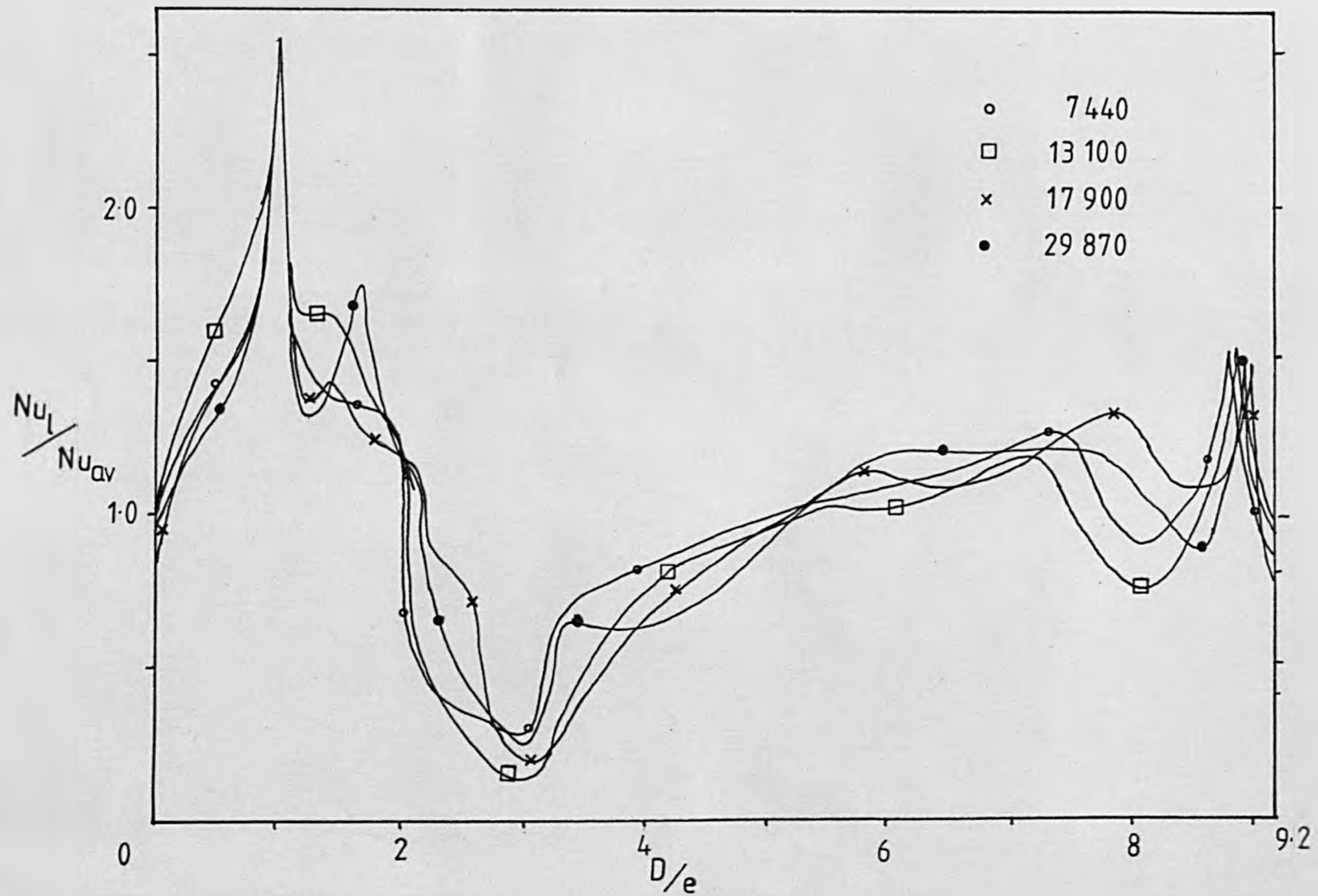
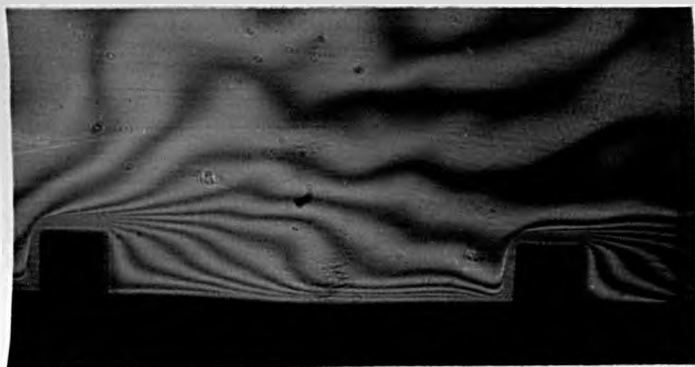
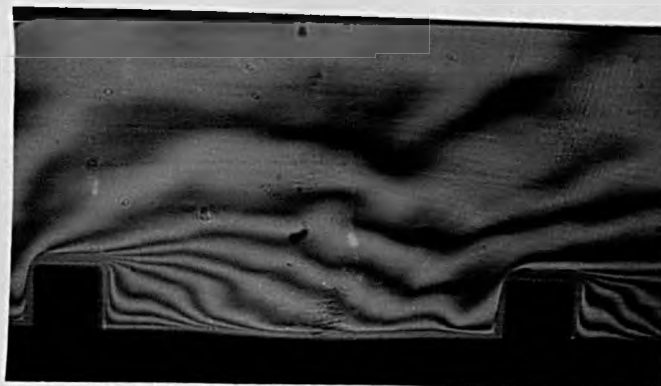


FIGURE 6.17. NUSSELT NUMBER DISTRIBUTION FOR SQUARE RIB

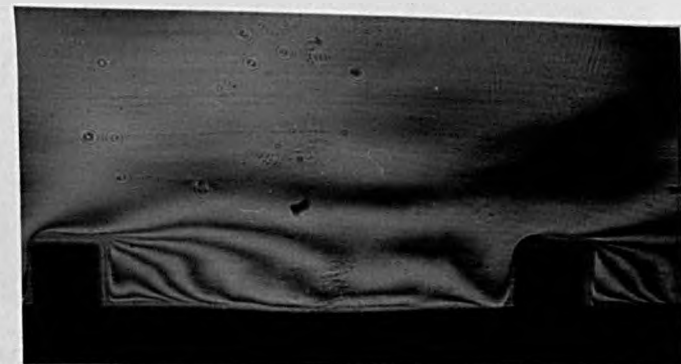
→ Flow



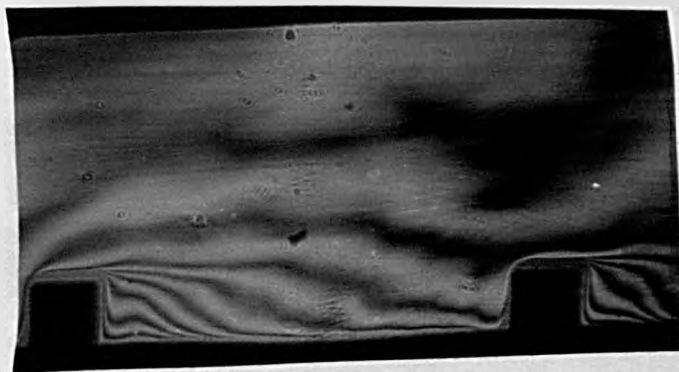
Re = 3540



Re = 9700



Re = 14200



Re = 20000



Re = 29700



Re = 40130

FIGURE 6.18. REAL TIME IMAGE OF SQUARE RIB

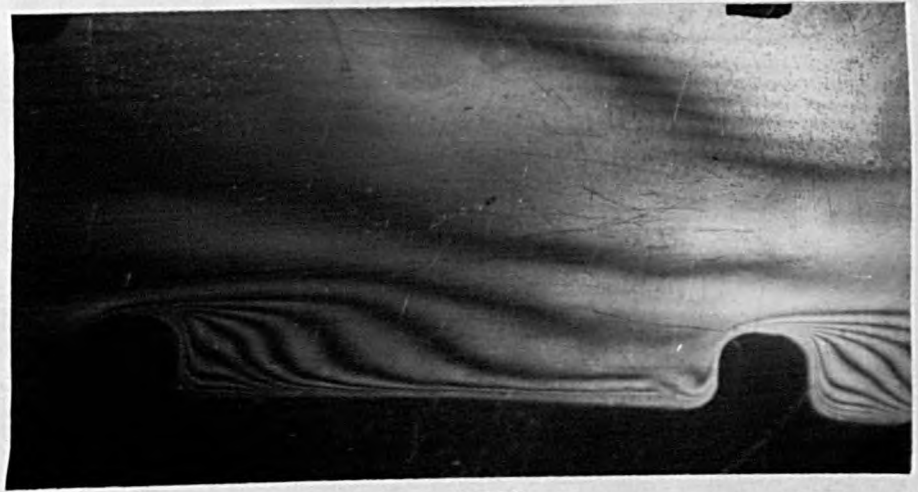
→ Flow



Re = 7330



Re = 9160



Re = 19530



Re = 53900

**FIGURE 6.19** DOUBLE EXPOSURE IMAGES OF ROUNDED RIB SURFACE

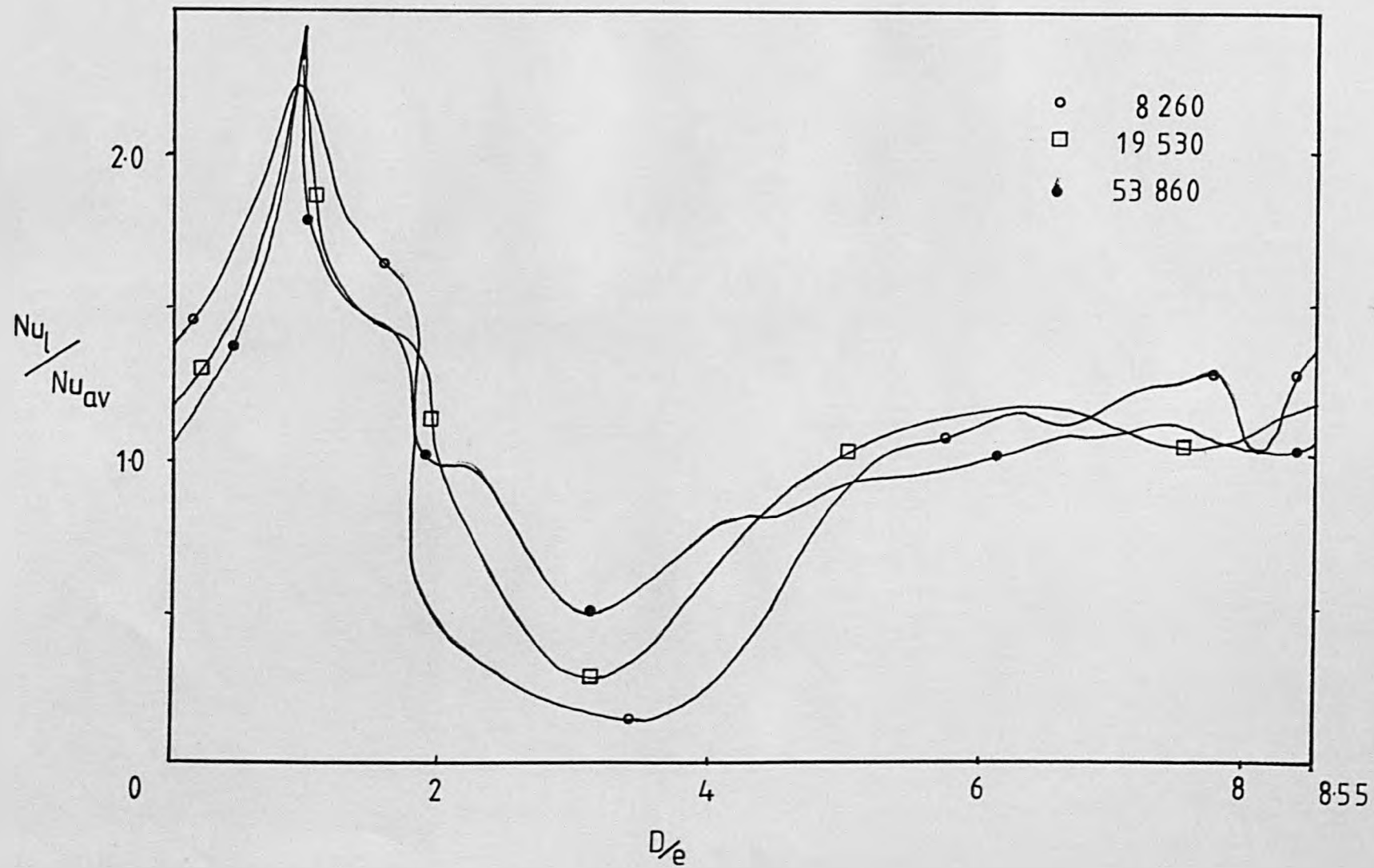
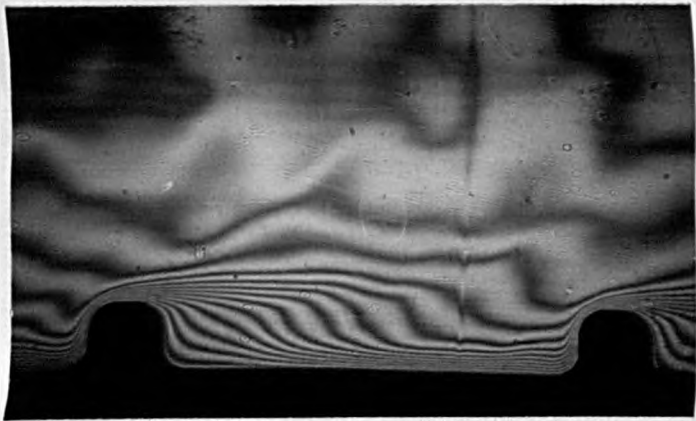
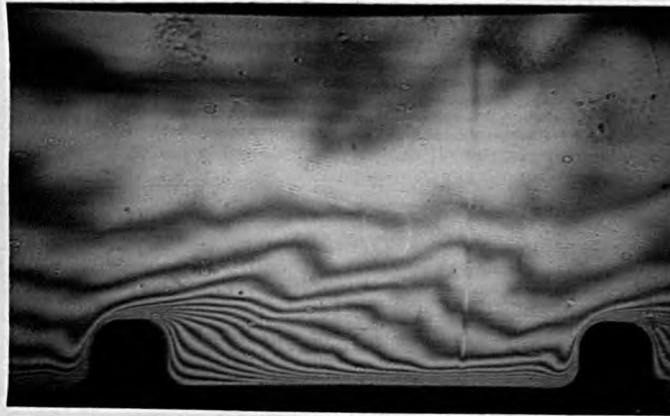


FIGURE 6.20. NUSSELT NUMBER DISTRIBUTION FOR ROUNDED RIB

←—————→ Flow



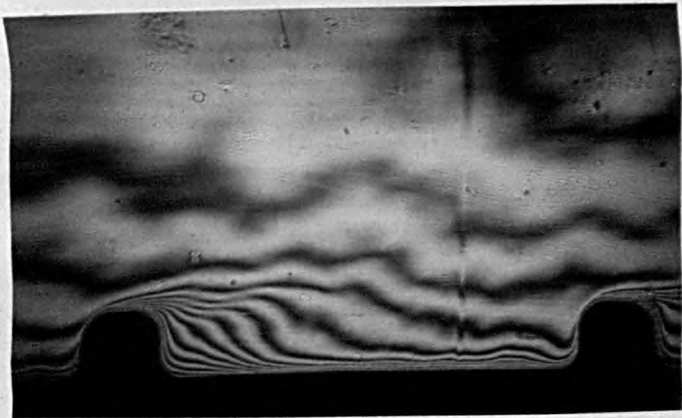
Re = 4130



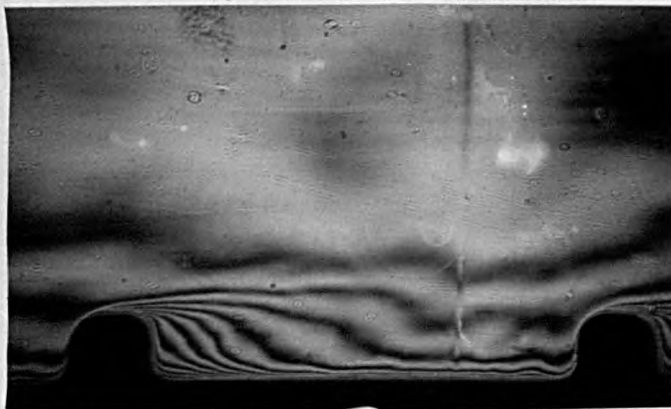
Re = 7200



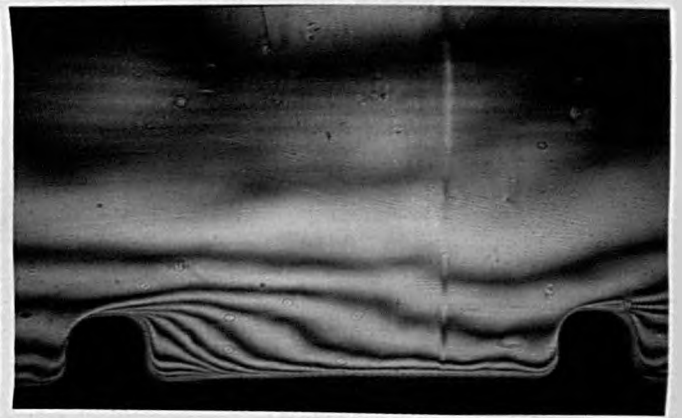
Re = 9820



Re = 18430



Re = 29,560



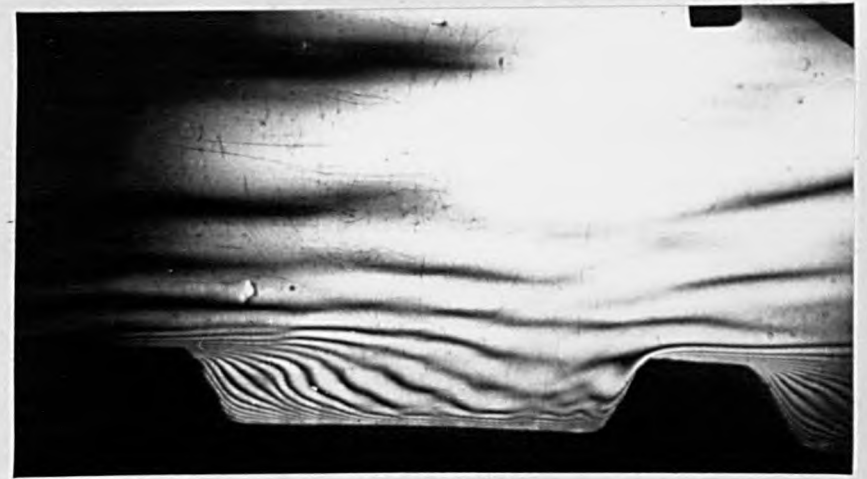
Re = 41250

FIGURE 6.21 REAL TIME IMAGES OF ROUNDED RIB

→ Flow



Re = 7440



Re = 15610



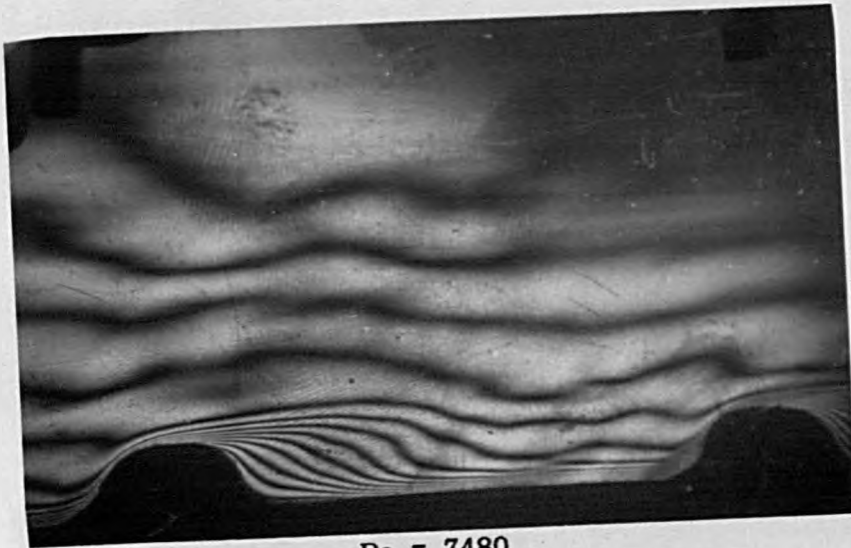
Re = 41250



Re = 50096

FIGURE 6.22 DOUBLE EXPOSURE IMAGES OF SQUARE RIB DEPOSITED SURFACE

→ Flow



Re = 7480



Re = 15500



Re = 20490



Re = 41660

FIGURE 6.23 DOUBLE EXPOSURE IMAGES OF ROUNDED RIB DEPOSITED SURFACE

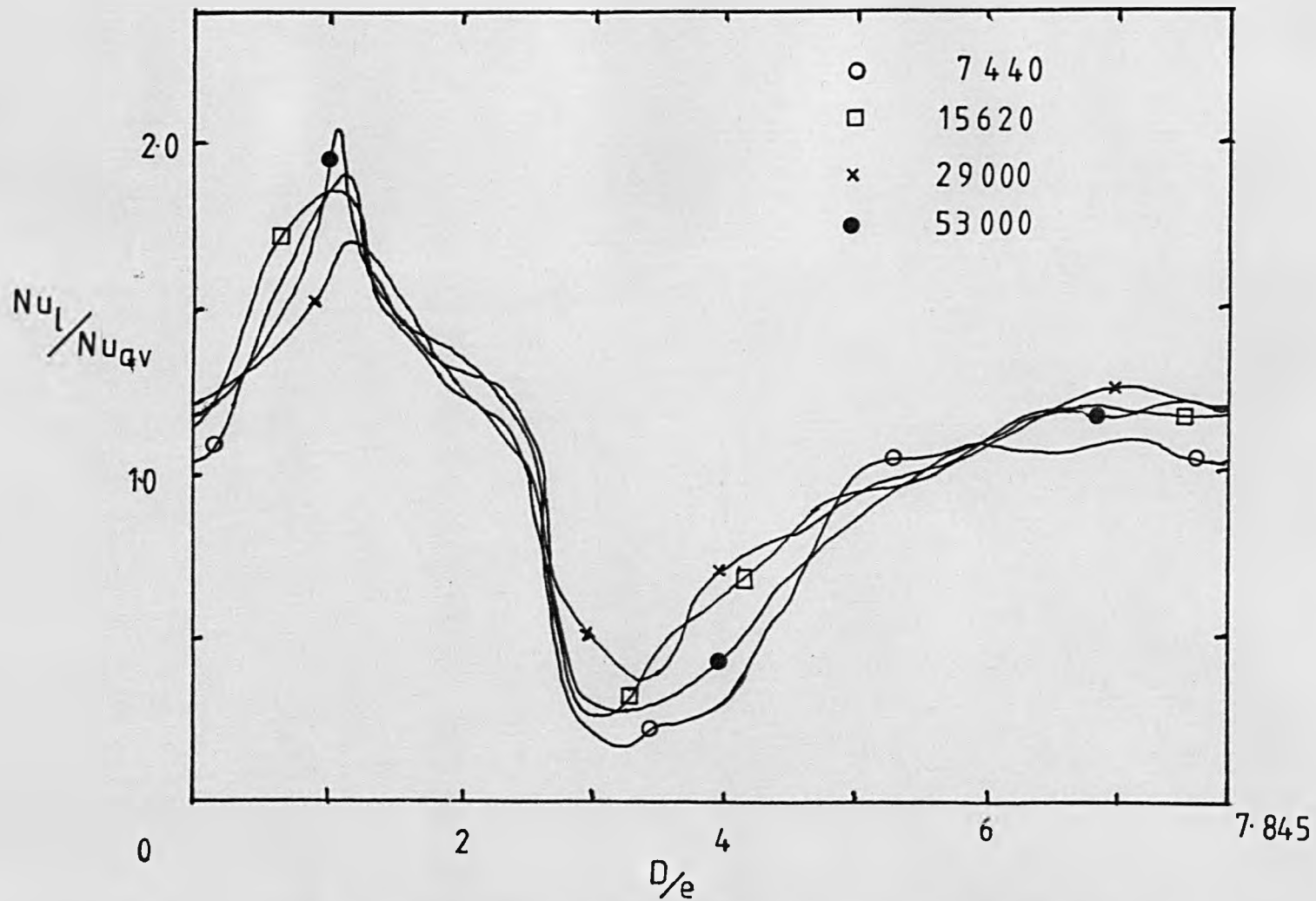


**FIGURE 6.24. NUSSELT NUMBER DISTRIBUTION FOR SQUARE RIB DEPOSITED SURFACE**

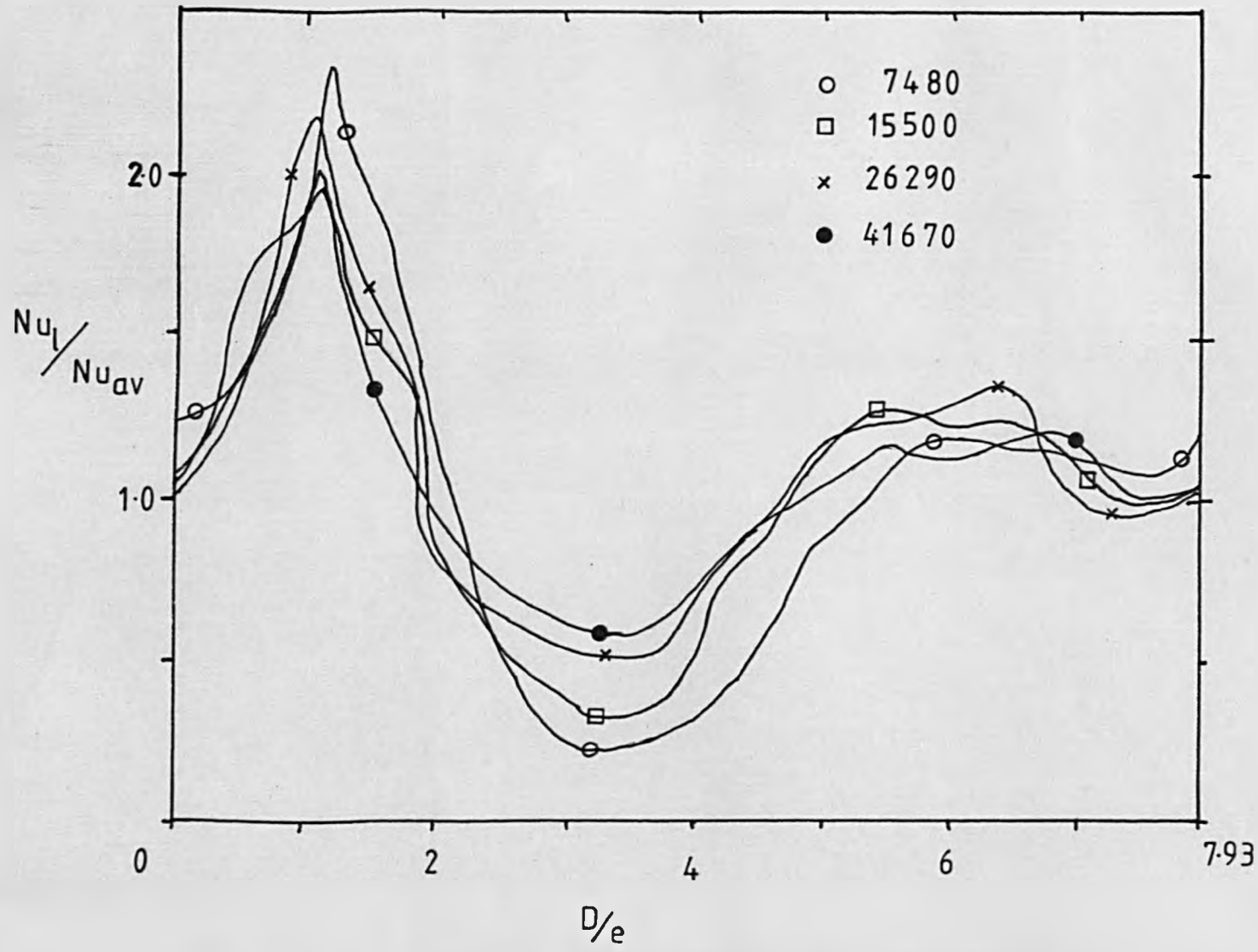
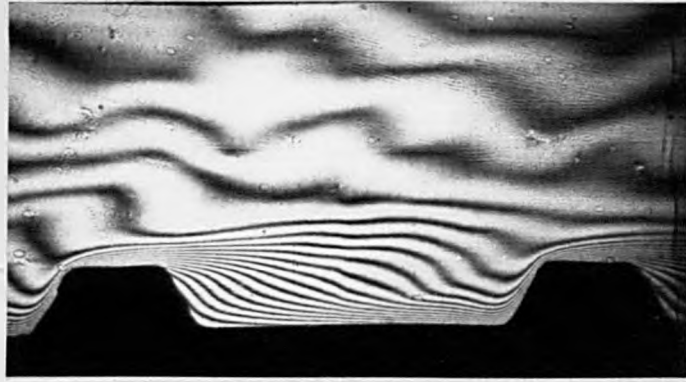
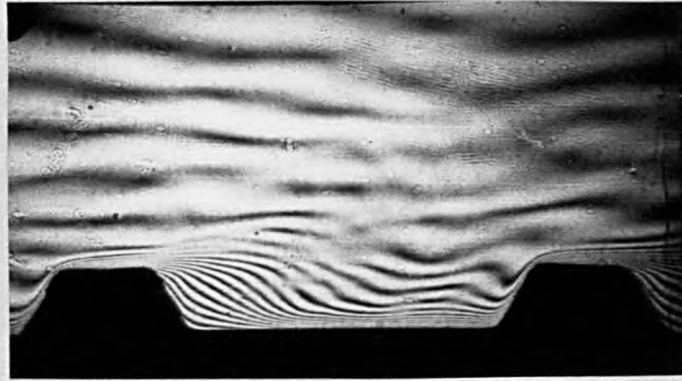


**FIGURE 6.25. NUSSELT NUMBER DISTRIBUTION FOR ROUNDED RIB DEPOSITED SURFACE.**

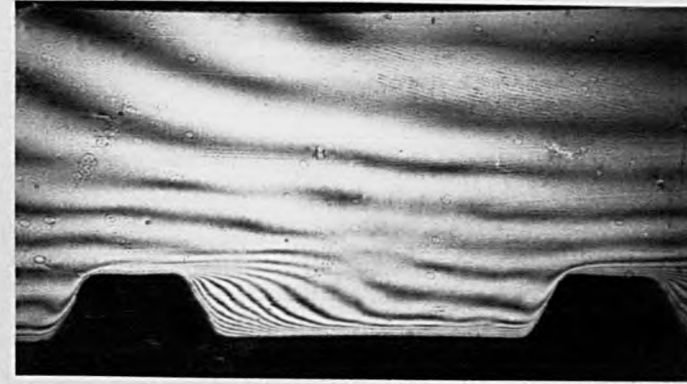
←—————→ Flow



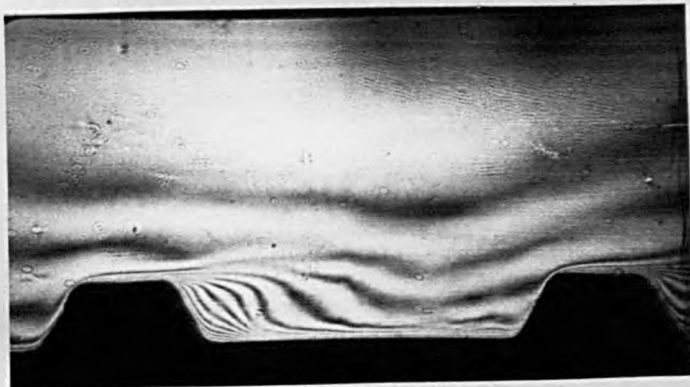
Re = 4140



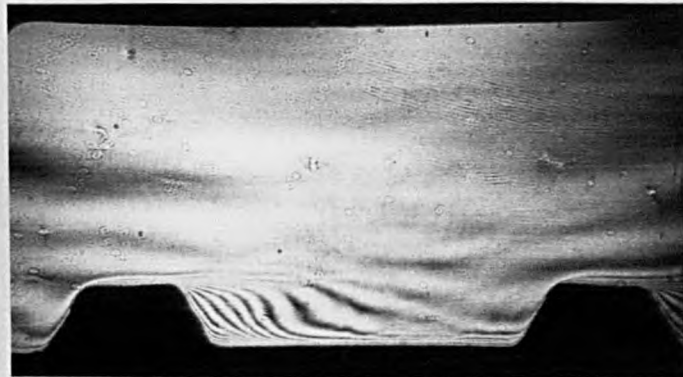
Re = 14140



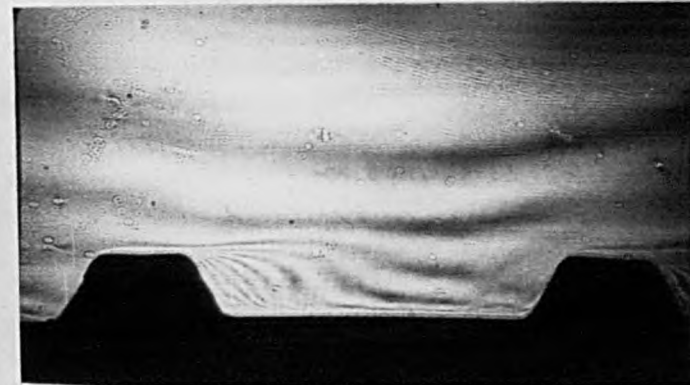
Re = 23040



Re = 27170



Re = 41280



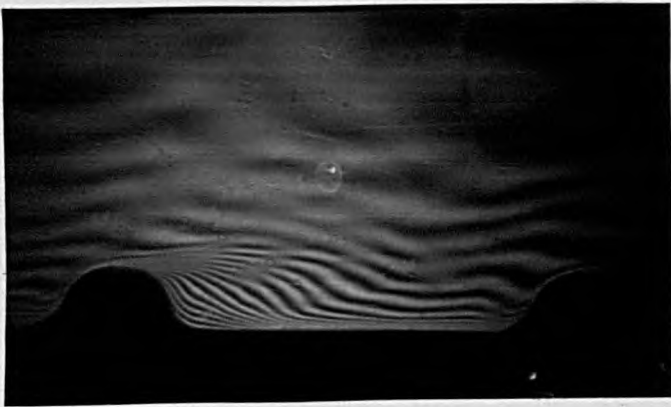
Re = 49150

FIGURE 6.26 REAL TIME IMAGES FOR SQUARE RIB DEPOSITED SURFACE

→ Flow



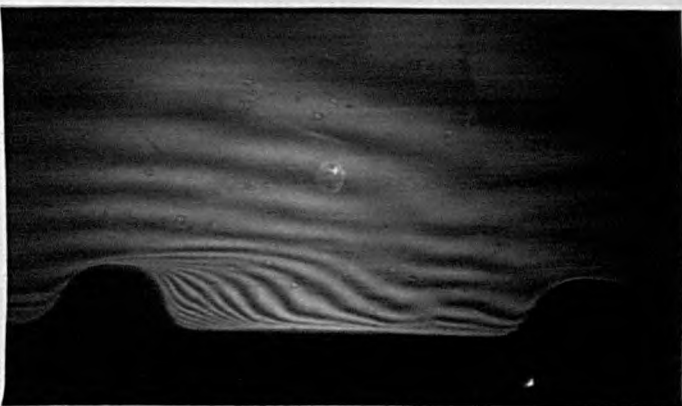
Re = 3620



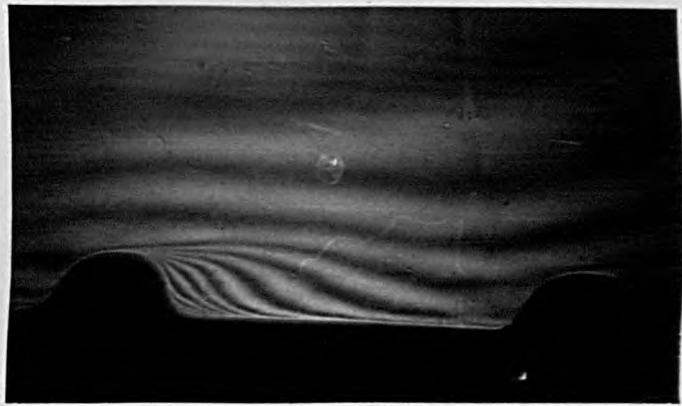
Re = 5610



Re = 13600



Re = 19560



Re = 28670



Re = 40200

FIGURE 6.27 REAL TIME IMAGES OF ROUNDED RIB DEPOSITED SURFACE

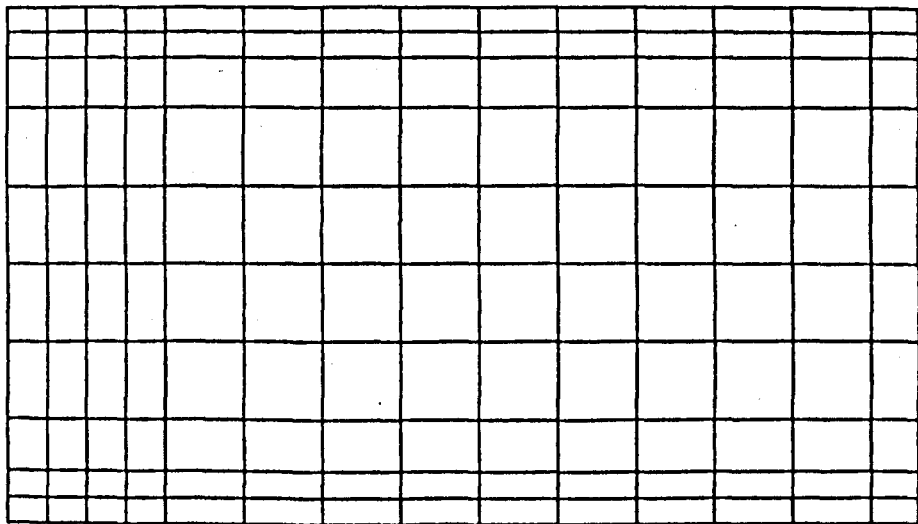


**FIGURE 6.28. INITIAL TEST MESH (14 X 10 elements)**

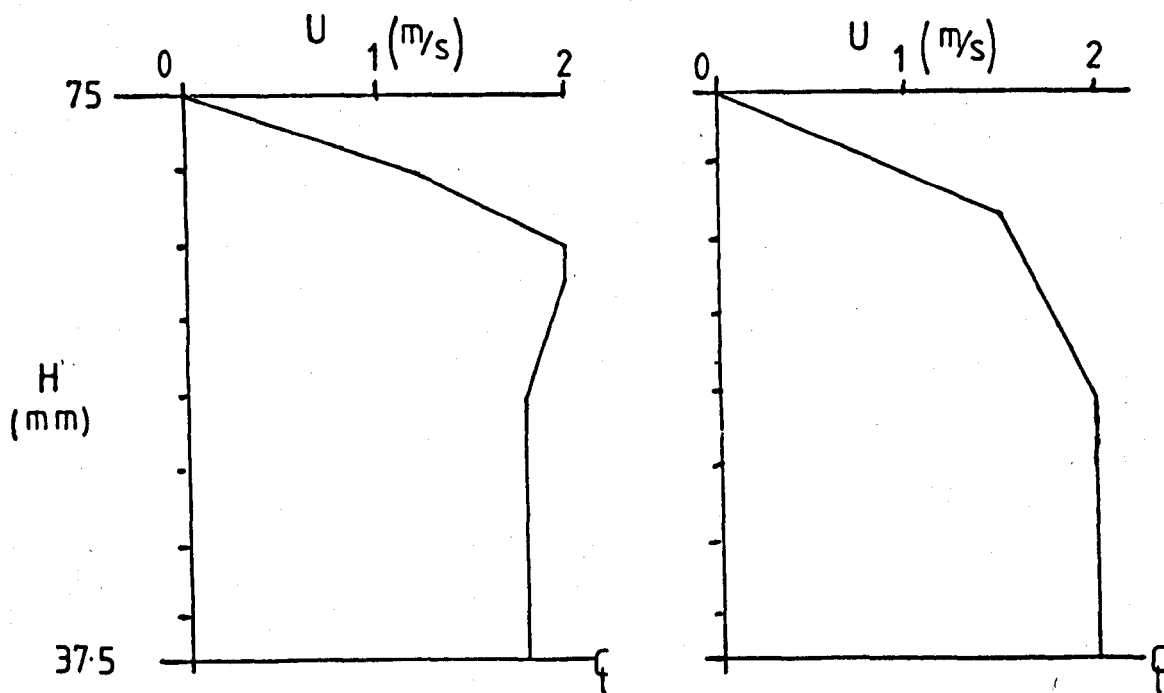


**FIGURE 6.29. INLET TEST VELOCITIES**

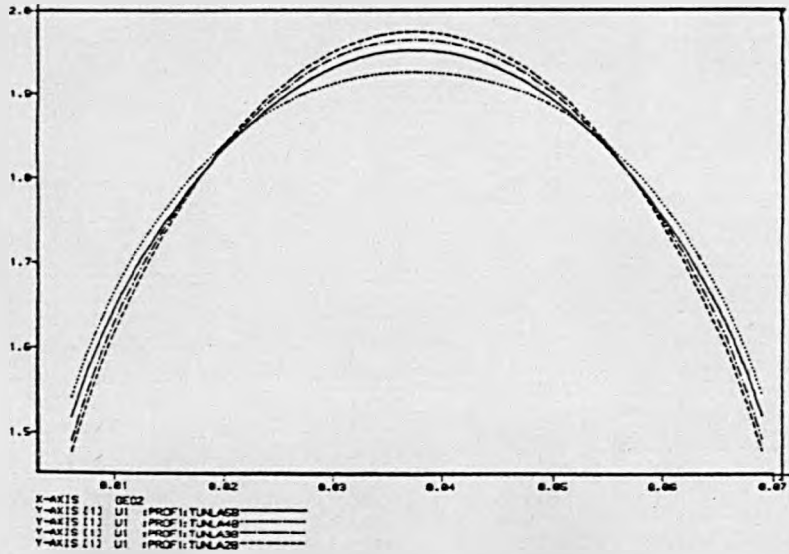


FIGURE 6.30. PREDICTED VELOCITY PROFILES AT WORKING SECTION

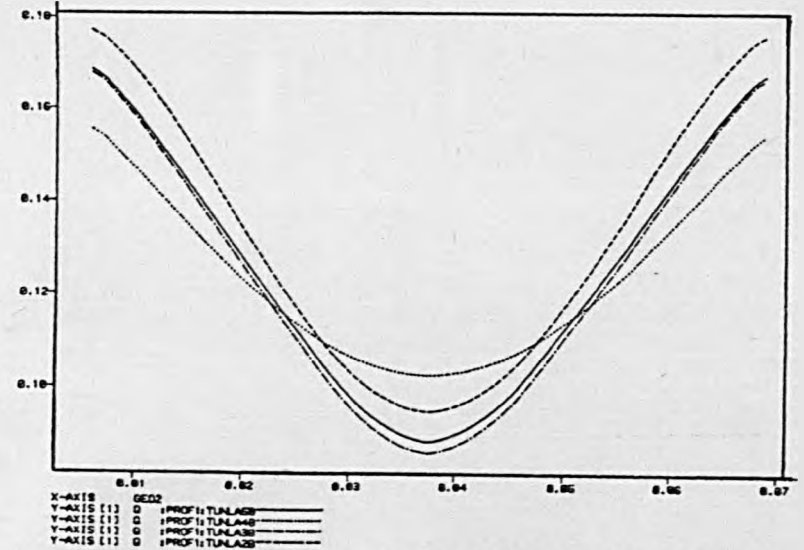
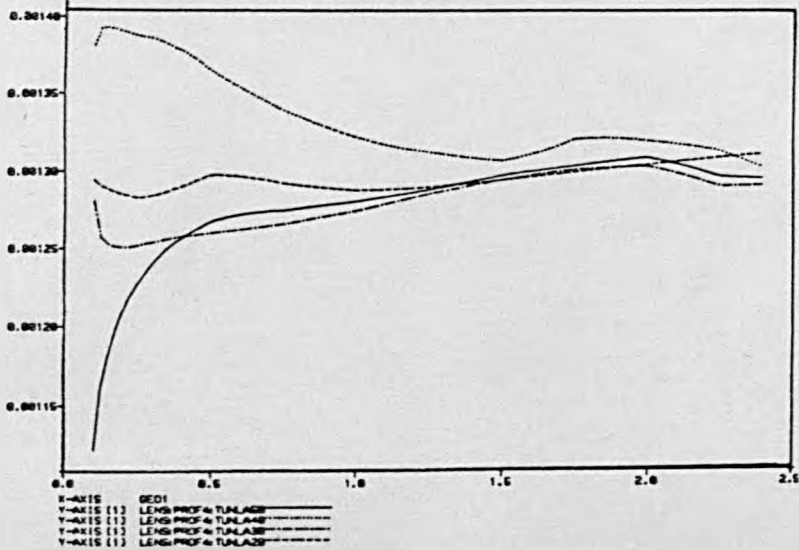
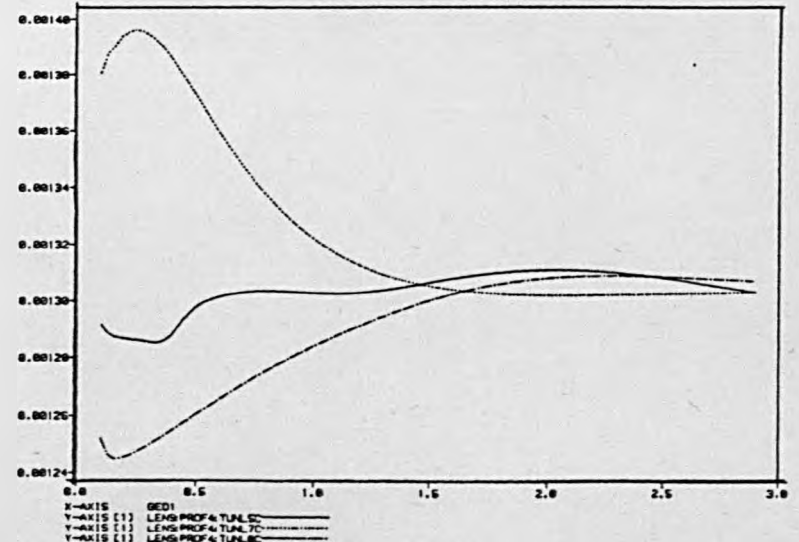


FIGURE 6.31. PREDICTED TURBULENCE LEVELS AT WORKING SECTION



6.32(a) LENGTH SCALE PREDICTED USING A COARSE MESH



6.32(b) LENGTH SCALE PREDICTED USING A FINER MESH

FIGURE 6.32. ILLUSTRATION OF MESHING PROBLEMS

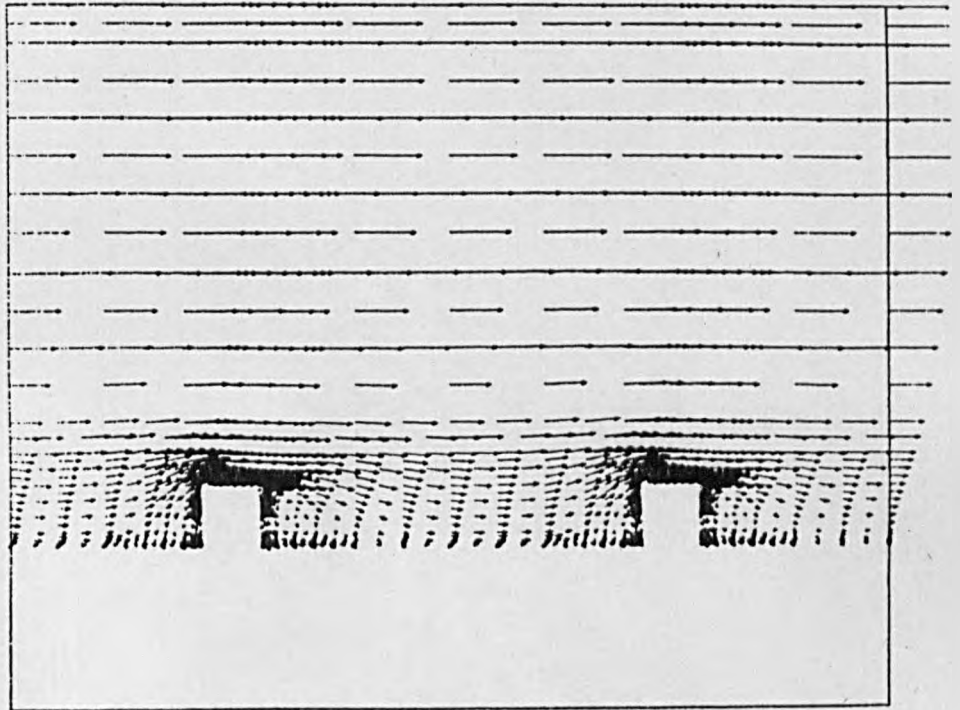


FIGURE 6.33(a)      SQUARE RIB

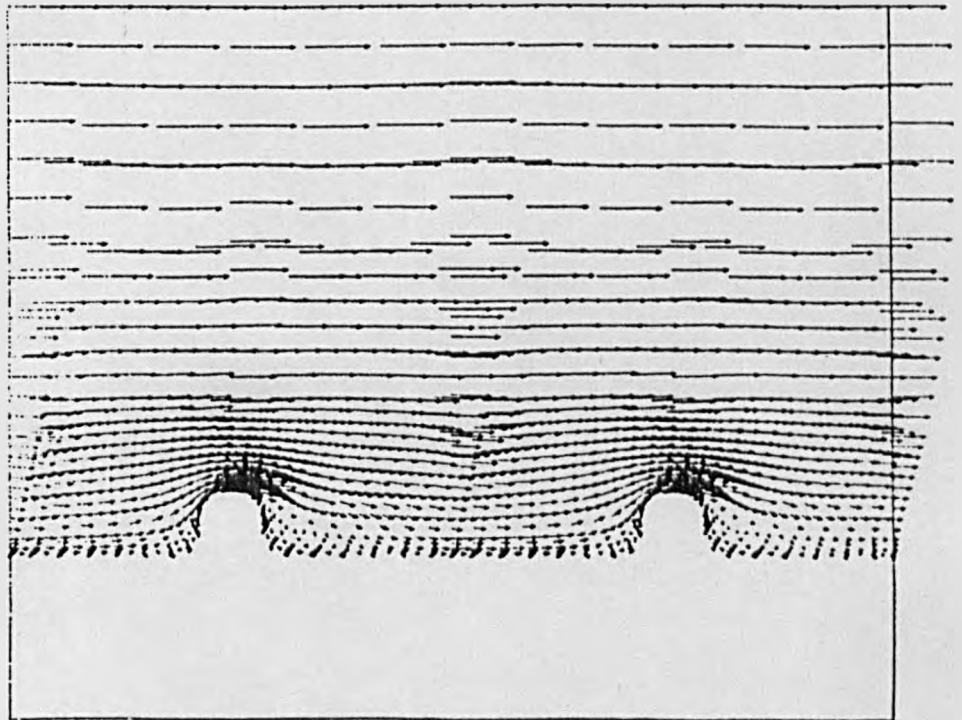


FIGURE 6.33(b)      ROUNDED RIB

FIGURE 6.33.      MOMENTUM FIELD PREDICTIONS FOR RIBBED GEOMETRIES

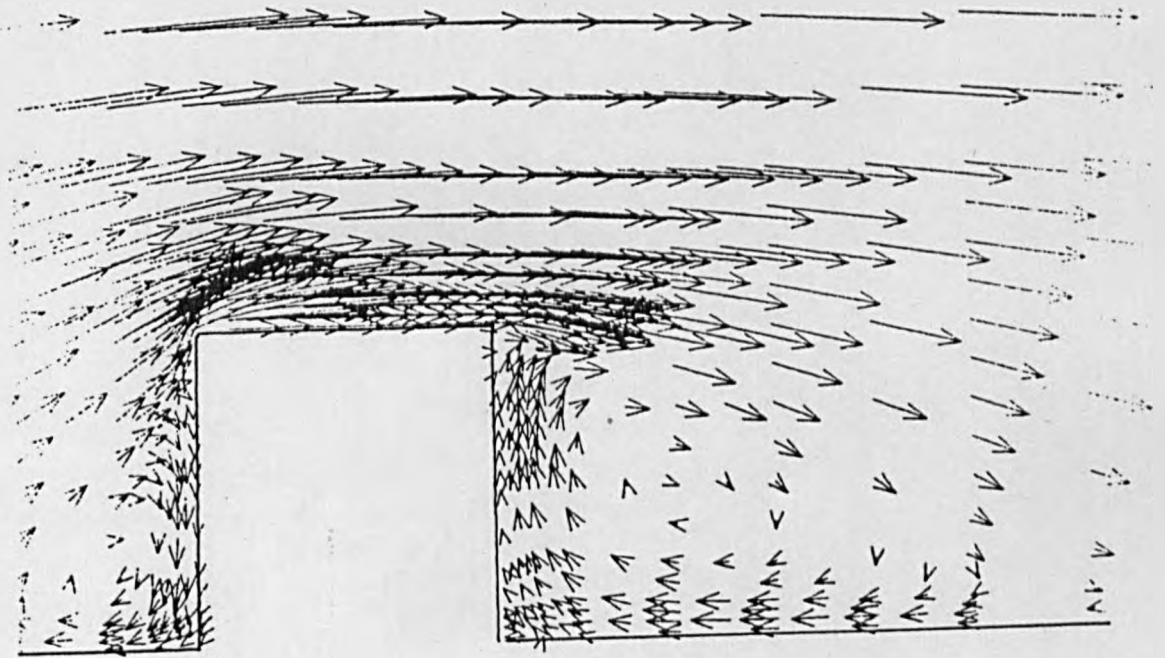


FIGURE 6.34(a)      SQUARE RIB

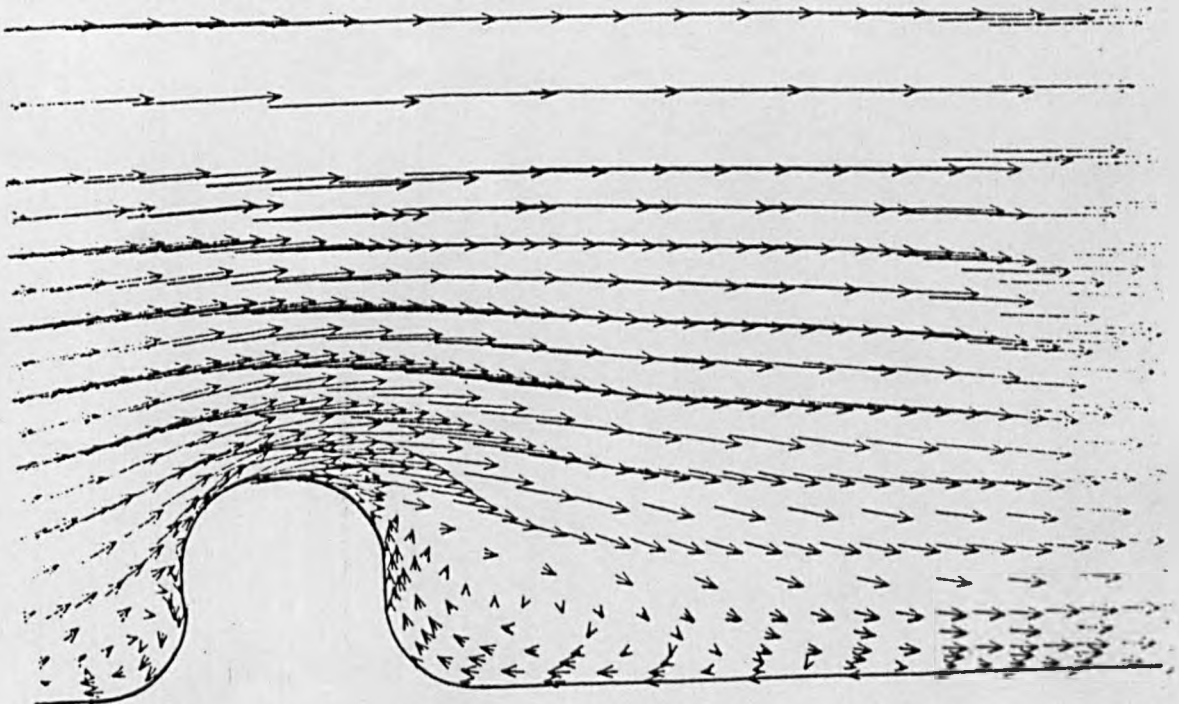
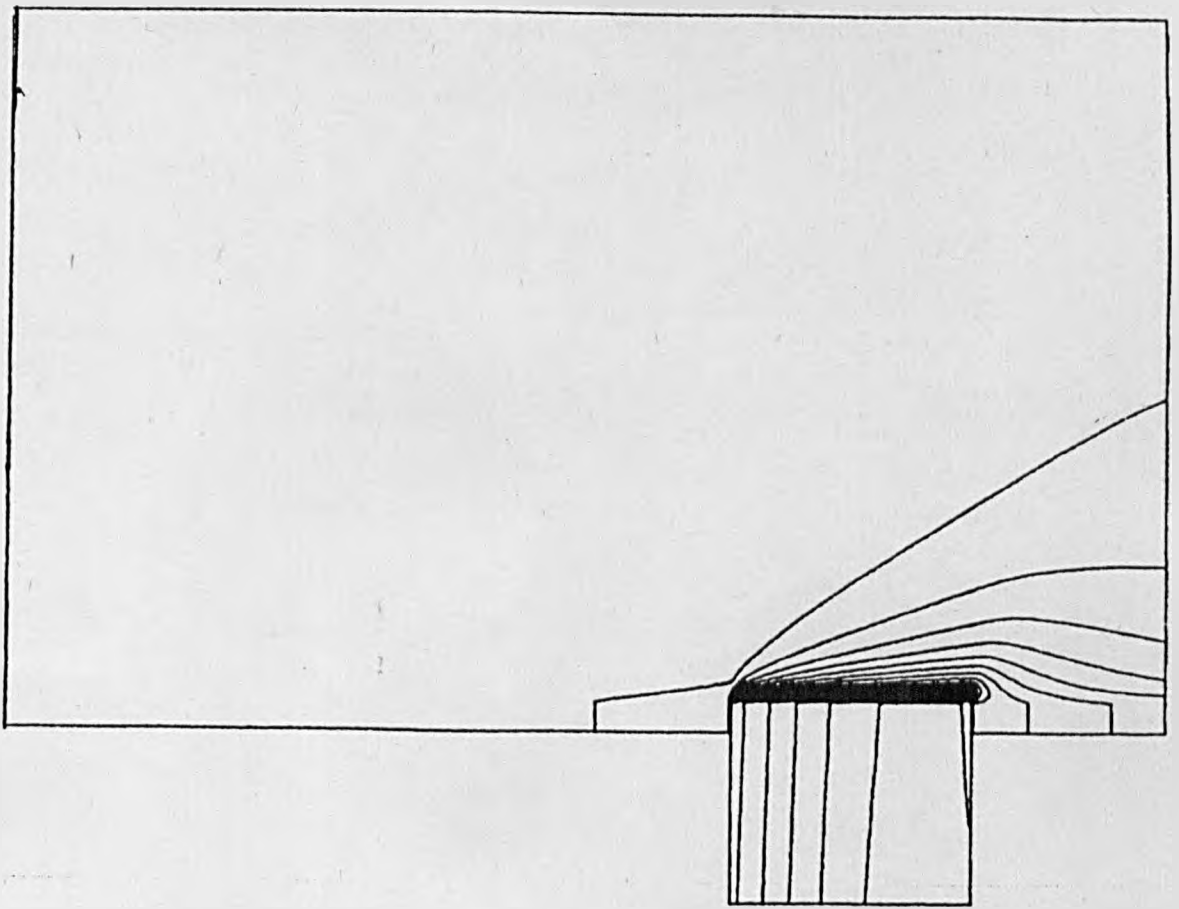
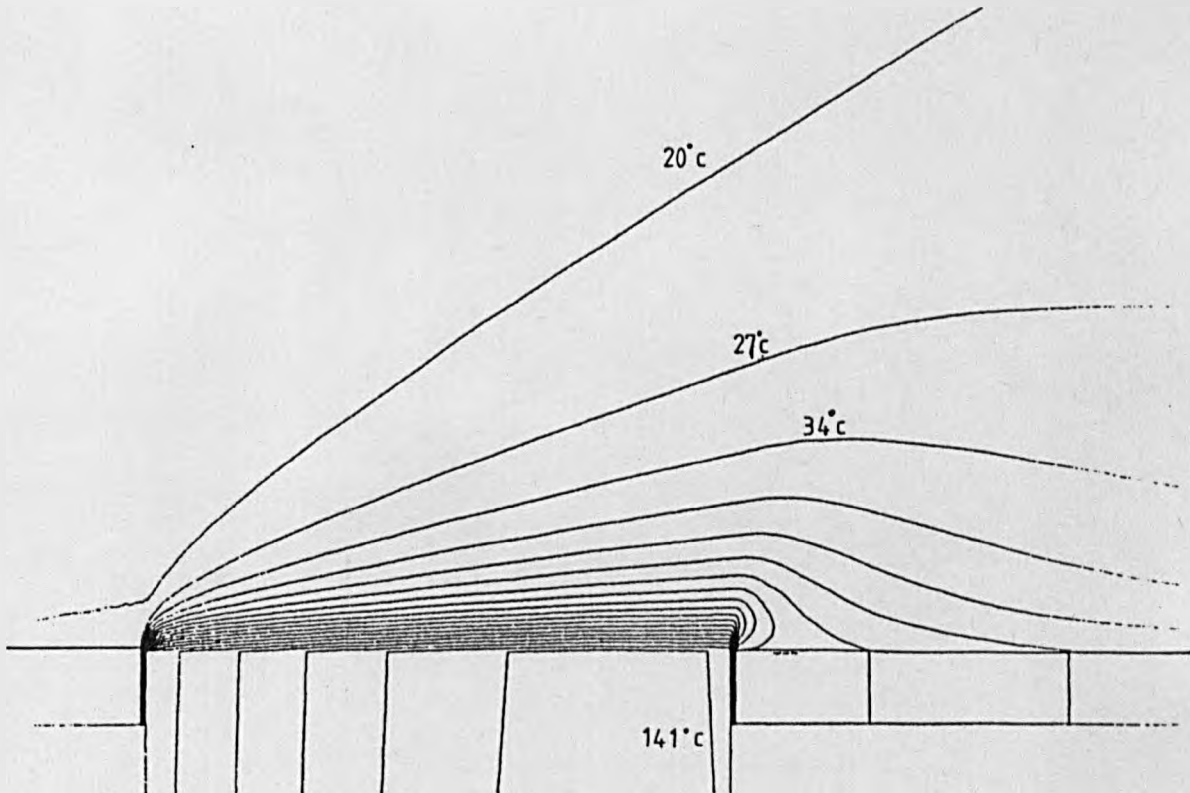


FIGURE 6.34(b)      ROUNDED RIB

FIGURE 6.34.      ENLARGED MOMENTUM FIELD AROUND RIB



**FIGURE 6.35. THERMAL FIELD PREDICTIONS FOR SMOOTH TUNNEL.**



**FIGURE 6.36. HEATER PLATE SECTION FOR SMOOTH TUNNEL.**

→ Flow

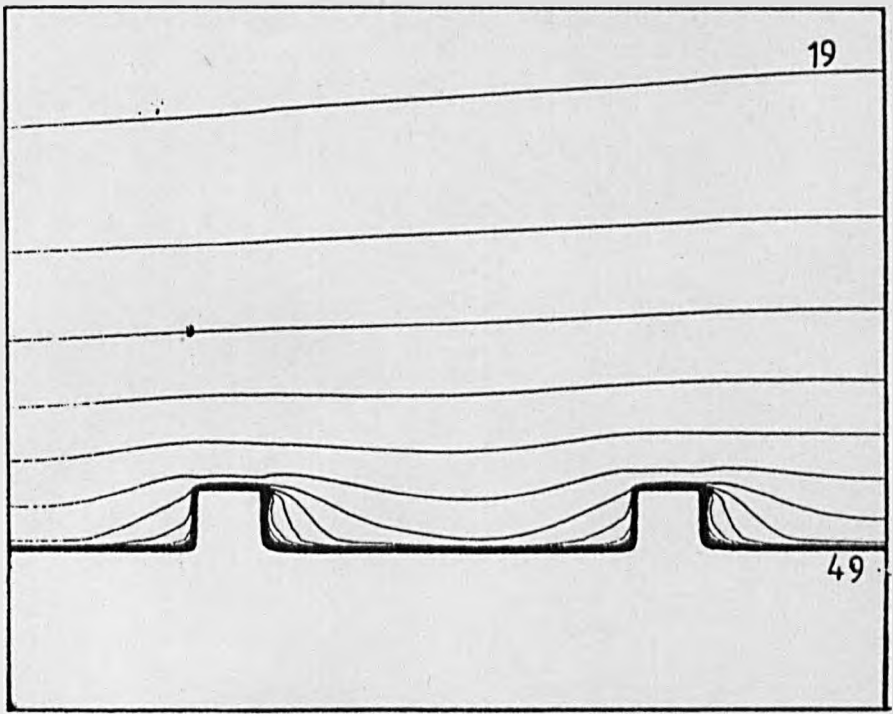


FIGURE 6.37(a) SQUARE RIB

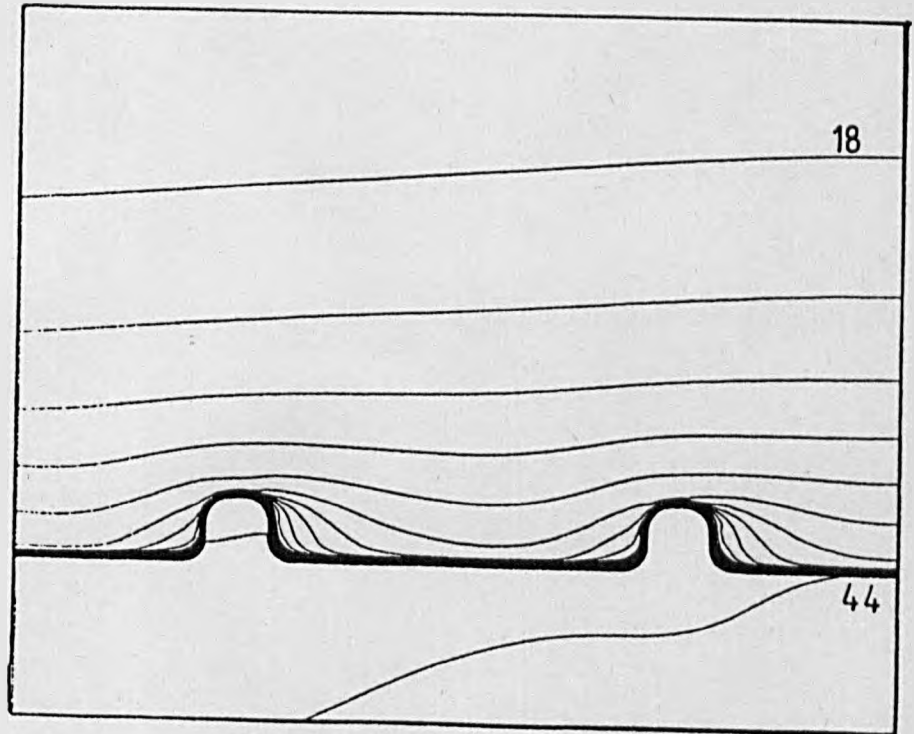


FIGURE 6.37(b) ROUNDED RIB

FIGURE 6.37. THERMAL FIELD PREDICTIONS FOR RIBBED GEOMETRIES

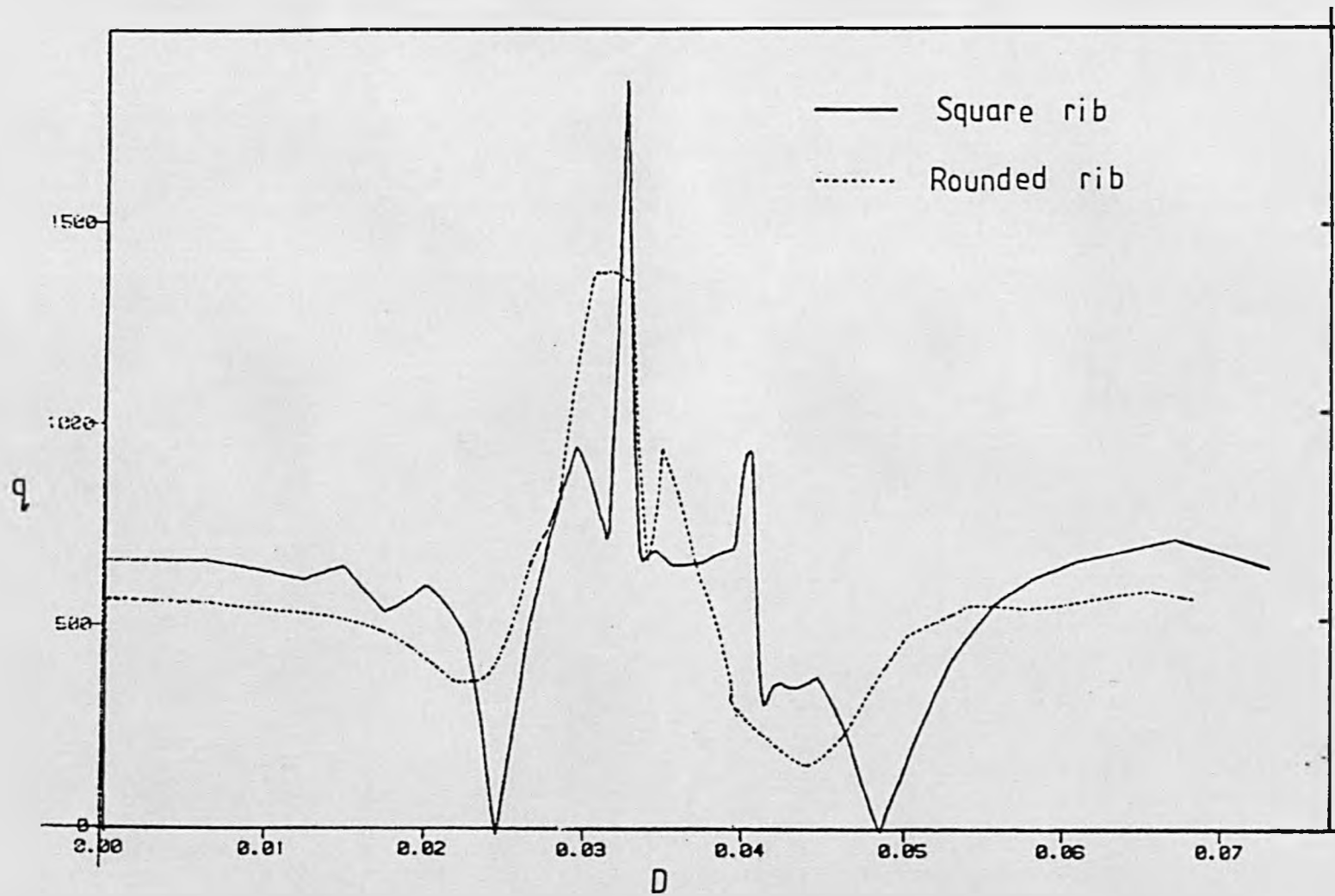


FIGURE 6.38. HEAT FLUX DISTRIBUTION FOR RIBBED GEOMETRIES